New developments in the theory of current sheet instabilities in collisionless plasmas

Camille Granier

Camille Granier. New developments in the theory of current sheet instabilities in collisionless plasmas. Plasma Physics [physics.plasm-ph]. Université Côte d'Azur; Politecnico di Torino, 2022. English. NNT : 2022COAZ4109 . tel-04047928

HAL Id: tel-04047928
https://theses.hal.science/tel-04047928v1

Submitted on 27 Mar 2023

PhD Thesis in co-supervision between:

Université Côte d'Azur

Politecnico di Torino

New developments in the theory of current sheet instabilities in collisionless plasmas

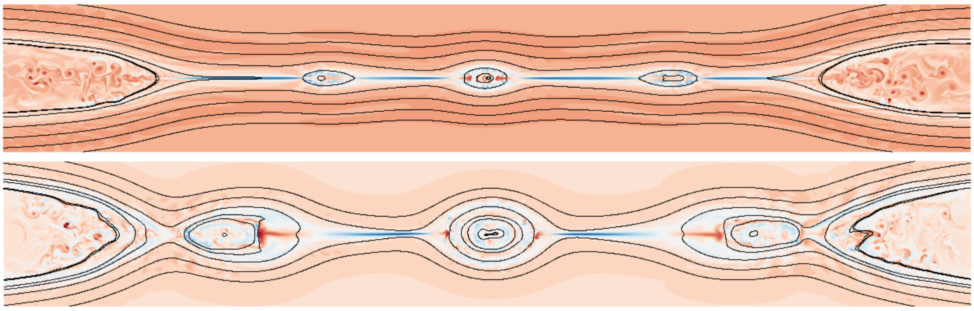

Camille Granier

Jury:

Emanuele Tassi	Supervisor - Chargé de recherche at CNRS, Laboratoire Lagrange, France
Daniela Grasso	Co-supervisor - Researcher at Istituto dei Sistemi Complessi, CNR, Politecnico di Torino, Italy
Philippa Browning	Referee - Full Professor at Manchester University, UK
Matthew Kunz	Referee - Associate Professor at Princeton University, US
Magali Muraglia	Examiner - Maitre de conférence at Université Aix Marseille, Laboratoire Physique des Interactions Ioniques et Moléculaires, France
Francesco Pegoraro	Examiner - Full Professor Emeritus at the Università di Pisa, Italy
Thierry Passot	Examiner - Directeur de recherche at CNRS, Laboratoire Lagrange, France

UNIVERSITÉ CÔTE D'AZUR

ÉCOLE DOCTORALE
SCIENCES FONDAMENTALES ET APPLIQUÉES

POLITECNICO DI TORINO

THÈSE DE DOCTORAT

Nouveaux développements sur la théorie des instabilités des feuilles de courant dans les plasmas non-collisionels

Camille Granier

Université Côte d'Azur, Observatoire de la Côte d'Azur, CNRS, Laboratoire Lagrange
Politecnico di Torino

Présentée en vue de l'obtention du grade de docteur en Physique
de l'Université Côte d'Azur
Dirigée par : Emanuele Tassi
Co-encadrée par : Daniela Grasso
Soutenue le : 16 Décembre 2022

Devant le jury composé de :
Emanuele Tassi
Daniela Grasso
Philippa Browning
Matthew Kunz
Magali Muraglia
Francesco Pegoraro
Thierry Passot

UNIVERSITÉ FRANCO ITALIENNE | UNIVERSITÀ ITALO FRANCESE

New developments in the theory of current sheet instabilities in collisionless plasmas

Referees

Philippa Browning
Full Professor at Manchester University, UK

Matthew Kunz
Associate Professor at Princeton University, US

Examiners

Emanuele Tassi
Chargé de recherche at CNRS, Laboratoire Lagrange, France

Daniela Grasso
Researcher at Istituto dei Sistemi Complessi, CNR, Politecnico di Torino, Italy

Magali Muraglia
Maitre de conférence at Université Aix Marseille, Laboratoire Physique des Interactions Ioniques et Moléculaires, France

Francesco Pegoraro
Full Professor Emeritus at the Università di Pisa, Italy

Thierry Passot
Directeur de recherche at CNRS, Laboratoire Lagrange, France

Abstract

Abstract Magnetic reconnection is a change of topology of the magnetic field, responsible for the explosive release of magnetic energy in astrophysical plasmas, as in the case of magnetospheric substorms and coronal mass ejections, as well as in laboratory plasmas, as in the case of sawtooth crashes in tokamaks. In collisionless plasmas as, for instance, the magnetosphere and the solar wind, electron inertia becomes particularly relevant to drive reconnection at regions of intense localized current, referred to as current sheets. In these collisionless, magnetized environments, the temperature can often be anisotropic with respect to the magnetic field direction and effects at the electron scale on the reconnection process can become non-negligible.

In this Thesis, the stability of two-dimensional current sheets with respect to reconnecting perturbations in collisionless plasmas with a strong guide field is analysed on the basis of gyrofluid models assuming cold ions. These models take into account the possibility of an equilibrium temperature anisotropy, and a finite β_e, the latter being a parameter corresponding to the ratio between equilibrium electron kinetic pressure and magnetic pressure.

We derive and analyze a dispersion relation for the growth rate of collisionless tearing modes accounting for equilibrium electron temperature anisotropy. The analytical predictions are tested against numerical simulations, showing a very good quantitative agreement. In the isotropic case, accounting for finite-β_e effects, we observe a stabilization of the tearing growth rate when electron finite Larmor radius effects become important. In the nonlinear phase, stall phases and faster than exponential phases are observed, similarly to what occurs in the presence of ion finite Larmor radius effects.

We also investigate the marginal stability conditions of secondary current sheets for the development of plasmoids, in collisionless plasmas. In the isotropic $\beta_e \rightarrow 0$ limit, we analyze the geometry that characterizes the reconnecting current sheet, and identify the conditions under which it is plasmoid unstable. Our study shows that plasmoids can be obtained, in this context, from current sheets with an aspect ratio much smaller than in the collisional regime. Furthermore, we investigate plasmoid formation comparing gyrofluid and gyrokinetic simulations. We show that the effect of finite β_e promotes the plasmoid instability. Finally, we study the impact of the closure applied on the moments, performed during the derivation of the gyrofluid model, on the distribution and conversion of energy during reconnection.

Keywords Magnetic reconnection, gyrofluid models, collisionless plasma, plasmoids

Résumé La reconnexion magnétique est une modification de la topologie du champ magnétique, responsable d'une libération explosive d'énergie magnétique dans les plasmas astrophysiques. Elle intervient dans les orages magnétiques, les éjections de masse coronale, ainsi que dans les plasmas de laboratoire. Dans les plasmas sans collisions comme ceux de la magnétosphère et le vent solaire, l'inertie des électrons devient particulièrement pertinente pour provoquer la reconnexion des lignes de champs dans les régions de courant intense, appelées feuilles de courant. Dans ces environnements non collisionnels, la température peut souvent être anisotrope et les effets présent à l'échelle électronique peuvent affecter le processus de reconnexion.

Dans cette thèse, la stabilité des feuilles de courant bidimensionnelles dans des plasmas sans collisions avec un fort champ guide est analysée à partir de modèles gyrofluides qui considèrent des ions froids. Ces modèles peuvent prendre en compte une anisotropie de température d'équilibre, et un β_e fini. Le paramètre β_e correspondant au rapport entre la pression cinétique électronique d'équilibre et la pression magnétique.

Nous dérivons et analysons une relation de dispersion pour le taux de croissance des modes tearing sans collisions en tenant compte de l'anisotropie de la température d'équilibre des électrons. Les prédictions analytiques sont testées par des simulations numériques, montrant un très bon accord quantitatif. Dans le cas isotrope, en prenant en consideration des effets de β_e finis, nous observons une stabilisation du taux de croissance du mode tearing lorsque les effets du rayon de Larmor fini des électrons deviennent non négligeables. Dans la phase non linéaire, des phases de ralentissement et des phases d'accélération sont observées, identiquement à ce qui se produit en présence d'effets de rayon de Larmor fini des ions.

Nous étudions également les conditions de stabilité marginale des feuilles de courant secondaires, pour le développement de plasmoïdes. Dans le régime isotrope $\beta_e \rightarrow 0$, nous analysons la géométrie qui caractérise le feuillet de courant, et identifions les conditions pour lesquelles elle devient instable à l'instabilité plasmoïde. Cette étude montre que des plasmoïdes peuvent être obtenus, dans ce contexte, à partir de feuille de courants aillant un rapport d'aspect beaucoup plus petit que dans le régime collisionnel. De plus, nous étudions la formation de plasmoïdes en comparant les simulations gyrofluides et gyrocinétiques. Ceci a permis de montrer que l'effet de β_e favorise l'instabilité plasmoïde. Enfin, nous étudions l'impact de la fermeture appliquée sur les moments, effectuée lors de la dérivation du modèle gyrofluide, sur la distribution et la conversion de l'énergie lors de la reconnexion.

Mots-Clés Reconnection magnétique, modèles gyrofluides, plasmas non collisionels, plasmoïdes

Sommario La riconnessione magnetica è un cambiamento nella topologia del campo magnetico, responsabile del rilascio esplosivo di energia magnetica nei plasmi astrofisici, come nelle tempeste magnetosferiche e nelle espulsioni di massa coronale, nonché nei plasmi di laboratorio, come nel caso delle oscillazioni a dente di sega nei tokamak. Nei plasmi non-collisionali come, ad esempio, la magnetosfera e il vento solare, l'inerzia elettronica diventa particolarmente efficace nel causare la riconnessione in regioni di corrente intensa e localizzata, detti strati di corrente. In tali plasmi non-collisionali, la temperatura può essere spesso anisotropa e gli effetti su scala elettronica sul processo di riconnessione possono diventare non trascurabili.

In questa tesi, viene analizzata la stabilità di strati di corrente bidimensionali in plasmi non-collisionali con un forte campo guida, sulla base di modelli girofluidi che assumono ioni freddi. Questi modelli possono tenere conto di un'anisotropia di temperatura di equilibrio e di un β_e finito. Quest'ultimo è un parametro corrispondente al rapporto tra la pressione cinetica elettronica di equilibrio e la pressione magnetica.

Deriviamo e analizziamo una relazione di dispersione per il tasso di crescita dei modi tearing non-collisionali tenendo conto dell'anisotropia della temperatura di equilibrio degli elettroni. Le previsioni analitiche sono verificate mediante simulazioni numeriche, che mostrano un ottimo accordo quantitativo. Nel caso isotropico, tenendo conto degli effetti di β_e finito, si osserva una stabilizzazione del tasso di crescita del modo tearing quando diventano rilevanti gli effetti del raggio finito di Larmor degli elettroni. Nella fase non lineare si osservano fasi di decelerazione e fasi di accelerazione, simili a quanto avviene in presenza di effetti del raggio di Larmor finito ionico.

Studiamo anche le condizioni di stabilità marginale degli strati di corrente secondaria, per lo sviluppo di plasmoidi, in plasmi senza collisioni. Nel regime isotropico con $\beta_e \to 0$, analizziamo la geometria che caratterizza lo strato di corrente e identifichiamo le condizioni in cui esso diventa instabile a causa di un'instabilità che genera plasmoidi. Il nostro studio mostra che i plasmoidi possono essere ottenuti, in questo contesto, da strati di corrente aventi un rapporto d'aspetto molto più piccolo rispetto al regime collisionale. Inoltre, studiamo la formazione di plasmoidi confrontando simulazioni girofluidi e girocinetiche. Ciò ha permesso di dimostrare che l'effetto di β_e promuove l'instabilità che genera plasmoidi. Infine, si studia l'impatto della chiusura applicata ai momenti, eseguita durante la derivazione del modello girofluido, sulla distribuzione e conversione dell'energia durante la riconnessione.

Parole Chiave Riconnessione magnetica, modelli girofluidi, plasmi non-collisionali, plasmoidi

Acknowledgments

First of all, I would like to thank my advisors who have been a source of knowledge and support throughout this PhD. I am extremely grateful to Emanuele Tassi who has followed my progress since the beginning of my Master's Thesis. His methods, approaches and guiding ideas have shaped my research. My life has been, and will certainly continue to be, enriched from knowing him. I would like to thank Daniela Grasso, for her clear advice on how to conduct my research. Her inspiring determination has been a source of admiration. I would like to thank Dario Borgogno for his considerable input in my supervision, notably on the numerical side. Dario and Daniela have always supported and encouraged me, even when my simulations were far from making any sense.

I would like to thank all my committee members, which includes Magali Muragli and Francesco Pegoraro, for providing me with valuable feedback (and passing me). Philippa Browning and Matthew Kunz deserve special mention, for agreeing to evaluate my manuscript carefully. I also particularly thank Thierry Passot for having chaired the jury, and for having followed my progress throughout my PhD. I am deeply thankful to him, as well as to Pierre Louis Sulem, who granted me the opportunity to undertake a short-term postdoc after my PhD.

I would like to thank Ryusuke Numata for his availability which led to an easy and fruitful collaboration. The same acknowledgments extend to Luca Comisso, for teaching me about plasmoids and for his hospitality during my visit at Columbia University.

The work environment was extremely pleasant, which was made possible thanks to the non-exhaustive list of people mentioned hereafter. I thank the members of the Fluid, Plasma and Turbulence group, for giving me the time to converse about my work and raising interesting questions. Silvio Cerri deserves special recognition, for sharing his *experience*, and I hope we now share a good friendship that will persist throughout my career. To the chef, Khaled, thank you so much for your exquisite meals. To Christine Delobelle, thank you for smoothly handling all administrative details that arose during my PhD. I also acknowledges the financial support provided by the Université Franco-Italienne through the Vinci program.

I cannot give enough thanks to all the friends who have provided good company and warm support during these three years. However, I **must** single out Nicolàs Müller, Max Mahlke and Julia Maia. There have been many more, from the Observatory in Nice, from Politecnico in Turin, from conferences and schools, who enriched my experience thanks to their friendships.

My deepest gratitude goes to Simon. His help in completing this thesis was invaluable, not only because he gave me a lot of support, but also because my mental strength has grown while taking his as an example. Finally, and most of all, I must thank my family: my parents, grandparents, my brother, and my cats for all the support they have given me. Thank you.

Contents

List of Publications

International Refereed Journals

Submitted **C. Granier**, R. Numata, D. Borgogno, E. Tassi, D. Grasso, *Investigation of the collisionless plasmoid instability based on fluid, gyrofluid and gyrokinetic integrated approach.* Preprint on ArXiv: `https://arxiv.org/abs/2302.03073`

2022 **C. Granier**, D. Borgogno, L. Comisso, D. Grasso, E. Tassi, R. Numata, *Marginally Stable Current Sheets in Collisionless Magnetic Reconnection.* Phys. Rev. E. 106, L043201 `https://doi.org/10.1103/PhysRevE.106.L043201`

2022 **C. Granier**, D. Borgogno, D. Grasso, E. Tassi, *Gyrofluid analysis of electron β_e effects on collisionless reconnection*, J. Plasma Phys. 88 905880111. `https://doi.org/10.1017/S0022377822000010`

2021 **C. Granier**, E. Tassi, D. Borgogno, D. Grasso, *Impact of electron temperature anisotropy on the collisionless tearing mode instability in the presence of a strong guide field*, Physics of Plasmas, 28 022112. `https://doi.org/10.1063/5.0037227`

2020 **C. Granier** & E. Tassi, *Linear stability of magnetic vortex chains in a plasma in the presence of equilibrium electron temperature anisotropy*, J. Phys. A: Math and Theor., 53 385702. `https://doi.org/10.1088/1751-8121/aba466`

Proceedings

2022 **C. Granier**, D. Borgogno, L. Comisso, D. Grasso, R. Numata, E. Tassi *Fluid and gyrokinetic simulations of plasmoid formation in collisionless plasmas*, Proceedings of the 48th EPS Conference on Plasma Physics, O1.402

List of Symbols

For the benefit of the reader, we provide here a list of symbols used in this thesis. For each symbol the meaning is indicated, as well as the reference to the formula where such symbol is first used and defined.

Distribution functions

$\mathrm{f}_{\mathrm{micro}}$	microscopic distribution function	2.1
f_s	particle distribution function	# 2.3
$\widetilde{\mathrm{f}}_s$	perturbed particle distribution function	2.3, 2.15
$\mathcal{F}_{eq_s}$	equilibrium distribution function	2.15
$\widetilde{f}_s$	gyrocenter distribution function	2.15
$\widetilde{g}_s$	generalized perturbed distribution function	2.35

Coordinates

$\mathbf{x}$	particle position	2.1, Fig. 2.20
$\mathbf{X}_s$	guiding center position	2.20, Fig. 2.20
$\mathbf{r}_{L_s}$	Larmor radius of the particle	2.21, Fig. 2.20
$\mathbf{v}$	particle velocity	2.18
$v_{\|\|}$	particle parallel velocity	2.18
$v_{\perp}$	particle perpendicular velocity	2.18
μ_s	magnetic moment of the particle	2.18
θ	gyroangle angle	
$A^{eq}_{\|\|0}$	amplitude of the equilibrium magnetic flux	2.155

Lengths

L_y, L_x	lengths of the domain	# 2.155
λ_D	Debye length	1.1
$d_{i,e}$	ion or electron skin depth	1.2
$\rho_{i,e}$	ion or electron gyroradius based on the thermal velocity	1.3
$\rho_{i,e\perp}$	ion or electron gyroradius based on the perpendicular temperature	# 2.50
ρ_s	ion-sound Larmor radius	1.5
$\rho_{s\perp}$	perpendicular ion-sound Larmor radius	# 2.64
$\mathbf{k}^{-1}$	wave number (= (k_x, k_y, k_z))	2.26

L	equilibrium length scale	# 2.109
L_{cs}	full length of the current sheet	# 5.2
δ_{cs}	full width of the current sheet	# 5.2
a	half width of the current sheet ($= \delta_{\mathrm{cs}}/2$)	

Times

$\omega_{p_{i,e}}^{-1}$	inverse of the plasma frequency	# 1.3
ω_{ci}^{-1}	inverse of the cyclotron frequency	# 1.2
τ_A	Alfvén time ($= L/v_A$)	2.109
τ_D	diffusion time scale	
$\tau_\star$	time scale for the plasma to be expelled from the current sheet	5.14

Velocities

$v_{th_{\|s}}$	parallel velocity based on the parallel temperature	2.23
$\mathbf{u}_\perp$	perpendicular plasma flows	
v_A	Alfvén speed	2.109
c_s	ion-sound velocity, based on electron temperature	1.5

Fluid and gyrofluid moments

n_s	particle density	2.40
N_s	gyrocenter density	2.40
u_s	particle parallel velocity	2.40
U_s	gyrocenter parallel velocity	2.40
$t_{\|s}$	parallel particle temperature	2.57
$T_{\|s}$	parallel gyrocenter temperature	2.40
$t_{\|s}$	perpendicular particle temperature	2.58
$T_{\perp s}$	perpendicular gyrocenter temperature	2.40

Electromagnetic fields and potentials

$\mathbf{E}$	electric field	2.9
$\mathbf{B}$	magnetic field	2.8
ϕ	electrostatic potential	2.9
$\mathbf{A}$	magnetic vector potential	2.8
$A_\|^{(0)}$	equilibrium magnetic potential	2.155, 2.156
$\phi^{(0)}$	equilibrium electrostatic potential	# 2.155
$A_\|$	perturbation of parallel magnetic potential	2.8
$B_\|$	perturbation of parallel magnetic field	2.8

Dimensionless parameters

δ	square root of the mass ratio	2.77
β_s	ratio thermal pressure to magnetic pressure	1.4

$\beta_{\perp_s}$	ratio perpendicular thermal pressure to magnetic pressure	2.33
Θ_s	equilibrium temperature anisotropy parameter ($= T_{0_{\perp s}}/T_{0_{\parallel s}}$)	2.24
τ_i	ratio ion to electron equilibrium temperature	# 2.66
$\tau_{\perp_i}$	ratio ion to electron perpendicular equilibrium temperature	2.66
A_{rec}	aspect ratio of the current sheet	# 1.10
R_{rec}	reconnection rate	1.13
λ	stretching factor of the equilibrium magnetic field	2.155

Other amplitudes and constants

B_0	guide field amplitude	# 2.8
n_0	equilibrium densities	# 2.23
$T_{0_{\parallel s}}$	equilibrium parallel temperature	2.23
$T_{0_{\perp s}}$	equilibrium perpendicular temperature	2.23
μ_s	magnetic moment based on the perpendicular velocity	2.23
S	Lundquist number	1.13

1 Introduction

Magnetic reconnection can be roughly summarized by saying that oppositly oriented magnetic-field lines, under some conditions, break and reconnect to a new configuration. Once the modification of the topology has taken place, strongly curved magnetic-field lines drive Alfvénic outflows. During this process, the magnetic energy initially stored is converted into kinetic energy, accelerated particles, and heating. This process takes place in a wide variety of astrophysical plasmas and underlies many transient phenomena in nature. Solar flares, magnetic substorms, and $\gamma-$ray bursts are typical examples. In addition to the astrophysical applications, a better understanding of this phenomenon is also relevant for the control of instabilities in fusion plasmas. A series of fundamental studies and experiments have been dedicated to shed light on the different mechanisms that cause this phenomenon, and to predict the very fast reconnection process observed in nature. A major obstacle for understanding reconnection is that it results from a dynamic, multi-scale coupling. This requires a coalition of many contributions using several combined approaches.

In this Introduction, we set the scene by presenting the different scales in plasma physics, focusing in particular on those that are the main subjects of this Thesis (Sec. 1.1). After giving some relevant examples of reconnection events, we present the conditions allowing it to take place (Secs. 1.2 and 1.3). This Introduction also highlights some crucial aspects, such as the difference between collisional and collisionless reconnection. Finally, because this Thesis deals with the analysis of various effects on the reconnection process, although always studied in the context of current sheet instability, a final section provides an overview of such analyses, and presents in particular the motivations behind each of these studies (Sec. 1.4).

1.1 What is a plasma?

1.1.1 Description of a plasma

The term ”plasma” was introduced for the first time in the year 1922, by the physicist Irvin Langmuir, who studied electric discharges in weakly ionized gases. The peculiarity of a plasma lies in its self-consistent behavior — the charged particles themselves generate fields and are thus subject in return to the action of these fields. This produces a collective motion of particles which can often take the form of waves. This coherent particle motion reproduces itself periodically in space and in time, which is the origin of the plasma's own oscillations.

During a rise in temperature, matter converts from a solid state to a liquid state, by melting, then converts in the state of gas, by vaporisation. The molecules will break apart and dissociate into atoms between 5×10^3 and 10^4 K. At temperatures exceeding 10^4K the last bounds are broken and atoms decompose into electrons and positive ions. The latter state is what is called a plasma, and is also called the fourth state of matter. More than 99.9% of the visible universe is made of matter in the plasma state, as it constitutes the matter of the sun, stars, inter-stellar and inter-galactic mediums, white dwarfs,.. etc.

The temperature range covered by the plasma state is vast. In cold plasmas (electric discharge lamps, electric arcs, plasma torches, etc.), the temperature T_0 hardly exceeds 10^4 K. In these cases, the average energy of the thermal agitation is insufficient to ensure complete ionization, and these plasmas are often weakly ionised. However, in hot thermonuclear fusion plasmas, confined by magnetic confinement or by inertial confinement, the temperature reaches around 10^8 K. For comparison, the temperature at the center of the sun is around 10^7 K.

As in the case of the temperature, the density of electrons, n_e, and ions, n_i, within a plasma, can vary widely. It can be of the order of 1 m^{-3} in the interstellar medium, and reaches more than 10^{12} m^{-3} in the Earth's ionosphere. It can be $\sim 10^{14}$ m^{-3} in the solar corona, and get close to 10^{20} m^{-3} in a magnetic fusion plasma. It approaches 10^{32} m^{-3} at the center of the sun or in an inertial confinement fusion plasma.

Nevertheless, not all ionized gases can be considered as plasmas, and not all plasmas can be considered in the same way. It depends, of course, on their characteristics, but above all, it depends on the scales of the phenomena in which we are interested. While ionized gases are still mainly dominated by short-range collisions, plasmas are mainly dominated by long-range electromagnetic interactions.

> Basically, **a plasma** is a hot ionized gas consisting of approximately equal numbers of positively charged ions and negatively charged electrons, to ensure a state electrically *quasi-neutral*, responding to electric and magnetic field better than gases. The motion of particles generates microscopic electromagnetic fields. These fields affect the motion of other charged particles far away, which generates *collective behavior.*

The conditions to affirm that our system can be treated as a plasma are the following. The first criteria is that the characteristic spatial scale of the process which interests us, L, must be greater than the average distance between the particles, $\sim n^{1/3}$. This condition ensures the interaction of particles with mean fields generated by the other charges.

The second criteria is given by a scale of particular importance, called the *Debye length*, $\lambda_D = \sqrt{T_0/4\pi n_0 e^2}$, [1] which is the typical distance over which any charge imbalance is shielded by the electrostatic field. In a tokamak, for instance, the fusion plasma has $\lambda_D \sim 10^{-3}$ cm. If the characteristic length of our system satifies $L > \lambda_D$ the plasma is assumed to be "quasi-"neutral. Given these two criteria, the conditions

$$Ln^{1/3} \gg 1, \qquad L \gg \lambda_D, \tag{1.1}$$

define the domain of parameters where matter is in the plasma state.

Fig. 1.1 shows the different plasmas existing in nature and laboratory experiments on a diagram based on the temperature (T) and density (n).

We anticipate now that, in this manuscript, the plasmas of interest are *hot plasmas*, with large mean-free-path so that the plasma is in a *collisionless regime*, i.e the collisions between particle are negligible. This type of plasma corresponds to those circled in red in the figure 1.1.

1.1.2 Many scales

Plasmas are composed of different ionized species. With mass of a proton being 1836 times that of the electron, we expect the behavior of the components to be very different. One can first define the time scales by introducing the characteristic frequencies for each species. Assume that, for example, in a plasma made by electrons and ions, we displace a certain amount of particles of one species with respect to their original configuration. Then the system will then respond by trying to restore itself to its initial state. Plasma electrostatic waves are then generated and the particles oscillate at the plasma frequency, defined as $\omega_{p_{i,e}} = \sqrt{4\pi e^2 n/m_{i,e}}$. In traditional electron-ion plasmas, the plasma frequency appears in the dispersion relation for all elementary plasma waves in which particles are oscillating. If a particle moves at the thermal velocity $v_{th_{i,e}} = \sqrt{2T_{0_{i,e}}/m_{i,e}}$ on a time scale $\omega_{p_{i,e}}$, it will be able to travel the distance λ_D before the system is restored by forces maintaining quasi-neutrality, which gives us the simple relation $v_{th_{i,e}} = \lambda_D \omega_{p_{i,e}}$. The inverse of the plasma frequency, $\omega^{-1}_{p_{i,e}}$ corresponds to the characteristic response time of the particles to the exterior perturbations. For waves characterized by frequencies that are higher than the plasma frequency, the length scale associated to this response is called the *inertial length*

$$d_{i,e} = \frac{c}{\omega_{p_{i,e}}}. \tag{1.2}$$

---

[1] $n_0 \sim n_i \sim n_e$ and $T_0 \sim T_i \sim T_e$ are the usual plasma density and temperature.

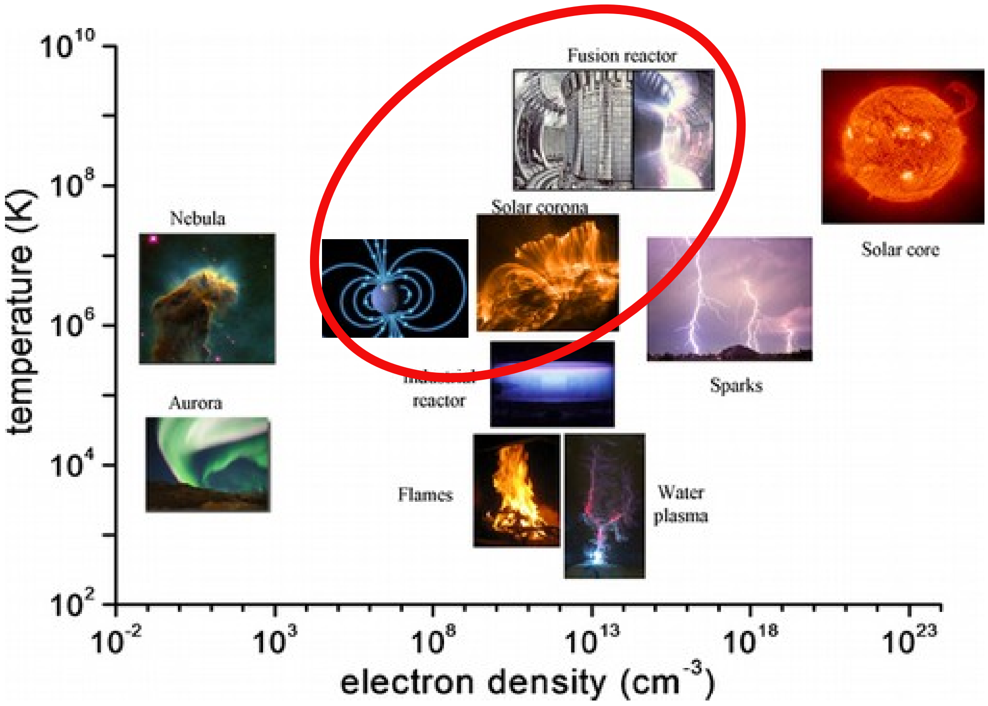

Figure 1.1: Diagram showing the different plasmas in nature and laboratory.

The trajectory of a particle projected on the plane perpendicular to the mean magnetic-field direction is the sum of a rectilinear motion due to the displacement of the field line and of a circular motion called the *gyro-motion*, where the radius of the circular motion is referred to as Larmor radius. We point out that the presence of a magnetic-field component that is constant in one direction, which is referred to a configuration with a *guide field*, can substantially modify the behavior of the plasma. A strong guide field introduces transport anisotropy, because the circular particle motion tends to be preferentially in the plane perpendicular to this guide field. Two important quantities that describe this *gyro-motion* are the thermal Larmor radius, also called the thermal gyro-radius, and the *cyclotron frequency*, also called the gyro-frequency,

$$\rho_{i,e} = \frac{m_{i,e} c v_{th_{i,e}}}{eB_0}, \qquad \omega_{c_{i,e}} = \frac{eB_0}{m_{i,e} c}, \tag{1.3}$$

respectively, where B_0 is the magnetic-field strength. For a very strongly magnetized plasma, the gyration of the particles around the field lines can be reasonably ignored. The importance of the amplitude of the magnetic field in the plasma is quantified by a parameter called the plasma $\beta_{i,e}$, defined, for each species, as the ratio between the square of the thermal gyro-radius and the square of the skin depth. Making use of the definitions (1.2) and (1.3), one can see that $\beta_{e,i}$ also corresponds to the ratio between the thermal pressure, for each species, and the magnetic pressure. Thus, it follows that

$$\beta_{i,e} = \frac{\rho_{i,e}^2}{d_{i,e}^2} = \frac{8\pi n_0 T_{0_{i,e}}}{B_0^2}. \tag{1.4}$$

The thermal pressure of the particles brings in the scale of the effective ion-sound Larmor radius, which will be of particular importance for us,

$$\rho_s = \sqrt{\frac{T_{0_e}}{m_i}} \frac{m_i c}{eB_0} \tag{1.5}$$

based on the ion−sound speed $c_s = \sqrt{T_{0_e}/m_i}$. At this scale the electron compressibility parallel to the magnetic field has to be taken into account.

Another important length corresponds to the mean free path between the particles λ_{mfp}, or, in other words, an important frequency, corresponds to the electron-ion collision rate ν_{ei}, which measures the rate at which electrons are scattered by ions. As already anticipated, all the work presented in this manuscript applies to plasmas for which collisions between particles are neglected. Therefore, we will not detail this point any further, and we will just assume that our characteristic length is always such that $L \ll \lambda_{mfp}$.

We give here a summary of some useful relationships between the different plasma scales.

$$d_i = \sqrt{\frac{2}{\beta_e}}\rho_s, \qquad d_e = \sqrt{\frac{2}{\beta_e}}\sqrt{\frac{m_e}{m_i}}\rho_s, \tag{1.6}$$

$$\rho_i = \sqrt{\tau}\rho_s, \qquad \rho_e = \sqrt{\frac{m_e}{m_i}}\rho_s = \sqrt{\frac{\beta_e}{2}}d_e. \tag{1.7}$$

with

$$\tau = \frac{T_{0_i}}{T_{0_e}} \tag{1.8}$$

the ratio between the background ion and electron temperature.

1.2 Qualitative description of magnetic reconnection

1.2.1 Early history of magnetic reconnection

The first attempt to deal with the processes that we would group today under the name ’magnetic reconnection’ is generally attributed to Giovannelli (1947), who in 1947 used the concept of changing magnetic-field line connectivity to explain the acceleration of particles occurring during solar flares. A few years after, as part of his Thesis, James Dungey studied the properties of current sheets and showed that the connectivity can change assuming the existence of a dissipation process (Dungey (1953)). Dungey was the first to invoke the name magnetic reconnection.

The Sweet-Parker model

With the first observation of solar flares (Carrington (1859)), several authors, notably Sweet and Parker, developed a simple model for how steady-state reconnection might work. For this, they used a model that considers the plasma as a single conducting fluid, using equations describing mass, momentum, and energy conservation, as well as an induction equation for the magnetic field. This set of equations is commonly called the resistive *magnetohydrodynamic* (MHD) model. In this model, unlike the models we use in this Thesis, the plasma is subject to diffusion effects caused by electrical resistivity generated by collisions between particles.

The basic configuration of Sweet and Parker reconnection is shown on Fig. 1.2. Such a two-dimensional picture qualitatively shows the key features of a stationary reconnection site — a *current sheet* (with out-of-plane current), magnetic-field lines before and after reconnection (shown by the red and blue lines), a so-called *diffusion region* (gray region) with a neutral point at the center, called the *X-point* (not shown on this sketch), and the plasma flow (green arrows). The flow may be divided into an inflow

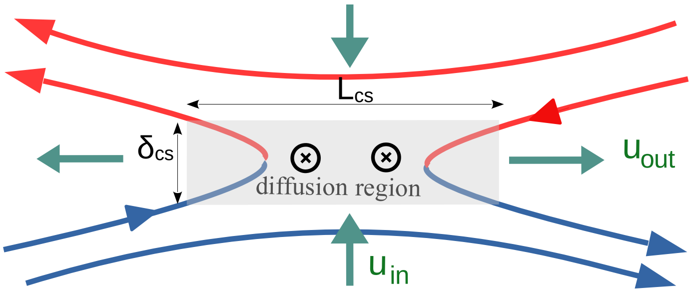

Figure 1.2: Qualitative picture of Sweet-Parker reconnection. *Credit: adapted from Rhouni (2012)*

converging towards the diffusion region and an outflow pointing away from the diffusion region. Here, the newly reconnected magnetic field moves outward under its own tension, accelerating the out-flowing plasma in the process. In the 2D Sweet-Parker model of reconnection, the diffusion region is a rectangular domain with a length $L_{\rm cs}$, and a width $\delta_{\rm cs}$. The reconnection rate refers to the magnetic flux reconnected per unit time. As a first approximation this amounts to calculating the ratio of plasma velocities upstream and downstream of the reconnection site,

$$R_{\rm rec} = \frac{u_{\rm in}}{u_{\rm out}}. \tag{1.9}$$

The Sweet and Parker analysis consists in applying mass continuity in 2D to the diffusion region, to first obtain the relation

$$u_{\rm in} L_{\rm cs} \sim u_{\rm out} \delta_{\rm cs}. \tag{1.10}$$

Therefore, the reconnection rate, can be approximated by what is commonly called the aspect ratio of the current sheet $A_{\rm cs} = \delta_{\rm cs}/L_{\rm cs}$.

We now consider the equation deduced from the electron momentum conservation, called the resistive Ohm's law, given by $\mathbf{E} + \mathbf{v} \times \mathbf{B} = \eta \mathbf{j}$, where η is the electrical resistivity, $\mathbf{j}$ is the current density and $\mathbf{v}$ is the fluid velocity (the generalized Ohm's law, obtained from the complete equation of motion will be described in Section 1.3.2). Far from the current sheet, where the current density is small, resistivity can be neglected. However, inside the current sheet, the change of field-line connectivity takes place at a point where the magnetic field is null. In addition, Sweet and Parker considered a steady reconnection process, and for such a thing to be possible, the electric field must be uniform on the domain. This gives the relations

$$E \sim u_{\rm in} B_{\rm in} \sim \eta j, \tag{1.11}$$

where the current density can be approximated by Ampère's law $j \sim B_{\rm in}/4\pi\delta_{\rm cs}$.

If the magnetic energy of the reconnecting field is almost entirely converted into kinetic energy of the out-flowing plasma, then energy conservation also requires equating the upstream magnetic pressure with the downstream dynamic pressure, which leads to $B_{\rm in}^2 u_{\rm in} L_{\rm cs}/4\pi \sim m_i n_0 u_{\rm out}^3 \delta_{\rm cs}$. This implies a condition on the outflow velocity

$$u_{\rm out} \sim \sqrt{\frac{B_{\rm in}^2}{4\pi m_i n_0}} = v_A, \tag{1.12}$$

where v_A is the Alfvén speed. As already mentioned, using the approximation (1.10), we can express the reconnection rate $R_{\rm rec} = u_{\rm in}/u_{\rm out} \sim \delta_{\rm cs}/L_{\rm cs}$, while using (1.11), we obtain the relation $R_{\rm rec} \sim \eta/4\pi v_A \delta_{\rm cs}$. This gives us the Sweet-Parker reconnection rate

$$R_{\rm rec} \sim \left(\frac{\eta}{v_A L_{\rm cs}}\right)^{1/2} = S^{-1/2}, \tag{1.13}$$

where S is the Lundquist number defined as the ratio of a global Ohmic diffusion time to the global Alfvén time. In space plasmas S is usually very large. Here are some values taken from Ji & Daughton (2011):

- Magnetopause and solar corona: $S \sim 1 \times 10^{13}$,
- Solar wind: $S \sim 3 \times 10^{12}$,
- Sgr A* flares: $S \sim 5 \times 10^{20}$.

In plasma experiments, it can be smaller:

- ITER Tokamak: $S \sim 6 \times 10^8$.

Consequently, the Sweet–Parker reconnection is *usually too slow to account for some weakly collisional and collisionless plasma phenomena.* The typical example is the solar flare. Simply considering the Sweet-Parker reconnection rate (1.13) in the corona provides time scales (years) that are considerably larger than that observed for flares (minutes).

Although the Sweet-Parker model has limitations, the features of the diffusion region is common to most reconnection problems.

The Petschek model

In 1964, Petschek (1964) introduced another reconnection model where he, instead, reduced the length of the diffusion region, providing a much greater inflow speed needed for fast reconnection. In his model, he overcame the elongation of the current layers by invoking the appearance of standing shock waves that develop at the edges of the current layer. The Petschek reconnection rate is many orders of magnitude greater than the Sweet–Parker rate and was the first model of fast reconnection to be proposed. However, its mechanism was proved not to be reproducible in numerical simulations by Biskamp (1986), unless a non-uniform resistivity was accounted for (Uzdensky & Kulsrud (2000).

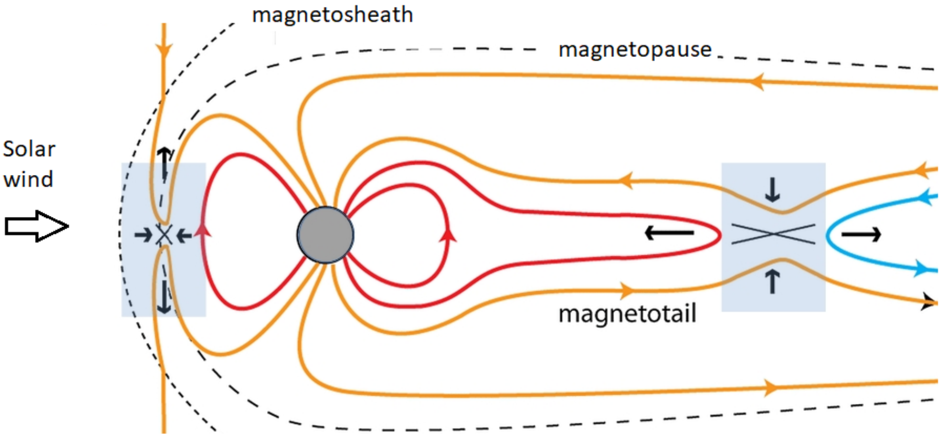

Figure 1.3: Sketch of magnetic-field lines of Dungey's open magnetosphere model, in the meridian plane. The two blue regions are the two main reconnection sites. The plasma flow is indicated by the solid black arrows. *Credit: adapted from Eastwood et al. (2017).*

Dungey's model

A conceptual model of an open magnetosphere by Dungey (1961) addressed the interaction between the magnetized interplanetary medium and the Earth's magnetosphere. This interaction is sketched on Fig. 1.3. In this Figure, the two main reconnection regions are shown by gray squares.

The solar wind, near the Earth (at 1 AU from the Sun), is made of a plasma with a lower density and magnetic-field strength than the magnetosphere. Together, they constitute two different magnetized media in interaction. The solar wind is transported towards the Earth at hundreds of kilometers per second, a speed which is greater than the local fast magnetosonic speed, and must slow down to wrap around the magnetosphere, which leads to the formation of standing shock in the magnetosheath. In this region, a current sheet and reconnection exhausts are observable (e.g., Phan et al. (2007)), allowing for a mixing of the two different magnetized background. The dayside magnetosphere, which is a first main reconnection site, is characterised by hot (1 – 10 keV) but dilute plasma ($n < 1$ cm^{-3}), which is composed mainly of protons and electrons.

The combined action of the flow of the solar wind and shock on the dayside, drive the newly reconnected field lines to accumulate in the tail of the magnetosphere, where they reconnect a second time. This time, the jets are oriented towards the Earth and towards the interplanetary medium. This acceleration of particles towards the Earth leads to the formation of polar aurora. In the thin magnetotail, the plasma density is about 1 cm^{-3} and goes down below 0.1 cm^{-3} in the magnetotail lobes.

The tearing instability

On the experimental plasma side, reconnection began to attract attention due to its interest in the magnetic confinement of fusion plasma in the Sawtooth instability, during which the plasma current and density profiles periodically reorganize through reconnection (von Goeler et al. (1974), Hastie (1997)). This interest led to one of the most important developments in the theory of reconnection, when Furth, Killeen, and Rosenbluth published their fundamental paper (Furth et al. (1963)). Compared to the Sweet-Parker and Petchek models, in which the system is in a steady-state and the question of the reason of the occurrence of reconnection is not addressed, they showed that certain magnetic-field equilibria can be unstable to small perturbations, called *tearing modes* that reconnect the field lines. A simple potential candidate for an instability that changes the magnetic topology is a one-dimensional current sheet with a reversal in the magnetic-field direction. Starting from this equilibrium magnetic field, the dispersion relation of an instability leading to spontaneous reconnection was derived. This instability tears and reconnects the field lines, hence the name of the *tearing instability*.

Collisionless reconnection

The Sweet-Parker and Petschek reconnection models are resistive-MHD models, in which the plasma resistivity is provided by collisions between the charged particles. However, as we will present in the following Sections, the plasma in the magnetosphere and solar wind, which regularly undergoes reconnection, is so dilute that collisions between particles are extremely infrequent. This means that this model is not applicable to many plasmas. It was shown in a series of papers by Coppi et al. (1976), Ottaviani & Porcelli (1993) and Drake & Lee (1977) that, *in the collisionless regime, two-fluid effects driving reconnection can provide a way for achieving fast reconnection.* The width of the reconnection region in the collisionless regime typically depends on the length of the electron skin depth (1.2), defined as the depth in a plasma to which electromagnetic radiation can penetrate. The resulting inertial reconnection rate, obtained by a scaling proposed by Wesson (1990), is given by $\tau_i \sim \tau_A L_{\mathrm{cs}}/d_e$, and is much faster than its counterpart in the resistive models, obtained with the Sweet-Parker scaling and given by $\tau_{SP} \sim \tau_A \sqrt{S}$. In Wesson (1990), the Authors considered parameters of an experiment done with the JET tokamak, given by $S \sim 9{\times}10^6$, $d_e \sim 10^{-3}\,\mathrm{m}^{-1}$, $\tau_A \sim 10^{-6}$ s and $L_{\mathrm{cs}} \sim 0.3$ cm. experimental conditions, the resistive time scale is $\tau_{SP} \sim 3 \times 10^{-3}\ s$ and the inertial reconnection time scale is $\tau_i \sim 3 \times 10^{-4}\ s$ which is much closer to the collapse times observed in JET due to reconnection, of the order of $\sim 10^{-4}\ s$.

After the above mentioned pioneering works, the modelling of magnetic reconnection evolved enormously following different directions and approaches. Nevertheless, such early models are still an important reference and, also in the context of this Thesis, use will be made of concepts such as the Sweet-Parker reconnection.

1.2.2 Examples of magnetic reconnection events

Observations of reconnection in space plasmas

The magnetosphere represents a natural laboratory for the study of reconnection in the immediate proximity of our planet. Coherent structures and reconnection sites have been directly studied in much detail in near-Earth plasmas by space missions, including *Pionneer 5* (Coleman et al. (1960)), *Explorer 12* (Freeman Jr. (1964)), or *Explorer 14* (Cahill Jr. (1966)). In 2000, the four satellites *Cluster* (Escoubet et al. (2001)) were launched, flying in a tetrahedral configuration with adjustable inter-spacecraft distance. These multi-spacecraft missions allowed one to measure plasma fluctuations and particle spectra in the solar wind and magnetosphere. In 2015 the *Magnetosphere Multi Scale* (MMS) mission was launched. This mission was specifically designed to identify ion and electron diffusion regions, as well as to study the impact of small-scale plasma turbulence on the acceleration and heating of particles. It was indeed able to observe electron diffusion regions in the magnetosphere, with and without strong guide field, as well as in the magnetotail (Torbert et al. (2018)).

The two main reconnection sites are therefore the dayside and the nightside of the magnetosphere. However, recently, high-resolution measurements from MMS have been used to provide evidence of reconnection driven by electron dynamics also in the magnetopause (Burch et al. (2016)). In addition, it turns out that magnetopause reconnection often occurs with a non-negligible magnetic guide field (Pu et al. (2007)).

We note that reconnection is not unique to Earth's magnetosphere and has been observed for other planets of the solar system. Indeed, some signatures have been observed around Mercury, which has a weak planetary magnetic field (Slavin et al. (2009)).

The many space missions mentioned above also make it possible to probe the solar wind. Some survey of the Wind spacecraft observations revealed the presence of reconnection in the solar wind with large guide field (Gosling et al. (2007a)) as well as large plasma β_e (Gosling (2007)).

Observations in experiments

Recently, dedicated experiments for controlled reconnection in laboratories allowed to probe different plasma regimes. This is the case, for instance, of the MRX (Magnetic Reconnection Experiment), and the upcoming FLARE (Facility for Laboratory Reconnection Experiments) devices. In these experiments, in response to external drive coils, a current sheet forms and extends between two flux cores. A simulation from Ji et al. (2022) is shown on figure 1.4 to depict the scenario. In this thinning current sheet, tearing instabilities grow and become unstable, forming eventually several X-points.

After this brief survey, it is not surprising that magnetic reconnection is nowadays

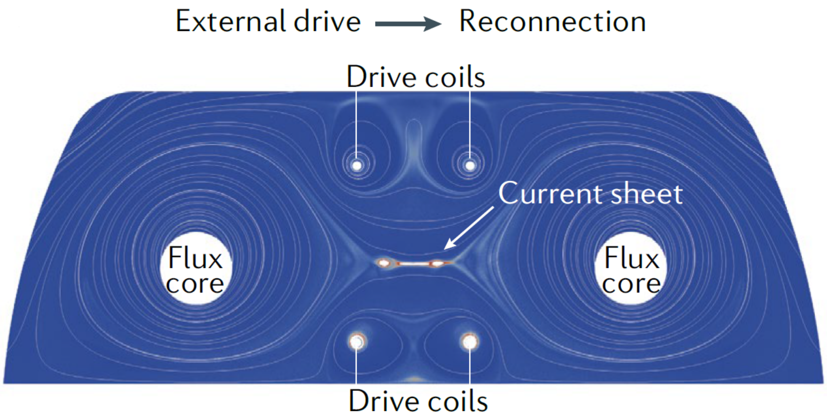

Figure 1.4: Numerical simulation of the Facility for Laboratory Reconnection Experiments, which illustrates the reconnection driven by inductive coils. *Credit: Ji et al. (2022).*

actively studied on dedicated laboratory experiments and has been the main purpose of some spacecraft missions. The main problems are that, this phenomenon involves many scales, and the rates at which magnetic energy is converted into kinetic energy, obtained by different models, often fail to account for the experimental evidence and observations.

1.3 Quantitative description of magnetic reconnection

1.3.1 Topology and flux conservation

Two important notions to define reconnection are the *magnetic topology* and the *magnetic flux conservation* properties. The former means that two fluid elements connected by a magnetic-field line at a given time, will be connected by a field line at every subsequent time. The latter means that the magnetic flux through any surface, whose boundary moves with the plasma velocity, is constant in time, or, in other words, that the magnetic field is *frozen-in* the plasma.

Topology conservation

We consider a magnetic field (but this definition of topology conservation is applicable to any vector field), $\mathbf{B}(\mathbf{x}, t)$, represented as the derivative of a flow, $\mathbf{F}_B(\mathbf{x}, t, s)$ with $\mathbf{F}_B(\mathbf{x}, t, 0) = \mathbf{x}$, given by

$$\frac{\partial \mathbf{F}_B(\mathbf{x}, t, s)}{\partial s} = \mathbf{B}(\mathbf{F}_B(\mathbf{x}, t, s), t), \tag{1.14}$$

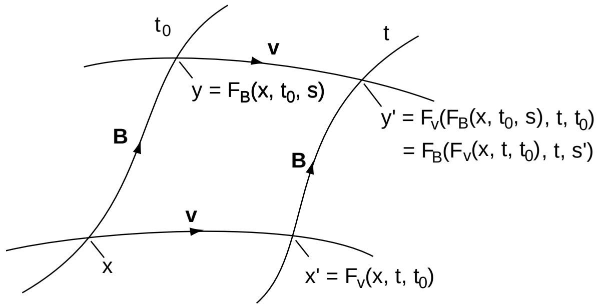

Figure 1.5: Scheme of the transport of **B** by **v** from its position at time t_0 to its position at time t. *Credit: Birn & Priest (2007). The original picture has been modified.*

such that $\mathbf{F}_B(\mathbf{x}, s, t)$ is parameterized by s at a fixed time t and maps the points $\mathbf{x}$ along the field lines.

The same procedure can be applied to a fluid moving with a velocity field $\mathbf{v}(\mathbf{x}, t)$ that can be described by a flow $\mathbf{F}_v(\mathbf{x}, t, t_0)$ with $\mathbf{F}_v(\mathbf{x}, t_0, t_0) = \mathbf{x}$ such that

$$\frac{\partial \mathbf{F}_v(\mathbf{x}, t, t_0)}{\partial t} = \mathbf{v}(\mathbf{F}_v(\mathbf{x}, t, t_0), t). \tag{1.15}$$

The perfect transport of the field lines of **B** by the generating vector previously defined **v** can be described, in terms of the corresponding flows, by the condition

$$\mathbf{F}_v(\mathbf{F}_B(\mathbf{x}, t_0, s), t, t_0) = \mathbf{F}_B(\mathbf{F}_v(\mathbf{x}, t, t_0), t, s'). \tag{1.16}$$

The condition (1.16) describes how a point $\mathbf{x}$ will be mapped along the field line while this field line is transported by the flow of $\mathbf{v}$ from a time t_0 to t. Figure 1.5 shows the transport of a field line from its initial position t_0 to an arbitrary time t. When deriving by t and s and using the definitions $\partial_t \mathbf{F}_v = \mathbf{v}$ and $\partial_s \mathbf{F}_B = \mathbf{B}$ we obtain the condition

$$\frac{\partial \mathbf{B}}{\partial t} + \mathbf{v}.\nabla \mathbf{B} - \mathbf{B}.\nabla \mathbf{v} = \lambda \mathbf{B}, \tag{1.17}$$

where $\lambda = \partial^2 s' / \partial s \partial t$ is a free function and accounts for the fact that, in general, we allowed for a different parametrization, in terms of the parameter s' of the field line of **B** mapped at the time t.

In conclusion, the evolution of a smooth vector field $\mathbf{B}(\mathbf{x}, t)$ conserves the topology if a generating vector field $\mathbf{v}(\mathbf{x}, t)$ and a scalar function $\lambda(\mathbf{x}, t)$ exist and satisfy the condition (1.17) (Hornig & Schindler (1996)).

The right-hand side (r.h.s) of (1.17) vanishes at the null points of the field, so topology conservation, according to this definition, requires the preservation of points where the field vanishes. For a smooth divergence-free field, like the magnetic field, this

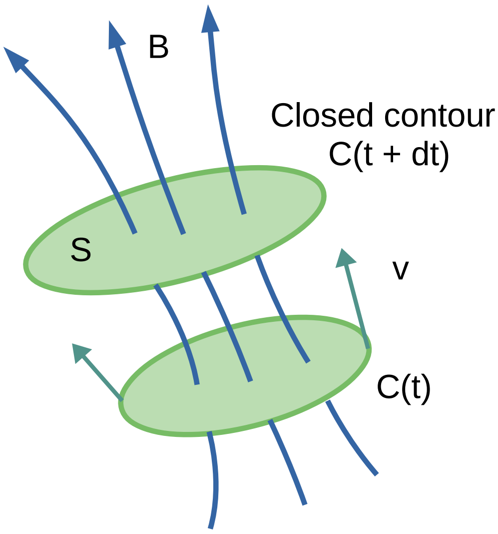

Figure 1.6: Flux passing through an arbitrary surface S, with contour C, moving with the velocity $\mathbf{v}$.

equation becomes,

$$\frac{\partial \mathbf{B}}{\partial t} - \nabla \times (\mathbf{v} \times \mathbf{B}) = \lambda \mathbf{B}. \tag{1.18}$$

If we now consider the case in which $\mathbf{B}$ is a magnetic field, for which Faraday's equation $\partial_t \mathbf{B} = -\nabla \times \mathbf{E}$ holds, we can write the final condition for the conservation of the topology

$$\nabla \times (\mathbf{E} + \mathbf{v} \times \mathbf{B}) = -\lambda \mathbf{B}. \tag{1.19}$$

Flux conservation

In a conducting fluid , we consider an arbitrary surface S with normal $\mathbf{n}$ and bounded by a curve C, which is moving with the velocity $\mathbf{v}$ of the fluid. The flux passing through it remains constant in time:

$$\frac{d}{dt} \int_S \mathbf{n}.\mathbf{B}\, dS = \int_S \left(\frac{\partial \mathbf{B}}{\partial t} - \nabla \times (\mathbf{v} \times \mathbf{B}) \right) .\mathbf{n}\, dS. \tag{1.20}$$

The first contribution in (1.20) comes simply from the time dependence of the magnetic field, while the second term is the part of the flux swept out of the contour C due to the surface motion. To conserve the flux, $d_t \int_S \mathbf{n}.\mathbf{B}\, dS = 0$, one finds that the condition is

$$\frac{\partial \mathbf{B}}{\partial t} - \nabla \times (\mathbf{v} \times \mathbf{B}) = 0. \tag{1.21}$$

This condition can be seen as a particular case of the condition for the conservation of the topology of $\mathbf{B}$ (1.18). Consequently, it is easy to see that if there is a flux-conserving velocity then this velocity is also field-line conserving. Hence, a break down of topology conservation results in a non-flux conserving velocity. For a magnetic field, using Faraday's equation, the magnetic flux conservation can also be written as $-\int_S (\nabla \times (\mathbf{E} + \mathbf{v} \times \mathbf{B})) . \mathbf{n}\, dS = 0$, so that the condition (1.21) can be expressed as

$$\nabla \times (\mathbf{E} + \mathbf{v} \times \mathbf{B}) = 0. \tag{1.22}$$

Summary

$$\nabla \times (\mathbf{E} + \mathbf{v} \times \mathbf{B}) = \lambda \mathbf{B} \quad \Rightarrow \quad \text{Topology conservation,} \tag{1.23}$$

$$\nabla \times (\mathbf{E} + \mathbf{v} \times \mathbf{B}) = 0 \quad \Rightarrow \quad \text{Flux conservation} \tag{1.24}$$

Since magnetic reconnection requires only a change in the magnetic connectivity of plasma elements, for any form of reconnection, a nonideal term **R**, whose curl is not in the form $\nabla \times \mathbf{R} = -\lambda \mathbf{B}$, is required for the topology of the magnetic field **B** not to be preserved by the flow **v**. Such a non-ideal term would appear on the right-hand side of the following expression

$$\mathbf{E} + \mathbf{v} \times \mathbf{B} = \mathbf{R}. \tag{1.25}$$

In two dimensions, which is the situation considered in this Thesis, reconnection can take place if the magnetic field possesses a hyperbolic point, referred to as X-point, and such non-ideal term is non-vanishing in a region including the hyperbolic point. There must be also a velocity field **v** crossing the magnetic-field lines passing by the X-point, called the *separatrices*. Fig. 1.7 shows the evolution of two magnetic-field lines and four fluid elements represented by the points A, B, C and D. These fluid elements drift with a velocity represented by the green arrows. This velocity field crosses the separatrices and allows a change of connectivity between the fluid elements. Note that if this term is represented by the gradient of a function ϕ, i.e. $\mathbf{R} = \nabla \phi$, then it will not cause reconnection since its curl will be zero. In such case, indeed, there exists no global smooth velocity field that can satisfy (1.25) in the non-ideal region and coincide with the velocity $\mathbf{v} = \mathbf{E} \times \mathbf{B}/|\mathbf{B}|^2$ in the ideal region where the non-ideal term **R** vanishes (Schindler (2006)). The situation remains similar in the case where a guide field is present and the projection of the magnetic field in the plane perpendicular to the guide field still presents X-points. The pure 3D case, on the other hand, is considerably more complicate (Schindler (2006); Priest & Forbes (2000)). Furthermore, if $\mathbf{R} = \mathbf{w} \times \mathbf{B}$, then we obtain the induction equation $\partial \mathbf{B}/\partial t - \nabla \times (\mathbf{v} - \mathbf{w}) \times \mathbf{B} = 0$. This is not considered as a magnetic reconnection but often called a *slippage*.

In conclusion, not all **R** actually do lead to magnetic reconnection and the following part will be dedicated to the description of some situations for some particular choices of **R**.

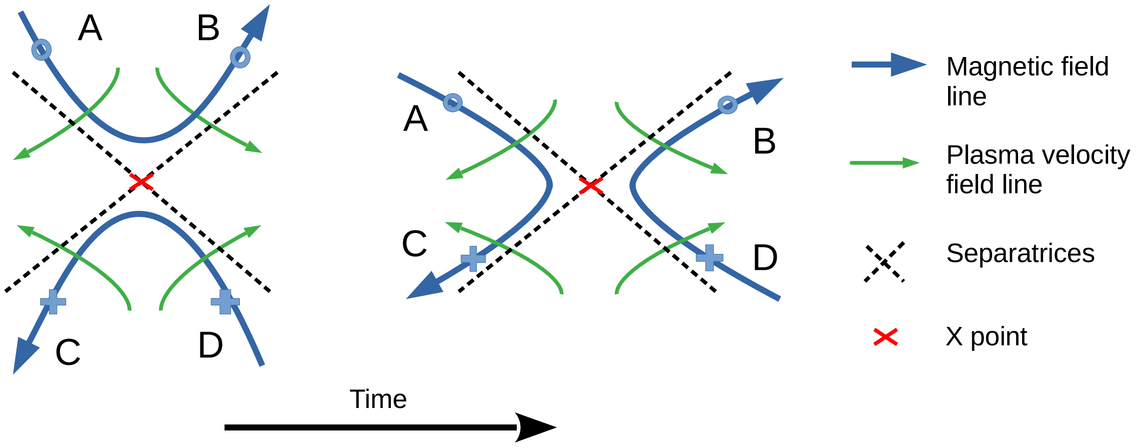

Figure 1.7: Time evolution of antiparallel magnetic-field lines (blue lines), as well as fluid elements that are frozen (points A, B, C, D) near a magnetic hyperbolic point, with a velocity field crossing the reconnection site (green lines).

1.3.2 What can drive reconnection: Ohm's law

In this section, we apply the general concepts introduced in Section 1.3.1 to the plasma magnetic field.

We will present the different dissipation mechanisms, that are susceptible to break the frozen-in condition. These mechanisms appear in the *generalized Ohm's law*, derived from the equation of electron motion, and are associated with an energy release at specific spatial scales. In principle, for reconnection to take place, it is sufficient that these non-ideal effects, normally negligible at large scales, become locally dominant in the diffusion region.

The resistive Ohm's law, as was introduced to describe the Sweet-Parker reconnection in the resistive-MHD context, is not valid at all scales. Starting from the momentum equation of motion for the electron fluid we can obtain the following generalized Ohm's law:

$$\mathbf{E} + \mathbf{v}_i \times \mathbf{B} = \eta \mathbf{j} + \frac{\mathbf{j} \times \mathbf{B}}{ne} - \frac{1}{en_e} \nabla . \mathbf{P}_e - \frac{m_e}{e} \frac{\mathrm{d}\mathbf{v}_e}{\mathrm{d}t}, \tag{1.26}$$

where $\mathbf{v}_i \simeq \mathbf{u}$ is the ion velocity, which, nearly coincides to that of the center-of-mass fluid velocity $\mathbf{u}$, $\mathbf{j}$ is the current density, n_0 is the particle density, m_e is the electron mass, and $\mathbf{P}_e$ is the electron pressure tensor. In the last term, the derivative is defined as $\mathrm{d}/\mathrm{d}t = \partial/\partial t + \mathbf{v}_e \cdot \nabla$. This equation is part of the two-fluid description of the plasma and must obviously be accompanied by the equations for mass continuity, the ion momentum, and the pressure tensors and by closure relations.

Equation (1.26) is of the form of Eqs. (1.25). On the r.h.s of (1.26), the first term is called the resistive term and is due to electrical resistivity. The second term is the Hall term and has to do with the fact that electrons and ions, at sufficiently small scales, can decouple and move separately. The third term is due to the force associated with the divergence of the electron pressure tensor. Finally, the last term comes from electron inertia. This equation can be greatly simplified by noting that not all of the terms are important at every scale. They are all associated with different microscopic length-scales that were introduced in Section 1.1. In addition, some of the terms on the r.h.s can break the frozen-flux condition, while others do not. We will see which of them do so, by moving from one scale to another and trying to give a (as) complete (as possible) overview (actually not so complete because we will consider $\rho_{i,e} \sim d_{i,e}$, which implies $\beta_{i,e} \sim 1$).

For $L \gg \rho_{i,e}, d_{i,e}$:

At scale lengths larger than the ion gyro-radius and skin depth, when $L \gg \rho_{i,e}, d_{i,e}$, the MHD equations (single-fluid description) are found to be appropriate to describe phenomena. At these scales, the three last terms in the r.h.s of (1.26) can be ignored. We must then decide if the mean free path of the particles is large (or not) compared to this characteristic length, for neglecting or not the electrical resistivity. We will first start by assuming a very large mean free path, so collisions exist, but they are not frequent enough to be significant. The resulting equation is the ideal Ohm's law,

$$\mathbf{E} + \mathbf{v}_i \times \mathbf{B} = 0, \quad \Rightarrow \quad \frac{\partial \mathbf{B}}{\partial t} = \nabla \times (\mathbf{v}_i \times \mathbf{B}), \tag{1.27}$$

describing a perfectly conducting plasma. This induction equation contains only an advective term and has no dissipative term, so no reconnection is possible. This property is extremely important because (1.27) is always valid on very very large scale. Meaning that, to an excellent approximation, on a large scale, magnetized structures do not mix their connectivity.

If we now take into account the collisions between the particles, we obtain the Ohm's law considered in the resistive MHD, and which leads to the following induction equation:

$$\mathbf{E} + \mathbf{v}_i \times \mathbf{B} = \eta \mathbf{j}, \quad \Rightarrow \quad \frac{\partial \mathbf{B}}{\partial t} = \nabla \times (\mathbf{v}_i \times \mathbf{B}) + \eta \Delta \mathbf{B}. \tag{1.28}$$

The second term on the r.h.s can break the frozen-flux condition. By equating the left-hand side (l.h.s) with the diffusion term we can obtain the diffusion time scale $1/\tau_D$,

$$\tau_D = \frac{L^2}{\eta}, \tag{1.29}$$

with ∇ scaling as $1/L$ and $\partial/\partial t$ scaling as $1/\tau_D$. The importance of the resistivity is usually evaluated by comparing τ_D with the Alfvén time, defined as a time scale of a typical MHD process. This comparison leads to the definition of the Lundquist number, that we already introduced, $S = \frac{\tau_D}{\tau_A} = \frac{Lv_A}{\eta}$, with $v_A = B_0/\sqrt{4\pi m_i n_0} = \omega_{c_i} d_i$, the Alfvén speed.

This plasma description is certainly appropriate for some astrophysical environments that might be weakly conllisional ($\lambda_{mfp} \lesssim L$), as for instance

- Intra-cluster medium: $\lambda_{mfp} \sim 1$ kpc for a system length of about $L \sim 100$ kpc
- Sgr A^*: $\lambda_{mfp} \sim 0.01$ pc for $L \sim 0.1$ pc.

However, as previously mentioned, many of the environments in which reconnection occurs constitute collisionless plasmas. Therefore, the resistive MHD model suffers from the fact that the scale associated with the resistivity is very small compared to the characteristic dimensions of the environments spatial locations where reconnection is assumed to occur.

For $L \sim d_i, \rho_i$

At scales $L \sim d_i, \rho_i$, where ions and electrons cannot be considered to move together, the Hall term and the electron pressure tensor become important.

The Hall term will introduce a slippage of the fluid, related to the motional separation between electrons and ions. In this scenario, the fluctuations are too small and fast to affect the ions so they are no longer frozen-in to the magnetic-field lines. But the electrons, thanks to their small mass, can still create a perfectly conducting current, and therefore constitute the only frozen species. The magnetic field is frozen-in the electron fluid velocity, and not in the plasma bulk velocity, therefore the Hall term is ideal and cannot break the frozen-flux in condition. However, when taken into account, along with a non-ideal term, it can greatly amplify the reconnection process. Its importance was pointed out by Birn et al. (2001). The authors investigated numerically different expressions of the Ohm's law (1.26) and it was found that all the codes including the Hall effect provided higher reconnection rates and behaved similarly. Figure 1.8 shows the results of the Geospace Environmental Modeling (GEM) of magnetic reconnection challenge from Birn et al. (2001).

Since applying the curl operation makes all irrotational contributions vanish, leaving just the rotational terms contributing to the induction equation, only the off-diagonal elements of the electron pressure tensor, or non-barotropic pressure ($P_e \neq P_e(n)$), will break the flux conservation. Indeed, if the divergence of the pressure tensor can be written in the form of the gradient of a scalar (polytropic law for example) this contribution, just as the Hall term, will not be able to drive reconnection. The off-diagonal components of the electron pressure tensor, on the other hand, can in principle cause reconnection, and can be attributed to nongyrotropic effects (FLR effects).

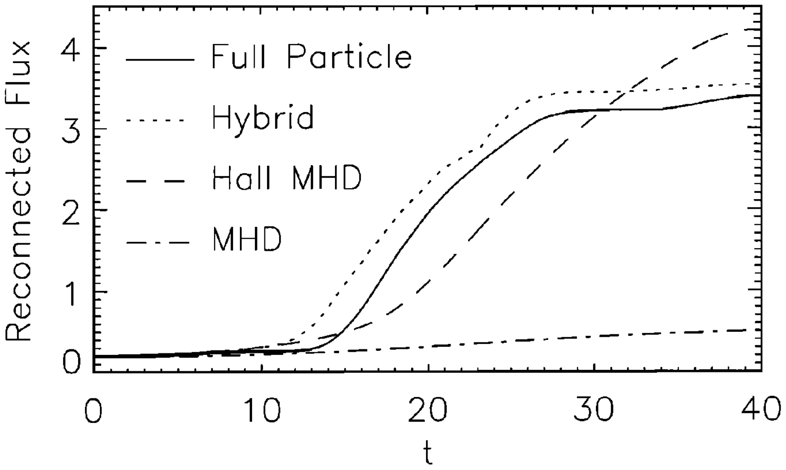

Figure 1.8: Results of the GEM challenge, where full particle, hybrid, Hall MHD, and resistive MHD were tested to investigate the effects of the nonlinear terms described in the generalised Ohm's law. *Credit: Birn et al. (2001).*

For $L \sim d_e, \rho_e$

At the scale $L \sim d_e, \rho_e$, the electron inertia term, becomes important due to the non-negligible mass of the electrons that makes their response to the electric field not instantaneous and thus prevents the plasma from being a perfect conductor. This effect can drive reconnection, and allows to reach growth rates[2] of the tearing mode that are faster than exponential (Ottaviani & Porcelli (1993)).

Collisionless diffusion region

Field lines are frozen to the plasma everywhere in a global region where an ideal flow drives the field lines to a small localized diffusion region, in which they reconnect. When several non-ideal effects are taken into account, given the multiple spatial scales involved with two-fluid physics, the description of the diffusion region has to be adapted into a hierarchy of sub-regions. In these sub-regions, each term of the generalized Ohms law will gain or lose its importance.

The internal structures are shown on Fig. 1.9, taken from Zweibel & Yamada (2009). On this figure, there is a large and constant guide field in the out-of-plane direction. The presence of a strong guide field tightly couples the electron and ion motions everywhere outside the diffusion regions.

In the ion-diffusion region, at a distance of about d_i from the X-point, ions and electrons are decoupled. The electrons continue to flow ideally toward the X-point until

---

[2] The growth rate of the tearing instability is related to the amount of magnetic flux reconnected per unit time.

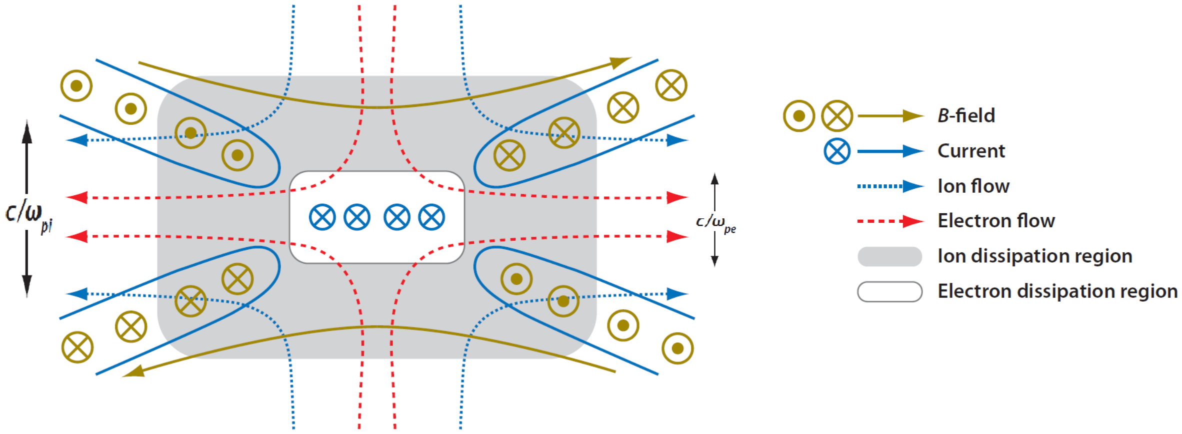

Figure 1.9: Sketch of the collisionless reconnection. *Credit: Zweibel & Yamada (2009).*

they enter the thin electron diffusion region, where field line reconnect. In the electron diffusion region, around the smallest plasma scales, d_e, a decoupling between the electrons and the magnetic field is attributed to the non-instantaneous response of the electrons to electric field fluctuations, due to their non negligible mass. Therefore, the ion and electron diffusion regions are characterized by nongyrotropic ions and electrons, respectively. The ion diffusion region is larger than the electron one since stronger magnetic fields are required to make the ions gyrotropic.

The current resulting from the decoupling of ions and electrons leads to the appearance of the Hall magnetic field (out of plane magnetic field on Fig. 1.9). In the solar wind, the Hall out-of-plane magnetic field has been observed (Mistry et al. (2016); Yamada et al. (2010)), and the Hall effect is assumed to take place on scales of about d_i.

1.4 Thesis overview

After having recalled some basic concepts of plasma physics and introduced the phenomenon of magnetic reconnection, we provide here an overview of the next chapters, where the original results will be presented. In particular, we summarize here the motivations for treating the different problems concerning the theory of current-sheet instabilities in collisionless plasmas, which make the object of this Thesis.

Chapter 2: Modelling of the problem

A considerable progress in the understanding of the collisionless tearing instability has been achieved through the fluid description of plasmas. In particular, the fluid framework is less costly in terms of computational resources, and physically more intuitive when compared to the kinetic framework. Also, in general, it is more suitable for analytical treatment. Thanks to the model reductions, the fluid and gyrofluid[3] approaches allow effectively for a great simplification of the system, enabling one to isolate relevant effects. So far, fluid modelling has afforded a good understanding of the roles of many effects, as for instance, electron inertia, electron temperature, electron parallel incompressibility, and finite-ion-Larmor radius effectd (e.g. Aydemir (1992); Ottaviani & Porcelli (1993); Schep et al. (1994); Cafaro et al. (1998); Grasso et al. (1999); Del Sarto et al. (2006); Fitzpatrick & Porcelli (2007); Grasso & Tassi (2015)).

This Thesis aims to extend this hierarchy of investigation to other effects, such as the electron equilibrium temperature anisotropy and finite-electron-Larmor-radius effects. We therefore conducted this work through such type of modelling method. Indeed, the study is carried out by means of two different gyrofluid models that have been derived from gyrokinetic equations, assuming an isothermal and a quasi-static closure, respectively.

Chapter 2, is a transitional chapter that aims to introduce the two models employed in this thesis and their numerical implementation. In order to better detail the regimes of validity of these models, we present the major steps of their derivations. For that, we make a brief review of what the gyrokinetic, and therefore the gyrofluid, approach can describe, by presenting the gyrokinetic ordering. We then explain the two different closures applied on the gyrofluid moments. Finally, we present and discuss the main assumptions that allowed for the reduction of the two models involved in this work.

Chapter 3: The tearing instability with background temperature anisotropy

A feature of collisionless plasmas is that they can exhibit particle distribution functions that are anisotropic with respect to the direction of the magnetic field. This can lead in particular to anisotropic temperature distributions. A natural question in the theory of collisionless plasmas concerns then the influence of temperature anisotropy on characteristic features of reconnection, such as the linear growth rate of the tearing mode.

The influence of equilibrium temperature anisotropy on the reconnection growth rate has actually been the object of several studies (Forslund (1968); Chen & Palmadesso (1984); Shi et al. (1987); Chiou & Hau (2002); Karimabadi et al. (2004); Daughton & Karimabadi (2005); Matsui & Daughton (2008); Quest et al. (2010)) carried out with kinetic and fluid approaches. Such studies agree in predicting that temperature (and in particular electron temperature) anisotropy enhances the tearing growth rate, meaning that the growth rate increases as the ratio between the perpendicular and parallel temperature increases, where perpendicular and parallel are referred to the direction of the equilibrium magnetic field. Such studies, on the other hand, consider the case of absent or moderate magnetic guide field. The investigation of Shi et al. (1987) also

---

[3] Gyrofluid models include finite-Larmor-radius effects. The concept is presented in more detail in Chapter 2.

indicates that, when the amplitude of the guide field is increased from zero to 2.5 times the amplitude of the equilibrium field in the reconnection plane, the enhancement of the growth rate gets weakened.

In **Chapter** 3 we present an analytical and numerical investigation of the influence of electron temperature anisotropy on the reconnection growth rate in the opposite regime, i.e., the regime of strong guide field, which is still little explored. For this, we use an analytical approach to derive a dispersion relation, and test this dispersion relation against numerical simulations.

Chapter 4: The tearing instability with finite β_e and ρ_e

Fluid models, in general, neglect the effects of the electron Larmor radius, which makes it impossible to describe phenomena taking place at microscopic scales comparable to the electron thermal gyro-radius, ρ_e. Gyrofluid models are effective tools to fill this gap. Indeed, although obtained by truncating the infinite hierarchy of equations evolving the moments of the gyrokinetic equations, gyrofluid models, unlike fluid models, allow for finite Larmor radius effects and are thus valid on thermal Larmor radius scales.

Electron FLR effects arise from the combination of electron inertia and a finite β_e parameter. The study of reconnection for a finite β_e can be relevant especially for plasmas with relatively large temperatures, such as in the Earth magnetosheath, where some $\beta > 1$ values are observed, in the presence of a guide field, during reconnection events (Man et al., 2020; Eastwood et al., 2018). Some studies of the tearing instability for finite β_e have been carried out, such as Numata & Loureiro (2015) in a gyrokinetic framework. In this Reference, although two-fluid effects were accounted for, the resistivity was considered as the element driving reconnection.

Also, most of the available reduced gyrofluid models, to the best of our knowledge, neglect the perturbations of the magnetic field along the direction of a guide field, the latter typically corresponding to the mean magnetic field in astrophysical plasmas (e.g. Schekochihin et al. (2009)) or to an imposed external field in laboratory plasmas. However, even in the case of a strong guide field, such perturbations can be relevant in some nearly collisionless environments as the solar wind, which motivates their inclusion in an analysis of collisionless reconnection.

In **Chapter** 4, we make use of a gyrofluid model to study the linear and nonlinear evolution of the tearing instability with finite β_e effects, and, in particular, electron FLR, in a collisionless plasma with strong guide field. A new dispersion relation of the tearing instability is derived for the case $\beta_e = 0$, which contains a corrective term with respect to a dispersion relation already existing (Porcelli (1991)), and tested against numerical simulations.

Chapter 5: The collisionless plasmoid instability

It is well established that the secondary instability of thin current sheets, known as the plasmoid instability, has a fundamental impact on the reconnection rate (Daughton et al. (2009); Bhattacharjee et al. (2009)). Indeed, even in the resistive MHD framework, the development of plasmoids in the reconnection layer induces a fast magnetic reconnection regime characterized by a reconnection rate that can exceed the estimates based on the Sweet-Parker (SP) theory (Sweet (1958); Parker (1957)) by several orders of magnitude. In collisional current sheets, it has been shown that plasmoids develop when the Lundquist number exceeds the threshold value $S_\star \sim 10^4$ (Biskamp (1986)). The other quantities are the plasma resistivity η, the speed of light c, and the Alfvén speed v_A. The threshold value on the Lundquist number, $S_\star$, separates the Sweet-Parker regime from the plasmoid-mediated regime of collisional reconnection. In addition, it controls the dimensional reconnection rate R_{rec} in the plasmoid-mediated regime, $R_{\text{rec}} \sim S_\star^{-1/2} v_A B_{\text{up}}$ (Huang & Bhattacharjee (2010); Uzdensky et al. (2010); Comisso et al. (2015a); Comisso & Grasso (2016)), where B_{up} is the reconnecting magnetic field. The extension of the resistive reconnection regime with the inclusion of the ion dynamics associated with the ion sound Larmor radius, ρ_s, or the ion inertial length, d_i, complicates the picture. The community that studies the formation of plasmoids often represents the results in the form of a 2D parameter phase diagram to explain when the generation of magnetic islands occurs, and better understand the role of the macroscopic scale (d_i or ρ_s) and resistive scale (Ji & Daughton (2011); Daughton & Roytershteyn (2012); Huang & Bhattacharjee (2013); Karimabadi & Lazarian (2013); Comisso et al. (2015b); Le et al. (2015); Loureiro & Uzdensky (2015); Bhat & Loureiro (2018)).

In contrast, the marginal stability of reconnecting current sheets in the purely collisionless regime has seen relatively little investigation. This subject was approached in Ji & Daughton (2011), in which it is argued that, below the scales d_i or ρ_s, no plasmoids were formed. Yet, it is acknowledged that reconnection in nature is often driven by collisionless effects beyond the resistive MHD description.

In **Chapter** 5, we investigate a phase space described by the two kinetic scales d_e (electron inertial length) and ρ_s, compared to the current length L_{cs}. We show how the aspect ratio of the marginally stable reconnection layer depends on these relevant kinetic scales. We identify the conditions for the marginal stability of a reconnecting collisionless current sheet that forms self-consistently during the nonlinear evolution of a tearing-unstable configuration. For this study we use the two-fluid collisionless model presented in the previous section. In a second part, we use a gyrofluid model to investigate the role of β_e and of the finite-electron-Larmor-radius on the plasmoid instability, and compare these results with a gyrokinetic approach. This will help to validate the above mentioned results on the plasmoid instability and also to identify possible limitations of the gyrofluid approach.

2 Plasma modeling

The vast parameter space of the plasma physics inevitably leads to the derivation of several models to address specific multiscale problems such as reconnection.

In this Chapter, we briefly review some different approaches, starting with the statistical description. We gradually introduce the hypotheses that are applied to reach our final destination: the two systems of gyrofluid equations that are used for the reconnection analysis in this Thesis.

To do so, we start by introducing the complete description of the single particle motion, called the *Klimontovich-Maxwell system*, which is the richest one in information but also the most complex one. We briefly explain how it is connected to the continuum kinetic description, called the *Vlasov-Maxwell equations*. This system governs the evolution of distribution functions, representing the probability density of finding a particle of the plasma at a given point in phase space, coupled with the evolution of electromagnetic fields. The continuum kinetic models on a 6-dimensional phase space are now numerically solvable, but require substantial computational resources. On the other hand, in the presence of a uniform strong guide field, strong anisotropies are introduced and a possible reduction consist in averaging out the particle gyro-motion from the Vlasov equation, thus leading to a 5-dimensional reduced problem (see Brizard & Hahm (2007) and also Frieman & Chen (1982); Howes et al. (2006)). This is the so-called *gyrokinetic* modelling, an example of which is presented in this Chapter.

Although reduced by one dimension in phase space, the gyrokinetic model is still complex and computationally demanding. In order to lessen the computational expense of the gyrokinetic simulations, alternative *gyrofluid* methods have been developed (Brizard (1992); Beer & Hammett (1996); Strintzi et al. (2005); Madsen (2013); Keramidas Charidakos et al. (2015); Tassi (2019); Tassi et al. (2020)) and operate instead on the velocity moments, corresponding to macroscopic quantities, of the gyrokinetic set of equations. Compared to the Vlasov-Maxwell system, gyrokinetic models are valid for frequencies much less than the lowest cyclotron frequency in the system, and evolve distribution functions of *gyrocenters*. These can be approximately interpreted as point-like-particles with respect to which the actual plasma particles execute their gyro-motion.

In this Thesis we choose essentially a gyrofluid/fluid approach, with the expectation that this yields models that include relevant kinetic effects, while remaining practical for realistic simulations and physical intuitions. The reduction from gyrokinetic to gyrofluid for obtaining these models was carried out in detail in the articles Tassi (2019); Tassi et al. (2020); Granier et al. (2021). The resulting equations correspond to mass and momentum conservation and describe the evolution of the gyrocenter moments, such as the gyrocenter density, velocity and the electromagnetic fields. Despite the fact that these macroscopic quantities hold less information compared to distribution function, they are more intuitive to understand. The gyrofluid methods, however, encounter inevitably a closure problem. In this Thesis, the two models employed originate from different closures, namely an *isothermal closure* and a *quasi-static closure*. These closures were chosen to be suitable for preserving the Hamiltonian structure of the system, and are presented in Appendix A.

To solve the equations of the gyrofluid model, a code used in Tassi et al. (2018) and Grasso et al. (2020) has been adapted to the new equations to include the gyroaverage operators and the parallel perturbation of the magnetic field.

In this Chapter, our goal is to indicate the key stages of the derivation, in order to present the validity regime of our models. The model with an isothermal closure is presented in Sect. 2.3, while the model with a quasi-static closure is presented in Sect. 2.4. Finally, in Sec. 2.6 we present the numerical implementation of the gyrofluid model with isothermal closure and the set up of the tearing instability, used to study reconnection.

Some text of this Chapter also appear in Granier et al. (2021) and Granier et al. (2022a).

2.1 Kinetic descriptions

2.1.1 Kinetic equations

The most complete, description of a system of N particles in a volume V, consists of describing the coordinates $\mathbf{x}_i(t)$ and the velocity $\mathbf{v}_i(t)$ of all the particles over time. We introduce a microscopic distribution function, $\mathrm{f}_{\mathrm{micro}}(\mathbf{x},\mathbf{v},t)$, which characterizes the number of particles found at a time t in the volume of phase space $\mathrm{d}^3\mathbf{x}\mathrm{d}^3\mathbf{v}$, given by $\mathrm{d}N = \mathrm{f}_{\mathrm{micro}}(\mathbf{x},\mathbf{v},t)\mathrm{d}^3\mathbf{x}\mathrm{d}^3\mathbf{v}$. The function $\mathrm{f}_{\mathrm{micro}}$ is called the *Klimontovich distribution function*, and can be expressed as the product of a Dirac functions for all the coordinates of the set of particles

$$\mathrm{f}_{\mathrm{micro}}(\mathbf{x},\mathbf{v},t) = \sum_{i=1}^{N} = \delta(\mathbf{x}-\mathbf{x}_i(t))\delta(\mathbf{v}-\mathbf{v}_i(t)), \tag{2.1}$$

where, $\delta(\mathbf{x}) = \delta(x)\delta(y)\delta(z)$ is the Dirac function in three dimensions.

In the case of a gas of charged particles, where only electromagnetic forces are considered, the equation of conservation of particles and momentum in the phase space, can be written

$$\frac{\partial \mathrm{f}_{\mathrm{micro}}}{\partial t} + \mathbf{v} \cdot \nabla \mathrm{f}_{\mathrm{micro}} + \frac{q_s}{m_s} \left(\mathbf{E}_{\mathrm{micro}} + \frac{\mathbf{v} \times \mathbf{B}_{\mathrm{micro}}}{c} \right) \cdot \frac{\partial \mathrm{f}_{\mathrm{micro}}}{\partial \mathbf{v}} = 0, \tag{2.2}$$

called the equation of Klimontovich. The fields $\mathbf{E}_{\mathrm{micro}}(\mathbf{x}, t)$ and $\mathbf{B}_{\mathrm{micro}}(\mathbf{x}, t)$ are the exact microscopic fields, and result from the superposition of the external fields and the self-consistent fields generated by the other particles and acting on the considered particle at the time t. When averaged on spatial scales larger than the average distance between particles, but small compared to the Debye length on which electric potentials are screened by the plasma, they give the macroscopic fields $\langle \mathbf{E}_{\mathrm{micro}} \rangle = \mathbf{E}$, $\langle \mathbf{B}_{\mathrm{micro}} \rangle = \mathbf{B}$.

The Klimontovich equation retains all information about the microstate of a system and contains the exact trajectories of all particles. This is far too much information to be practical, and it is much more convenient to work with an averaged distribution function, $\langle \mathrm{f}_{\mathrm{micro}} \rangle = \mathrm{f}_s$. The ensemble average of $\mathrm{f}_{\mathrm{micro}}$ is called the *particle distribution function.* Using this average and neglecting binary interactions between discrete charged particle, a new equation can be written, called the *Vlasov kinetic equation*

$$\frac{\partial \mathrm{f}_s}{\partial t} + \mathbf{v} \cdot \nabla \mathrm{f}_s + \frac{q_s}{m_s} \left(\mathbf{E} + \frac{\mathbf{v} \times \mathbf{B}}{c} \right) \cdot \frac{\partial \mathrm{f}_s}{\partial \mathbf{v}} = 0. \tag{2.3}$$

It was proposed by Anatoly Vlasov in 1945 to give a theoretical explanation of plasma oscillations, and is currently the basis of kinetic models for particles bound by long-range forces.

Since we are interested in collisionless plasmas, for which the typical length is much smaller than the collision mean free path, we will neglect the collisional operator, that arises from averaging the scalar product between the Lorentz force and the velocity gradient of $\mathrm{f}_{\mathrm{micro}}$, and originates from particle collisions that are interactions at small distances of the order of a Debye length. If the collisional effects were to be considered, they would be approximated by the so-called collision operator, which would generally appear in the right hand side of (2.3).

The kinetic equation (2.3) must be completed using equations for the mean fields. A self-consistent description is given by coupling (2.3) with Maxwell's equations

$$\nabla \cdot \mathbf{E} = 4\pi \sum_s q_s \int \mathrm{d}^3\mathbf{v}\mathrm{f}_s, \tag{2.4}$$

$$\nabla \cdot \mathbf{B} = 0, \tag{2.5}$$

$$\nabla \times \mathbf{E} + \frac{1}{c}\frac{\partial \mathbf{B}}{\partial t} = 0, \tag{2.6}$$

$$\nabla \times \mathbf{B} - \frac{1}{c}\frac{\partial \mathbf{E}}{\partial t} = \frac{4\pi}{c} \sum_s q_s \int \mathrm{d}^3\mathbf{v}\mathbf{v}\mathrm{f}_s. \tag{2.7}$$

The system (2.3)-(2.7) is the aforementioned Vlasov-Maxwell system. The fully kinetic description based on the model is the most straightforward and accurate representation, and is now realizable for computer simulations. However, although Eq. (2.3) it is already simplified compared to the single-particle description, it requires solving a nonlinear problem in the 6-dimensional phase space, which is really expensive to carry out in practice. Moreover, such simulations are possible only for a limited number of physical scenarios. It has therefore proved extremely useful to reduce the Vlasov equation in order to adapt it to the properties of the system we want to describe, and to introduce a set of approximations to retain only these spatial and time scales relevant for the physical effects studied here.

2.1.2 Gyrokinetic ordering

In this Thesis, we study a high-temperature plasma strongly magnetized by a uniform guide field, which introduces a striking scale separation between the parallel and the perpendicular dynamics:

$$\mathbf{B} \approx B_0\mathbf{z} + \widetilde{B}_{\|}\mathbf{z} + \nabla\widetilde{A}_{\|} \times \mathbf{z}, \tag{2.8}$$

where the constant magnetic field is of amplitude B_0 along the z direction defined as the parallel direction, $\widetilde{A}_{\|}$ is the fluctuation of the z component of the magnetic vector potential, and $\widetilde{B}_{\|}$ is the parallel magnetic fluctuation. The expression for **B** in Eq. (2.8) is approximate as it is not divergence-free and represents the expression of the magnetic field at the first order in the fluctuations. The higher-order contributions, which guarantee $\nabla\cdot\mathbf{B} = 0$, turn out to be negligible with the adopted ordering. The perturbed electric field can be written as

$$\widetilde{\mathbf{E}} = -\nabla\widetilde{\phi} - \frac{1}{c}\frac{\partial \widetilde{\mathbf{A}}}{\partial t}, \quad \text{with} \quad \nabla \times \widetilde{\mathrm{A}}_{\|} = \widetilde{\mathrm{B}}_{\|}\mathbf{z} + \nabla\widetilde{\mathrm{A}}_{\|} \times \mathbf{z}, \tag{2.9}$$

with $\widetilde{\phi}$ the electrostatic potential.

In this case, it is possible to identify small parameters, motivated by experimental findings and theoretical considerations, and develop an ordering called the *gyrokinetic* *ordering*.

We introduce an expansion parameter ϵ (not to be confused with the thickness of the inner region in the tearing theory)[1]. The main ideas and assumptions entering the gyrokinetic derivation are summarized in the following (Frieman & Chen (1982)):

- **1) Strongly magnetized plasma**
  The Larmor radius is very small compared to the length scales corresponding to magnetic field variations, justifying the assumption of purely circular gyro-orbits. This can be expressed as

  $$\frac{\rho_{i,e}}{L} \sim \epsilon. \tag{2.10}$$

  We point out that the presence of a strong guide field does not prescribe a large $\beta_{i,e}$ parameter, and in fact, we can add the assumption $\beta_{i,e} \sim 1$, without loss of generality.

- **2) Low frequency**
  The gyromotion of the particles around the guide magnetic-field lines is considered to be very fast compared to the fluctuation time scale. This will allow us to ignore the gyromotion, and can be expressed as

  $$\frac{\omega}{\omega_{c,i}} \sim \epsilon, \tag{2.11}$$

  where ω is the relevant frequency scale of the fluctuations.

- **3) Anisotropic fluctuation**
  The fluctuations in the plasma are assumed to be highly anisotropic. We denote by $k_\perp$ and $k_{||}$ the parallel and perpendicular wavenumbers of the fluctuations. Perturbations along the guide field occur on length scales of the order of the macroscopic length scale L, which can be expressed as

  $$k_{||}L \sim 1, \tag{2.12}$$

  while perturbations perpendicular to the mean magnetic field occur on length scales comparable to the Larmor radius of the particles, which can be expressed as

  $$k_\perp \rho_i \sim 1. \tag{2.13}$$

  These give the wavenumber ordering

  $$\frac{k_{||}}{k_\perp} \sim \epsilon. \tag{2.14}$$

---

[1] In principle, each small quantity should have its own ϵ, but the *maximal ordering principle* allows to neglect the differences and use a generic ϵ.

- **4) δf splitting**
  A method commonly used in the derivation of gyrokinetic equations is the splitting of the distribution function into an equilibrium part and a fluctuation. This approximation is valid in systems in which the total distribution function does not deviate too much from its equilibrium state $\mathcal{F}_{eq_s}$. The total particle distribution function can therefore be expressed as

$$\mathrm{f}_s = \widetilde{\mathrm{f}}_s + \mathcal{F}_{eq_s}, \tag{2.15}$$

with $\mathcal{F}_{eq_s}$ being the equilibrium distribution function and $\widetilde{\mathrm{f}}_s$ bieng a perturbation, which is assumed to be small,

$$\frac{\widetilde{\mathrm{f}}_s}{\mathcal{F}_{eq_s}} \sim \epsilon. \tag{2.16}$$

The amplitude of the field perturbations are also assumed to be small compared to the equilibrium electromagnetic fields, which can be expressed

$$\frac{\widetilde{B}_{\|}}{B_0} \sim \frac{q\widetilde{\phi}}{T_{0_e}} \sim \epsilon. \tag{2.17}$$

Note carefully that here, to remain consistent with the notation used in Tassi et al. (2020), perturbations are indicated by a tilde, whereas, in general, in other gyrokinetic articles, they are often indicated by a delta symbol: $\delta \mathrm{f}_s$.

Guiding-center phase-space transformation and ring average

The second stage of the reduction that is specific to gyrokinetics is the guiding-center phase-space transformation, which eliminates the gyroangle dependence. The gyrokinetic equations employ the phase-space coordinates transformation

$$\{v_x, v_y, v_z\} \longrightarrow \{v_{\|}, \mu_s, \theta\}, \tag{2.18}$$

with the particle velocity written $\mathbf{v} = v_{\|}\mathbf{z} + v_{\perp}(\cos\theta\mathbf{x} + \sin\theta\mathbf{y})$. In (2.18), $v_{\|}$ is the velocity parallel to the equilibrium magnetic field and is used as a first velocity coordinate in the phase space. The velocity $v_{\perp}$ is the perpendicular velocity, and allows to express the magnetic moment, $\mu_s = m_s v_{\perp}^2/2B_0$, which is used as a second velocity coordinate in the phase space. The third coordinate is the gyroangle, $\theta = \arctan(v_y/v_x)$. These three coordinates allow one to define the integration over the volume element,

$$\int_0^{2\pi} \frac{\mathrm{d}\theta}{2\pi} \int_0^{+\infty} \mathrm{d}\mathcal{W}_s = \int_0^{2\pi} \frac{\mathrm{d}\theta}{2\pi} \int \mathrm{d}v_{\|} \int_0^{+\infty} \frac{2\pi B_0}{m_s} \mathrm{d}\mu_s. \tag{2.19}$$

We now define the position of the guiding centers $\mathbf{X}_s = (X_s, Y_s, Z_s)$, which is the

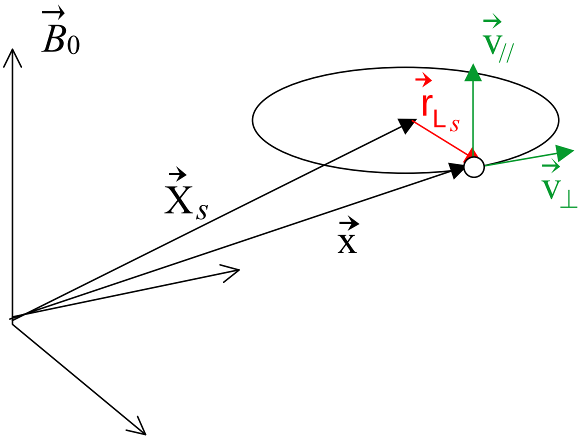

Figure 2.1: Description of the guiding-center phase-space coordinate. The circle represents the particle trajectory.

center of the particle orbit around the guide field, as shown on Fig. 2.1,

$$\mathbf{X}_s = \mathbf{x} - \frac{\mathbf{v} \times \mathbf{z}}{\omega_{cs}}, \tag{2.20}$$

with

$$\mathbf{r}_{L_s} = \frac{\mathbf{v} \times \mathbf{z}}{\omega_{cs}} \tag{2.21}$$

bing the Larmor radius of the particle, shown in Fig. 2.1. Finally, we introduce the ring average, which is an average over a ring centered about $\mathbf{X}_s$ of a radius $\mathbf{r}_{L_s}$, aimed at reducing the number of variables by integrating over θ

$$\left\langle a(\mathbf{x}, \mathbf{v}, t) \right\rangle_{\mathbf{X}_s} = \int_0^{2\pi} \frac{d\theta}{2\pi} a\left(\mathbf{X}_s + \frac{\mathbf{v} \times \mathbf{z}}{\omega_{cs}}, v_\parallel, \mu_s, \theta, t\right). \tag{2.22}$$

which is a generic function of phase space coordinates, a. Compared to the guiding centers, the coordinates of the aforementioned gyrocenters, are found when the elimination of the dependence on the gyroangle is carried out in the presence of the electromagnetic fluctuations (Brizard & Hahm (2007)).

2.1.3 Gyrokinetic equations of Kunz et al. 2015

The two gyrofluid models used in this work were derived taking as a starting point the slab gyrokinetic equations of Kunz et al. (2015), valid for a possibly non-Maxwellian equilibrium distribution functions and multiple ionic species with relative mean drifts along the direction parallel to the guide field. However, during the gyrofluid reduction procedure, a plasma composed of only electrons and ions was assumed, with no mean parallel drift.

The equilibrium distribution function we chose is the bi-Maxwellian, which allows us to take into account an equilibrium temperature anisotropy:

$$\mathcal{F}_{eq_s}(v_\parallel, \mu_s) = \left(\frac{m_s}{2\pi}\right)^{3/2} \frac{n_0}{T_{0_{\parallel s}}^{1/2} T_{0_{\perp s}}} \mathrm{e}^{-\frac{m_s v_\parallel^2}{2T_{0_{\parallel s}}} - \frac{\mu_s B_0}{T_{0_{\perp s}}}}, \tag{2.23}$$

giving us the uniform equilibrium density $n_0 = \int \mathrm{d}\mathcal{W}_s \mathcal{F}_{eq_s}$. The temperatures $T_{0_{\parallel s}}$ and $T_{0_{\perp s}}$ are the parallel and perpendicular equilibrium temperatures, and $v_{th_{\parallel s}} = \sqrt{T_{0_{\parallel s}}/m_s}$ is the parallel thermal speed.

We define the temperature anisotropy parameter

$$\Theta_s = \frac{T_{0_{\perp s}}}{T_{0_{\parallel s}}}. \tag{2.24}$$

When applying the phase-space coordinate transformation and ring average to the particle distribution, Kunz et al. (2015) obtain the relation between the perturbed particle distribution function f_s and that of the gyrocenters $\widetilde{f}_s$, given by

$$\begin{aligned}\widetilde{\mathrm{f}}_{s_\mathbf{k}} e^{i\mathbf{k}.\mathbf{x}} = \widetilde{f}_{s_\mathbf{k}} e^{i\mathbf{k}.\mathbf{x}} &+ \frac{q_s}{T_{0_{\perp s}}} \mathcal{F}_{eq_s} \left(J_0(a_s)(\widetilde{\phi}_\mathbf{k}(t) + \frac{v_\parallel}{c}(\Theta_s - 1)\widetilde{A}_\mathbf{k}(t)) e^{i\mathbf{k}\cdot(\mathbf{x}+\boldsymbol{r}_{L_s})} \right) \\ &- \frac{q_s}{T_{0_{\perp s}}} \mathcal{F}_{eq_s} \left((\widetilde{\phi}_\mathbf{k}(t) + \frac{v_\parallel}{c}(\Theta_s - 1)\widetilde{A}_\mathbf{k}(t)) e^{i\mathbf{k}\cdot\mathbf{x}} \right) \\ &+ \frac{q_s}{T_{0_{\perp s}}} \mathcal{F}_{eq_s} \left(2\frac{\mu_s B_0}{q_s} \frac{J_1(a_s)}{a_s} \frac{\widetilde{B}_{\parallel_\mathbf{k}}(t)}{B_0} e^{i\mathbf{k}\cdot(\mathbf{x}+\boldsymbol{r}_{L_s})} \right) \Bigg) = 0,\end{aligned} \tag{2.25}$$

where we consider a Fourier representation $\widetilde{\mathrm{f}}_s = \sum_\mathbf{k} \widetilde{\mathrm{f}}_{s_\mathbf{k}} e^{i\mathbf{k}\cdot\mathbf{x}}$ and where $a_s = k_\perp r_{L_s}$ is the perpendicular wave number times the gyroradius of the particle of species s defined by (2.21). The gyroaverage operators J_{0s} and J_{1s} are defined, in the Fourier space, as multiplications by $J_0(a_s)$ and $J_1(a_s)$, the latter being the zero- and first-order Bessel functions of the first kind, respectively. Therefore one has

$$J_{0s} f(\mathbf{x}, v_\parallel, \mu_s) = \sum_\mathbf{k} J_0(a_s) f_\mathbf{k}(v_\parallel, \mu_s) e^{i\mathbf{k}\cdot\mathbf{x}}, \tag{2.26}$$

$$J_{1s} f(\mathbf{x}, v_\parallel, \mu_s) = \sum_\mathbf{k} \frac{J_1(a_s)}{a_s} f_\mathbf{k}(v_\parallel, \mu_s) e^{i\mathbf{k}\cdot\mathbf{x}}, \tag{2.27}$$

where the vector $\mathbf{k} = (k_x, k_y, k_z)$. Expanding all fields in powers of ϵ and keeping contributions up to the first order and expressing the system in terms of the gyrocenter distribution function gives (Appendix C of Kunz et al. (2015))

$$\frac{\partial}{\partial t}\left(\widetilde{f_s} + \frac{q_s}{T_{0_{\parallel s}}}\frac{v_\parallel}{c}\mathcal{F}_{eq_s}J_{0s}\widetilde{A}_\parallel\right) + \frac{c}{B_0}\left[J_{0s}\widetilde{\phi} - \frac{v_\parallel}{c}J_{0s}\widetilde{A}_\parallel + \frac{m_s v_\perp^2}{q_s}J_{1s}\frac{\widetilde{B}_\parallel}{B_0}, \widetilde{f_s} + \frac{q_s}{T_{0_{\parallel s}}}\frac{v_\parallel}{c}\mathcal{F}_{eq_s}J_{0s}\widetilde{A}_\parallel\right]$$
$$+ v_\parallel \frac{\partial}{\partial z}\left(\widetilde{f_s} + \frac{q_s}{T_{0_{\parallel s}}}\mathcal{F}_{eq_s}\left(J_{0s}\widetilde{\phi} + \frac{m_s v_\perp^2}{q_s}J_{1s}\frac{\widetilde{B}_\parallel}{B_0}\right)\right) = 0, \tag{2.28}$$

$$\sum_s q_s \int \mathrm{d}\mathcal{W}_s\, J_{0s}\widetilde{f_s} = \sum_s \frac{q_s^2}{T_{0_{\perp s}}}\int \mathrm{d}\mathcal{W}_s\, \mathcal{F}_{eq_s}\left(1 - J_{0s}^2\right)\widetilde{\phi} - \sum_s q_s \int \mathrm{d}\mathcal{W}_s\, \frac{m_s v_\perp^2}{T_{0_{\perp s}}}\mathcal{F}_{eq_s}J_{0s}J_{1s}\frac{\widetilde{B}_\parallel}{B_0}, \tag{2.29}$$

$$\sum_s q_s \int \mathrm{d}\mathcal{W}_s\, v_\parallel J_{0s}\widetilde{f_s} = -\frac{c}{4\pi}\nabla_\perp^2 \widetilde{A}_\parallel, \tag{2.30}$$

$$\sum_s \frac{\beta_{\perp_s}}{n_0}\int \mathrm{d}\mathcal{W}_s\, \frac{m_s v_\perp^2}{T_{0_{\perp s}}}\mathcal{J}_{1s}\widetilde{f_s} = -\sum_s \frac{\beta_{\perp_s}}{n_0}\frac{q_s}{T_{0_{\perp s}}}\int \mathrm{d}\mathcal{W}_s\, \frac{m_s v_\perp^2}{T_{0_{\perp s}}}\mathcal{F}_{eq_s}J_{0s}J_{1s}\widetilde{\phi}$$
$$-\left(2 + \sum_s \frac{\beta_{\perp_s}}{n_0}\int \mathrm{d}\mathcal{W}_s\, \mathcal{F}_{eq_s}\left(\frac{m_s v_\perp^2}{T_{0_{\perp s}}}J_{1s}\right)^2\right)\frac{\widetilde{B}_\parallel}{B_0}. \tag{2.31}$$

We denote by

$$[f, g] := \frac{\partial f}{\partial x}\frac{\partial g}{\partial y} - \frac{\partial f}{\partial y}\frac{\partial g}{\partial x}, \tag{2.32}$$

the canonical bracket.

One parameter is included:

$$\beta_{\perp_s} = 8\pi\frac{n_0 T_{0_{\perp s}}}{B_0^2}, \tag{2.33}$$

corresponding to the ratio between the perpendicular equilibrium kinetic pressure and the magnetic pressure.

Equation (2.28) is obtained from the Vlasov equation, following the procedure in Kunz et al. (2015), and describes the evolution of the perturbed gyrocenter distribution function. Equation (2.29) represents the quasineutrality constraint expressed in terms of the perturbed gyrocenter distribution function. It can be derived from the Poisson's equation (2.4), assuming that the length scale of the fluctuation is much larger than the Debye length.

Equations (2.30) and (2.31) are the parallel and perpendicular components of Ampère's law (2.7), written in terms of the perturbed gyrocenter distribution function. They can be derived using the expression of the current density

$$\mathbf{j} = \sum_s q_s \int \mathrm{d}\theta \mathrm{d}v_\parallel \mathrm{d}\mu_s \frac{B_0}{m_s} \mathbf{v} \widetilde{f}_s = 0, \tag{2.34}$$

and using Faraday's law (2.6).

In order to remain consistent with the notation and parameters used in the articles Tassi (2019); Tassi et al. (2020), we introduce the generalized perturbed distribution function $\widetilde{g}_s$, which is connected to the perturbed gyrocenter distribution function $\widetilde{f}_s$ by the relation

$$\widetilde{g}_s = \widetilde{f}_s + \frac{q_s}{T_{0_{\parallel s}}} \frac{v_\parallel}{c} \mathcal{F}_{eq_s} J_{0s} \widetilde{A}_\parallel, \tag{2.35}$$

and allows use to write the Eqs. (2.28) - (2.31) in the form

$$\begin{aligned} &\frac{\partial \widetilde{g}_s}{\partial t} + \frac{c}{B_0} \left[J_{0s} \widetilde{\phi} - \frac{v_\parallel}{c} J_{0s} \widetilde{A}_\parallel + 2 \frac{\mu_s B_0}{q_s} J_{1s} \frac{\widetilde{B}_\parallel}{B_0}, \widetilde{g}_s \right] \\ &+ v_\parallel \frac{\partial}{\partial z} \left(\widetilde{g}_s + \frac{q_s}{T_{0_{\parallel s}}} \mathcal{F}_{eq_s} \left(J_{0s} \widetilde{\phi} - \frac{v_\parallel}{c} J_{0s} \widetilde{A}_\parallel + 2 \frac{\mu_s B_0}{q_s} J_{1s} \frac{\widetilde{B}_\parallel}{B_0} \right) \right) = 0, \end{aligned} \tag{2.36}$$

$$\begin{aligned} &\sum_s q_s \int \mathrm{d}\mathcal{W}_s \, J_{0s} \widetilde{g}_s = \sum_s \frac{q_s^2}{T_{0_{\perp s}}} \int \mathrm{d}\mathcal{W}_s \, \mathcal{F}_{eq_s} \left(1 - J_{0s}^2\right) \widetilde{\phi} \\ &- \sum_s q_s \int \mathrm{d}\mathcal{W}_s \, 2 \frac{\mu_s B_0}{T_{0_{\perp s}}} \mathcal{F}_{eq_s} J_{0s} J_{1s} \frac{\widetilde{B}_\parallel}{B_0}, \end{aligned} \tag{2.37}$$

$$\begin{aligned} &\sum_s q_s \int \mathrm{d}\mathcal{W}_s \, v_\parallel J_{0s} \left(\widetilde{g}_s - \frac{q_s}{T_{0_{\parallel s}}} \frac{v_\parallel}{c} \mathcal{F}_{eq_s} J_{0s} \widetilde{A}_\parallel \right) = -\frac{c}{4\pi} \nabla_\perp^2 \widetilde{A}_\parallel \\ &+ \sum_s \frac{q_s^2}{m_s} \int \mathrm{d}\mathcal{W}_s \, \mathcal{F}_{eq_s} \left(1 - \frac{1}{\Theta_s} \frac{v_\parallel^2}{v_{th_{\parallel s}}^2} \right) \left(1 - J_{0s}^2\right) \frac{\widetilde{A}_\parallel}{c}, \end{aligned} \tag{2.38}$$

$$\begin{aligned} &\sum_s \frac{\beta_{\perp_s}}{n_0} \int \mathrm{d}\mathcal{W}_s \, 2 \frac{\mu_s B_0}{T_{0_{\perp s}}} J_{1s} \widetilde{g}_s = -\sum_s \frac{\beta_{\perp_s}}{n_0} \frac{q_s}{T_{0_{\perp s}}} \int \mathrm{d}\mathcal{W}_s \, 2 \frac{\mu_s B_0}{T_{0_{\perp s}}} \mathcal{F}_{eq_s} J_{0s} J_{1s} \widetilde{\phi} \\ &- \left(2 + \sum_s \frac{\beta_{\perp_s}}{n_0} \int \mathrm{d}\mathcal{W}_s \, \mathcal{F}_{eq_s} \left(2 \frac{\mu_s B_0}{T_{0_{\perp s}}} J_{1s} \right)^2 \right) \frac{\widetilde{B}_\parallel}{B_0}. \end{aligned} \tag{2.39}$$

This formulation of the equations has the advantage that they are written as a dynamical system of the form $\partial_t \widetilde{g}_s = F(\widetilde{g}_s)$. From the numerical point of view, the benefits of this formulation are mentioned in, for instance, Numata et al. (2010).

2.2 From gyrokinetic to gyrofluid: the closure problem

Perturbations of the gyrofluid moments, such as the perturbations of the gyrocenter density, parallel velocity, and parallel and perpendicular temperatures, are computed as moments in normalized form of the perturbation of the gyrocenter distribution function $\widetilde{f_s}$. We express here, for instance, the first four moments, given by

$$N_s = \int \mathrm{d}\mathcal{W}_s \widetilde{f_s}, \qquad \frac{U_s}{v_{th_{\parallel s}}} = \frac{1}{n_0} \int \mathrm{d}\mathcal{W}_s \frac{v_\parallel}{v_{th_{\parallel s}}} \widetilde{f_s}, \tag{2.40}$$

$$\frac{T_{\parallel s}}{T_{0_{\parallel s}}} = \frac{1}{n_0} \int \mathrm{d}\mathcal{W}_s \left(\frac{v_\parallel^2}{v_{th_{\parallel s}}^2} - 1 \right) \widetilde{f_s}, \qquad \frac{T_{\perp s}}{T_{0_{\perp s}}} = \frac{1}{n_0} \int \mathrm{d}\mathcal{W}_s \left(\frac{\mu_s B_0}{T_{0_{\perp s}}} - 1 \right) \widetilde{f_s},$$

where N_s is the gyrocenter density fluctuation, U_s is that of the parallel velocity, $T_{\parallel s}$ of the parallel temperature, and $T_{\perp s}$ of the perpendicular temperature.

We derive evolution equations for the gyrocenter density and parallel velocity fluctuations. The evolution equation for each gyrofluid moment, turns out to depend, in principle, on an infinite number of higher-order moments due to the presence of the gyroaverage operators J_{0s} in the gyrokinetic equations. In order to obtain a closed gyrofluid system, it is therefore necessary to impose closure relations to truncate the infinite hierarchy of equations. We will need to take into account gyrocenter temperature fluctuations in order to impose a closure on the temperature fluctuations.

The perturbed gyrocenter distribution function can be developed as a series of its gyrocenter moments using Hermite polynomials H_m and Laguerre polynomials L_n,

$$H_m(x) = (-1)^m e^{x^2} \frac{d^m}{dx^m} e^{-x^2}, \qquad L_n(x) = \frac{e^x}{n!} \frac{d^n}{dx^n} x^n e^{-x}. \tag{2.41}$$

where H_n are polynomials of $v_\parallel / v_{th_{\parallel s}}$ and L_m are polynomials of $\mu_s B_0 / T_{0_{\perp s}}$, with m and n are non-negative integers. This expansions are used in, for instance, Scott et al. (2010); Mandell et al. (2018); Gorbunov & Teaca (2022).

The expansion reads

$$\widetilde{f_s}(\mathbf{x}, v_\parallel, \mu_s, t) = \sum_{m,n=0}^{+\infty} \frac{1}{\sqrt{m!}} f_{mn_s}(\mathbf{x}, t) H_m \left(\frac{v_\parallel}{v_{th_{\parallel s}}} \right) L_n \left(\frac{\mu_s B_0}{T_{0_{\perp s}}} \right) \mathcal{F}_{eq_s}(v_\parallel, \mu_s). \tag{2.42}$$

The functions f_{mn_s} are coefficients of the expansion and are related to the moments of $\widetilde{f_s}$. For instance, considering the couples $(m, n) = (0, 0)$ and $(m, n) = (1, 0)$, we obtain the gyrocenter density and parallel velocity respectively. These polynomials satisfy convenient orthogonality relations

$$\int e^{-x^2} H_m(x) H_n(x) \mathrm{d}x = \sqrt{\pi} 2^n n! \delta_{mn}, \tag{2.43}$$

$$\int_0^\infty e^{-x} L_m(x) L_n(x) \mathrm{d}x = \delta_{mn}, \tag{2.44}$$

which will be useful in the derivation of the gyrofluid models.

2.3 The isothermal closure

2.3.1 The closure

We now drop the tilde $\tilde{}$ *on the perturbed electromagnetic fields* ϕ, $A_\|$ *and* $B_\|$.

In this Section, the imposed closure relation consists in setting the perturbations of the parallel and perpendicular *particle* temperatures to zero, $t_{\|_s} = 0$ and $t_{\perp_s} = 0$, and in setting equal to zero also all the perturbations of the *gyrocenter* moments of order higher than those temperatures. The isothermal closure is a rather standard one in fluid models for plasmas. In the gyrofluid approach, however, it requires to be formulated in terms of the gyrocenter temperatures.

Using the orthogonality relations of Hermite and Laguerre polynomials, and retaining the first four moments, the gyrokinetic function $\widetilde{f_s}$ is written as

$$\widetilde{f_s} = \mathcal{F}_{eq_s} \left(\frac{N_s}{n_0} + \frac{v_\|}{v_{th_{\|s}}} \frac{U_s}{v_{th_{\|s}}} + \frac{1}{2} \left(\frac{v_\|^2}{v_{th_{\|s}}^2} - 1 \right) \frac{T_{\|s}}{T_{0_{\|s}}} + \left(\frac{\mu_s B_0}{T_{0_{\perp s}}} - 1 \right) \frac{T_{\perp s}}{T_{0_{\perp s}}} \right). \tag{2.45}$$

Inserting this expression for $\widetilde{f_s}$ in the gyrokinetic equation and integrating over $\mathrm{d}\mathcal{W}_s$, yields the evolution equation for N_s

$$\begin{aligned} \frac{\partial}{\partial t} \frac{N_s}{n_0} + \frac{c}{B_0} \left[G_{10_s} \phi + \frac{T_{0_{\perp s}}}{q_s} 2 G_{20_s} \frac{B_\|}{B_0}, \frac{N_s}{n_0} \right] - \frac{c}{B_0} \left[G_{11_s} \phi + \frac{T_{0_{\perp s}}}{q_s} 2 G_{21_s} \frac{B_\|}{B_0}, \frac{T_{\perp s}}{T_{0_{\perp s}}} \right] \\ - \frac{1}{B_0} \left[G_{10_s} A_\|, U_s \right] + \frac{\partial U_s}{\partial z} = 0. \end{aligned} \tag{2.46}$$

Multiplying the gyrokinetic equation by $v_\| / (n_0 v_{th_{\|s}})$ and integrating over $\mathrm{d}\mathcal{W}_s$, gives the evolution equation for U_s

$$\begin{aligned}&\frac{\partial}{\partial t}\left(\frac{U_s}{v_{th_{\parallel s}}} + \frac{q_s v_{th_{\parallel s}}}{T_{0_{\parallel s}} c} G_{10_s} A_\parallel\right) + \frac{c}{B_0}\left[G_{10_s}\phi + \frac{T_{0_{\perp s}}}{q_s} 2G_{20_s}\frac{B_\parallel}{B_0}, \frac{U_s}{v_{th_{\parallel s}}}\right]\\
&\quad - \frac{v_{th_{\parallel s}}}{B_0}\left[G_{10_s}A_\parallel, \frac{N_s}{n_0} + \frac{T_{\parallel s}}{T_{0_{\parallel s}}}\right] + \frac{v_{th_{\parallel s}}}{B_0}\left[G_{11_s}A_\parallel, \frac{T_{\perp s}}{T_{0_{\perp s}}}\right] + \frac{q_s v_{th_{\parallel s}}}{T_{0_{\parallel s}} B_0}\sum_{n=0}^{+\infty}\left[G_{1n_s}\phi, G_{1n_s}A_\parallel\right]\\
&\quad + \frac{\Theta_s v_{th_{\parallel s}}}{B_0}\sum_{n=0}^{+\infty}\left[2G_{2n_s}\frac{B_\parallel}{B_0}, G_{1n_s}A_\parallel\right] + v_{th_{\parallel s}}\frac{\partial}{\partial z}\left(\frac{q_s}{T_{0_{\parallel s}}}G_{10_s}\phi + 2\frac{T_{0_{\perp s}}}{T_{0_{\parallel s}}}G_{20_s}\frac{B_\parallel}{B_0} + \frac{N_s}{n_0} + \frac{T_{\parallel s}}{T_{0_{\parallel s}}}\right) = 0,\end{aligned} \tag{2.47}$$

where the operators G_{1n_s} and G_{2n_s} are defined in Fourier space so that (Brizard (1992))

$$\begin{aligned}G_{1n_s} f_{\mathbf{k}} e^{i\mathbf{k}\cdot\mathbf{x}} &= \sum_{\mathbf{k}} \frac{B_0}{T_{0_{\perp s}}}\int \mathrm{d}\mu_s\, e^{-\frac{\mu_s B_0}{T_{0_{\perp s}}}} L_n\left(\frac{\mu_s B_0}{T_{0_{\perp s}}}\right) J_0(a_s) f_{\mathbf{k}} e^{i\mathbf{k}\cdot\mathbf{x}}\\
&= \sum_{\mathbf{k}} \frac{e^{-b_s/2}}{n!}\left(\frac{b_s}{2}\right)^n f_{\mathbf{k}} e^{i\mathbf{k}\cdot\mathbf{x}},\end{aligned} \tag{2.48}$$

$$\begin{aligned}G_{2n_s} f_{\mathbf{k}} e^{i\mathbf{k}\cdot\mathbf{x}} &= \sum_{\mathbf{k}} \frac{B_0}{T_{0_{\perp s}}}\int \mathrm{d}\mu_s\, e^{-\frac{\mu_s B_0}{T_{0_{\perp s}}}} L_n\left(\frac{\mu_s B_0}{T_{0_{\perp s}}}\right) \frac{\mu_s B_0}{T_{0_{\perp s}}}\frac{J_1(a_s)}{a_s} f_{\mathbf{k}} e^{i\mathbf{k}\cdot\mathbf{x}}\\
&= -\sum_{\mathbf{k}} \frac{e^{-b_s/2}}{2}\left(\left(\frac{b_s}{2}\right)^{n-1}\frac{1}{(n-1)!} - \left(\frac{b_s}{2}\right)^n \frac{1}{n!}\right) f_{\mathbf{k}} e^{i\mathbf{k}\cdot\mathbf{x}}, \quad \text{for } n \geq 1,\end{aligned} \tag{2.49}$$

$$G_{20_s} f_{\mathbf{k}} e^{i\mathbf{k}\cdot\mathbf{x}} = \sum_{\mathbf{k}} \frac{e^{-b_s/2}}{2} f_{\mathbf{k}} e^{i\mathbf{k}\cdot\mathbf{x}}, \tag{2.50}$$

with b_s given by $b_e = \hat{k}_\perp^2 \rho_{e\perp}^2$ and $b_i = \hat{k}_\perp^2 \rho_{i\perp}^2$ for the electrons and for the ions respectively, and with $\rho_{i,e\perp}$ the Larmor radius based on the equilibrium perpendicular temperatures.

For the range of parameters adopted in our analysis, in particular for b_s not largely exceeding 1, the gyroaverage operators, corresponding to those introduced by Brizard (1992), are shown to be adequate. Nevertheless, different gyroaverage operators, described in Dorland & Hammett (1993) and Mandell et al. (2018), have proven to provide a very good agreement with the linear kinetic theory for a wider range of scales and are widespread in gyrofluid numerical codes.

With regard to the static equations (2.37) - (2.39), by inserting the expansion (2.45), we obtain

$$\sum_s q_s \left(G_{10_s} \frac{N_s}{n_0} - G_{11_s} \frac{T_{\perp s}}{T_{0_{\perp s}}} + \frac{q_s}{T_{0_{\perp s}}} (\Gamma_{0s} - 1)\phi + (\Gamma_{0s} - \Gamma_{1s}) \frac{B_\parallel}{B_0} \right) = 0, \tag{2.51}$$

$$-\nabla_\perp^2 A_\parallel = \frac{4\pi n_0}{c} \sum_s q_s \left(G_{10_s} U_s + \frac{q_s}{m_s} \left(1 - \frac{1}{\Theta_s} \right) (\Gamma_{0s} - 1) \frac{A_\parallel}{c} \right), \tag{2.52}$$

$$\sum_s \beta_{\perp_s} \left(2G_{20_s} \frac{N_s}{n_0} - 2G_{21_s} \frac{T_{\perp s}}{T_{0_{\perp s}}} \right) = -\sum_s \beta_{\perp_s} \frac{q_s}{T_{0_{\perp s}}} (\Gamma_{0s} - \Gamma_{1s})\phi - 2\frac{B_\parallel}{B_0} \tag{2.53}$$

$$- \sum_s \beta_{\perp_s} 2(\Gamma_{0s} - \Gamma_{1s}) \frac{B_\parallel}{B_0}, \tag{2.54}$$

where

$$\Gamma_{0s} f_{\mathbf{k}} e^{i\mathbf{k}\cdot\mathbf{x}} = \sum_{\mathbf{k}} I_0(b_s) e^{-b_s} f_{\mathbf{k}} e^{i\mathbf{k}\cdot\mathbf{x}}, \tag{2.55}$$

$$\Gamma_{1s} f_{\mathbf{k}} e^{i\mathbf{k}\cdot\mathbf{x}} = \sum_{\mathbf{k}} I_1(b_s) e^{-b_s} f_{\mathbf{k}} e^{i\mathbf{k}\cdot\mathbf{x}} \tag{2.56}$$

and I_n are the modified Bessel functions of order n.

The system given by Eqs. (2.46), (2.47) and (2.51), (2.52), (2.54) requires a closure on the temperature fluctuations. The isothermal closure imposes

$$\frac{t_{\parallel_s}}{T_{0_{\parallel s}}} = \frac{1}{n_0} \int_0^{2\pi} \frac{d\theta}{2\pi} \int \mathrm{d}\mathcal{W}_s \left(\frac{v_\parallel^2}{v_{th_{\parallel s}}^2} - 1 \right) \mathrm{f}_s = 0, \tag{2.57}$$

$$\frac{t_{\perp_s}}{T_{0_{\perp s}}} = \frac{1}{n_0} \int_0^{2\pi} \frac{d\theta}{2\pi} \int \mathrm{d}\mathcal{W}_s \left(\frac{\mu_s B_0}{T_{0_{\perp s}}} - 1 \right) \mathrm{f}_s = 0. \tag{2.58}$$

We make use of the relation (2.25), expressing the perturbation of the particle distribution function f_s in terms of that of the gyrocenter $\widetilde{f_s}$, into Eqs. (2.57) - (2.58), to express the closure in terms of the gyrocenter temperature fluctuations. By means of the identity (Kunz et al. (2015))

$$J_0(a_s) f_{s_{\mathbf{k}}} = \frac{1}{2\pi} \int_0^{2\pi} \mathrm{d}\theta f_{s_{\mathbf{k}}} e^{i\mathbf{k}\cdot\boldsymbol{r}_{L_s}}, \tag{2.59}$$

we obtain that Eqs. (2.57) and (2.58) lead to the following closure relations in terms of gyrocenter variables

$$t_{\parallel_s} = G_{10_s} T_{\parallel s} = 0, \tag{2.60}$$

$$\frac{t_{\perp_s}}{T_{0_{\perp s}}} = -G_{11_s} \frac{N_s}{n_0} + \left(G_{10_s} - 2G_{11_s} + G_{12_s} \right) \frac{T_{\perp s}}{T_{0_{\perp s}}} - \frac{q_s}{T_{0_{\perp s}}} G_{T0_s} \phi - G_{T1_s} \frac{B_\parallel}{B_0} = 0, \tag{2.61}$$

with two additional operators defined as

$$G_{T0_s} f_{\mathbf{k}} e^{i\mathbf{k}\cdot\mathbf{x}} = \sum_{\mathbf{k}} b_s e^{-b_s} \left(I_0(b_s) - I_1(b_s) \right) f_{\mathbf{k}} e^{i\mathbf{k}\cdot\mathbf{x}}, \tag{2.62}$$

$$G_{T1_s} f_{\mathbf{k}} e^{i\mathbf{k}\cdot\mathbf{x}} = \sum_{\mathbf{k}} 2e^{-b_s} \left(\left(b_s - \frac{1}{2} \right) I_0(b_s) - b_s I_1(b_s) \right) f_{\mathbf{k}} e^{i\mathbf{k}\cdot\mathbf{x}}. \tag{2.63}$$

We remark that the relations included in Eqs. (2.60) and (2.61), permitting to express particle temperature fluctuations in terms of gyrocenter temperature fluctuations, agree with those of Brizard (1992)[2]. In particular, we note that such relations do not depend explicitly on Θ_e.

2.3.2 Normalization by ρ_s, and assumptions

The adopted dimensionless variables are

$$\begin{aligned}
&\hat{x} = \frac{x}{\rho_{s\perp}}, \qquad \hat{y} = \frac{y}{\rho_{s\perp}}, \qquad \hat{z} = \sqrt{\frac{\beta_{\perp_e}}{2}} \frac{z}{\rho_{s\perp}}, \qquad \hat{t} = \omega_{ci} t, \\
&\hat{N}_s = \frac{N_s}{n_0}, \qquad \hat{U}_s = \sqrt{\frac{\beta_{\perp_e}}{2}} \frac{U_s}{c_{s\perp}}, \qquad \hat{T}_{\perp_s} = \frac{T_{\perp s}}{T_{0_{\perp s}}}, \qquad \hat{T}_{\|_s} = \frac{T_{\| s}}{T_{0_{\| s}}}, \\
&\hat{\phi} = \frac{e\phi}{T_{0_{\perp e}}}, \qquad \hat{B}_\| = \frac{B_\|}{B_0}, \qquad \hat{A}_\| = \frac{1}{\rho_{s\perp}} \sqrt{\frac{2}{\beta_{\perp_e}}} \frac{A_\|}{B_0}.
\end{aligned} \tag{2.64}$$

Where $\rho_{s\perp} = \sqrt{T_{0_{\perp e}}/m_i}(m_i c/eB_0)$ is the sonic Larmor radius based on the perpendicular electron equilibrium temperature. *For the ease of notation, we now drop the hat over the dimensionless variables.* From (2.64) and until the end of the Thesis, when we mention the model with our isothermal closure, it will be in reference to the equations obtained after the normalization. Concerning the normalization of $A_\|$, U_e and z in Eq. (2.64), we tpoint out that, in comparison for instance with Tassi et al. (2018), the factor $\sqrt{2/\beta_{\perp_e}}$ was introduced here in order to make the limit $\beta_{\perp_e} \rightarrow 0$ more transparent. This also explains the presence of the coefficient $\sqrt{\beta_{\perp_e}/2}$ appearing in the following normalized expression of the magnetic field in dimensionless variables

$$\mathbf{B} \approx \mathbf{z} + B_\| \mathbf{z} + \sqrt{\frac{\beta_{\perp_e}}{2}} \nabla A_\| \times \mathbf{z}, \tag{2.65}$$

A new parameter, naturally emerging from the normalization, is given by

$$\tau_{\perp_s} = \frac{T_{0_{\perp s}}}{T_{0_{\perp e}}}, \tag{2.66}$$

---

[2] up to a misprint in the sign of I_1 in Brizard (1992).

corresponding to the ratio between the equilibrium perpendicular temperatures, which becomes $\tau_i = T_{0i}/T_{0e}$ is case of isotropic equilibrium temperature.

The complete 4-field dimensionless evolution equations are given by

$$\begin{aligned}&\frac{\partial N_s}{\partial t} + \left[G_{10_s}\phi, N_s\right] + \operatorname{sgn}(q_s)\tau_{\perp_s}\left[2G_{20_s}B_\parallel, N_s\right] - \left[G_{11_s}\phi, T_{0_{\perp s}}\right] - \left[G_{10_s}A_\parallel, U_s\right] \\ &- \operatorname{sgn}(q_s)\tau_{\perp_s}\left[2G_{21_s}B_\parallel, T_{0_{\perp s}}\right] + \frac{\partial U_s}{\partial z} = 0,\end{aligned} \tag{2.67}$$

$$\begin{aligned}&\frac{\partial}{\partial t}\left(\frac{2}{\beta_{\perp_e}}\frac{m_s}{m_i}U_s + \operatorname{sgn}(q_s)G_{10_s}A_\parallel\right) + \frac{2}{\beta_{\perp_e}}\left[G_{10_s}\phi, \frac{m_s}{m_i}U_s\right] + \operatorname{sgn}(q_s)\tau_{\perp_s}\frac{2}{\beta_{\perp_e}}\left[2G_{20_s}B_\parallel, \frac{m_s}{m_i}U_s\right] \\ &- \frac{\tau_{\perp_s}}{\Theta_s}\left[G_{10_s}A_\parallel, N_s + T_{\parallel s}\right] + \frac{\tau_{\perp_s}}{\Theta_s}\left[G_{11_s}A_\parallel, T_{0_{\perp s}}\right] + \operatorname{sgn}(q_s)\sum_{n=0}^{+\infty}\left[G_{1n_s}\phi, G_{1n_s}A_\parallel\right] \\ &+ \tau_{\perp_s}\sum_{n=0}^{+\infty}\left[2G_{2n_s}B_\parallel, G_{1n_s}A_\parallel\right] + \frac{\partial}{\partial z}\left(\operatorname{sgn}(q_s)G_{10_s}\phi + 2\tau_{\perp_s}G_{20_s}B_\parallel + \frac{\tau_{\perp_s}}{\Theta_s}\left(N_s + T_{\parallel s}\right)\right) = 0,\end{aligned} \tag{2.68}$$

and the static equations correspond to

$$\sum_s \operatorname{sgn}(q_s)\left(G_{10_s}N_s - G_{11_s}T_{0_{\perp s}} + \frac{\operatorname{sgn}(q_s)}{\tau_{\perp_s}}(\Gamma_{0s} - 1)\phi + (\Gamma_{0s} - \Gamma_{1s})B_\parallel\right) = 0, \tag{2.69}$$

$$\sum_s \left(\frac{\beta_{\perp_s}}{2}\frac{2}{\beta_{\perp_e}}\operatorname{sgn}(q_s)G_{10_s}U_s + \left(1 - \frac{1}{\Theta_s}\right)(\Gamma_{0s} - 1)\frac{m_i}{m_s}\frac{\beta_{\perp_s}}{2}A_\parallel\right) = -\nabla_\perp^2 A_\parallel, \tag{2.70}$$

$$\sum_s \beta_{\perp_s}\frac{\operatorname{sgn}(q_s)}{\tau_{\perp_s}}(\Gamma_{0s} - \Gamma_{1s})\phi + 2B_\parallel + 2\sum_s \beta_{\perp_s}(\Gamma_{0s} - \Gamma_{1s})B_\parallel = -2\sum_s \beta_{\perp_s}\left(G_{20_s}N_s - G_{21_s}T_{0_{\perp s}}\right), \tag{2.71}$$

$$\left(G_{10_s} - 2G_{11_s} + G_{12_s}\right)T_{0_{\perp s}} - G_{11_s}N_s - G_{T0_s}\frac{\operatorname{sgn}(q_s)}{\tau_{\perp_s}}\phi - G_{T1_s}B_\parallel = 0, \tag{2.72}$$

$$G_{10_s}T_{\parallel s} = 0. \tag{2.73}$$

The system (2.67)-(2.73) is a new gyrofluid model accounting for parallel magnetic perturbations, FLR effects, and equilibrium temperature anisotropies.

This gyrofluid model, although greatly simplified with respect to the original gyrokinetic system, is still amenable to further reductions. Because of the complexity of the model, for the purpose of an analytical investigation of the tearing instability, we simplify it by applying a number of assumptions. In particular, we aim at reducing the model to a two-field model consisting of the evolution equations for the fluctuations of the electron density and electron parallel velocity.

Firstly, we consider a cold ion regime, assuming that the value of the ion to electron perpendicular equilibrium temperature ratio is small

$$\tau_{\perp_i} \rightarrow 0. \tag{2.74}$$

In particular, assuming $\tau_{\perp_i} \ll d_e^2$ as $d_e \rightarrow 0$ effectively removes all finite ion temperature effects, except for the one associated with the ion polarization in the quasi-neutrality relation[3], which introduces the diamagnetic drift. The cold ion limit also implies a negligible ion Larmor radius since, $\rho_{i\perp} = \sqrt{\tau_{\perp_i}}\rho_{s\perp}$.

Secondly, ions are assumed to be an immobile background, so all the involved fluctuations of the ion *gyrocenter* moments, i.e. N_i, U_i, $T_{\perp_i}$ and $T_{\|_i}$, are assumed to be negligible in the static relations, which effectively decouples the electron dynamics from the ion gyrocenter dynamics,

$$N_i = U_i = T_{\perp_i} = T_{\|_i} = 0. \tag{2.75}$$

Note that (2.75) does not prevent a fluctuation of the *particle* ion density. Indeed, as we will see later, $n_i \neq 0$.
These assumptions on the ions are of course very strong. The expressions given in Eq. (2.75) are not solutions of the equations for the ion gyrofluid moments. However, they are solutions up to terms of order $\beta_{\perp_e}$ and in the following we will assume $\beta_{\perp_e} \ll 1$. Also, at least in the case of initial conditions $N_i = U_i = 0$, ion gyrocenter density and parallel velocity fluctuations appear not to substantially modify the reconnection process (Comisso et al. (2013); Numata et al. (2011)).
We also assume an isotropic ion temperature, and consider a temperature anisotropy only for the electrons, i.e.

$$\Theta_i = 1. \tag{2.76}$$

To simplify the notation, the square root of the mass ratio will be denoted

$$\delta = \left(\frac{m_e}{m_i}\right)^{1/2}. \tag{2.77}$$

Finally, we further reduce the system by considering the following ordering, where

---

[3] 3rd term in (2.69) for $s = i$.

$\beta_{\perp_e}$ is used as an expansion parameter:

$$\partial_x \sim \partial_y \sim \Theta_e = O(1), \tag{2.78}$$

$$\partial_t \sim \partial_z \sim N_e \sim \phi \sim A_\| \sim U_e = O(\varepsilon) \ll 1, \tag{2.79}$$

$$B_\| \sim T_{\perp e} = O(\varepsilon\beta_{\perp_e}), \tag{2.80}$$

$$\delta^2 \ll \beta_{\perp_e} \ll 1. \tag{2.81}$$

The ordering (2.78) fixes equal to $\rho_{s\perp}$ the characteristic scale length for the variations of the fluctuations in the perpendicular plane, and assumes the electron temperature anisotropy to remain finite as the expansion parameters tend to zero. The ordering (2.79), on the other hand, refers to small-amplitude, low-frequency, and strongly anisotropic fluctuations, which are typical assumptions of the δf gyrokinetic approach (note, on the other hand, that due to our subsidiary ordering in the parameter $\beta_{\perp_e}$, the ordering (2.79) is not equivalent to the one assumed in Kunz et al. (2015) for deriving the parent gyrokinetic model (2.28)-(2.31)). All the lowest-order terms in the gyrofluid equations (2.67)-(2.68) are of order ε^2 and no further expansion will be performed in the parameter ε.

According to Eq. (2.81), we consider a small value of the $\beta_{\perp_e}$ parameter, although much larger than the mass ratio δ^2. The reason for the latter ordering is that it will allow to neglect electron FLR effects, while retaining electron inertia term in Ohm's law, which is required for reconnection. As a consequence, the fluctuations $B_\|$ and $T_{\perp e}$ will turn out to be subdominant with respect to the other fluctuations, as indicated by Eq. (2.80).

We focus, in the coming steps, on the reduction of the gyroaverage operators using the assumptions (2.81) and (2.74). The cold ion limit and the ordering (2.74) indicate that the normalized parameter b_s for each species, corresponding to $b_e = \delta^2 k_\perp^2$ and $b_i = \tau_{\perp_i} k_\perp^2$, can be expanded, allowing us to simplify the gyroaverage operators G_{1n_s} and G_{2n_s}, whose general form is given by Eqs. (2.48) and (2.49). For the sake of clarity, we write below the explicit expression of the normalized operators acting on the moments that will be considered for the reduction (operators of higher order moment will be negligible):

$$\begin{aligned}
G_{10_e} f_{\mathbf{k}} e^{i\mathbf{k}\cdot\mathbf{x}} &= 2G_{20_e} f_{\mathbf{k}} e^{i\mathbf{k}\cdot\mathbf{x}} = \sum_{\mathbf{k}} e^{-\frac{\delta^2}{2}k_\perp^2} f_{\mathbf{k}} e^{i\mathbf{k}\cdot\mathbf{x}},\\
G_{11_e} f_{\mathbf{k}} e^{i\mathbf{k}\cdot\mathbf{x}} &= \sum_{\mathbf{k}} \frac{\delta^2}{2} k_\perp^2 e^{-\frac{\delta^2}{2}k_\perp^2} f_{\mathbf{k}} e^{i\mathbf{k}\cdot\mathbf{x}},\\
G_{21_e} f_{\mathbf{k}} e^{i\mathbf{k}\cdot\mathbf{x}} &= -\sum_{\mathbf{k}} \frac{e^{-\frac{\delta^2}{2}k_\perp^2}}{2}\left(1 - \frac{\delta^2}{2}k_\perp^2\right) f_{\mathbf{k}} e^{i\mathbf{k}\cdot\mathbf{x}};
\end{aligned} \tag{2.82}$$

and for the ions:

$$
\begin{aligned}
G_{10_i} f_{\mathbf{k}} e^{i\mathbf{k}\cdot\mathbf{x}} &= 2G_{20_i} f_{\mathbf{k}} e^{i\mathbf{k}\cdot\mathbf{x}} = \sum_{\mathbf{k}} e^{-\frac{\tau_{\perp_i}}{2}k_\perp^2} f_{\mathbf{k}} e^{i\mathbf{k}\cdot\mathbf{x}}, \\
G_{11_i} f_{\mathbf{k}} e^{i\mathbf{k}\cdot\mathbf{x}} &= \sum_{\mathbf{k}} \frac{\tau_{\perp_i}}{2} k_\perp^2 e^{-\frac{\tau_{\perp_i}}{2}k_\perp^2} f_{\mathbf{k}} e^{i\mathbf{k}\cdot\mathbf{x}}, \\
G_{21_i} f_{\mathbf{k}} e^{i\mathbf{k}\cdot\mathbf{x}} &= -\sum_{\mathbf{k}} \frac{e^{-\frac{\tau_{\perp_i}}{2}k_\perp^2}}{2} \left(1 - \frac{\tau_{\perp_i}}{2}k_\perp^2\right) f_{\mathbf{k}} e^{i\mathbf{k}\cdot\mathbf{x}}.
\end{aligned}
\tag{2.83}
$$

Upon the ordering (2.81), these operators are written using their Taylor expansions as

$$
\begin{aligned}
G_{10_e} f &= 2G_{20_e} f = \left(1 + \frac{\delta^2}{2}\nabla_\perp^2\right) f + O(\delta^3), \\
G_{11_e} f &= -\frac{\delta^2}{2}\nabla_\perp^2 f + O(\delta^3), \\
G_{21_e} f &= -\frac{1}{2}\left(1 + \frac{\delta^2}{2}\nabla_\perp^2\right) f + O(\delta^3),
\end{aligned}
\tag{2.84}
$$

For the ions, upon the ordering (2.74),

$$
\begin{aligned}
G_{10_i} f &= 2G_{20_i} f = \left(1 + \frac{\tau_{\perp_i}}{2}\nabla_\perp^2\right) f + O(\tau_{\perp_i}^2), \\
G_{11_i} f &= -\frac{\tau_{\perp_i}}{2}\nabla_\perp^2 f + O(\tau_{\perp_i}^2), \\
G_{21_i} f &= -\frac{1}{2}\left(1 + \frac{\tau_{\perp_i}}{2}\nabla_\perp^2\right) f + O(\tau_{\perp_i}^2),
\end{aligned}
\tag{2.85}
$$

while the operators G_{1n_s} and G_{2n_s} with $n \geq 2$ are of higher order in $\tau_{\perp_i}$ and thus turn out to be negligible. Regarding the ion and electron Γ_{ns} operators whose general expression is given in Eq. (2.55), they can be simplified as well using Eqs. (2.81) and (2.74), and can be written as

$$
\begin{aligned}
\Gamma_{0e} f &= (1 + \delta^2\nabla_\perp^2) f + O(\delta^3), \qquad & \Gamma_{1e} f &= O(\delta^3), \\
\Gamma_{0i} f &= (1 + \tau_{\perp_i}\nabla_\perp^2) f + O(\tau_{\perp_i}^2), \qquad & \Gamma_{1i} f &= O(\tau_{\perp_i}^2).
\end{aligned}
\tag{2.86}
$$

Using the ordering (2.78) in the closure equations (2.60) and (2.61) and neglecting terms proportional to d_e^2 compared to terms of order one, we obtain the reduced closure equations,

$$
T_{\|e} = 0, \qquad T_{\perp e} = -B_\|. \tag{2.87}
$$

When applying the ordering, to the evolution equations (2.67) and (2.68), the assumption $\delta^2 \ll \beta_{\perp_e} \ll 1$ allows us to neglect terms proportional to δ^2, arising from the operators G_{1n_e} and G_{2n_e}, when compared to terms proportional to $\delta^2/\beta_{\perp_e}$ and, therefore, to neglect electron FLR effects. However, retaining first order corrections in $\beta_{\perp_e}$

allows us to keep some terms involving the perturbation $B_{\|}$[4].

$$\frac{\partial N_e}{\partial t} + [\phi - B_{\|}, N_e] - [A_{\|}, U_e] + \frac{\partial U_e}{\partial z} = 0, \tag{2.88}$$

$$\frac{\partial}{\partial t}\left(A_{\|} - \frac{2\delta^2}{\beta_{\perp_e}} U_e\right) + \left[\phi - B_{\|}, A_{\|} - \frac{2\delta^2}{\beta_{\perp_e}} U_e\right] + \frac{1}{\Theta_e}[A_{\|}, N_e] + \frac{\partial}{\partial z}\left(\phi - B_{\|} - \frac{N_e}{\Theta_e}\right) = 0. \tag{2.89}$$

Applying now the ordering to the static equations (2.69) - (2.71) and neglecting terms proportional to δ^2, while retaining first order corrections in $\beta_{\perp_e}$, yields the relations

$$N_e = \nabla_\perp^2 \phi, \tag{2.90}$$

$$U_e = \left(1 + \frac{\beta_{\perp_e}}{2}\left(1 - \frac{1}{\Theta_e}\right)\right) \nabla_\perp^2 A_{\|}, \tag{2.91}$$

$$B_{\|} = -\frac{\beta_{\perp_e}}{2 + \beta_{\perp_e}} \nabla_\perp^2 \phi. \tag{2.92}$$

By means of the first relation in Eq. (2.90), indicating that the electron gyrocenter density equals the **E**×**B** vorticity $\nabla_\perp^2 \phi$, Eq. (2.69) becomes an evolution equation for the vorticity. As is customary with gyrofluid models, Eqs. (2.88) and (2.89) are expressed in terms of gyrocenter variables, but in this limit, gyrocenter variable can easily be expressed in terms of particle variables

$$N_e = n_e, \qquad U_e = u_e + \left(\frac{\beta_{\perp_e}}{2}\left(1 - \frac{1}{\Theta_e}\right)\right) \nabla_\perp^2 A_{\|}, \qquad B_{\|} = -\frac{\beta_{\perp_e}}{2 + \beta_{\perp_e}} n_e. \tag{2.93}$$

Regarding the ions, further insight about the assumptions $N_i = U_i = 0$ can be obtained expressing these assumptions in terms of particle moments, instead of gyrocenter moments. The plasma quasi-neutrality implies $n_e - n_i = 0$ and therefore

$$n_i = \nabla_\perp^2 \phi. \tag{2.94}$$

Regarding the assumption on the gyrocenter ion parallel velocity, $U_i = 0$ it imposes $u_i = 0$.

For the study of the tearing instability, we take perturbation with $k_z = 0$, thus making the approach essentially 2D. Using the relations (2.87) and (2.92)-(2.93), and neglecting corrections of order $\beta_{\perp e}$, the 2D evolution equations (2.88) and (2.89) become

---

[4] Therefore, we can write the evolution equations, retaining the above mentioned corrections as well as the subdominant term $(2/\beta_{\perp_e})[B_{\|}, \delta^2 U_e]$ of order δ^2, allowing the system to keep a Hamiltonian formulation (a similar inconsistency in the ordering, possessing, on the other hand, the merit of preserving the Hamiltonian character of the parent gyrokinetic model, is discussed in Passot et al. (2018)).

$$\frac{\partial \nabla_\perp^2 \phi}{\partial t} + [\phi, \nabla_\perp^2 \phi] - [A_\|, \nabla_\perp^2 A_\|] = 0, \tag{2.95}$$

$$\frac{\partial}{\partial t}\left(A_\| - \frac{2\delta^2}{\beta_{\perp_e}}\nabla_\perp^2 A_\|\right) + \left[\phi, A_\| - \frac{2\delta^2}{\beta_{\perp_e}}\nabla_\perp^2 A_\|\right] - \frac{1}{\Theta_e}[\nabla_\perp^2 \phi, A_\|] = 0. \tag{2.96}$$

The model (2.95) - (2.96), is the one considered for studying the impact of temperature anisotropy on the tearing instability in **Chapter** 3.

To sum up the main characteristics of this model used to study reconnection:

- **Electron inertia** breaks the frozen-in condition
- **Cold ions** (negligible ion FLR effects) are assumed
- **Immobile ions** are assumed along the guide field direction, **but ion density fluctuations are allowed**
- **Temperature anisotropy** can be included
- In the application of reconnection, the model normalisation is such that a **microscopic current sheet** of characteristic length scale $\rho_{s\perp}$ is assumed (with respect to the macroscopic length scale L of MHD)

When taking the isotropic limit $\Theta_e = 1$ for the electron temperature, the system (2.95) - (2.96) corresponds, up to the normalization, to the two-field model (2.136) - (2.137) of Schep et al. (1994). However, unlike the present model, the model of Schep et al. (1994) has a characteristic length scale $L \gg \rho_{s\perp}$. As a consequence, in the latter model, the analogue of the last term on the right-hand side of Eq. (2.96) is typically a small perturbation, proportional to $(\rho_{s\perp}/L) \ll 1$, whereas, on the presently adopted scale $\rho_{s\perp}$, this term is comparable to other terms retained in the same equation.

Neglecting electron inertia as well as the term $-(1/\Theta_e)[\nabla_\perp^2 \phi, A_\|]$ in Eq. (2.96), the system corresponds to 2D low β reduced magnetohydrodynamics (Kadomtsev & Pogutse (1974); Strauss (1976)). A version of a similar model, neglecting electron inertia but accounting for parallel magnetic perturbations, was adopted in order to investigate the impact of electron temperature anisotropy on the linear stability of magnetic vortex chains (Granier & Tassi (2020)).

Using the relation $B_\| = -\frac{\beta_{\perp e}}{2}\nabla_\perp^2 \phi$ (coming from Eq. (2.132)) in the Eqs. (2.95) and (2.96), the resulting model is similar to electron magnetohydrodynamic (EMHD) (Kingsep et al. (1990)). Analogously to EMHD, ions are assumed to be immobile along the guide field direction. On the other hand the continuity equation (2.95) turns to be an evolution equation for the perturbation of the parallel magnetic field $B_\|$ and not of the field $B_{\|} - (2\delta^2/\beta_{\perp_e})\nabla_{\perp}^2 B_{\|}$ as is the case for EMHD.

Regarding the term $-(1/\Theta_e)[\nabla_{\perp}^2\phi, A_{\|}]$ in Eq. (2.96)[5], where the temperature anisotropy parameter Θ_e, appears in the denominator, and is usually not present in EMHD, this contribution is coming from the projection, along the magnetic field, of the divergence of the anisotropic pressure tensor. This term plays an important role in the linear stability analysis that we present in Chapter 3. In particular, with respect to the case of EMHD, it leads to modifications of the linearized system in the inner region, eventually leading to a dispersion relation different from those derived for EMHD systems in Refs. Bulanov et al. (1992) and Cai & Li (2008).

In Refs. Kuznetsova et al. (1995) and Cai & Li (2009), a fluid description for the electron species was adopted, in order to study collisionless tearing stability taking into account non-gyrotropic terms. In the stability analysis presented in **Chapter 3** we do not account for such terms, as they are associated with electron FLR corrections, that we neglect due to the small $\beta_{\perp_e}$ limit. Compared to such studies, where a space-dependent equilibrium pressure is also considered, our equations (2.95) - (2.96) are assuming, in terms of the perpendicular and parallel particle temperature fluctuations, an isothermal closure and we consider a homogeneous equilibrium pressure resulting from a bi-Maxwellian distribution function. This closure leads to the cancellation of a number of contributions coming from the pressure tensor, and the term $-(1/\Theta_e)[\nabla_{\perp}^2\phi, A_{\|}]$ is the remaining contribution.

2.3.3 Conserved energy

In this subsection, we give the expression of the conserved total energy of the system and of the different forms of energies contributing to it. We introduce the dynamical variable

$$A_e = A_{\|} - \frac{2\delta^2}{\beta_{\perp_e}} U_e. \tag{2.97}$$

The static relations (2.93) can be seen, in Fourier space, as an inhomogeneous linear system with the Fourier coefficients of ϕ and $B_{\|}$ as unknowns, for given $N_{i,e}$. From the solution of this system, one can express the fields ϕ and $B_{\|}$ in terms of N_i and N_e, by means of relations of the form

$$U_e = \mathcal{L}_{U_e}(A_e), \qquad B_{\|} = \mathcal{L}_B(N_e), \qquad \phi = \mathcal{L}_{\phi}(N_e), \tag{2.98}$$

where $\mathcal{L}_{U_e}$, $\mathcal{L}_{\phi}$ and $\mathcal{L}_B$ are symmetric operators, i.e., operators $\mathcal{L}$ such that $\int d^2x\, f\mathcal{L}g = \int d^2x\, g\mathcal{L}f$, for two functions f and g. They permit to express U_e, ϕ and $B_{\|}$ in terms of N_e and A_e by means of Eqs. (2.93).

The system (2.88)-(2.89) was shown to be Hamiltonian in Tassi (2019); Granier et al. (2021). Its Hamiltonian structure is presented in Appendix A. The total conserved

---

[5] in 3D there will also be the term $-(1/\Theta_e)\partial_z\nabla_{\perp}^2\phi$.

energy consists of the Hamiltonian functional

$$H(N_e, A_e) = \frac{1}{2}\int d^2x \left(\frac{N_e^2}{\Theta_e} - A_e\nabla_\perp^2\mathcal{L}_{U_e}A_e - N_e\mathcal{L}_\phi N_e + N_e\mathcal{L}_B N_e\right). \tag{2.99}$$

2.4 The quasi-static closure

In this section, we present a second model, derived by Tassi et al. (2020), that is used in **Chapter** 4, to study the impact of electron FLRs on the tearing mode growth rate. It is also used in **Chapter** 5, to study their effects on the plasmoid instability. This model is based on the so-called quasi-static closure, implying that the perturbations are assumed to propagate along the guide field with a phase velocity much smaller than the particle thermal velocities.

The field normalization applied to this model differs from that applied to the previous model. Here, instead of normalizing the lengths and the time by the sonic Larmor radius and the cyclotron frequency respectively, we use a macroscopic length L and the Alfvén time $\tau_A = L/v_A$.

2.4.1 The closure

The procedure for applying the quasi-static closure, derived in the Appendix of Tassi et al. (2020), consists of fixing a number of moments, for which a corresponding evolution equation is derived from the gyrokinetic model, and of applying to all remaining moments appearing in such evolution equations,

$$f_{mn_s} = -\delta_{m0}\left(-G_{1ns}\frac{e}{T_{0s}}\phi + 2G_{2ns}\frac{B_\parallel}{B_0}\right), \tag{2.100}$$

where δ_{m0} is a Kronecker delta and m and n are non-negative integers. We note that, using Eqs. (2.43)-(2.44) the gyrofluid moments f_{mn} can be expressed in terms of the perturbation of the gyrocenter distribution function as

$$f_{mn_s} = \frac{1}{n_0\sqrt{m!}}\int \mathrm{d}\mathcal{W}_s H_m\left(\frac{v_\parallel}{v_{th_{\parallel s}}}\right) L_n\left(\frac{\mu_s B_0}{T_{0_{\perp s}}}\right)\tilde{f}_s \tag{2.101}$$

This relation is originally obtained in Tassi et al. (2020) by linearizing the 3D gyrokinetic Eqs. (2.28) about an equilibrium $\phi_{eq} = A_{\parallel eq} = B_{\parallel eq} = 0$ and assuming waves with a small parallel phase velocity $\omega/k_z \ll v_{th_s}$, which justifies the term quasi-static. Although in 2D, with $k_z = 0$, this quasi-static closure can be obtained by linearizing the gyrokinetic equation about $\phi_{eq} = B_{\parallel eq} = 0, A_{\parallel eq} = ax$, with constant a, and be valid when the condition

$$\frac{\omega}{k_y} \ll v_{th_s} \tag{2.102}$$

is satisfied. For the tearing instability analysis, we indeed selected perturbations independent on z which effectively leads us to consider a 2D reduction of the models.

For obtaining the model considered in this Thesis it is enough to retain only the first two moments of the hierarchy for the two species, and apply the closure starting from the gyrocenter temperature fluctuations. Thus, (2.100) constrains all the moments, excluding $(m, n) \neq (0, 0)$ and $(m, n) \neq (1, 0)$, namely to exclude $N_{e,i}$ and $U_{e,i}$, and sets the moments with $m \neq 0$ to zero. For, instance, taking the couple $(m, n) = (2, 0)$ correspond to considering the gyrocenter parallel temperature fluctuation. Therefore, injecting (2.100) into (2.42), taking $(m, n) = (2, 0)$, implies that $T_{\|_{e,i}} = 0$.
The expansion of the gyrocenter perturbed distribution functions for the two species is thus given by

$$\widetilde{f}_s = \mathcal{F}_{eq_s}\left(\frac{N_s}{n_0} + \frac{v_\|}{v_{th_{\|s}}}\frac{U_s}{v_{th_{\|s}}} - \sum_{n=1}^{+\infty} L_n\left(\frac{\mu_s B_0}{T_{0_{\perp s}}}\right)\left(G_{1ns}\frac{q_s}{T_{0_{\|s}}}\phi + 2\Theta_s G_{2ns}\frac{B_\|}{B_0}\right)\right), \tag{2.103}$$

Applying the same procedure as described in the previous Section one can derive the following 4-field Hamiltonian gyrofluid model derived by Tassi et al. (2020), taken in the 2D limit (assuming that all the independent variables do not vary along the direction of the guide field),

$$\frac{1}{n_0}\frac{\partial N_s}{\partial t} + \frac{c}{B_0}\left[G_{10_s}\phi + \frac{T_{0_{\perp s}}}{q_s}2G_{20_s}\frac{B_\|}{B_0}, \frac{N_s}{n_0}\right] - \frac{1}{B_0}\left[G_{10_s}A_\|, U_s\right] = 0, \tag{2.104}$$

$$\begin{aligned}&\frac{\partial}{\partial t}\left(\frac{U_s}{v_{th_{\|s}}} + \frac{q_s v_{th_{\|s}}}{T_{0_{\|s}}c}G_{10_s}A_\|\right) + \frac{c}{B_0}\left[G_{10_s}\phi + \frac{T_{0_{\perp s}}}{q_s}2G_{20_s}B_\|, \frac{U_s}{v_{th_{\|s}}} + \frac{q_s v_{th_{\|s}}}{T_{0_{\|s}}c}G_{10_s}A_\|\right]\\ &- \frac{v_{th_{\|s}}}{B_0}\left[G_{10_s}A_\|, \frac{N_s}{n_0}\right] = 0,\end{aligned} \tag{2.105}$$

where G_{10_s} and G_{20_s} are the dimensional operators defined by Eqs. (2.48) - (2.50). The dimensional static relations are given by

$$\sum_s q_s \left(G_{10_s} \frac{N_s}{n_0} + \frac{q_s}{T_{0_{\perp s}}} (1 - \Theta_s) \Gamma_{0s} \phi + \frac{q_s}{T_{0_{\perp s}}} (\Theta_s G_{10_s} G^2_{10_s} - 1) \phi \right.$$
$$\left. + (1 - \Theta_s)(\Gamma_{0s} - \Gamma_{1s}) \frac{B_\parallel}{B_0} + \Theta_s 2 G_{10_s} G_{20_s} \frac{B_\parallel}{B_0} \right) = 0, \tag{2.106}$$

$$- \nabla^2_\perp A_\parallel = \frac{4\pi n_0}{c} \sum_s q_s \left(G_{10_s} U_s + \frac{q_s}{m_s} \left(1 - \frac{1}{\Theta_s} \right) (\Gamma_{0s} - 1) \frac{A_\parallel}{c} \right), \tag{2.107}$$

$$\frac{B_\parallel}{B_0} = -\frac{1}{2} \sum_s \beta_{\perp_s} \left(2 G_{20_s} \frac{N_s}{n_0} + \frac{q_s}{T_{0_{\perp s}}} (1 - \Theta_s)(\Gamma_{0s} - \Gamma_{1s}) \phi + 2 (1 - \Theta_s)(\Gamma_{0s} - \Gamma_{1s}) \frac{B_\parallel}{B_0} \right.$$
$$\left. + \Theta_s \frac{q_s}{T_{0_{\perp s}}} 2 G_{10_s} G_{20_s} \phi + \Theta_s 4 G^2_{20_s} \frac{B_\parallel}{B_0} \right). \tag{2.108}$$

2.4.2 Normalisation by L, and assumptions

We consider here an Alfvénic normalization, different from that used for the previous model, and given by

$$\begin{aligned} \hat{t} &= \frac{v_A}{L} t, & \hat{x} &= \frac{x}{L}, & \hat{y} &= \frac{y}{L}, \\ \hat{N}_s &= \frac{L}{d_i} \frac{N_s}{n_0}, & \hat{U}_s &= \frac{L}{d_i} \frac{U_s}{v_A}, & & \\ \hat{A}_\parallel &= \frac{A_\parallel}{L B_0}, & \hat{B}_\parallel &= \frac{L}{d_i} \frac{B_\parallel}{B_0}, & \hat{\phi} &= \frac{c}{v_A} \frac{\phi}{L B_0}. \end{aligned} \tag{2.109}$$

We also normalize the following lengths

$$\hat{d}_i = \frac{d_i}{L}, \qquad \hat{\rho}_s = \frac{\rho_s}{L}, \qquad \hat{d}_e = \frac{d_e}{L}. \tag{2.110}$$

The hat indicates dimensionless quantities, and $v_A = B_0 / \sqrt{4\pi m_i n_0}$ is the Alfvén speed. The length L is our characteristic reconnecting magnetic field length scale, appearing in the dimensional equilibrium. All times are normalized by the Alfvén time $\tau_A = L / v_A$. *For ease of notation, we now drop the hat over the dimensionless variables.*

This normalization has been used several times in the past for fluid and gyrofluid models (Grasso et al. (2001); Del Sarto et al. (2003); Grasso et al. (2006); Comisso et al. (2013)) and turns out to be more natural and convenient in order to make contact with previous work based on equilibrium current sheets with a characteristic length greater than the Larmor radius scales. This was not the case of the previous model, for which the tearing analysis focused on current sheets with size of the order of $\rho_{s\perp}$. A second advantage is that the parameters associated with different kinetic scales, d_e and ρ_s, are treated as small parameters (this was also not the case with the other normalization), which can make the approach more intuitive.

The complete normalized 4-field gyrofluid model is given by

$$\frac{\partial N_i}{\partial t} + [G_{10_i}\phi + \tau_{\perp_i}\rho_{s_\perp}^2 2G_{20_i}B_\|, N_i] - [G_{10_i}A_\|, U_i] = 0, \tag{2.111}$$

$$\frac{\partial}{\partial t}(d_i^2 U_i + G_{10_i}A_\|) + [G_{10_i}\phi + \tau_{\perp_i}\rho_{s_\perp}^2 2G_{20_i}B_\|, d_i^2 U_i + G_{10_i}A_\|] - \frac{\tau_{\perp_i}\rho_{s_\perp}^2}{\Theta_i}[G_{10_i}A_\|, N_i] = 0, \tag{2.112}$$

$$\frac{\partial N_e}{\partial t} + [G_{10_e}\phi - \rho_{s_\perp}^2 2G_{20_e}B_\|, N_e] - [G_{10_e}A_\|, U_e] = 0, \tag{2.113}$$

$$\frac{\partial}{\partial t}(G_{10_e}A_\| - d_e^2 U_e) + [G_{10_e}\phi - \rho_{s_\perp}^2 2G_{20_e}B_\|, G_{10_e}A_\| - d_e^2 U_e] + \frac{\rho_{s_\perp}^2}{\Theta_e}[G_{10_e}A_\|, N_e] = 0, \tag{2.114}$$

complemented by the static relations

$$\begin{aligned}
&G_{10_i}N_i - G_{10_e}N_e + (1-\Theta_i)\Gamma_{0i}\frac{\phi}{\tau_{\perp_i}\rho_{s_\perp}^2} + (1-\Theta_e)\Gamma_{0e}\frac{\phi}{\rho_{s_\perp}^2} + (\Theta_i G_{10_i}^2 - 1)\frac{\phi}{\tau_{\perp_i}\rho_{s_\perp}^2} \\
&+ (\Theta_e G_{10_e}^2 - 1)\frac{\phi}{\rho_{s_\perp}^2} + (\Theta_i G_{10_i} 2G_{20_i} - \Theta_e G_{10_e} 2G_{20_e})B_\| \\
&+ ((1-\Theta_i)(\Gamma_{0i} - \Gamma_{1i}) - (1-\Theta_e)(\Gamma_{0e} - \Gamma_{1e}))B_\| = 0,
\end{aligned} \tag{2.115}$$

$$\begin{aligned}
&\nabla_\perp^2 A_\| = \left(\left(1 - \frac{1}{\Theta_e}\right)(1-\Gamma_{0e})\frac{1}{d_e^2} + \left(1 - \frac{1}{\Theta_i}\right)(1-\Gamma_{0i})\frac{1}{d_i^2}\right)A_\| \\
&+ G_{10_e}U_e - G_{10_i}U_i,
\end{aligned} \tag{2.116}$$

$$\begin{aligned}
&B_\| = -\frac{\beta_{\perp_e}}{2}\Bigg(\tau_{\perp_i} 2G_{20_i}N_i + 2G_{20_e}N_e + (1-\Theta_i)(\Gamma_{0i} - \Gamma_{1i})\frac{\phi}{\rho_{s_\perp}^2} \\
&- (1-\Theta_e)(\Gamma_{0e} - \Gamma_{1e})\frac{\phi}{\rho_{s_\perp}^2} + \Theta_i G_{10_i} 2G_{20_i}\frac{\phi}{\rho_{s_\perp}^2} - \Theta_e G_{10_e} 2G_{20_e}\frac{\phi}{\rho_{s_\perp}^2} + \Theta_i \tau_{\perp_i} 4G_{20_i}^2 B_\| \\
&+\Theta_e 4G_{20_e}^2 B_\| + \tau_{\perp_i} 2(1-\Theta_i)(\Gamma_{0i} - \Gamma_{1i})B_\| + 2(1-\Theta_e)(\Gamma_{0e} - \Gamma_{1e})B_\|\Bigg)
\end{aligned} \tag{2.117}$$

In the gyroaverage operators, the normalized b_s parameter corresponds now to $\rho_e^2 k_\perp^2$ for the electron and $\rho_i^2 k_\perp^2$ for the ions. The gyroaverage operators are associated with corresponding Fourier multipliers in the following way

$$G_{10_e} f_{\mathbf{k}} e^{i\mathbf{k}\cdot\mathbf{x}} = 2G_{20_e} f_{\mathbf{k}} e^{i\mathbf{k}\cdot\mathbf{x}} = \mathrm{e}^{-k_\perp^2 \frac{\beta_{\perp e}}{4} d_e^2} f_{\mathbf{k}} e^{i\mathbf{k}\cdot\mathbf{x}}, \tag{2.118}$$

$$G_{10_i} f_{\mathbf{k}} e^{i\mathbf{k}\cdot\mathbf{x}} = 2G_{20_i} f_{\mathbf{k}} e^{i\mathbf{k}\cdot\mathbf{x}} = \mathrm{e}^{-k_\perp^2 \frac{\tau_{\perp i}}{2} \rho_{s_\perp}^2} f_{\mathbf{k}} e^{i\mathbf{k}\cdot\mathbf{x}}. \tag{2.119}$$

and

$$\Gamma_{0e} f_{\mathbf{k}} e^{i\mathbf{k}\cdot\mathbf{x}} = I_0 \left(k_\perp^2 \frac{\beta_{\perp_e}}{2} d_e^2 \right) e^{-k_\perp^2 \frac{\beta_{\perp_e}}{2} d_e^2} f_{\mathbf{k}} e^{i\mathbf{k}\cdot\mathbf{x}}, \tag{2.120}$$

$$\Gamma_{1e} f_{\mathbf{k}} e^{i\mathbf{k}\cdot\mathbf{x}} = I_1 \left(k_\perp^2 \frac{\beta_{\perp_e}}{2} d_e^2 \right) e^{-k_\perp^2 \frac{\beta_{\perp_e}}{2} d_e^2} f_{\mathbf{k}} e^{i\mathbf{k}\cdot\mathbf{x}}, \tag{2.121}$$

$$\Gamma_{0i} f_{\mathbf{k}} e^{i\mathbf{k}\cdot\mathbf{x}} = I_0 \left(k_\perp^2 \tau_{\perp_i} \rho_{s_\perp}^2 \right) e^{-k_\perp^2 \tau_{\perp_i} \rho_{s_\perp}^2} f_{\mathbf{k}} e^{i\mathbf{k}\cdot\mathbf{x}}, \tag{2.122}$$

$$\Gamma_{1i} f_{\mathbf{k}} e^{i\mathbf{k}\cdot\mathbf{x}} = I_1 \left(k_\perp^2 \tau_{\perp_i} \rho_{s_\perp}^2 \right) e^{-k_\perp^2 \tau_{\perp_i} \rho_{s_\perp}^2} f_{\mathbf{k}} e^{i\mathbf{k}\cdot\mathbf{x}}. \tag{2.123}$$

Also for this model, we intend to obtain a reduced version of the four-field model in order to retain some specific effects.
Again, we carry out most of the analysis in the isotropic cold-ion limit, a simplifying assumption which is also helpful for the comparison with previous works

$$\tau_{\perp_i} \rightarrow 0. \tag{2.124}$$

Nevertheless, in **Chapter** 4, some comments will be provided also with regard to the opposite limit of hot ions. Similar to the previous case, the limit (2.124) allows to develop the ion gyroaverage operators with a Taylor expansion.

The gyrocenter ion density fluctuations N_i and ion gyrocenter parallel velocity fluctuations U_i are neglected, and the equilibrium temperature of both species are isotropic. The latter conditions amount to impose

$$N_i = U_i = 0, \qquad \Theta_i = \Theta_e = 1. \tag{2.125}$$

It is important to point out that, in principle, in the case where d_e and ρ_s remain finite, $U_i = N_i = 0$ is solution of the 4-field parent model only if $\beta_e \ll 1$. Therefore, for a finite β_e, the parallel ion dynamics should be taken into account. In **Chapter** 5 one of the aims is indeed to discuss the admissibility of the suppression of the parallel ion dynamics by comparing with gyrokinetic simulations, that are considering the ion dynamic. The gyrokinetic simulations, that are compared to the gyrofluid model were performed in the same range of parameter and used the same initial conditions. We anticipate that it turns out that, for β_e values approaching 1 from below, the ion dynamics do not play an important role, and the growth rates of the tearing mode obtained from the two approaches remain in agreement. The formation of plasmoids is also not significantly impacted by the absence or presence of the ions.

Since we consider here the isotropic case, it is in fact possible to follow the derivation procedure, starting the reduction from gyrokinetic equations that consider a Maxwellian equilibrium distribution function (instead of a bi-Maxwellian). In this case, isotropy would be assumed from the start. The reason why anisotropy was retained until here, is because originally the model was derived in an attempt to describe instabilities due to temperature anisotropy and finite β_e, such as the *firehose instability.*

We can write the assumption $N_i = 0$ in terms of the normalized particle density fluctuation n_i as

$$n_i = N_i + \nabla_\perp^2 \phi + B_\|, \tag{2.126}$$

valid in the limit $\tau_{\perp_i} \longrightarrow 0$ and $\Theta_i = 1$ (Brizard, 1992).

Neglecting N_i in Eq. (2.126) thus amounts to assuming that the ion density response is due only to the ion polarization (second term on the right-hand side of Eq. (2.126)) and to the parallel magnetic perturbation $B_\|$. In the low-β limit, the influence of $B_\|$ becomes negligible and (2.126) corresponds to a solution for the ion response derived by the kinetic theory of Schep et al. (1994).

With regard to the assumption that neglects the evolution of the ion gyrocenter parallel velocity, $U_i = 0$, the relation with the normalized parallel ion velocity u_i is simply given by $U_i = u_i = 0$ and ions are assumed to be immobile along the guide field direction which is reasonable by virtue of the larger ion inertia.[6]

Given that $\beta_e = \rho_s^2/d_i^2$, from Eq. (2.112) in the $\tau_{\perp_i} - > 0$ limit, it is therefore apparent that the simplifying hypothesis $U_i = u_i = 0$ is reasonable for studying the impact of β_e values smaller than one, which is realistic in the case of a number of astrophysical and laboratory plasmas.

By applying the conditions (2.124)-(2.125) in the static relations (2.106)-(2.108) we obtain the final static relations

$$\left(\frac{G_{10_e}^2 - 1}{\rho_s^2} + \nabla_\perp^2 \right) \phi - \left(G_{10_e} 2 G_{20_e} - 1 \right) B_\| = G_{10_e} N_e, \tag{2.127}$$

$$\nabla_\perp^2 A_\| = G_{10_e} U_e, \tag{2.128}$$

$$\left(G_{10_e} 2 G_{20_e} - 1 \right) \frac{\phi}{\rho_s^2} - \left(\frac{2}{\beta_e} + 4 G_{20_e}^2 \right) B_\| = 2 G_{20_e} N_e. \tag{2.129}$$

The two evolution equations read

$$\frac{\partial N_e}{\partial t} + [G_{10_e}\phi - \rho_s^2 2 G_{20_e} B_\|, N_e] - [G_{10_e} A_\|, U_e] = 0, \tag{2.130}$$

$$\begin{aligned} &\frac{\partial}{\partial t}(G_{10_e} A_\| - d_e^2 U_e) + [G_{10_e}\phi - \rho_s^2 2 G_{20_e} B_\|, G_{10_e} A_\| - d_e^2 U_e] \\ &+ \rho_s^2 [G_{10_e} A_\|, N_e] = 0, \end{aligned} \tag{2.131}$$

---

[6] Such assumptions can also be justified by the fact that the evolution of ion gyrocenter density and parallel velocity, at least when their initial conditions are $N_i = U_i = 0$, have been shown to have a negligible role in simulations of reconnection (Comisso et al. (2012)).

Eqs. (2.130), (2.131) and (2.127)-(2.129) correspond to the gyrofluid model adopted for the analysis of magnetic reconnection in **Chapter** 4 and for the study of plasmoid instability in **Chapter** 5.

To sum up the main characteristics of this model:

- **Electron inertia and electron gyrations** break the frozen-in condition
- **Cold ions** (negligible ion FLR effects) are assumed
- **Immobile ions** are assumed along the guide field direction, **but ion density fluctuations are allowed**
- **Finite, but small,** β_e and **electron FLR effects** are retained
- **Subdominant (since** β_e **is small) fluctuations of the parallel magnetic field** are included

For the sake of the subsequent analysis, it can be useful also to express the relations between gyrofluid models and particle variables. Such relation, in particular, is affected by the quasi-static assumption, used in the derivation of the model (Tassi et al., 2020) to obtain a closure on the infinite hierarchy of moment equations obtained from a parent gyrokinetic system. As a consequence of such quasi-static closure the normalized density fluctuations and parallel velocity fluctuations of the electrons, indicated with n_e and u_e, respectively, are related to those of the corresponding gyrocenters by

$$N_e = G_{10_e}^{-1}\left(n_e + \left(G_{10_e}^2 - 1\right)\frac{\phi}{\rho_s^2} - G_{10_e}^2 B_\parallel\right), \tag{2.132}$$

$$U_e = G_{10_e}^{-1} u_e. \tag{2.133}$$

From the quasi-neutrality relation (2.127), Ampère's law (2.128)-(2.129), combined with Eqs. (2.132)-(2.133), we can obtain the relations

$$n_e = \frac{2}{2+\beta_e}\nabla_\perp^2\phi = -\frac{2}{\beta_e}B_\parallel, \tag{2.134}$$

$$u_e = \nabla_\perp^2 A_\parallel, \tag{2.135}$$

that permit to express the electron particle (as opposed to gyrocenter) density and parallel velocity fluctuations, in terms of electromagnetic perturbations such as ϕ, $B_\parallel$ and $A_\parallel$.

It is also particularly relevant to consider the limit $\beta_e \longrightarrow 0$ with d_e and ρ_s remaining finite (which implies $m_e/m_i \longrightarrow 0$). This limit to suppresses the effects of parallel magnetic perturbations and electron FLR effects. One of the purposes of our investigation is indeed to consider possible modifications, due to kinetic effects, of the plasmoid instability scenario described by Granier et al., to appear in Phys. Rev. E (2022), and which was conceived namely in the regime with $\beta_e \longrightarrow 0$ and finite d_e and ρ_s. Using this development in Eqs. (2.129) - (2.130) and neglecting the first-order corrections, we obtain the evolution equations (Schep et al. (1994))

$$\boxed{\begin{aligned} &\frac{\partial n_e}{\partial t} + [\phi, n_e] - [A_{\|}, u_e] = 0, && (2.136)\\ &\frac{\partial}{\partial t}\left(A_{\|} - d_e^2 u_e\right) + \left[\phi, A_{\|} - d_e^2 u_e\right] - \rho_s^2 [n_e, A_{\|}] = 0, && (2.137)\end{aligned}}$$

where the static relations (2.127) - (2.129) are replaced by

$$\nabla_\perp^2 \phi = N_e = n_e, \tag{2.138}$$
$$\nabla_\perp^2 A_{\|} = U_e = u_e, \tag{2.139}$$
$$B_{\|} = 0. \tag{2.140}$$

In this limit, particle density and parallel velocity fluctuations coincide with the corresponding gyrocenter counterparts. The system (2.136)-(2.137), complemented by the static relations (2.138)-(2.139), was originally derived from a more general three-field version by Schep et al. (1994) and applied for the first time to magnetic reconnection by Cafaro et al. (1998). Following this first study, the tearing instability has then been extensively studied (Porcelli (1991); Grasso et al. (2001, 1999)). We note that, if also the parallel compressibility of the electrons is neglected, which means $\rho_s \longrightarrow 0$ we obtain the 2D reduced ideal MHD equations.

In this Thesis we make use of and mention this model several times. Because of the absence of FLR effects, we will often refer to the model as the *fluid* limit of the general gyrofluid model (2.129) - (2.130).

2.4.3 Conserved energy

We define the dynamical variable

$$A_e = G_{10_e} A_{\|} - d_e^2 U_e. \tag{2.141}$$

The three relations (2.127)-(2.129), together with the definition of A_e in Eq. (A.7), make it possible to express $B_{\|}$, ϕ and U_e, in terms of the two dynamical variables N_e and A_e, according to

$$B_{\|} = \mathcal{L}_{B0} N_e, \qquad \phi = \mathcal{L}_{\phi 0} N_e, \qquad U_e = \mathcal{L}_{U_e 0} A_e. \tag{2.142}$$

The corresponding Hamiltonian, representing the conserved total energy of the system, consists of the functional

$$H(N_e, A_e) = \frac{1}{2}\int d^2x \, \left(\rho_s^2 N_e^2 - A_e \mathcal{L}_{U_e 0} A_e - N_e (G_{10_e} \mathcal{L}_{\phi 0} N_e - \rho_s^2 2 G_{20_e} \mathcal{L}_{B0} N_e)\right). \tag{2.143}$$

The complete Hamiltonian structure of this model is presented in Appendix A.

2.5 Remarks regarding the two closure choices

The isothermal closure derives from the assumptions $t_{\|_e} = 0$ and $t_{\perp_e} = 0$, and implies that gyrocenter temperature perturbations are coupled to the system by the Eqs. (2.72) and (2.73). For this closure, the hypothesis $\delta^2 \ll \beta_{\perp_e} \ll 1$ allowed us to neglect electron FLR effects and to greatly simplify Eq. (2.72) into $T_{\perp e} = -B_{\|}$. However, if we consider perpendicular electron temperature fluctuations in the system, we note that in the limit $\delta^2 \ll \beta_{\perp_e} \ll 1$, the evolution equation of $t_{\perp_e}$ is given by

$$\frac{\partial t_{\perp_e}}{\partial t} + [\phi, t_{\perp_e}] = O(\beta_{\perp_e}). \tag{2.144}$$

Therefore one can see that if we neglect the $\beta_{\perp_e}$ order corrections, as it is considered in Chapter 3 for studying the tearing instability, $t_{\perp_e}$ decouples from system.

For the quasi-static closure, in the case $\Theta_e = 1$ which is adopted in Chapters 4 and 5, the isothermal closure obtained for the electron temperatures emerges as a consequence of the quasi-static hypothesis $\omega/k_y \ll v_{th_e}$. This hypothesis of slowly varying fields also implies that $T_{\|_e} = 0$ and

$$T_{\perp_e} = -G_{11e}\frac{e}{T_{0e}}\phi + 2G_{21e}\frac{B_{\|}}{B_0}. \tag{2.145}$$

In the context of the tearing instability, we verified that the dispersion relations of the tearing mode that are derived in this Thesis satisfy the condition $\omega/k_y \ll v_{th_e}$. This relation indicates that electrons have time to thermalize along the field lines while the tearing mode develops. Similar comments have already been made in the context of the MHD model with pressure anisotropies. Shi et al. (1987) discussed the following two equations of state: double adiabatic and isothermal. According to Kulsrud (1983), a double adiabatic closure requires $L/t \gg v_{th_e}$, with t the characteristic scale of time variation and L the scale of the spatial variation. Shi et al. (1987) indicated that $L/t \gg v_{th_e}$ cannot be satisfied by most tearing modes with t and L taken to be the growth time and the wavelength of the mode, respectively. On the other hand, the isothermal closure for the electrons, valid in the opposite regime ($L/t \ll v_{th_e}$) can be a better approximation for the study of the tearing instability.

2.6 Numerical implementation of the gyrofluid model

2.6.1 Numerical scheme

In this Thesis, simulations have been carried out with the fluid code used in Refs. Tassi et al. (2018); Grasso et al. (2020), recently named `SCOP3D` (Solver for COllisionless Plasma Equations in 3D geometry). The code has been adapted to solve the set of Eqs. (2.130) and (2.131) coupled to the static relations (2.127) - (2.129). The equations are solved using a pseudo-spectral approach, with Fast Fourier Transform (FFT) algorithm used to compute nonlinear term. The computation is parallelized using message passing interface (MPI), where the computational domain is distributed among cores along y and z axes. The advancement in time is achieved through a third-order explicit Adams-Bashforth scheme, started with two Euler steps. Periodic boundary conditions are imposed along the x and the y-directions. The scheme uses numerical filters acting on typical length scales much smaller than the physical scales of the system (Lele (1992)).

The gyroaverage operators are introduced as they are defined in the Fourier space by Eqs. (2.118) and (2.119). Equations (2.127) and (2.129) permit us to express the field ϕ and $B_\|$ in terms of the advanced quantity N_e. They can be written, in Fourier space, as

$$\mathbf{a}_\mathbf{k}\phi_\mathbf{k} + \mathbf{b}_\mathbf{k} B_{\|\mathbf{k}} = N_{e\mathbf{k}}, \tag{2.146}$$

$$\frac{\mathbf{b}_\mathbf{k}}{\rho_s^2}\phi_\mathbf{k} + \mathbf{c}_\mathbf{k} B_{\|_\mathbf{k}} = N_{e\mathbf{k}}, \tag{2.147}$$

where

$$\mathbf{a}_\mathbf{k} = G_{10_e}^{-1}\left(\frac{G_{10_e}^{-1} - 1}{\rho_s^2} + k_\perp^2\right), \tag{2.148}$$

$$\mathbf{b}_\mathbf{k} = -G_{10_e}^{-1}(G_{10_e}^{-1} - 1), \tag{2.149}$$

$$\mathbf{c}_\mathbf{k} = -G_{10_e}^{-1}\left(\frac{2}{\beta_e} + G_{10_e}^2\right), \tag{2.150}$$

and where we used the relation $G_{10_e} = 2G_{20_e}$. At each time step, for each $\mathbf{k}$ and for a given $N_{e\mathbf{k}}$, the solution of (2.146) and (2.147) is given by

$$\phi_{\mathbf{k}} = \frac{\rho_s^2(\mathbf{c_k} - \mathbf{b_k})}{\rho_s^2\mathbf{a_k}\mathbf{c_k} + \mathbf{b_k}^2} N_{e\mathbf{k}}, \tag{2.151}$$

$$B_{\|\mathbf{k}} = \frac{\rho_s^2\mathbf{a_k} - \mathbf{b_k}}{\rho_s^2\mathbf{a_k}\mathbf{c_k} + \mathbf{b_k}^2} N_{e\mathbf{k}}. \tag{2.152}$$

Using Eq. (2.128), we can express $A_\|$ from $A_e = G_{10_e}A_\| - d_e^2U_e$, which is advanced in time by the Ohm's law (2.131). In Fourier space, we obtain

$$A_{\|\mathbf{k}} = (G_{10_e} - d_e^2 G_{10_e}^{-1} k_\perp^2)^{-1} A_{e\mathbf{k}}. \tag{2.153}$$

The parallel electron current is then obtained by solving

$$U_{e\mathbf{k}} = \frac{G_{10_e}A_{\|\mathbf{k}}}{d_e^2}. \tag{2.154}$$

Although the code is fully 3D, we have restricted the studies in this Thesis to the 2D case i.e., the fields are assumed to be independent on z.

The numerical simulations were performed using the EUROfusion high performance computer Marconi Fusion (project FUA35-FKMR) as well Marconi100 (grant n. HP10CY8TU5) hosted at CINECA, and the computing facilities provided by Mesocentre SIGAMME hosted by Observatoire de la Côte d'Azur.

2.6.2 Set up for the tearing instability

A part of this Thesis deals with the tearing instability which, as anticipated in Sec. 1.2.1, is a process through which reconnection can manifest itself. We find it useful, at this stage, to present the equilibrium states that will be used later to investigate tearing instability by means of the models introduced in Secs. 2.3 and 2.4.

The 2D tearing instability involves an equilibrium with oppositely directed field lines. Numerically, we consider the domain $\mathcal{D} = \{-L_x \leq x \leq L_x\,,\ -L_y \leq y \leq L_y\}$, with L_x and L_y being positive constants[7]. This equilibrium magnetic field reverses at $x = 0$.

---

[7] Although, in the linear theory, we will actually assume an infinite domain along x, corresponding to $-\infty < x < +\infty$.

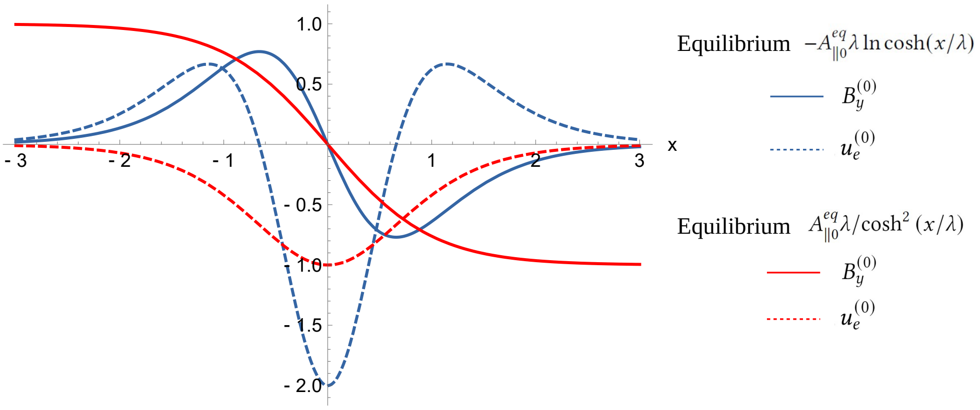

Figure 2.2: Profile along x of the sheared equilibrium magnetic field and current sheet for $A^{eq}_{\|0} = \lambda = 1$.

In this Thesis, two types of equilibrium for the magnetic flux are considered and are the following:

$$A_{\|}^{(0)}(x) = -A^{eq}_{\|0}\lambda \ln\cosh\left(\frac{x}{\lambda}\right), \tag{2.155}$$

$$A_{\|}^{(0)}(x) = \frac{A^{eq}_{\|0}\lambda}{\cosh^2\left(\frac{x}{\lambda}\right)}, \tag{2.156}$$

where $A^{eq}_{\|0}$ is a constant amplitude, changing between 1 and 1.299[a], and λ is a constant stretching factor of the magnetic-field. The two equilibrium magnetic field and current-sheet profiles associated to this equilibria are shown on Fig. 2.2. The equilibrium (2.155) is commonly called the *Harris sheet* (Harris (1962)), while (2.156) was adopted for the first time in Porcelli et al. (2002).

---

[a] $A^{eq}_{\|0} = 1.299$, is chosen in order to have $\max_x(B_y^{(0)}(x)) = 1$

No equilibrium flow is assumed, $\phi^{(0)}(x) = 0$. The two magnetic equilibria considered are not periodic, therefore, if only derivatives are applied to the equilibria, they will be treated outside the spectral part of the code. For the gyrofluid simulations where the operators (2.118) are adopted, we use the second equilibrium (2.156), that admits the following truncated approximated version in terms of a Fourier truncated series

$$A_{\|}^{(0)}(x) = A^{eq}_{\|0}\sum_{n=-30}^{30} a_n e^{inx}, \tag{2.157}$$

where a_n are the Fourier coefficients of the function $f(x) = \lambda/\cosh^2(x/\lambda)$ (Grasso et al. (2006)). The approximation (2.157) allows to satisfy the periodic boundary conditions.

3 Impact of electron temperature anisotropy

In this Chapter, we derive and analyze a dispersion relation for the growth rate of a marginally stable collisionless tearing mode, driven by electron inertia and accounting for equilibrium electron temperature anisotropy in a strong guide field regime.

In the absence of a guide field, the impact of temperature anisotropy on the tearing mode has been thoroughly investigated (Laval & Pellat (1968); Forslund (1968); Chen & Palmadesso (1984); Shi et al. (1987); Califano et al. (2001); Browning et al. (2001); Karimabadi et al. (2004); Quest et al. (2010)). In Forslund (1968), a dispersion relation was derived for a weak electron temperature anisotropy. It was found that the tearing mode is stabilized for $(1-T_{\perp_e}/T_{\|_e}) > \rho_e/(\delta_{\mathrm{cs}}/2)$. The principal results of the numerous studies seem to indicate that, in the absence of a guide field, an anisotropy such as $T_\perp > T_\|$ increases the growth rate. The guide field regime was actually touched in Shi et al. (1987), where it was suggested that the presence of a guide field reduces the enhancement of the growth rate due to temperature anisotropy. These results are visible on the right panel of Fig. 3.1 (taken from Shi et al. (1987)), showing the plot of the tearing growth rate for different $P_\perp/P_\|$ ratios, as a function of the guide field amplitude (in their study the guide-field is along y and the reconnecting magnetic field is along x). They considered a finite resistivity, but they claimed that their result is expected to be valid also for collisionless plasmas.

The strong guide-field regime has therefore seen very little investigation, perhaps in the belief that it would completely cancel the effects of anisotropy. But in reality, it can be interesting to explore this regime for many cases of astrophysical plasmas. The regions of particular interest are the magnetosheath and magnetopause, which are known to contain many small-scale current sheets in which reconnection occurs typically in the presence of a guide field (Phan et al. (2013); Burch & Phan (2016a); Øieroset et al. (2017); Phan et al. (2018); Eastwood et al. (2018)). In Phan et al. (2018), the Authors focus on observations of several electron-scale current sheets measured with MMS. Most of them had strong guide field. In this study, the authors emphasize the absence of ion diffusion regions and ion jets, which is consistent with our model assuming cold ions. Moreover, the discovery of electron-only reconnection reveals

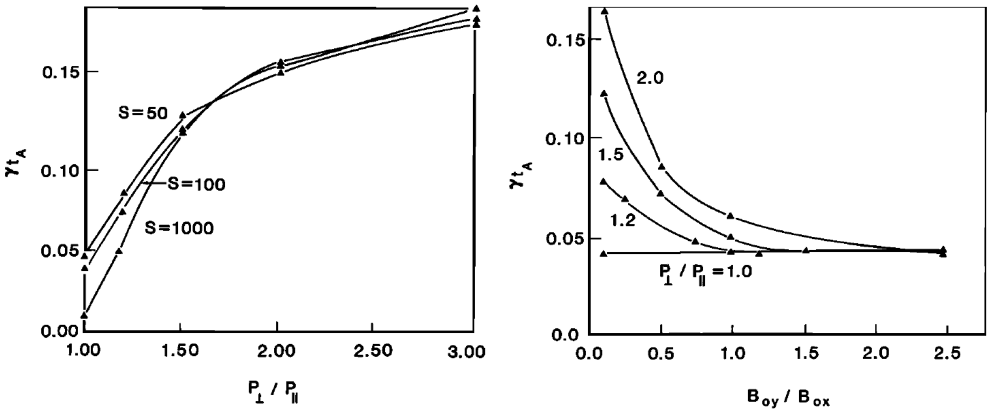

Figure 3.1: *Left:* growth rate of the tearing instability as a function of pressure anisotropy (directly related to temperature anisotropy) for $B_{0y}/B_{0x} = 0.1$ (here the guide field is along y and the reconnecting magnetic field is along x). *Right:* growth rate as a function B_{0y}/B_{0x}, for $S = 100$ and different values of the pressure anisotropy. One can see that, as the relative intensity of the guide field increases, the enhancement of the growth rate, due to the pressure anisotropy, decreases. *Credit: taken from Shi et al. (1987).*

that reconnection operates differently in current sheets with small dimensions. In most of these observational papers, temperature anisotropy is reported before, during, and after the reconnection onset, with, in particular, a sudden increase in the parallel electron temperature during reconnection. Figure 3.2 reports, for instance, the analyses of Burch et al. (2016). We see clearly that the electron distribution function has a bi-Maxwellian shape with an elongation in the $v_{||}$ direction.

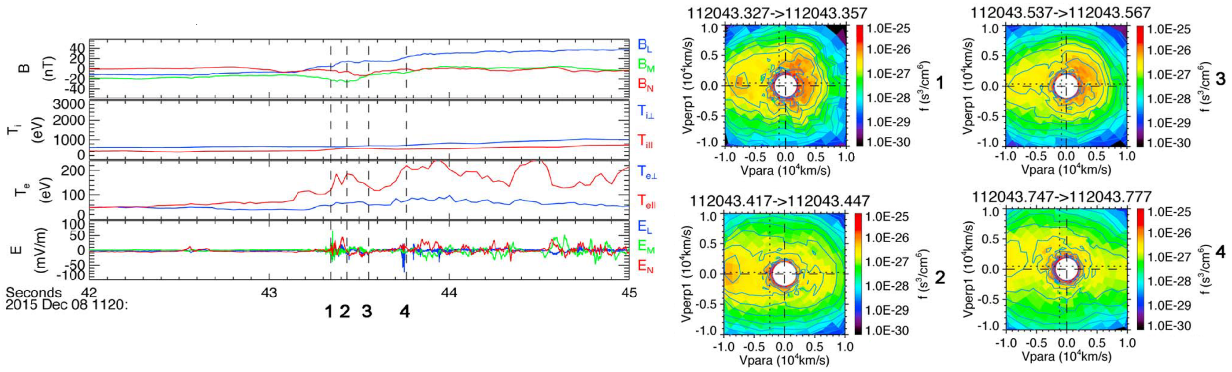

Figure 3.2: MMS is going from the magnetosheath to the magnetosphere and encountering a reconnecting magnetopause. *Left:* evolution of the magnetic field, of the ion and electron temperatures, and of the electric field. *Right:* the electron distribution function, measured at times 1, 2, 3 and 4 shown on the plot. *Credit: Taken from Burch & Phan (2016a)*

The above discussion motivates the investigation of the effect of temperature anisotropy on the growth rate of collisionless tearing modes in the presence of a strong guide field. Although both ion and electron temperature anisotropies are observed, for simplicity we focus on the role of electron anisotropy only, in a regime with $\beta_e \ll 1$.

The adopted tool for modelling inertial reconnection in the presence of electron temperature anisotropy is the strong guide field model provided by Eqs. (2.95) - (2.96). The choice of the perpendicular sonic Larmor radius, $\rho_{s\perp}$, as a characteristic length, implies that our study focuses on a microscopic current sheet, as opposed to the usually considered MHD macroscopic current sheet (Del Sarto & Ottaviani (2017)).

It is important to point out, however, that in most of the astrophysical plasmas the ion temperature is thought to be higher than that of the electrons (Fig. 3.2). This does not correspond to the regime considered in our model, since we took the opposite limit, $\tau_{\perp_i} \ll 1$ [1]. The presence of cold ions is not completely excluded in the magnetosphere, since the ionosphere can be a source of cold ions, but it is nevertheless infrequent. The cold ion limit is more suitable for laboratory plasmas. On the other hand, at the end of this Chapter we will discuss how, relying on an already existing dispersion relation, it is possible to infer the influence of electron temperature anisotropy for an arbitrary ion temperature.

In this Chapter, by applying the theory of asymptotic matching we derive a dispersion relation for the tearing mode, which does not predict an enhancement of the growth rate as the ratio Θ_e, between perpendicular and parallel equilibrium electron temperatures, increases. This indicates a significant difference with respect to the case of absent or moderate guide field (Karimabadi et al. (2004); Daughton & Karimabadi (2005)). Instead, we obtain that, in the strong guide field regime and in the limit $\beta_{\perp_e} \ll 1$ the dimensional growth rate increases with $v_{th_{\parallel e}}$ and therefore as $T_{0_{\parallel e}}^{1/2}$. We provide a detailed discussion of the range of validity of the derived dispersion relation and of the compatibility among the different adopted assumptions. The analytical treatment will also make it possible to compare the resulting dispersion relation for the growth rate, with a previously derived analytical formula, obtained assuming similar simplifying assumptions but not accounting for temperature anisotropy (Porcelli (1991); Fitzpatrick & Porcelli (2007); Fitzpatrick (2010); Tassi et al. (2018)).

The Chapter is organized as follows. Section 3.1 contains the derivation of the analytical dispersion relation for the growth rate. The predictions based on the analytical dispersion relation are checked against numerical simulations in Sec. 3.2. In Sec. 3.3 we first summarize and discuss the conditions of applicability of the analytical dispersion relation, and conclude, indicating also possible future developments. In Appendix B we describe a technical step, required to show that the outer solution for the electrostatic potential, derived in Sec. 3.1.1, satisfies the appropriate boundary condition.

---

[1] $T_{0_{\perp i}} \ll T_{0_{\perp e}}$

In this Chapter, some parts of the text and figures also appear in Granier et al. (2021).

3.1 Analytical investigation of the linear tearing mode stability

Tearing instability can occur in a plasma in the presence of non-ideal effects, by perturbing an equilibrium possessing a resonant surface. In the 2D case treated in this Thesis, resonant surfaces correspond to lines where the equilibrium magnetic field vanishes, in the planes perpendicular to the guide field. The tearing instability causes the formation of magnetic loops, denoted as magnetic islands, at the resonant surface. The size of magnetic islands can increase in time following the growth rate of the instability. The derivation of an analytical formula for the linear growth rate of the tearing instability in the presence of effects such as electron temperature anisotropy is namely one of the purposes of this Section. Our derivation follows the standard procedure adopted for tearing modes since the seminal work by Furth et al. (1963) and described also in monographs such as Priest & Forbes (2000), and which is based on matched asymptotic expansion.

We consider the model (2.95) - (2.96), complemented by the static relations (2.90) - (2.92). We linearize about the Harris sheet equilibrium given by (2.155) (i.e. $A_{\|}^{(0)}(x) = -\lambda \ln\cosh(x/\lambda)$). This equilibrium gives a magnetic field with components $B_x^{(0)} = 0$ and $B_y^{(0)}(x) = \sqrt{\beta_{\perp_e}/2}\tanh(x/\lambda)$. In this analysis, we take the equilibrium amplitude $A_{\|0}^{eq} = 1$, but λ varies. The positive parameter λ can be seen as a stretching factor for the equilibrium shear length given by $L_s = \lambda \rho_{s\perp}$, and is defined as being the characteristic scale at which the dimensional reconnecting magnetic field is varying, so that $d_{\hat{x}}\hat{B}_y^{(0)}(0) = B_0\sqrt{\beta_{\perp_e}/2}/L_s$. Finally, we linearize the equations considering uniform perturbations along the guide field with a sinusoidal variation along y,

$$A_{\|}^{(1)}(x,y,t) = \frac{1}{2}\left(\widetilde{A}_{\|}(x)e^{\gamma t + ik_y y} + \bar{\widetilde{A}}_{\|}(x)e^{\gamma t - ik_y y}\right), \tag{3.1}$$

$$\phi^{(1)}(x,y,t) = \frac{1}{2}\left(\widetilde{\phi}(x)e^{\gamma t + ik_y y} + \bar{\widetilde{\phi}}(x)e^{\gamma t - ik_y y}\right). \tag{3.2}$$

where γ is the growth rate of the instability, $k_y = 2\pi m/L_y$ is the wave number with $m \in \mathbb{N}$, and the overbar refers to the complex conjugate. The perturbations are subject to the boundary conditions $\widetilde{A}_{\|}$, $\widetilde{\phi} \longrightarrow 0$, as $x \longrightarrow \pm\infty$. In addition, we should seek for even solutions of $\widetilde{A}_{\|}(x)$ and odd solutions for $\widetilde{\phi}(x)$. This is a standard parity of the linear tearing mode, which is well respected by this particular model (2.136) - (2.137). As a consequence of such parity, $\widetilde{A}_{\|}$ and $\widetilde{\phi}$ are purely real and imaginary-valued functions, respectively. The perturbation used, in the form $A_{\|}^{(1)} \propto \cos(k_y y)$, introduces a singular point at the center of the current sheet where the field lines will reconnect.

Proceeding to the linearization of Eqs. (2.95) and (2.96) gives

$$g(\widetilde{\phi}'' - k_y^2\widetilde{\phi}) - iB_y^{(0)''}\widetilde{A}_\| + iB_y^{(0)}(\widetilde{A}_\|'' - k_y^2\widetilde{A}_\|) = 0, \tag{3.3}$$

$$g\left(\widetilde{A}_\| - \frac{2\delta^2}{\beta_{\perp_e}}(\widetilde{A}_\|'' - k_y^2\widetilde{A}_\|)\right) + i\widetilde{\phi}\left(B_y^{(0)} - \frac{2\delta^2}{\beta_{\perp_e}}B_y^{(0)''}\right) - \frac{iB_y^{(0)}}{\Theta_e}(\widetilde{\phi}'' - k_y^2\widetilde{\phi}) = 0, \tag{3.4}$$

where the prime notation denotes the derivative with respect to x and where

$$g = \frac{\gamma}{k_y}. \tag{3.5}$$

Due to the choice of normalization, the last term of the equation (3.4), proportional to $1/\Theta_e$, is of order 1. This makes the equations slightly different from that of the fluid model of Schep et al. (1994), in which this bracket is multiplied by the square of the sonic Larmor radius normalized by the scale length of a macroscopic equilibrium, which typically results in a small coefficient (see Eq. (2.137)). In our tearing analysis, the consequence is that the outer solution will be different from that obtained with the fluid model.

We consider the time variation of the perturbation to be slow, which, together with the assumption (2.81), leads to considering the following two small parameters:

$$g \ll 1, \qquad \frac{2\delta^2}{\beta_{\perp_e}} \ll 1. \tag{3.6}$$

The non-ideal term considered here is associated with the non-negligible mass of the electrons, present in the coefficient δ^2. This parameter being small, it will be important only at small spatial scale. In particular, one sees from Eqs. (3.3)-(3.4) that the terms with the small coefficients indicated in Eq. (3.6), are negligible everywhere, except where $B_y^{(0)}$ also vanishes. For the equilibria (2.155)-(2.156) this occurs at $x = 0$, which identifies the resonant surface. As is customary with linear tearing modes, the presence of small parameters allows then to separate the domain in two spatial scales, and the stability analysis leads to a *boundary layer problem*, implying that one has to calculate the solution in two separate regions involving two different scalings (Grasso et al. (2002), Fitzpatrick & Porcelli (2007)). The *outer region* is far from the resonant surface, characterized by a strong current layer, and is where the non-ideal terms are negligible. In this region, the current is weak, so terms proportional to electron inertia (which are identified by the combination $\sim \delta^2 u_e \sim \delta^2\nabla_\perp^2\widetilde{A}_\|$) can be neglected, and the coupling between the plasma and the field lines remains ideal. The *inner region* is where the X-point is located and non-ideal effects are important. In the inner region, the terms proportional to electron inertia, can no longer be ignored and they break the frozen in condition. The inner region is supposed to have a certain width, denoted ϵ, that has to be identified. Splitting the domain into two sub-domains according to the scale separation implies that a spatial rescaling $x = \epsilon \bar{x}$ will be involved.

From this method, two separate solutions will be obtained and they must match in an overlapping region called the *boundary layer*, i.e, the solutions for $\widetilde{\phi}$ have to satisfy the conditions

$$\widetilde{\phi}_{\text{out}} \underset{x\longrightarrow 0}{\sim} \widetilde{\phi}_{match_{\text{out}}}, \quad \text{and} \quad \widetilde{\phi}_{\text{in}} \underset{\text{x}\longrightarrow +\infty}{\sim} \widetilde{\phi}_{\text{match}_{\text{in}}},$$
$$\text{matching condition}: \quad \widetilde{\phi}_{\text{match}_{\text{out}}} = \widetilde{\phi}_{\text{match}_{\text{in}}}, \tag{3.7}$$

where the subscript *in* and *out* indicate the solutions obtained in the inner and outer region respectively. The same conditions have to be satisfied by the magnetic potential $\widetilde{A}_{\|}$.

A further matching condition, imposed between the logarithmic derivatives of the inner and outer solutions for $\widetilde{A}_{\|}$ will determine the dispersion relation that we are looking for, relating the growth rate γ with the equilibrium parameters.

3.1.1 Outer region

In the outer region, we keep terms of order one with respect to terms of order $2\delta^2/\beta_{\perp_e} \ll 1$. Therefore Eqs. (3.3) and (3.4) become

$$g(\widetilde{\phi}''_{\text{out}} - k_y^2 \widetilde{\phi}_{\text{out}}) - iB_y^{(0)''} \widetilde{A}_{\|\text{out}} + iB_y^{(0)} (\widetilde{A}''_{\|\text{out}} - k_y^2 \widetilde{A}_{\|\text{out}}) = 0, \tag{3.8}$$

$$g\widetilde{A}_{\|\text{out}} + iB_y^{(0)} \widetilde{\phi}_{\text{out}} - \frac{iB_y^{(0)}}{\Theta_e} (\widetilde{\phi}''_{\text{out}} - k_y^2 \widetilde{\phi}_{\text{out}}) = 0. \tag{3.9}$$

We then neglect the terms proportional to g in Eq. (3.8). On the other hand, we are looking for odd solutions for $\widetilde{\phi}_{\text{out}}$, which means $\widetilde{\phi}_{\text{out}}(0) = 0$, and have also to meet the boundary conditions $\widetilde{\phi}_{\text{out}} \rightarrow 0$ when $x \rightarrow 0$. To satisfy these conditions, it is necessary not to neglect the term $g\widetilde{A}_{\|\text{out}}$ in the equation (3.9). Using the equilibrium $B_y^{(0)} = \tanh(x/\lambda)$ we get the following equations

$$\widetilde{A}''_{\|\text{out}} - \widetilde{A}_{\|\text{out}} \left(k_y^2 - \frac{2}{\lambda^2 \cosh{(x/\lambda)}^2} \right) = 0, \tag{3.10}$$

$$\widetilde{\phi}''_{\text{out}} - \left(k_y^2 + \Theta_e \right) \widetilde{\phi}_{\text{out}} = -\frac{ig\,\Theta_e}{B_y^{(0)}} \widetilde{A}_{\|\text{out}}. \tag{3.11}$$

We remark that, although Eq. (3.10) corresponds to a standard equation in MHD linear tearing mode theory, yielding the outer solution for the perturbation $\widetilde{A}_{\text{out}}$ in the presence of a Harris sheet equilibrium, this is not the case for Eq. (3.11). In particular, the first two terms in Eq. (3.11) are absent in the outermost region in the tearing mode linear analysis of reduced MHD and of the two-field model of Cafaro et al. (1998). This difference comes from the fact that, in the present case, the magnetic equilibrium has a characteristic scale length corresponding to $\rho_{s\perp}$, in contrast with the current sheet of macroscopic length characteristic of MHD. The new terms in Eq. (3.11) are due to electron parallel compressibility, which becomes relevant on the scale length $\rho_{s\perp}$. They do not affect the outer solution for the magnetic flux function[2], but alter the outer solutions for the flow.

Given the assumed parities of $\widetilde{A}_{\|}$ and $\widetilde{\phi}$, we can solve the system for $x \geq 0$ and then extend the solutions to the whole domain, using $\widetilde{A}_{\|}(x) = \widetilde{A}_{\|}(-x)$ and $\widetilde{\phi}(x) = -\widetilde{\phi}(-x)$.

The solution of Eq. (3.10), satisfying the boundary condition at $x \to +\infty$, is given by (White (1986))

$$\widetilde{A}_{\|\text{out}}(x) = \frac{e^{-k_y x}}{\lambda}\left(\frac{\tanh(x/\lambda)}{k_y} + \lambda\right), \tag{3.12}$$

whereas the solution of (3.11) can be found by the method of the variation of parameters and corresponds to

$$\begin{aligned}\widetilde{\phi}_{\text{out}}(x) =& ie^{\alpha x}\left(C_1 - \frac{g\Theta_e}{2\alpha\lambda}\int_a^x \left(\frac{1}{k_y} + \frac{\lambda}{\tanh(t/\lambda)}\right) e^{-(\alpha+k_y)t} dt\right) \\ &+ ie^{-\alpha x}\left(C_2 + \frac{g\Theta_e}{2\alpha\lambda}\int_a^x \left(\frac{1}{k_y} + \frac{\lambda}{\tanh(t/\lambda)}\right) e^{(\alpha-k_y)t} dt\right),\end{aligned} \tag{3.13}$$

where we introduced the short-hand notation $\alpha^2 = k_y^2 + \Theta_e$. The lower integral bound a is a strictly positive arbitrary value that can be freely chosen. The constant C_1 is chosen to ensure that the boundary condition $\lim_{x\to+\infty} \widetilde{\phi}_{\text{out}} = 0$ is respected and is given by

$$C_1 = \frac{g\Theta_e}{2\alpha\lambda}\int_a^\infty \left(\frac{1}{k_y} + \frac{\lambda}{\tanh(t/\lambda)}\right) e^{-(\alpha+k_y)t} dt. \tag{3.14}$$

Note that the coefficient $\alpha - k_y$, present in the exponential of the second term of $\widetilde{\phi}_{\text{out}}$, is positive. The convergence of this term in the limit $x \to \infty$, which might be not obvious at first sight, is shown in detail in Appendix B. The constant C_2 will be chosen later to insure the matching condition (3.7).

The outer solution (3.12), $\widetilde{A}'_{\|\text{out}}$, has a discontinuous derivative at the point $x = 0$. This discontinuity characterizes the magnetic energy initially stored in the system, that will feed the reconnection process. Indeed, positive-real growth rate of the tearing modes will exist only if enough free magnetic energy exists in the equilibrium, and can be released. The amount of magnetic energy released by each unstable mode will therefore depend on the mode itself and on the choice of equilibrium, which will impact the form of the external solution.

The common way to determine if a mode is unstable or not is to look at the sign of

---

[2] and consequently, they do not affect the expression for the parameter Δ' that we will introduce later

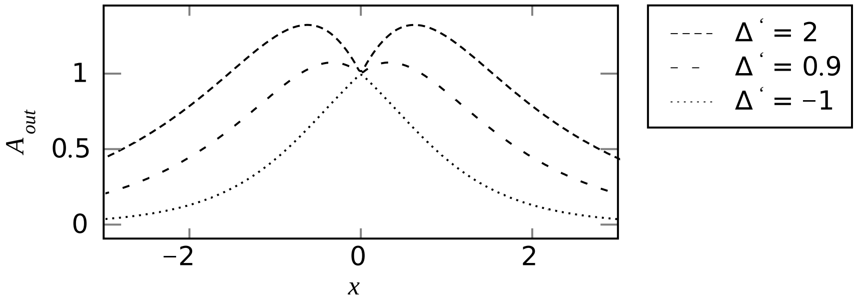

Figure 3.3: Outer MHD-type solution of the system (2.136) - (2.137), for the Harris sheet equilibrium, and different value of Δ'. The configuration is tearing unstable and reconnection occurs if Δ' is positive. The value of λ is 1.

a parameter called the *tearing parameter*, Δ', which measures the discontinuity of the logarithmic derivative of the outer solution, $\widetilde{A}_{\text{out}}$, at the boundary layer location, and which is defined by

$$\Delta'(k_y) = \lim_{x \to 0^+} \frac{\widetilde{A}'_{\text{out}}}{\widetilde{A}_{\text{out}}} - \lim_{x \to 0^-} \frac{\widetilde{A}'_{\text{out}}}{\widetilde{A}_{\text{out}}}. \tag{3.15}$$

Basically, Δ' quantifies the magnetic energy available and indicates the spectrum of unstable wavenumbers $k_y = \pi m/L_y$, for a given equilibrium, defined as the set of wave number satisfying

$$\Delta'(k_y) > 0. \tag{3.16}$$

The expression of $\Delta'(k_y)$ for solution (3.12) is well known and is given by

$$\Delta' = \frac{2}{\lambda}\left(\frac{1}{k_y\lambda} - k_y\lambda\right). \tag{3.17}$$

Figure 3.3 shows, on the left panel, the shape of the outer solution $\widetilde{A}_{\text{out}}(x)$ for a tearing parameter Δ' of -1, 0.9 and 2. In the limit $|x| \longrightarrow 0$ the outer solution can then be written in the form

$$\widetilde{A}_{\|\text{out}} = 1 + \frac{\Delta'}{2}|x| + O(x^2). \tag{3.18}$$

As mentioned, the parameter Δ' will depend on the chosen equilibrium. Figure 3.4 shows the dependence of Δ' on k_y for the two equilibria (2.155) and (2.156) considered in this Thesis, and for $\lambda = 1$.

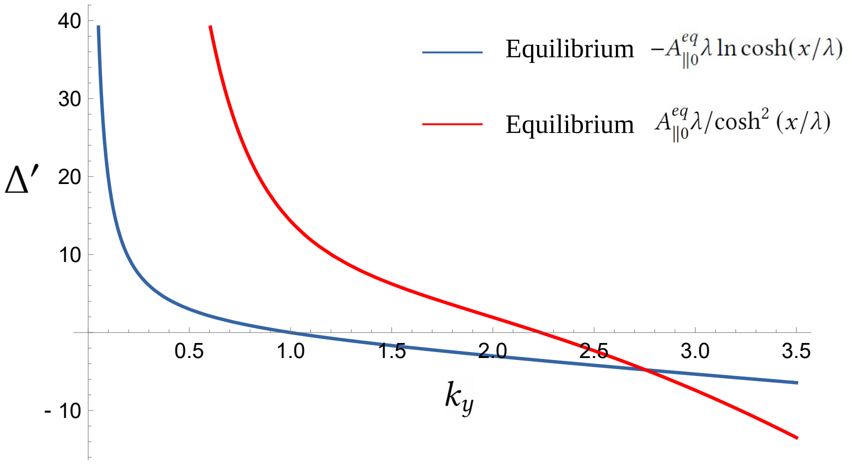

Figure 3.4: The tearing parameter Δ' as a function of k_y for the two different equilibria, with $\lambda = 1$.

3.1.2 Inner region

In the inner region, centered about the resonant surface where $x \ll 1$, we introduce the change of variable

$$x = \epsilon\bar{x}, rmwith \ \ \epsilon \ll 1, \tag{3.19}$$

and consider the unknown functions $\widetilde{A}_{\|\text{in}}(\bar{x})$ and $\widetilde{\phi}_{\text{in}}(\bar{x})$ defined by $\widetilde{A}_{\|}(x) = \widetilde{A}_{\|\text{in}}(\bar{x})$ and $\widetilde{\phi}(x) = \widetilde{\phi}_{\text{in}}(\bar{x})$.

Assuming that ϵ is a small parameter implies that x-derivatives are large in this region (i.e. $k_y \ll \partial_x$) since they will scale as $1/\epsilon$. Moreover, $B_y^{(0)}(x) = B_y^{(0)}(\epsilon\bar{x})$ can be substituted by its Taylor expansion as $\epsilon \longrightarrow 0$. Inspection of the ordering of the various terms of Eqs. (3.3) - (3.4) in the inner region, after rescaling, indicates that

$$\epsilon = g\delta\sqrt{\frac{2}{\beta_{\perp_e}}}, \tag{3.20}$$

is the distinguished limit allowing to keep the maximum number of terms in the system as $\epsilon \longrightarrow 0$ (Bender & Orszag (1999)). Thus (3.20) provides the appropriate choice for the scaling parameter ϵ.

The leading contributions of Eqs. (3.3) and (3.4) in the inner region are

$$\widetilde{A}''_{\|\text{in}} = \frac{ig\lambda}{\bar{x}\epsilon}\widetilde{\phi}''_{\text{in}}, \tag{3.21}$$

$$g\left(\widetilde{A}_{\|\text{in}} - \frac{2\delta^2}{\beta_{\perp_e}}\frac{1}{\epsilon^2}\widetilde{A}''_{\|\text{in}}\right) - \frac{i\bar{x}}{\Theta_e\lambda}\frac{1}{\epsilon}\widetilde{\phi}''_{\text{in}} = 0, \tag{3.22}$$

where we recall that now the prime denotes derivative with respect to the inner variable $\bar{x}$. Inserting (3.21) into (3.22) we get

$$\frac{i}{\epsilon}\widetilde{\phi}''_{\mathrm{in}} = \frac{g\bar{x}\widetilde{A}_{\|\mathrm{in}}}{\lambda(1+\frac{\bar{x}^2}{\Theta_e\lambda^2})}. \tag{3.23}$$

We introduce a re-scaled displacement function $\bar{\xi}_{in}$ related to $\widetilde{\phi}_{\mathrm{in}}$ by

$$\bar{\xi}_{in} = -\frac{i}{g\epsilon}\widetilde{\phi}_{\mathrm{in}}. \tag{3.24}$$

The rescaling in Eq. (3.24) makes $\bar{\xi}_{in}$ a purely real function, and allows one to eliminate the inner parameter ϵ from Eq. (3.23). This gives the following layer equation for $\bar{\xi}_{in}$:

$$\bar{\xi}''_{in} = \frac{-\bar{x}\widetilde{A}_{\|\mathrm{in}}}{\lambda\left(1+\frac{\bar{x}^2}{\Theta_e\lambda^2}\right)}. \tag{3.25}$$

Under the change of variables (3.19), the expansion (C.10) becomes $\widetilde{A}_{\|\mathrm{out}} = 1 + \frac{\Delta'}{2}\epsilon|\bar{x}| + O(\bar{x}^2)$. In this work we consider small values of Δ' allowing the use of the so-called *constant ψ approximation*, which consists in approximating the shear field in the vicinity of the neutral line by supposing $\widetilde{A}_{\|}$ constant at the neighbourhood of $x = 0$ (Furth et al. (1963)). Looking at (C.10), this assumption is valid for $\Delta'\epsilon \ll 1$. Thus, we can set $\widetilde{A}_{\|\mathrm{in}} = 1 + \widetilde{A}_{\|1}(\bar{x})$, where $\widetilde{A}_{\|1}(\bar{x}) \ll 1$. Combining Eqs. (3.21) and (3.25) one eventually finds that the solution for $\bar{\xi}_{in}$ is not required for determining the dispersion relation (which will be obtained by calculating the integral in Eq. (C.25)). Nevertheless, the solution of Eq. (3.25) has to be determined to make sure the matching does exist in the overlap region. Such solution is given by

$$\bar{\xi}_{in}(\bar{x}) = -\frac{\lambda\Theta_e}{2}\bar{x}\log\left(\lambda^2\Theta_e + \bar{x}^2\right) - \lambda^2\Theta_e^{3/2}\arctan\left(\frac{\bar{x}}{\lambda\Theta_e^{1/2}}\right) + \bar{x}(\lambda\Theta_e + D_2) + D_1. \tag{3.26}$$

We set $D_1 = 0$ in order to respect the condition $\lim_{\bar{x}\to 0}\bar{\xi}_{in} = 0$, following from $\widetilde{\phi}$ being an odd function.

In terms of the electrostatic potential $\widetilde{\phi}_{\mathrm{in}}$ and the outer variable $\bar{\xi}_{in}(\bar{x})$, Eq. (3.24) reads

$$\begin{aligned}\widetilde{\phi}_{\mathrm{in}}(\epsilon x) = &-\frac{i\Theta_e\lambda g}{2}x\log\left(\lambda^2\Theta_e + \frac{x^2\beta_{\perp_e}}{g^2\delta^2 2}\right) + igx(\lambda\Theta_e + D_2)\\ &- ig^2\delta\sqrt{\frac{2}{\beta_{\perp_e}}}\lambda^2\Theta_e^{3/2}\arctan\left(\sqrt{\frac{\beta_{\perp_e}}{2}}\frac{x}{g\delta\lambda\Theta_e^{1/2}}\right),\end{aligned} \tag{3.27}$$

We now choose the constants C_2 and D_2 in order to ensure the matching condition (3.7). This gives the constants

$$C_2 = g\Theta_e\lambda a - g^2\delta\sqrt{\frac{2}{\beta_{\perp_e}}}\lambda^2\Theta_e^{3/2}\frac{\pi}{2} - C_1, \tag{3.28}$$

and

$$D_2 = \frac{\alpha}{g}(C_1 - C_2) + \frac{a\Theta_e}{k_y\lambda} - ak_y\lambda\Theta_e + \lambda\Theta_e \log\left(\sqrt{\frac{\beta_{\perp_e}}{2}}\frac{a}{g\delta}\right). \tag{3.29}$$

As is customary in linear tearing mode theory, we impose a matching between the logarithmic derivatives of the inner and outer region. Under the constant-psi approximation, this condition gives

$$\Delta' = \int_{-\infty}^{\infty} \widetilde{A}''_{\|\mathrm{in}} \mathrm{d}x = \frac{1}{\epsilon}\int_{-\infty}^{\infty} \widetilde{A}''_{\|\mathrm{in}} \mathrm{d}\bar{x}. \tag{3.30}$$

The condition (C.25) will provide the dispersion relation giving the growth rate of the tearing mode as function of Δ' and of other parameters of the system. Combining Eqs. (3.21), (3.24) and (3.25) with the relation (C.25), and making use of the constant-ψ approximation, leads to

$$\Delta' = \frac{2g^2}{\epsilon}\int_0^{+\infty} \frac{d\bar{x}}{\left(1 + \frac{\bar{x}^2}{\Theta_e\lambda^2}\right)}. \tag{3.31}$$

Using the expression (3.20) for ϵ, we obtain the following **normalized** dispersion relation

$$\gamma = \frac{\Delta' k_y\delta}{\pi\lambda\sqrt{\Theta_e}}\sqrt{\frac{2}{\beta_{\perp_e}}}, \tag{3.32}$$

where we recall that $\Delta' = \frac{2}{\lambda}\left(\frac{1}{k_y\lambda} - k_y\right)$, given by Eq. (3.17).

The dispersion relation (3.32) accounts for well known features of inertial reconnection in the small Δ' regime, such as the linear dependence on Δ' and on the square root of the mass ratio δ (Porcelli (1991); Fitzpatrick & Porcelli (2007); Fitzpatrick (2010)). The growth rate (3.32), for $\Theta_e = 1$, reduces to the one found in Ref. Tassi et al. (2018), the difference being the factor $\sqrt{2/\beta_{\perp_e}}$ emerging from the fact that we used a different normalization of the perturbed magnetic potential, which amounts to taking a different dimensional magnetic equilibrium. The main element of novelty is given by the dependence on the electron temperature anisotropy parameter Θ_e. The formula (3.32) predicts a decrease of the reconnection growth rate as Θ_e increases. The evolution of the dispersion relation as a function of Θ_e is shown on Fig. 3.6 in Section 3.2.

In order to make the dependence of the growth rate (3.32) on various physical quantities, more transparent, and to facilitate the comparison with the formula derived in Ref. Porcelli (1991) for the isotropic case, we rewrite the relation (3.32) in the following dimensional form:

$$\hat{\gamma} = \frac{2}{\lambda \hat{\rho}_{s\perp}} \left(\frac{1}{\hat{k}_y \lambda \hat{\rho}_{s\perp}} - \hat{k}_y \lambda \hat{\rho}_{s\perp} \right) \frac{\hat{k}_y v_{th_{\parallel e}} \hat{d}_e^2}{\pi \lambda \hat{d}_i}, \tag{3.33}$$

where dimensional quantities are indicated with a hat and where we used the dimensional expression for the tearing parameter

$$\hat{\Delta}' = \frac{2}{\lambda \hat{\rho}_{s\perp}} \left(\frac{1}{\hat{k}_y \lambda \hat{\rho}_{s\perp}} - \hat{k}_y \lambda \hat{\rho}_{s\perp} \right), \tag{3.34}$$

which allows to see its dependence on $\hat{\rho}_{s\perp}$ and, consequently, its dependence on $T_{0_{\perp e}}$ (we recall that $\hat{\rho}_{s\perp} = c_{s_\perp} \omega_{c_i} = \sqrt{T_{0_{\perp e}}/m_i}\,\omega_{c_i}$). We also used the expression for the electron thermal speed based on the parallel electron temperature $v_{th_{\parallel e}} = \sqrt{T_{0_{\parallel e}}/m_e}$.

In the dimensional expression, the dependence in $T_{0_{\perp e}}$ coming from the parameters $\beta_{\perp e}$ and Θ_e of the normalized expression (3.32), is canceled. This implies that the equilibrium perpendicular temperature appears in the final expression (3.33) from the fact that it affects the current sheet width, and consequently the tearing parameter as well.

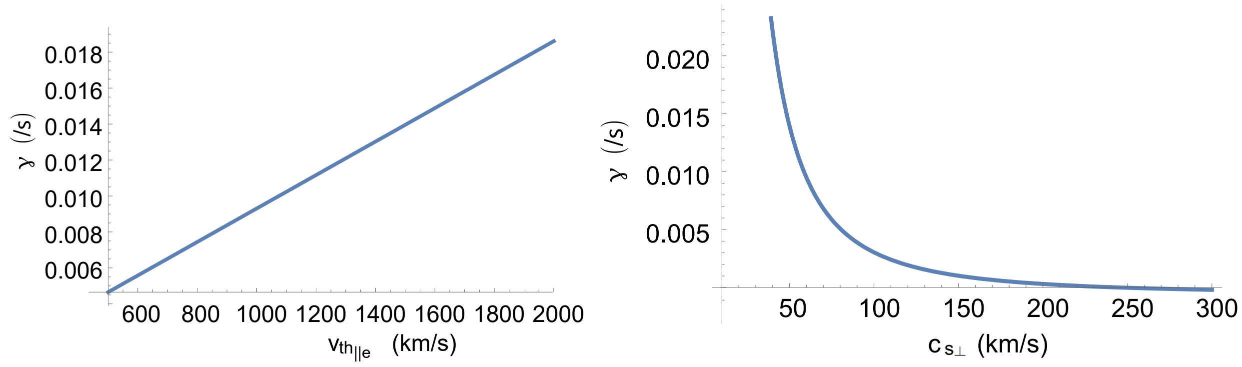

Figure 3.5: *Right:* Dimensional growth rate (in s^{-1}) as a function of $v_{th_{\parallel e}} \propto \sqrt{T_{0_{\parallel e}}}$. *Left:* Same quantity as a function of $c_{s_\perp} \propto \sqrt{T_{0_{\perp e}}}$ (in $\mathrm{km.s}^{-1}$). The value used for the plots are: $\hat{d}_e = 1$ km, $\hat{d}_i = 40$ km, $\hat{\omega}_{c_i} = 0.81\ \mathrm{s}^{-1}$, $\lambda = 1$, $\hat{k}_y = 5 \times 10^{-3}$ km. For the left plot, $c_{s_\perp} = 50\ \mathrm{km.s}^{-1}$. For the right plot $v_{th_{\parallel e}} = 1500\ \mathrm{km.s}^{-1}$. These values are taken from Jovanović et al. (2020) and correspond to the solar wind plasma with a weak magnetic field and β_e values close to unity.

Figure 3.5 shows the dimensional growth rate (3.33) as a function of $v_{th_{\|e}} \propto \sqrt{T_{0_{\|e}}}$ and $c_{s_\perp} \propto \sqrt{T_{0_{\perp e}}}$ for values taken from Jovanović et al. (2020). We can make, in the first place, the following two comments:

- This dispersion relation predicts that $T_{0_{\perp e}} < T_{0_{\|e}}$ increases the tearing growth rate. This differs from what occurs in the case of weak and absent guide field (Forslund (1968); Chen & Palmadesso (1984); Shi et al. (1987); Karimabadi et al. (2004); Quest et al. (2010)) where, as already mentioned in Sec. 3, an enhancement of the growth rate is observed as Θ_e increases.

- However the dependence of the normalized dispersion relation on $T_{0_{\perp e}}$ only comes from the fact that the equilibrium is of characteristic length $\rho_s \propto \sqrt{T_{0_{\perp e}}}$.

According to our normalization (2.109) and to our choice (2.155) for the equilibrium magnetic flux function, we are considering a dimensional equilibrium magnetic field $\hat{B}_y^{(0)}(\hat{x}) = B_0\sqrt{\beta_{\perp_e}/2}\tanh(\hat{x}/(\lambda\rho_{s\perp}))$ whose amplitude contains the factor $\sqrt{\beta_{\perp_e}/2}$ and is given by $B_0\sqrt{\beta_{\perp_e}/2}$. Considering this equilibrium, in the isotropic case, $\Theta_e = 1$, and with $\lambda = 1$, the dimensional growth rate is given by (Porcelli (1991))

$$\hat{\gamma}_{iso} = \frac{\hat{\Delta}'\hat{k}_y v_{th_e}\hat{d}_e^2}{\pi L}\sqrt{\frac{\beta_e}{2}}, \tag{3.35}$$

where L is the shear length, $v_{th_e} = \sqrt{T_{0_e}/m_e}$ is the isotropic electron thermal speed and β_e is the isotropic electron beta parameter. Our growth rate (3.32) reduces to the one given in Eq. (3.35) in the absence of temperature anisotropy and for $L = \lambda\rho_{s\perp}$. Therefore, the comparison shows that the extension of the formula for $\hat{\gamma}_{iso}$, to account for equilibrium electron temperature anisotropy is obtained by replacing the electron thermal speed with the parallel electron thermal speed and by considering the appropriate equilibrium scale length. Note, on the other hand, that the dispersion relation (3.33) differs from those derived in Refs. Bulanov et al. (1992); Cai & Li (2008) for EMHD models. In particular, for such models, the growth rate depends quadratically on Δ', whereas, in our case, the dependence is linear.

3.2 Numerical results

3.2.1 Numerical validation of the dispersion relation

We made the use, for this study, of a 2D domain where $L_y = 4\pi$ and $L_x = 10\pi$. We made the choice of $\lambda = 3$ which, according to the relation (3.17), gives the fixed values $\Delta' = 0.38$ with $k_y = 0.24$ for the mode $m = 1$. The mass ratio has been taken equal to $\delta^2 = 0.01$ while different values of $\beta_{\perp_e}$ have been considered.

We point out that, considering that $\beta_{\perp_e} = 2\rho_{s\perp}^2/d_i^2$, where $\rho_{s\perp}$ can be explicitly written as $\rho_{s\perp} = \sqrt{T_{0_{\perp e}} m_i c^2/e^2 B_0^2}$, a variation of $\beta_{\perp_e}$ can be interpreted in two different ways. On one hand, it can mean a variation of d_i performed by modifying the background density n_0 and keeping a current sheet of a fixed thickness. Alternatively, it can also be interpreted as a variation of the perpendicular equilibrium temperature $T_{0_{\perp e}}$, which implies a variation of the thickness of the current sheet $\rho_{s\perp}$, for a fixed density n_0. Both ways leave B_0 and m_i (and in turn ω_{ci}) constant, thus guaranteeing that one is comparing different values of the growth rate, normalized with respect to the same unit of time.

The numerical growth rate is determined by the formula

$$\gamma_N = \frac{d}{dt} \log \left| A_{\|}^{(1)} \left(\frac{\pi}{2}, 0, t \right) \right|, \tag{3.36}$$

where $x = \pi/2$, $y = 0$ is the location of the X point, during the linear phase. Figure 3.6 shows a very good agreement between the analytical formula (3.32) and the numerical results. In particular, a stabilizing, although weak, role of electron temperature anisotropy at a fixed $\beta_{\perp_e}$ is clearly visible, as Θ_e increases. The stabilizing role, for the adopted normalization, of the $\beta_{\perp_e}$ parameter is also confirmed.

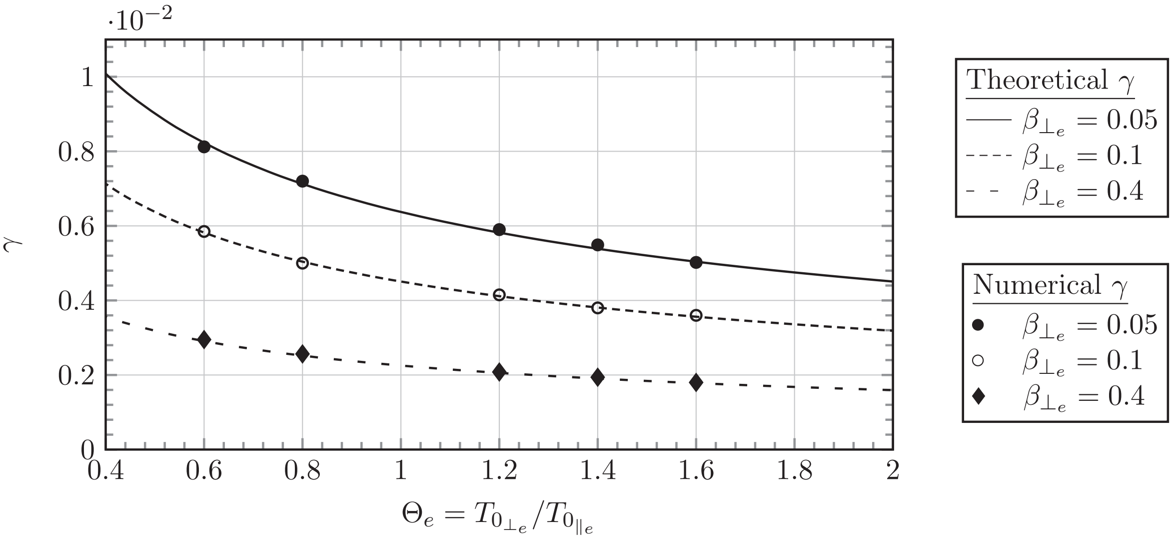

Figure 3.6: Growth rate as a function of the electron temperature anisotropy for different values of $\beta_{\perp_e}$ and taking the parameters $\delta = 0.1$ and $\Delta' = 0.38$ fixed. For the filled circle, the run has been made taking $n_x = 300$, for the open circles $n_x = 600$, and for the diamonds $n_x = 1200$. We recall that γ is normalized with respect to ω_{ci}, the ion gyrofrequency.

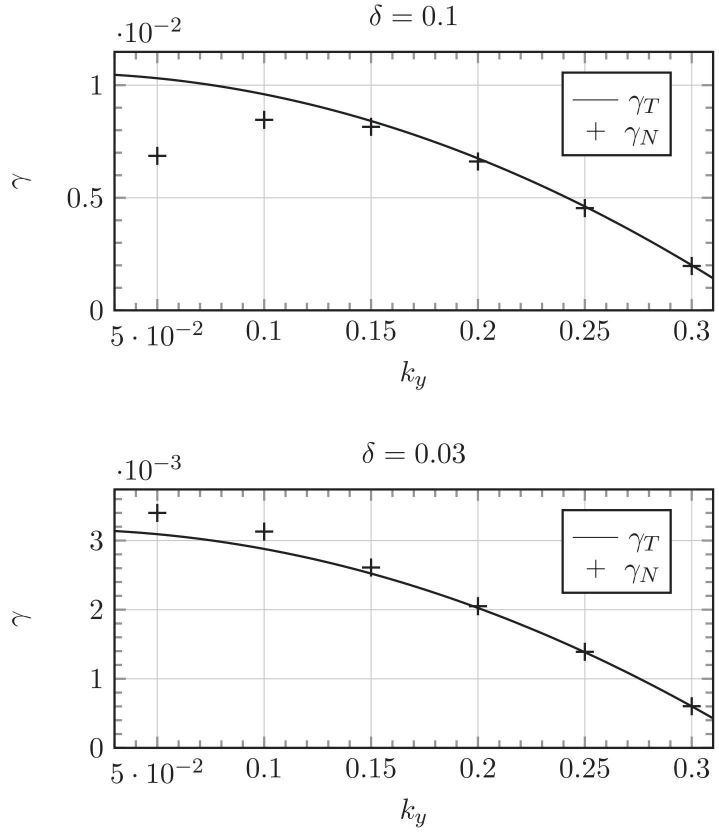

Figure 3.7: Comparison between the theoretical growth rate predicted by Eq. (3.32) (denoted γ_T on this figure) and the numerical growth rate (γ_N) as a function of the wave number k_y, for the cases $\delta = 0.1$ and $\delta = 0.03$. The values of the parameters are $\Theta_e = 1$, $\beta_{\perp_e} = 0.1$, $\lambda = 3$ and the numerical simulations were carried out using the modes $1 \leq m \leq 6$.

We find it also useful to analyze how the theoretical predictions based on Eq. (3.32) compare with the numerical results, for different values of k_y. Figure 2 shows the numerical and theoretical growth rates for different k_y values in the cases $\delta = 0.1$ and $\delta = 0.03$. We recall that the relation between Δ' and k_y is given by Eq. (3.17). In order to obtain higher values of Δ' for low modes, the length L_y has been increased to $L_y = 20\pi$, while we kept $L_x = 10\pi$.

As shown in Fig. 3.7, in the two cases, the agreement between the theoretical and the numerical values is very satisfactory for $k_y > 0.15$ (corresponding to $\Delta' < 1.15$). For $\delta = 0.1$, the lowest mode (associated to $k_y = 0.05$, $\Delta' = 4.3$) gives a relative error between γ and γ_N of 33%. In this case we have $\epsilon\Delta' = 0.4$ and $\gamma/k_y = 0.2$, which appear to be too large for the formula (3.32) to be valid. However, in the case of $\delta = 0.03$, which leads to a smaller γ/k_y ratio, the error for the lowest mode is reduced to 9%. In the latter case we have $\epsilon\Delta' = 0.03$ and $\gamma/k_y = 0.06$. To conclude, the error between γ_N and γ is well decreasing with the ratio γ/k_y and the product $\epsilon\Delta'$, in consistency with the assumptions No. 1 and 4 of Table 1 (note that ϵ depends linearly on γ/k_y). Small values of γ/k_y increase the upper bound of (44) and allow for larger values of Δ'.

3.2.2 Comparison between the numerical and analytical solutions

Since our outer solution $\widetilde{\phi}_{\text{out}}$, given by (3.13) differs from the outer solution obtained in the framework of the reduced MHD, we proceed here to a comparison between the analytical solution and the numerical solution.

Using the outer and inner solution, (3.13) and (3.27), respectively, it is possible to build an approximate solution of the system (2.95) - (2.96). The approximate solution is given by (Bender & Orszag (1999))

$$\widetilde{\phi}_{\text{unif}} = \widetilde{\phi}_{\text{out}} + \widetilde{\phi}_{\text{in}} - \widetilde{\phi}_{\text{match}}, \tag{3.37}$$

where $\widetilde{\phi}_{\text{match}} = \widetilde{\phi}_{\text{match}_{\text{in}}} = \widetilde{\phi}_{\text{match}_{\text{out}}}$ defined by (3.7). Figure 3.8 shows the comparison between the numerical and approximated solution for a given set of parameter, at $t = 50$ and $y = 2\pi$. The figure shows a good agreement, although a slight difference could come from a time sampling too wide or from the amplitude of the initial perturbation used in the code.

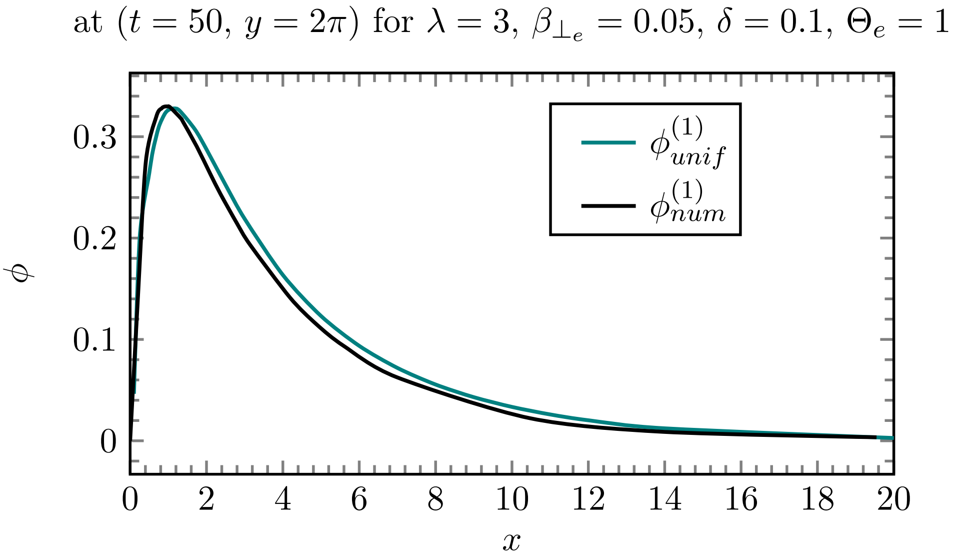

Figure 3.8: Comparison between $\tilde{\phi}_{\text{unif}}(x)$ and a profile along x of the numerical solution, at a certain time. All the values are given on top of the plot.

No.	Adopted assumptions	
1	Time variation of the perturbation is slow	$g \ll 1$
2	Smallness of the inner scale	$\epsilon \ll 1$
3	Keeping electron inertia terms while neglecting electron FLR	$\delta^2 \ll \beta_{\perp_e} \ll 1$
4	Use of the constant-ψ approximation	$\epsilon\Delta' \ll 1$
5	Neglecting electron FLR effects in the inner region	$\delta \ll \epsilon$

Table 3.1: Table summarizing the various assumptions identifying small parameters adopted to derive the relation (3.32).

3.3 Discussion

3.3.1 Limits of validity of the dispersion relation

The dispersion relation (3.32) was derived on the basis of a number of assumptions imposing some parameters to be small. We find it useful to summarize and discuss here such assumptions.

Neglecting electron FLR in the inner region

The adopted model (2.95) - (2.96) neglects electron FLR effects. It is thus valid for scales much larger than the electron Larmor radius. Therefore, we must ensure that, when moving to the spatial scale of the order of ϵ, after the rescaling (3.19), we do not approach the scale of the electron Larmor radius. In the inner region, the perpendicular wave number is normalized such that $\hat{k}_\perp = k_\perp/\epsilon\rho_{s\perp}$. Thus, written in terms of ϵ, electron FLR corrections would lead to the presence of operators of the form $(\delta^2/\epsilon^2)(\partial^2/\partial\bar{x}^2)$. To make sure that these operators are negligible, compared to the other effects retained in the inner region, we must ensure $\rho_e k_\perp/\epsilon\rho_{s\perp} \ll 1$, with $k_\perp$ of order 1. Using the relation $\rho_e = \delta\rho_{s\perp}$, it is evident to see that, for our linear analysis to be consistent with the assumptions of the model, ϵ, has to satisfy the condition

$$\delta \ll \epsilon. \tag{3.38}$$

Summary of the assumptions and discussions

Relation (3.38) and the other assumptions adopted for the tearing analysis are numbered in Table 3.3.1. Given the expressions for ϵ (3.20) and for γ (3.32), it is possible to see that the assumptions 1, 2 and 3 are compatible. Combining the assumptions 4 and

5 gives the following additional constraint on Δ'

$$\frac{\pi\lambda\sqrt{\Theta_e}}{\delta}\frac{\beta_{\perp_e}}{2} \ll \Delta' \ll \frac{\sqrt{\pi\lambda\sqrt{\Theta_e}}}{\delta}\sqrt{\frac{\beta_{\perp_e}}{2}}. \tag{3.39}$$

The assumption, for neglecting the electron FLR effects in the inner region (No. 5 in the Table 3.3.1), provides the lower bound of (3.39). It compels us, in order to be perfectly consistent with the derivation of the model, not to take too small values for Δ'. Fulfilling such condition forces the admissible values for Δ' to lie in a rather narrow interval, given in Eq. (3.39). Although the derivation of the dispersion relation (3.32), starting from the system (2.95) - (2.96), was obtained using only assumptions 1 - 4, violating the assumption 5 leaves the doubt about whether electron FLR effects might have played an important role in the inner region.

In assumption 3, the condition $\beta_{\perp_e} \ll 1$ allows to neglect the FLR effects in the general model while retaining electron inertia. Recalling that $\beta_{\perp_e} = 8\pi n_0 T_{0_{\perp e}}/B_0^2$, the low-$\beta_{\perp_e}$ regime is consistent with the strong guide field configuration.

3.3.2 Keeping small $\beta_{\perp_e}$ corrections

Although negligible at the leading order, if we keep first order corrections in $\beta_{\perp_e}$ in the evolution equations (2.95) - (2.96), we find the modified growth rate

$$\gamma = \frac{\delta\Delta' k_y}{\pi\lambda}\left(\frac{2}{\beta_{\perp_e}} + 1 - \frac{1}{\Theta_e}\right)\sqrt{\frac{1}{\Theta_e} - \frac{\beta_{\perp_e}}{\beta_{\perp_e}+2}}\sqrt{\frac{\beta_{\perp_e}}{2}},$$

which is non-negative if

$$\frac{\beta_{\perp_e}}{2+\beta_{\perp_e}} \leq \Theta_e \leq \frac{2+\beta_{\perp_e}}{\beta_{\perp_e}}. \tag{3.40}$$

By comparing Eq. (3.40) with Eq. (3.32), it emerges that the inclusion of first-order corrections in $\beta_{\perp_e}$ introduces, in the dispersion relation, new modifications due to the temperature anisotropy, which are not merely due to the specific choice of the equilibrium scale length. We remark that the condition on the lower bound for Θ_e in Eq. (3.40), corresponds to the condition for firehose stability (Hasegawa (1975)). However, under the adopted assumptions $\beta_{\perp_e} \ll 1$ and $\Theta_e = O(1)$, violating this condition leads outside the range of validity of the model.

Figure 3.9 shows the evolution of the normalized growth rate (3.40) as a function of Θ_e. The value of β_e for this plot were 0.3, 0.4 and 0.5. We see that the stabilization of the tearing mode, appears only for an important temperature anisotropy (for $\theta_e < 0.1$ or $\theta_e > 5$).

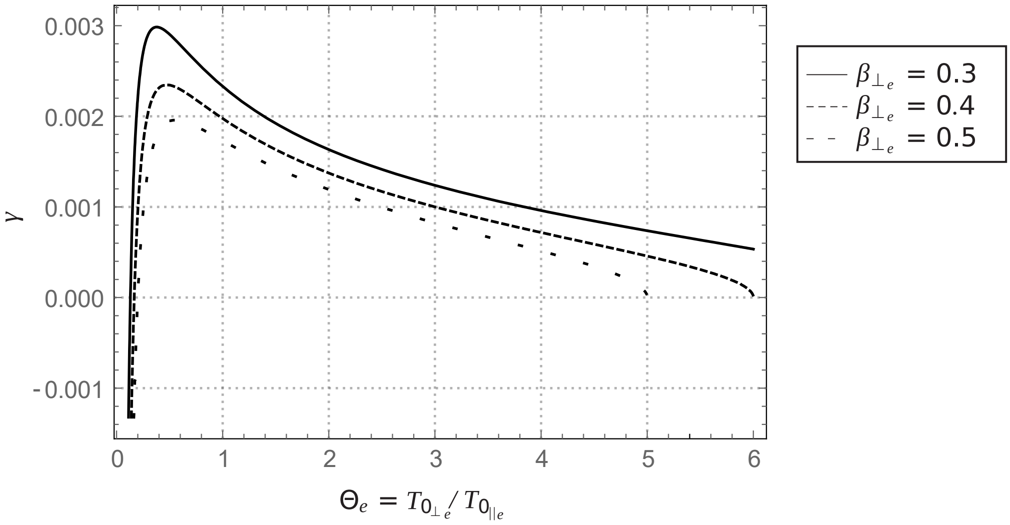

Figure 3.9: Growth rate (3.40) as a function of the electron temperature anisotropy for different values of $\beta_{\perp_e}$ and taking the parameters $\delta = 0.1$ and $\Delta' = 0.38$ fixed. We recall that γ is normalized with respect to ω_{ci}, the ion gyrofrequency.

3.3.3 Possible extension to arbitrary ion temperature

The gyrofluid equations, derived using the isothermal closure, can be reduced to obtain a 2-field fluid model, similar to a model which has been studied by Grasso et al. (2000), but which contains temperature anisotropy. In this discussion, we will just give the list of stages of the model reduction leading to the above-mentioned model.

Starting from Eqs. (2.46) - (2.47), the reduction procedure is the following:

- We assume the normalisation by the Alfvén time (2.109) (instead of (2.64)).
- We assume, as for all the models in this Thesis, that the **gyrocenter** ion density and parallel velocity are negligible $N_i = U_i = 0$.
- We assure the regime $\beta_e \ll 1$, which implies a negligible electron Larmor radius and allows to Taylor expand the electron gyroaverage operators.
- We relax the hypoThesis of cold ions (consisting in taking $\tau_{\perp_i} \ll 1$), and assume an arbitrary (but isotropic) ion temperature.

In this case the model is reduced to

$$\frac{\partial n_e}{\partial t} + [\phi, n_e] - [A_\|, u_e] = 0, \tag{3.41}$$

$$\frac{\partial}{\partial t}\left(A_\| - d_e^2 u_e\right) + \left[\phi, A_\| - d_e^2 u_e\right] - \frac{\rho_{s\perp}^2}{\Theta_e}[n_e, A_\|] = 0, \tag{3.42}$$

$$\tag{3.43}$$

where the static relations (2.127) - (2.129) are replaced by

$$N_e = n_e = \frac{1}{\rho_{i\perp}^2}\left(\Gamma_{0i} - 1\right)\phi, \tag{3.44}$$

$$U_e = u_e = \nabla_\perp^2 A_\parallel, \tag{3.45}$$

$$B_\parallel = 0. \tag{3.46}$$

In (3.44) we used the relation $\rho_{i\perp} = \rho_{s\perp}\sqrt{\tau_{\perp_i}}$.

It is possible to absorb the parameter Θ_e, by assuming an effective $\rho_{s\parallel}$ given by

$$\rho_{s\parallel} = \frac{\rho_{s\perp}}{\sqrt{\Theta_e}}, \tag{3.47}$$

which corresponds to the ion-sound Larmor radius based on the parallel temperature. Following this change of variable, the model is identical to the model used in Ref. Grasso et al. (2000) when the latter is taken in the collisionless limit, and to the models of Refs. Grasso et al. (2010) and Comisso et al. (2013) when the latter are taken in the limit $n_i = 0$. For this model, the linear theory of the tearing instability of Porcelli (1991) can be recovered.

The dispersion relation, in the case of short wavelength, reduces to the relation

$$\gamma_\tau = \frac{2k_y}{\pi\lambda}\frac{d_e\Delta'}{\Theta_e}\sqrt{\rho_{s\perp}^2 + \rho_{i\perp}^2}, \tag{3.48}$$

which, if we write it in such a way as to bring out the contributions $T_{0_{\perp e}}$ and $T_{0_{\parallel e}}$, is expressed as

$$\gamma_\tau = \frac{2k_y}{\pi\lambda}d_e\Delta'\frac{T_{0_{\parallel e}}}{T_{0_{\perp e}}}\sqrt{\frac{T_{0_{\perp e}}}{m_i\omega_{c_i}^2} + \rho_{i\perp}^2}. \tag{3.49}$$

The normalized dispersion relation (3.49) is valid for an arbitrary (isotropic) ion temperature. It also predicts an increase of the tearing growth rate in the case of $T_{0_{\parallel e}} > T_{0_{\perp e}}$.

3.4 Conclusion and discussion

In this Chapter, a dispersion relation of the tearing instability depending on temperature anisotropy is obtained by applying the theory of asymptotic matching. For a magnetic equilibrium shear length of the order of $\rho_{s\perp}$ we showed that the dimensional growth rate, in the $\beta_{\perp_e} \ll 1$ limit that we considered, increases as $T_{0_{\parallel e}}^{1/2}$. Let us try to consider the characteristics of a plasma in the magnetosheath assuming, for example, values estimated from Phan et al. (2018), giving a plasma immersed with a guide field with a $\beta_e \sim 0.3$ and $\hat{T}_{0_{\parallel e}} \sim 65$ eV. We consider a current sheet with the dimensions $\hat{L}_{\text{cs}} \sim \hat{d}_i \sim 50$ km, and $\hat{a}_{\text{cs}} \sim \hat{d}_e \sim 1$ km which are typical lengths observed in the magnetosheath. Applying now (3.33), these values give us a reconnection time $\tau \sim 160$ ms. However, (3.33) assumes cold ions, while in Phan et al. (2018) ions are about 3 times hotter than the electrons. In this Chapter, we have also obtained a possible dispersion relation valid for arbitrary ion to electron equilibrium temperature ratio given by Eq. (3.48). Considering $T_i \sim 3T_e$ in Eq. (3.48), we obtain a reconnection time of $\tau \sim 80$ ms, which is closer to the observed exhaust time in Phan et al. (2018) of $\tau_{obs} \sim 45$ ms.

It is therefore shown that, in the strong guide field regime, the effect of equilibrium electron temperature anisotropy is different from what occurs in the case of absent or weak guide field. The enhancement of the growth rate observed in the latter case is indeed absent in the strong guide field case. In this respect we remark that, in Shi et al. (1987), the tendency of a finite guide field to weaken such enhancement was observed (although with a guide field of amplitude at maximum only 2.5 greater than that of the equilibrium field). The analytical predictions are tested against numerical simulations showing a very good quantitative agreement. In this Chapter, we also provide a dispersion relation valid for small FLR effects.

4 Gyrofluid analysis of β_e effects on the tearing instability

In this Chapter, we make use of the gyrofluid model (2.130) - (2.131) to study the impact of a finite β_e, assuming now isotropic equilibrium temperature, on the linear and nonlinear evolution of the tearing instability.

An important progress in the understanding of magnetic reconnection has been possible thanks to fluid models. However, many of these models are either collisional, or collisionless with a focus on the limit $\beta_e \ll 1$. This limit is indeed often adopted, which is not so surprising given that plasmas where reconnection is observable have in general $\beta_e \lesssim 1$. For example, some values that are calculated from the paper of Kivelson & Russell (1995) and Hughes (1995) give us: solar Wind, at 1 AU: $\beta_e \sim 0.65$, magnetosheath: $\beta_e \sim 0.22$, magnetotail lobes: $\beta_e \sim 2.8 \times 10^{-4}$. On the other hand, it is nevertheless not unusual to find $\beta_e \sim 1 - 2$ in the magnetosheath, even when strong guide fields are observed. In addition, as we show in this Chapter, the tearing growth rate can actually be affected even by a small, but finite, β_e. The study of reconnection for a finite β_e can also be relevant for diluted plasmas with relatively large temperatures. For instance, in the intracluster medium, plasma β_e as large as $\beta_e \sim 10^2$ are expected.

Among the studies that have taken into account the effects of β_e for reconnection in the strong guide field regime, we can point to Numata et al. (2011); Numata & Loureiro (2015), in which a gyrokinetic model is used to study the tearing instability as well as the electron and ion heating during reconnection. In these studies, different β_e values were considered. Figure 4.1 is a plot taken from Numata & Loureiro (2015), showing the growth rate of the tearing instability scaling as $\beta_e^{-1/2}$ for ρ_s and m_e/m_i fixed. However, in this work, the resistivity was the main responsible for breaking the frozen in condition, and the width of the current sheet was too large to be affected by electron inertia or electron larmor radius effects, which implies a difference compared to our study in which these effects are retained. In Muraglia et al. (2009), the effects of β_e are investigated, and are also associated with the presence of magnetic field curvature and equilibrium pressure gradient. In a different context, large β_e were also considered in Alt & Kunz (2019); Winarto & Kunz (2022), in which also the temperature anisotropy

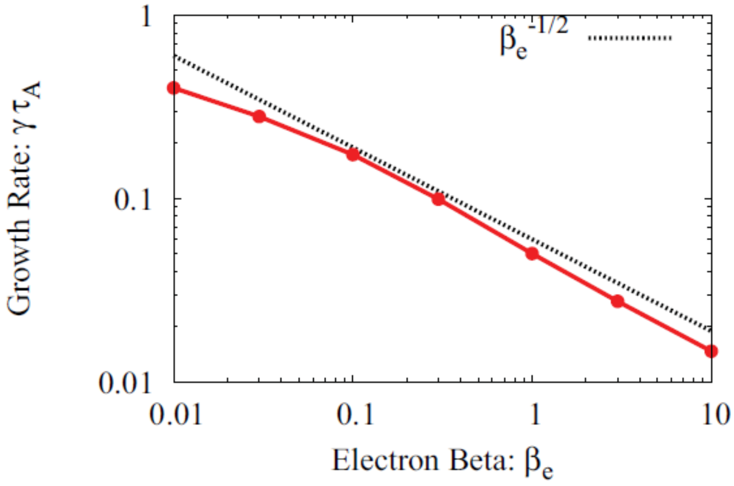

Figure 4.1: Growth rate of the tearing instability as a function of the electron β_e. The electron skin depth varies as $d_e = \sqrt{2m_e/\beta_e m_i}\rho_s$, for ρ_s and m_e/m_i fixed. The temperature ratio is $\tau = 1$. *Credit: Taken from Numata & Loureiro (2015).*

is included in order to study the impact of the mirror instability on the tearing mode instability threshold. We also remark that finite β_e effects were taken into account in the fluid model of Fitzpatrick & Porcelli (2004, 2007). However, also in that model, electron FLR effects were neglected.

The gyrofluid model used in this Chapter accounts for both finite electron Larmor radius effects and perturbations parallel to the direction of the guide field. The regime is taken within the asymptotic cold ion limit, although we present a small set of simulations performed in the limit of hot ions to reflect the differences and possible consequences of this limit.

In the limit $\beta_e \rightarrow 0$ (in the following also referred to as the "fluid" limit), the model corresponds to the two-field fluid model of Schep et al. (1994). A relevant dispersion relation for the collisionless tearing mode, applicable to this model, has been derived by Porcelli (1991). For the $\beta_e \rightarrow 0$ regime, we present in this Chapter a new analytical formula, whose derivation is presented in Appendix and follows the procedure used by Grasso et al. (2002), which is carried out in real space and resorts to the constant-ψ approximation (Furth et al. (1963)). This new formula differs from the small tearing parameter Δ' limit of the formula of Porcelli (1991), by the presence of a small corrective term. These two formulas are tested against numerical simulations and, in its regime of validity, our new relation shows a better agreement with the numerical growth rate.

In this Chapter, we also study numerically the effect of a finite β_e in the linear and nonlinear phase of the tearing instability. For $\beta_e \ll 1$ the equilibrium electron temperature is seen to enhance the linear growth rate, whereas we observe a stabilizing role when electron finite Larmor radius effects become more relevant. In the nonlinear phase, stall phases and faster-than-exponential phases are observed, similarly to what occurs in the presence of ion finite Larmor radius effects. Energy transfers are also analyzed, but a more detailed analysis of energy conversion in the presence of β_e will be provided in Chapter 5, when comparing with simulations performed with a gyrokinetic code in Numata et al. (2010).

The Chapter is organized as follows. In Sec. 4.1 we present a new dispersion relation for the case $\beta_e = 0$. Section 4.2 contains the results of numerical simulations in the linear phase, for finite β_e and we present a dispersion relation valid for small FLR effects. In Sec. 4.3 the results obtained in the nonlinear phase are presented and the gyrofluid case is compared to the fluid case. In this Section, we also study the impact of a finite β_e on the evolution of the different energy components. In the Appendix C we present the derivation of the new dispersion relation for the $\beta_e \longrightarrow 0$ limit, which is based on the asymptotic matching theory.

In this Chapter, some parts of the text and figures also appear in Granier et al. (2022b).

4.1 Dispersion relation for $\beta_e \longrightarrow 0$

In this Subsection we focus on the regime for which the electron FLR effects and the parallel magnetic perturbations are negligible. The limit of vanishing thermal electron Larmor radius, $\rho_e = d_e\sqrt{\beta_e/2} \longrightarrow 0$, is adopted by considering $\beta_e \longrightarrow 0$ and $m_e/m_i \longrightarrow 0$. This limit enables to reduce the gyrofluid model (2.130)-(2.129) to the fluid model (2.136)-(2.137). We assume an equilibrium given by (2.156), $A_\parallel^{(0)}(x) = \lambda/\cosh^2(x/\lambda)$. With this equilibrium the tearing parameter is

$$\Delta' = 2\frac{\left(5-\lambda^2 k_y^2\right)\left(\lambda^2 k_y^2+3\right)}{\lambda^3 k_y^2(\lambda^2 k_y^2+4)^{1/2}}. \tag{4.1}$$

Because of the requirement of periodic boundary conditions, the equilibrium is approximated by (2.157). We consider the perturbations (3.1).

We consider the linear theory of tearing modes in collisionless plasmas presented in Porcelli (1991) and the results can be adapted to the model (2.136)-(2.137). In particular, a dispersion relation has been derive for the tearing instability, valid for arbitrary values of Δ', and is given by

$$\frac{\pi}{2}\left(\frac{\lambda\gamma_p}{2k_y}\right)^2 = -\rho_s\frac{\pi}{\Delta'} + \rho_s^2 d_e\frac{2k_y}{\gamma_p\lambda}. \tag{4.2}$$

In general, the spectrum can be divided in two different regimes, a long-wavelength regime $\Delta'\epsilon \ll 1$ giving a large set of unstable modes, and a short-wavelength regime,

No.	Assumptions used	
1	Time variation of the perturbation is slow	$\frac{\gamma}{k_y} \ll 1$
2	Smallness of the inner scales	$\frac{\gamma d_e}{k_y \rho_s} \ll \rho_s \ll 1$
3	Use of the constant-ψ approximation	$\frac{\gamma d_e}{k_y \rho_s}\Delta' \ll \rho_s \Delta' \ll 1$
4	Neglecting FLR effects in the inner regions	$\rho_e \ll \frac{\gamma d_e}{k_y \rho_s},$

Table 4.1: Table summarizing the various assumptions adopted for deriving the dispersion relation.

$\Delta' \epsilon \gg 1$. In the small-wavelength regime, the relation is reduced to

$$\gamma = \frac{2k_y}{\lambda}\frac{d_e \rho_s}{\pi}\Delta', \qquad \text{for} \qquad \rho_\mathrm{s} \sim d_\mathrm{e}, \tag{4.3}$$

$$\gamma = \frac{2k_y}{\lambda}\left[\frac{\Gamma(1/4)}{2\pi\Gamma(3/4)}\right]^2 \Delta'^2 d_e^3, \qquad \text{for} \qquad \rho_\mathrm{s} \to 0. \tag{4.4}$$

In the large-wavelength regime, the dispersion relation reduces to

$$\gamma = \frac{2k_y}{\lambda}\left(\frac{d_e 2}{\pi}\right)^{1/3} \rho_\mathrm{s}^{2/3}, \qquad \text{for} \qquad \rho_\mathrm{s} \sim d_\mathrm{e}, \tag{4.5}$$

$$\gamma = \frac{2k_y}{\lambda} d_e, \qquad \text{for} \qquad \rho_\mathrm{s} \to 0. \tag{4.6}$$

In Appendix C, we present the derivation of a new dispersion relation valid in the limit $(\gamma d_e/(k_y \rho_s))\Delta' \ll 1$. The method adopted for the derivation is essentially the same used in Sec. 3.1, although in the present case, two inner scales are required. In the appropriate regime of validity, the new dispersion relation includes a corrective term to Eq. (4.3). We derived this dispersion relation using an asymptotic matching method and various assumptions, slightly different from those adopted by Porcelli (1991). Table 4.1 gives a review of the assumptions that were adopted on the parameters during the analysis. The result of our linear theory (details are provided in Appendix C) is given by the dispersion relation

$$\gamma_u = \frac{2k_y}{\lambda}\frac{d_e \rho_s}{\pi}\Delta' + \frac{\gamma_u^2 d_e \pi \lambda}{4 k_y \rho_s^2}. \tag{4.7}$$

The first term on the r.h.s of (4.7) is exactly that of the formula (4.3), for $\lambda = 1$. In the parameter regime indicated by Table 4.1, the second term in (4.7) is a small term that provides a correction to the formula (4.3).

With regard to the assumptions of Table 4.1, we remark that the assumption No. 1 indicates a slow time variation of the perturbation. No. 2 is the assumption on the scales of the inner region, where electron inertia becomes important and allows the break of the frozen-flux condition. The assumption No. 3 allows the use of the so-called *constant-ψ approximation*, implying that the dispersion relation is valid for large wave numbers (Furth et al. (1963)). The condition No. 4, imposed to neglect electron FLR, can be verified for a low-β_e plasma. From a technical point of view, our new dispersion relation is obtained by solving the equations in the inner layer in real space, unlike in Porcelli (1991) where the corresponding equations are transformed and solved in Fourier space.

A solution of the dispersion relation (4.7), considered in the regime identified by the assumptions of Table 4.1, is

$$\gamma_u = 2k_y \left(\frac{\rho_s^2}{\pi d_e \lambda} - \frac{\rho_s^{3/2}\sqrt{\rho_s - 2d_e^2\Delta'}}{\pi d_e \lambda} \right), \tag{4.8}$$

and is real for $\rho_s > 2d_e^2\Delta'$.

This new dispersion relation is tested against numerical simulations and compared to the expression (4.3). Just for testing this formula, we also performed additional tests on the Harris-sheet equilibrium (2.155).

The numerical value chosen and indicated for Δ' will always be associated to that of the mode $m = 1$, and we change its value by taking different box lengths along the y direction. The results obtained with the two different equilibria are presented on Figs. 4.2 and 4.3. The agreement between the theoretical and the numerical values appears to be improved by this new formula, when the latter is applied in its regime of validity. Consequently, (4.8) can be seen as an upgrade of the formula (4.3) in the regime of parameters indicated by the Table 4.1.

Figure 4.4 gives a comparison between the theoretical growth rate predicted by Eqs. (4.2), (4.3) and (4.8), and the numerical growth rate γ_N as a function of the wave number k_y. According to these tests, γ_u seems to give a very good prediction for wave numbers $k_y > 1.1$. The discrepancy observed for lower values of k_y comes from the fact that the condition allowing the use of the *constant ψ approximation*, $(\gamma d_e/(k_y\rho_s))\Delta' \ll \rho_s\Delta' \ll 1$, is no longer satisfied for a small wave number. The breakdown of γ_u for $k_y \ll 0.95$ is due to the fact that for $\Delta' > \rho_s/(2d_e^2)$, the solution (4.8) is no longer real.

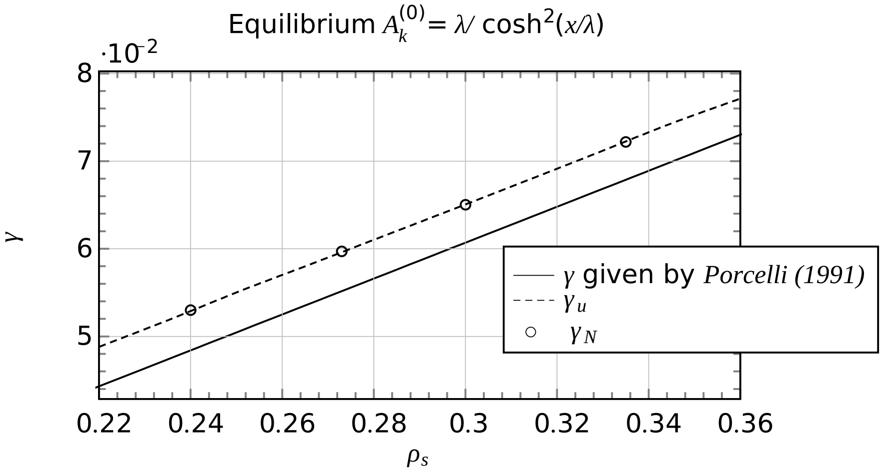

Figure 4.2: Comparison between the analytical growth rate, γ_u, obtained from the new formula (4.8) (dashed line), the analytical growth rate obtained from the formula (4.3) (solid line) and the numerical growth rate γ_N defined in Eq. (5.24) (circles). The parameters are $d_e = 0.1$, $\lambda = 1$, $\Delta' = 0.72$, $m = 1$. The box size is given by $-10\pi < x < 10\pi$, $-0.48\pi < y < 0.48\pi$. The values of the parameters lie in the regime of validity of the new formula (4.8). One can see that, for different values of ρ_s, the correction present in Eq. (4.8) yields a better agreement with the numerical values.

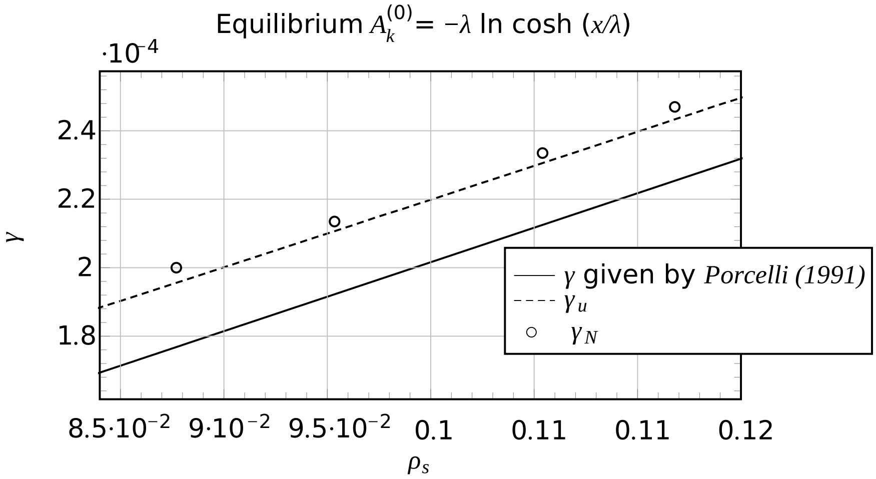

Figure 4.3: This plot is showing additional tests, analogous to those of Fig. 4.2, but with the Harris sheet equilibrium $A_{\|}^{(0)}(x) = -\lambda \ln\cosh(x/\lambda)$, and $\phi^{(0)}(x) = 0$, for which $\Delta^{'} = (2/\lambda)\left(1/(k_y\lambda) - k_y\lambda\right)$ and using the mode $m = 1$. The parameters are $d_e = 0.2$ and $\lambda = 3$. The box size is $-10\pi < x < 10\pi$, $-4\pi < y < 4\pi$. For this case, $\Delta' = 0.38$. For this equilibrium the dispersion relation corresponds to $\gamma_u = k_y\left(\rho_s^2/(\pi d_e\lambda) - \rho_s^{3/2}(\rho_s - 2d_e^2\Delta^{'})^{1/2}/(\pi d_e\lambda)\right)$ and differs from (4.8) by a factor 2 coming from the evaluation of dB_{y0}/dx at the X-point. Symbols are the same as on Fig. 4.2 . Also in this case, the new formula yields a better agreement with the numerical values.

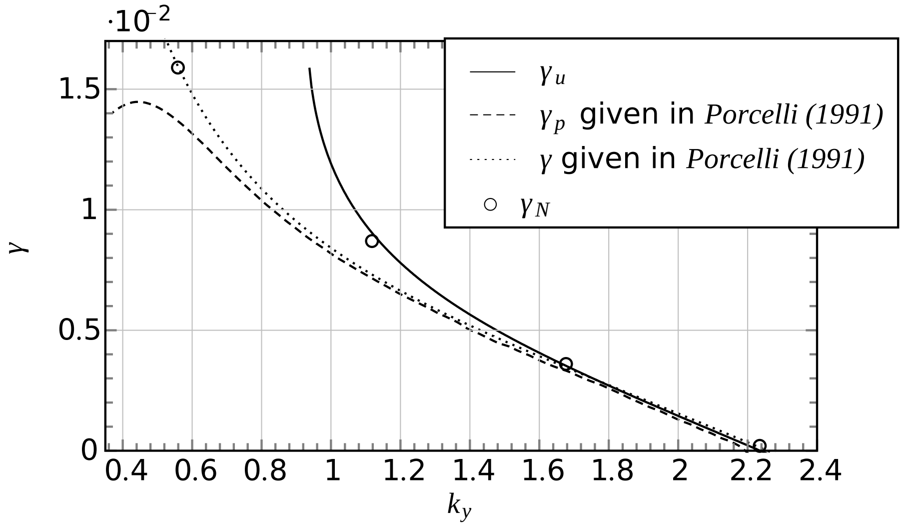

Figure 4.4: Comparison between the theoretical growth rate predicted by Eqs. (4.2), (4.3) and (4.8), and the numerical growth rate γ_N as a function of the wavenumber, $k_y = \pi m/L_y$. The parameters are $d_e = 0.03$, $\rho_s = 0.03$, $\lambda = 1$. The runs were done with the modes $1 \leq m \leq 4$ and $L_y = 1.789\pi$. The corresponding values of the tearing stability parameter lie in the interval $0.005 \leq \Delta' \leq 47.86$. The new formula yields a better agreement with numerical results for large k_y, where the Δ' approximation is better fulfilled. For $k_y < 0.95$ the new formula is no longer valid and the numerical results are better approximated by the formulas (4.2) and (4.3).

4.2 Linear growth rate for finite β_e

We now proceed to a numerical study of the model (2.130) and (2.131), complemented by (2.127), (2.128) and (2.129). The numerical set-ups are the same as those presented in the previous Section, relative to the equilibrium (2.156), but the code accounts now for finite β_e effects. For the linear tests we focus on a weakly unstable regime for which $0 < \Delta' < 1$. The strongly unstable case shows interesting behaviors in the nonlinear phase and will be studied in the Section 4.3. For all the tests, we use $\lambda = 1$.

4.2.1 For a varying mass ratio

In order to isolate the contribution coming from purely varying β_e, we first scan β_e from 10^{-3} to 1 while ρ_s and d_e remain fixed, which is equivalent to considering a different mass ratio for each β_e value. We recall that the parameters are indeed linked by the relations (1.7). We repeat this scan for three different values of d_e. The results are presented in Fig. 4.5 and show that increasing β_e and m_e/m_i stabilize the tearing mode. This is consistent with the results obtained in the gyrokinetic and collisional study of Numata et al. (2011), where β_e and the mass ratio are also varied. Figure 4.5 also shows the competition between the destabilizing effect of the electron inertia and the stabilizing effect of β_e. For this set of parameters, the influence of β_e on the weakly unstable regimes is almost negligible until $\beta_e = 1$. For relatively low values of β_e, the highest growth rate corresponds to that for which the parameter d_e is the largest. We recall that, for $\beta_e \ll 1$, the formulas (4.3) and (4.8) hold. Such formulas, for $d_e \ll 1$, predict that the growth rate increases linearly with d_e. Conversely, when β_e becomes large enough, as appears for $\beta_e > 0.15$, the growth rate for which d_e is the largest, decreases drastically under the effect of the finite ρ_e and of the parallel magnetic perturbations induced by β_e.

Dispersion relation for small FLR effects

Some information about the stabilizing role of β_e can be inferred by taking the small FLR limit of the equation (2.131), which consists in considering the regime of parameters

$$d_e \ll 1, \qquad \rho_s \ll 1, \qquad \frac{d_e}{\rho_s} \ll 1, \qquad \beta_e = O(1), \tag{4.9}$$

and assuming,

$$\nabla_\perp^2 = O(1). \tag{4.10}$$

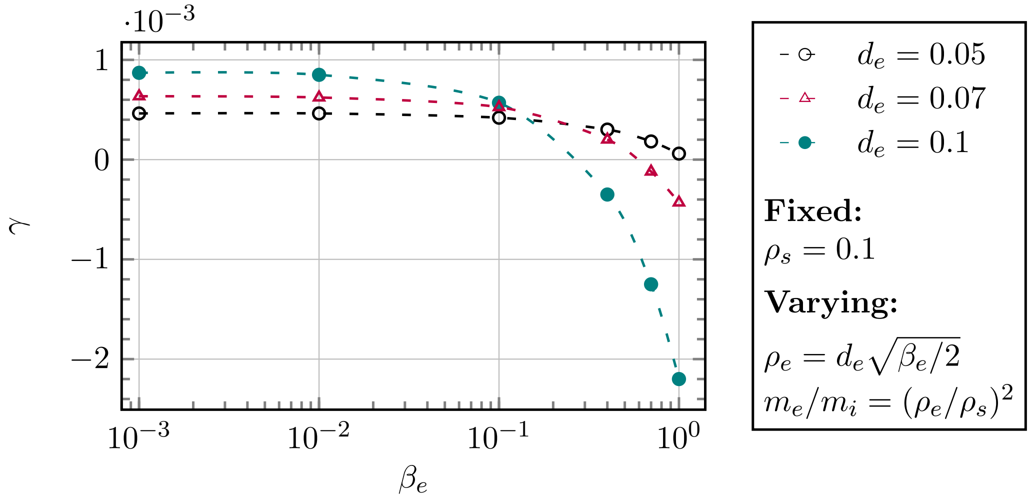

Figure 4.5: Numerical growth rates of the collisionless tearing mode as a function of β_e, for three different values of d_e. The box length along y is such that $-0.45\pi < y < 0.45\pi$, yielding a value of the tearing instability parameter of $\Delta' = 0.067$ for the largest mode in the system. We stand in a very small Δ' regime, close to a marginal stability when $\beta_e < 0.1$. One sees that for higher values of β_e, and depending on the value of d_e, the mode is stabilized.

If we retain the first-order FLR corrections as $d_e, \rho_s \to 0$, the resulting Ohm's law reads

$$\frac{\partial}{\partial t}\left(A_\| + \left(\frac{\beta_e}{4} - 1\right) d_e^2 \nabla_\perp^2 A_\|\right) + \left[\phi, A_\| + \left(\frac{\beta_e}{4} - 1\right) d_e^2 \nabla_\perp^2 A_\|\right] \\ + \rho_s^2 \left(\frac{\beta_e}{2+\beta_e} - 1\right) [\nabla_\perp^2 \phi, A_\|] = 0. \tag{4.11}$$

The new contributions in Eq. (4.11) are those due to finite β_e and are not present in the usual two-field model by Schep et al. (1994). In particular, the contributions proportional to $(\beta_e/4)d_e^2$ come from electron FLR effects and the contribution proportional to $\beta_e \rho_s^2/(2+\beta_e)$ is due to the presence of the finite $B_\|$. In Eq. (4.11), comparing with Eqs. (2.136)-(2.137), it is possible to identify an effective electron skin depth d_e' and an effective sonic Larmor radius ρ_s', given by,

$$\frac{d_e'}{d_e} = \sqrt{1 - \frac{\beta_e}{4}}, \tag{4.12}$$

and

$$\frac{\rho_s'}{\rho_s} = \sqrt{\frac{2}{\beta_e + 2}}, \tag{4.13}$$

respectively. This argument holds for d_e' purely real and consequently for $\beta_e < 4$. Because $d_e' < d_e$, one can infer that the contribution of β_e, at the leading order in the expansion (4.9)-(4.10), reduces the amplitude of the term that breaks the frozen-in condition. For this reason, one could indeed expect a stabilizing role of β_e. Deriving rigorously a dispersion relation for tearing modes from the model (2.130)-(2.129), in the general case with finite β_e, is a very challenging task. In the absence of a rigorous dispersion relation for finite β_e, a rough but readily available approximation can be obtained from the $\beta_e = 0$ dispersion relation (4.8) (or (4.3)), by replacing d_e and ρ_s with the effective parameters d_e' and ρ_s', respectively. This amounts to taking into account the leading-order electron FLR corrections, according to the ordering (4.9)-(4.10), in Ohm's law, while neglecting all the β_e effects in the electron continuity equation. In particular, higher-order derivative terms (coming from the gyroaverage operators, assuming it is possible to identify the multiplication operator for k_x with ∂_x) are neglected, although these can become relevant around the resonant surface and thus influence the growth rate. Using this approximation, it follows immediately that the inclusion of finite-β_e corrections reduces the growth rate, given that $\gamma \propto d_e' \rho_s'$ (if one considers the leading-order relation given by Eq. (4.3)) and that $d_e' < d_e$ and $\rho_s' < \rho_s$. However, the error made with this approximation needs to be checked numerically. We carried out this check by first determining the approximated growth rate in the following way. When replacing d_e and ρ_s by the effective d_e' and ρ_s' in our formula (4.8), valid for small Δ', we obtain the dispersion relation

$$\boxed{\gamma_{appr} = \frac{k_y\left(8\rho_s^2 - (\beta_e+2)\left(\frac{8\rho_s^2}{\beta_e+2}\right)^{3/4}\sqrt{\sqrt{\frac{8\rho_s^2}{\beta_e+2}} + (\beta_e-4)\Delta' d_e^2}\right)}{\pi\sqrt{4-\beta_e}(\beta_e+2)d_e\lambda}. \qquad (4.14)}$$

We tested the dispersion relation (4.14) against small Δ' simulations and the results are shown on Fig. (4.6). By comparing the analytical formula (4.14) (solid black curve) and the numerical results obtained by the gyrofluid code (black circles), we can see that γ_{appr} gives a reasonably good approximation for low β_e values, as expected. The red circles on Fig. (4.6) show the growth rate obtained using, as input in the fluid code, the effective d_e' and ρ_s', that were calculated on the basis of the values $d_e = 0.1$ and $\rho_s = 0.3$ that we used in the gyrofluid code. The numerical and analytical growth rates obtained from the fluid model replacing d_e and ρ_s with the effective parameters, exhibit a behavior qualitatively similar to that of the gyrofluid growth rate. However, a significant quantitative difference emerges as β_e increases. This could be due to the higher electron FLR contributions that are absent in the approximation. From Fig. 5 it emerges that the net effect of such contributions is that of further reducing the growth rate, as the curve obtained from the gyrofluid model always lies below those obtained from the effective fluid model.

4.2.2 For a fixed mass ratio

Varying ρ_s

A further analysis we carried out consists of investigating the effect of β_e on the linear growth rate, but at a fixed mass ratio. In order to keep a constant mass ratio during the scan in β_e, we carried out a study with β_e ranging from 10^{-3} to 2 with ρ_s varying simultaneously. Physically, this might be interpreted as investigating the effect of the variation of the equilibrium electron temperature T_{0e}, supposing that n_0, B_0, m_i, L (and thus the Alfvén frequency, which is the unit of measure of the dimensional growth rate) are fixed. We fix the relation $d_e = \sqrt{m_e/m_i}$ (implying $\rho_s = \sqrt{\beta_e/2}$) and we evaluate the cases $d_e = 0.07$, $d_e = 0.15$, $d_e = 0.1$. Figure 4.7 shows that when β_e and ρ_s are increased simultaneously there seems to be a competition between the destabilizing effect of ρ_s and the stabilizing effect of β_e. Also in this case, the behavior at small β_e, can be interpreted on the basis of the formulas (4.3) and (4.8), predicting an increase of the growth rate with increasing ρ_s. When electron FLR effects come into play at larger β_e, the growth rates decreases. The values chosen for the mass ratio in Fig. 4.7 are not realistic. Such values were chosen to show the dependence on the β_e parameter more clearly. On the other hand, the mass ratio is not taken as a small parameter in

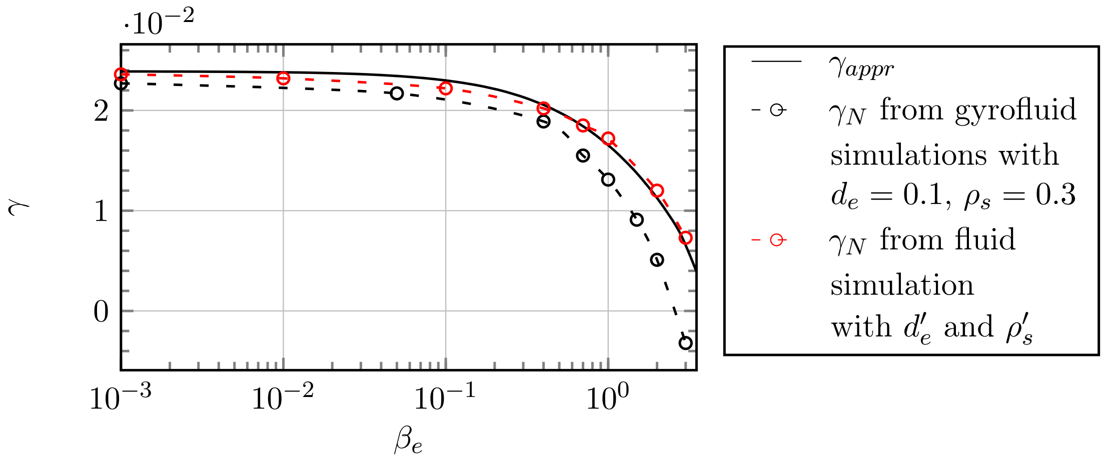

Figure 4.6: Numerical growth rates of the collisionless tearing mode as a function of β_e. The parameters are $d_e = 0.1$, $\rho_s = 0.3$, $\Delta' = 0.59$, $m = 1$, $k_y = 2.12$, $\lambda = 1$. The solid black curve is showing the approximate-β_e dispersion relation (4.14). The black circles are showing the results obtained with the gyrofluid code. The red circles are showing the results obtained with the fluid code, using, instead of d_e and ρ_s, d_e' and ρ_s', given by (4.12)-(4.13).

the derivation of the model, so these values are respecting the validity conditions of the model. In the case of the artificial value of $d_e = \sqrt{m_e/m_i} = 0.15$, the stabilizing effect takes over the destabilizing effect of ρ_s even for $\beta_e < 1$. However, for the case $\sqrt{m_e/m_i} = 0.07$, much closer to a real mass ratio, the effect of ρ_s appears to be dominant. Indeed, decreasing d_e at a fixed β_e amounts to decreasing ρ_e. Thus, for $d_e = 0.07$ the stabilizing effect of the electron FLR terms gets weakened, with respect to the other values of d_e, even at large β_e.

Varying d_e and comments about the $N_i = U_i = 0$ hypothesis

Figure 4.8 shows the variation of the growth rate of the tearing instability as a function of β_e, for a fixed value of $\rho_s = 10\rho_e = 0.3$. Here, the parameter d_e is varied. The obtained results are confirming the scaling of the growth rate as $\beta_e^{-1/2}$ (or, equivalently, as d_e) has been determined with the gyrokinetic study of Numata & Loureiro (2015) and the fluid theory of Fitzpatrick & Porcelli (2007). This shows the capability of the gyrofluid model to reasonably reproduce gyrokinetic results (Numata et al. (2011); Numata & Loureiro (2015)) in a quantitative way, although, in the gyrokinetic study, the ion dynamic is taken into account consistently, which is not the case with our model. Thus, this comparison also allows us to deduce that, at least up to values of $\beta_e \sim 0.8$ and in the linear phase, the simplifying hypothesis of suppressing ion gyrocenter density and parallel velocity fluctuations still permits to obtain predictions in

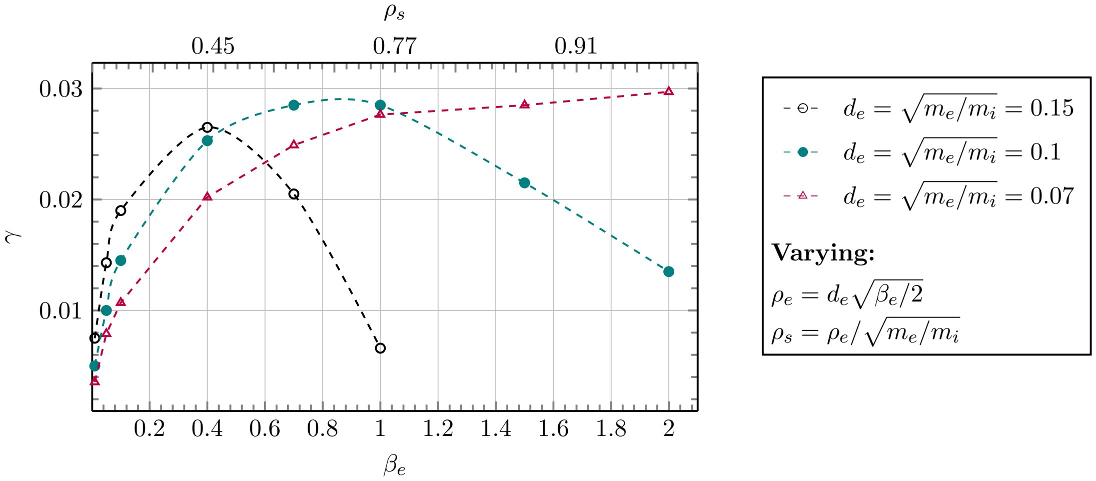

Figure 4.7: Numerical growth rates of the collisionless tearing mode as a function of β_e and ρ_s, for different values of $d_e = \sqrt{m_e/m_i}$. The box size is $-\pi < x < \pi$, $-0.47\pi < y < 0.47\pi$, which leads to $\Delta' = 0.59$.

good agreement with gyrokinetic results.

4.2.3 The hot-ion limit, $\tau_i \longrightarrow +\infty$

In this Chapter we have focused, so far, on the cold-ion limit, but in this Subsection we temporarily deviate from the cold-ion case, to consider the opposite limit, in which $\tau_i \longrightarrow +\infty$. We only carry out the comparison between the cold and hot-ion limits in the linear regime and leave the comparison of the nonlinear evolution for a future work. The hot-ion limit can actually be of greater interest for space plasmas such as the solar wind. When considering the gyrofluid model in the hot-ion limit, the ion gyrocenter density fluctuation and the ion gyrocenter parallel velocity are still neglected, and therefore the evolution equations remain unchanged. Only the assumption (2.124) is taken in the opposed limit, with respect to the cold-ion limit, which has an impact on the development of ion gyroaverage operators. The static relations (2.127) and (2.129) are thus changed to

$$\phi = \frac{\rho_s^2 N_e}{\left(1 - \frac{\beta_e}{2}\right) G_{10e} - G_{10e}^{-1}}, \tag{4.15}$$

$$B_{\parallel} = \frac{\beta_e}{2\rho_s^2}\phi. \tag{4.16}$$

The linear results obtained in the hot-ion limit are compared to the results obtained

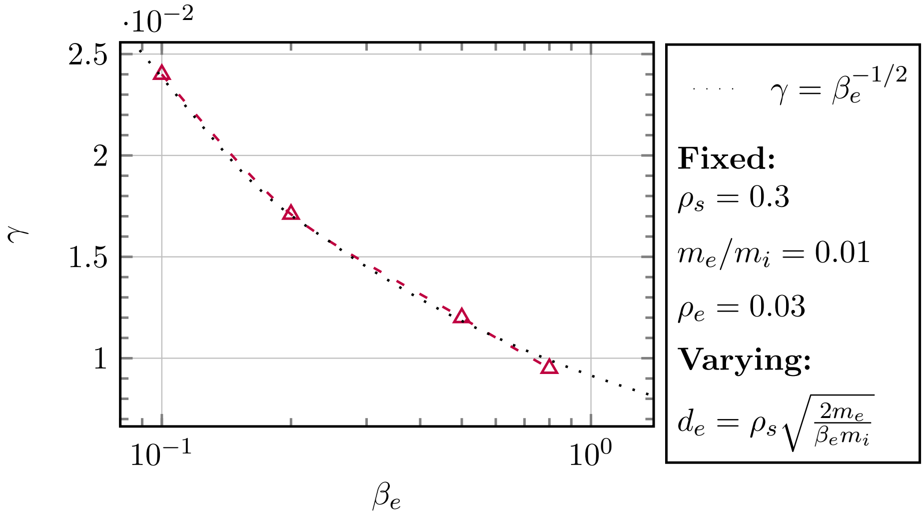

Figure 4.8: The value of d_e for each run increases as $d_e = \sqrt{2m_e/(\beta_e m_i)}\rho_s$. The box size is $-\pi < x < \pi$, $-0.47\pi < y < 0.47\pi$. The numerical values (triangles) are compared with the curve $\gamma = \beta_e^{-1/2}$ (dotted line), which is the scaling predicted by Fitzpatrick & Porcelli (2007) on the basis of a fluid model, and confirmed by gyrokinetic simulations by Numata & Loureiro (2015). The comparison shows that also our gyrofluid model confirms such scaling.

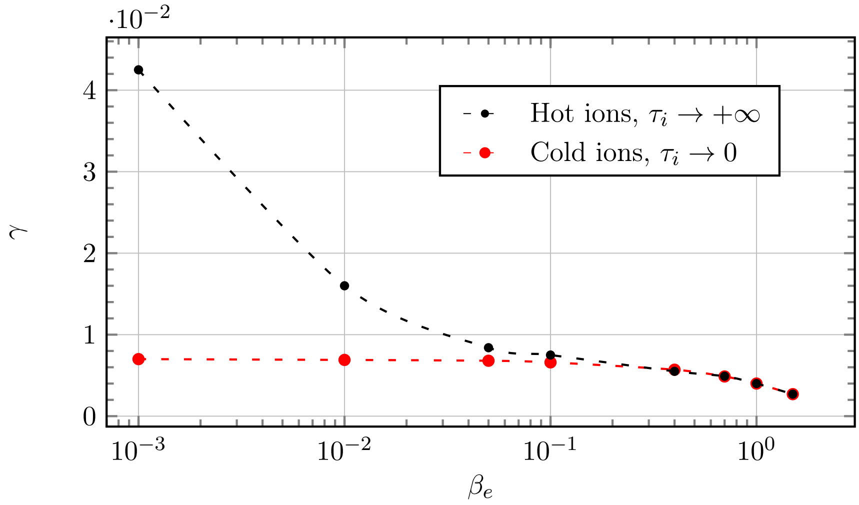

Figure 4.9: Comparison between the linear growth rate obtained in the cold-ion regime and the hot-ion regime. The box size is $-\pi < x < \pi$, $-0.47\pi < y < 0.47\pi$, which leads to $\Delta' = 0.59$.

in the cold-ion regime on Figure 4.9. The parameters are $d_e = 0.1$, $\rho_s = 0.1$. Our results seem to indicate that, for $\beta_e > 0.5$, the growth rate is insensitive to the temperature of the ions, which is in agreement with the results obtained by Numata et al. (2011). Studies have been carried out with arbitrary ratios between the equilibrium ion and electron temperature in the low-β limit, by Porcelli (1991); Grasso et al. (1999), and predict that the growth rate is significantly higher when the temperature of the ion background temperature is higher than that of the electrons. This is indeed what we observe for $\beta_e < 10^{-2}$.

4.3 Nonlinear phase

4.3.1 Identification of a slowdown

To study the impact of a finite β_e on the nonlinear evolution of the magnetic island, we focus on the strongly unstable case, $\Delta' = 14.31$ ($m = 1$), resulting from a box length along y given by $-\pi < y < \pi$. In this case, the mode $m = 2$ has a positive tearing parameter $\Delta'_2 = 1.23$. The higher harmonics are linearly stable. The box along x is chosen to be $-1.5\pi < x < 1.5\pi$ and allows to reach a large island without incurring in boundary effects. We make use of a resolution up to 2880×2880 grid points. The mass ratio will be taken as $m_e/m_i = 0.01$ for the following tests.

The first tests are carried out by making a scan in β_e from $\beta_e = 0.1$ to $\beta_e = 1.5$

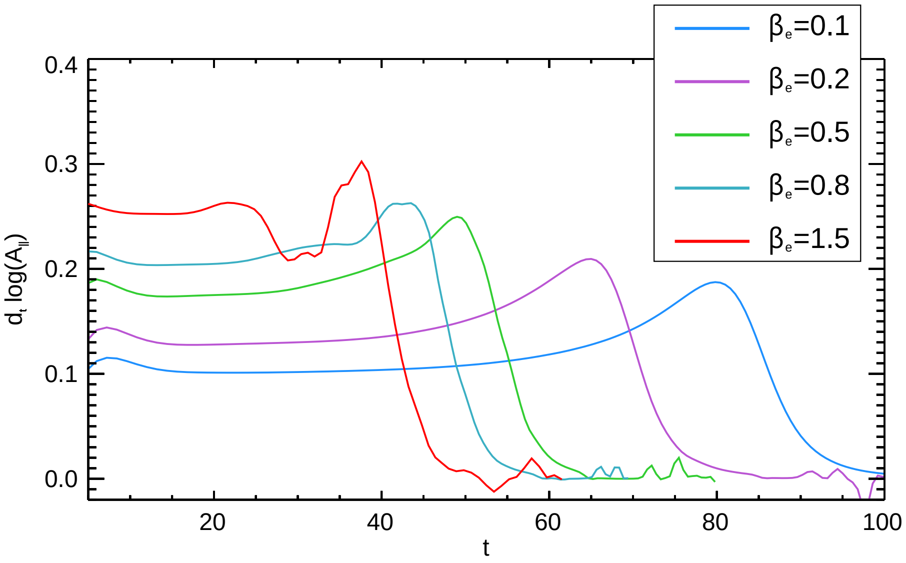

Figure 4.10: Plot of the effective growth rate $\frac{d}{dt}\log\left|A_{\|}^{(1)}\left(\frac{\pi}{2},0,t\right)\right|$, as a function of time. The corresponding values of β_e are shown in the table. The value of the electron skin depth is kept fixed to $d_e = 0.08$, whereas ρ_s is varied (and ranges from 0.17 to 0.69) so to keep the mass ratio fixed to $m_e/m_i = 0.01$. All the growth rates, except for the case $\beta_e = 1.5$ exhibit the same behavior, characterized by linear, faster-than-exponential, and saturation phase. The case $\beta_e = 1.5$ exhibits also a slowdown phase.

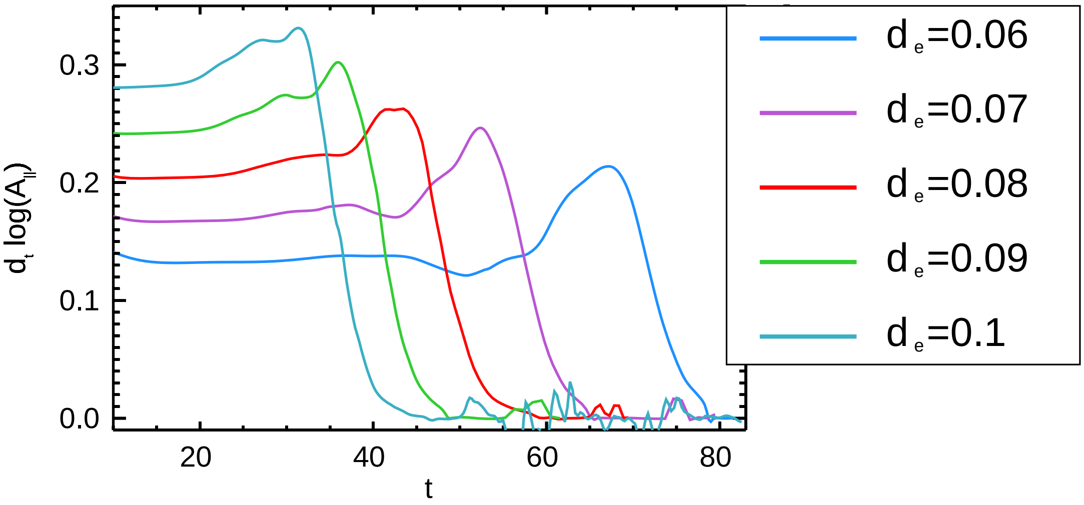

Figure 4.11: Plot of the effective growth rate $\frac{d}{dt}\log\left|A_{\|}^{(1)}\left(\frac{\pi}{2},0,t\right)\right|$, as a function of time. The parameters are $\beta_e = 0.8$, implying $\rho_e = \sqrt{0.4}d_e$ and $\rho_s = 10\sqrt{0.4}d_e$.

while keeping $d_e = 0.08$ and varying ρ_s as $\rho_s = 0.8\sqrt{\beta_e}/\sqrt{2}$. Increasing β_e and ρ_s simultaneously in this way, as stated in Sec. 4.2.2, amounts to varying the electron background temperature T_{0e}. Figure 4.10 shows the evolution in time of the effective growth rate, given by Eq. (5.24), for each simulation. In all these cases, with the exception of $\beta_e = 1.5$, we identify three phases: (1) a linear phase during which the perturbation evolution scales as $\exp(\gamma t)$; (2) a faster-than-exponential phase, which is delayed in the case $\beta_e = 0.1$, given that the linear growth rate is smaller, with respect to the case $\beta_e = 0.8$ for which the instability reaches the nonlinear phase faster; (3) a saturation during which the growth rate drops to 0. The fact that the linear growth rate increases with increasing β_e is related to the fact that ρ_s is also increased for each run. As discussed in the previous Section, the isolated effect of an increasing β_e in the equations actually implies a stabilization of the linear growth rate. In the case $\beta_e = 0.8$, the nonlinear growth shows a slightly different behavior from the cases $\beta_e \leq 0.5$ and exhibits a stall phases, during which the growth rate slows down. This stall phase seems to separate two faster-than-exponential phases. Similar stall phase have been studied in (Comisso et al., 2013), where a finite ion Larmor radius is considered, and appear to be obtained when considering a large ion Larmor radius. For the case $\beta_e = 1.5$, on which we will focus later, this slowdown is enhanced.

We focus now on the case $\beta_e = 0.8$ in order to consider more in detail the observed slowdown. We scan the values of d_e from 0.06 to 0.1, and with ρ_s and ρ_e varying accordingly, given that $\rho_s = 10\rho_e = 10\sqrt{0.4}d_e \approx 6.32 d_e$. The results are shown on Fig. 4.11. These curves are compared for a fixed time unit (fixed v_A), while keeping β_e and the mass ratio constant, which corresponds to varying $B_0 \sim n_0^{1/2}$ while keeping the elec-

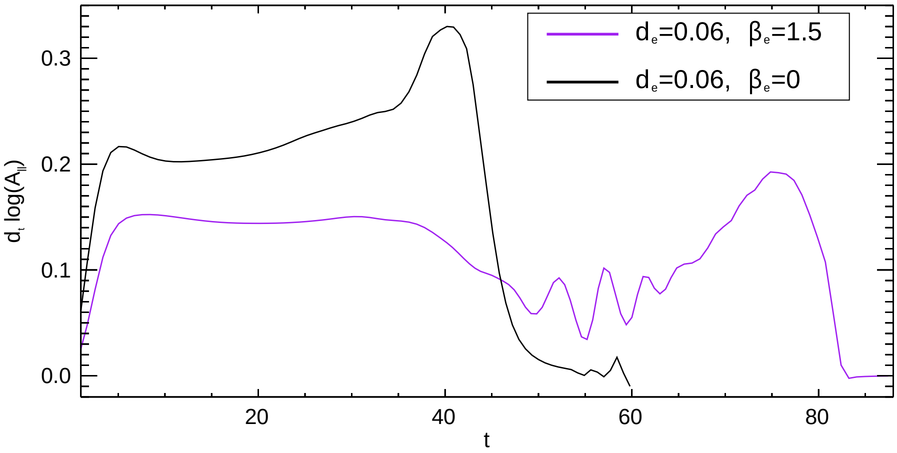

Figure 4.12: Plot of the effective growth rate $\frac{d}{dt}\log\left|A_\parallel^{(1)}\left(\frac{\pi}{2},0,t\right)\right|$, for the cases $\beta_e = 0$ (black curve) and $\beta_e = 1.5$ (purple curve). The other parameters are $\rho_s = 0.519$ and $d_e = 0.06$.

tron temperature T_{0e} fixed. For the case of $d_e = 0.06$, which corresponds to $\rho_s \sim 0.37$, we observe the slowdown at the end of the linear phase, followed by the faster-than-exponential phase. On the other hand, in the case of $d_e = 0.1$, for which $\rho_s \sim 0.63$, the slowdown appears at a later stage of the evolution process and seems to interrupt the faster-than-exponential phase by introducing a stall phase. We conclude that, the effects of β_e, and consequently the effects of electron gyrations, causes the appearance of a slowing down phase of the growth of the island during the nonlinear evolution. The larger β_e, the more distinguishable this slowing phase will be. For a fixed values of β_e and m_e/m_i, the fact of increasing d_e and ρ_s, and consequently increasing the radius of gyration of the electrons, will delay the appearance of this slowing phase.

The last test consists in studying an extreme case for which the slowing down phase is accentuated, which corresponds to the case of $d_e = 0.06$, $\rho_s = 0.519$, $\beta_e = 1.5$. We also perform the simulation for $\beta_e = 0$, and the same values for d_e and ρ_s, using a code that solves the fluid equations (2.136) - (2.137). Figure 4.12 shows the overplot of the evolution of the growth rate for both simulation as a function of time. The slowing down phase is followed by an oscillation of the nonlinear growth rate. This oscillation was obtained in other tests for which $\beta_e = 1.5$.

In order to understand in detail what causes this slowing down and these oscillations of the island growth that we observe between $t = 43$ and $t = 65$, we compared all the fields for the cases $\beta_e = 0$ and $\beta_e = 1.5$ of Fig. 4.12. A remarkable difference between these two regimes concerns the evolution of the inflow and outflow perpendicular velocities. In the fluid case, the latter is given by $\mathbf{u}_\perp = \hat{z} \times \nabla\phi$. In the gyrofluid case, in addition to electron FLR effects, a nonlinear grad-B drift, due to the

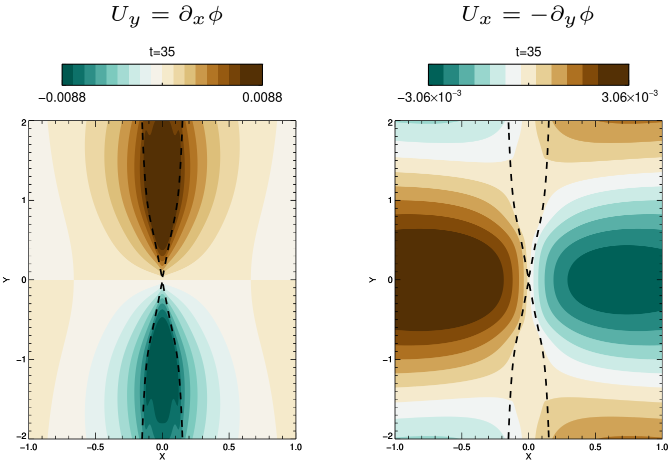

Figure 4.13: Contour plot of the perpendicular velocity component for $\beta_e = 0$ at $t = 35$. *Left:* u_y. *Right:* u_x. The parameters are the same as those on Fig. 4.12. The magnetic island edges are shown by the dotted lines. Not the entire domain is shown.

non-uniformity of the parallel magnetic field, is affecting the perpendicular velocity given by $\mathbf{u}_\perp = \hat{z} \times \nabla(G_{10_e}\phi - \rho_s^2 2G_{20_e}B_\parallel)$. Fig. 4.13 shows the contour of the components u_x and u_y of the advecting perpendicular velocity for $\beta_e = 0$. These contours do not show the entire box so that we focus on the island region drawn by the dotted lines. As expected, the contour of u_y shows an outflow leaving the X-point and u_x shows an inflow in the direction of the X-point.

Figure 4.14 shows u_x and u_y, for $\beta_e = 1.5$, at two different times . For a better comparison we also show the part of the perpendicular velocity only induced by the electrostatic potential $\hat{z} \times \nabla G_{10_e}\phi$ on Fig. 4.15 to identify the role of $G_{10_e}\phi$ and show that its behavior in the case $\beta_e = 1.5$ is similar to that of the case $\beta_e = 0$. The first time shown in Fig. 4.14 corresponds to the beginning of the slow down of the island growth. We observe that, close to the reconnection region, there is a small region where the velocity changes sign, with respect to the standard $\beta_e = 0$ case. This inversion is more visible for u_y, where, inside the island, the fluid velocity is dominated by $B_\parallel$. We can conclude that $G_{10_e}\phi \leq \rho_s^2 2G_{20_e}B_\parallel$ in the reconnected region. Consequently, the slowing down of the island growth can be explained by the fact that the advection velocity contains an additional grad-B drift due to the presence of the magnetic perturbation along the guide field. This effect decelerates the convergence of the field lines towards the reconnection region, where their evolution will be decoupled from that of the fluid. At the time $t = 66$, when the island begins to grow faster-than-exponentially, the region where $G_{10_e}\phi \leq \rho_s^2 2G_{20_e}B_\parallel$ shrinks and the advection towards the X-point becomes much more effective, allowing the explosive growth.

We now focus on the behavior of u_y during the small oscillations of the growth rate,

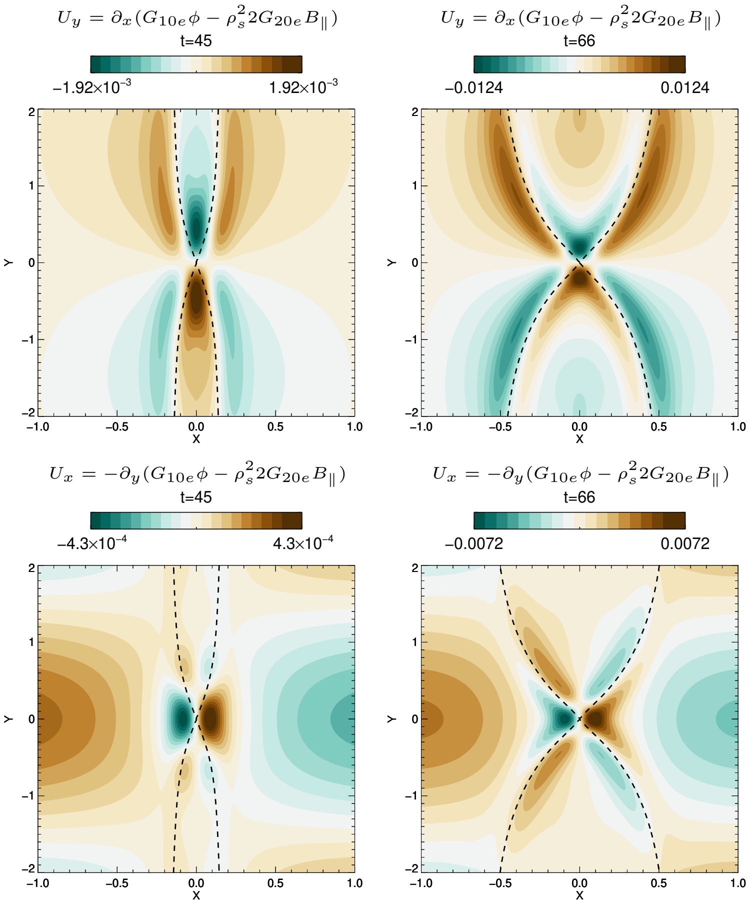

Figure 4.14: *Top left and right:* u_y. *Bottom left and right:* u_x. For all these contours we used $\beta_e = 1.5$ and the other parameters are the same as those on the Fig. 4.12. The magnetic island edges are shown by the dotted lines. Not the entire domain is shown and $t = 45$.

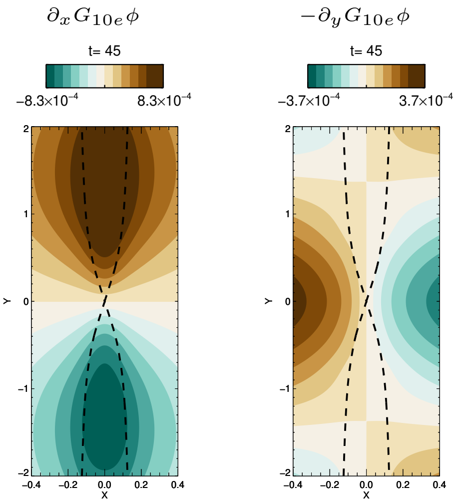

Figure 4.15: Contour plot of the velocity components of $\hat{z} \times \nabla G_{10_e}\phi$, at t=45. This corresponds to the case $\beta_e = 1.5$ and the other parameters are the same as those on the Fig. 4.12. The magnetic island edges are shown by the dotted lines. Not the entire domain is shown and $t = 45$.

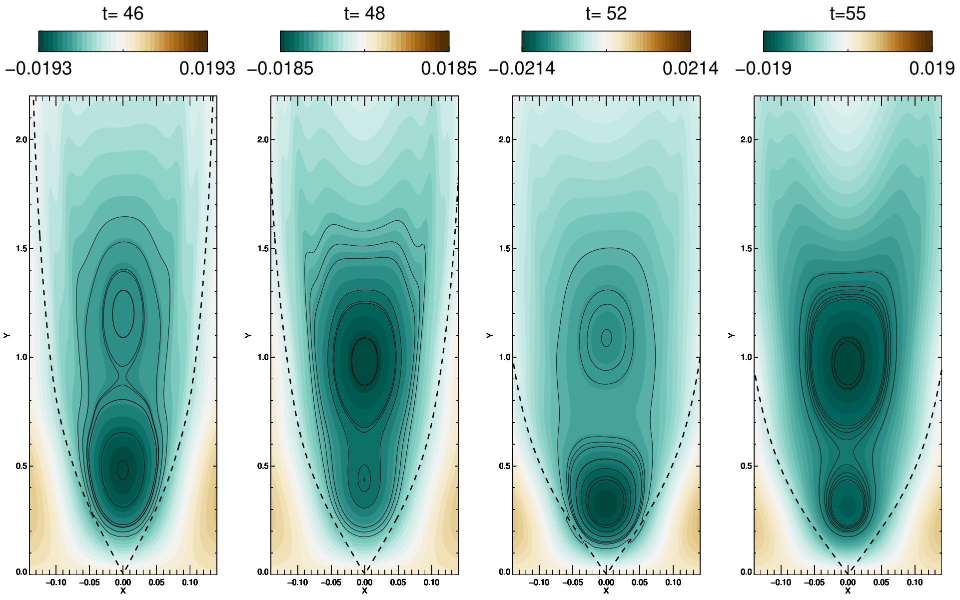

Figure 4.16: Contour plot of u_y showing the upper part of the domain for $\beta_e = 1.5$. The parameters are the same as those on Fig. 4.12. The magnetic island edges are shown by the dotted lines. u_y is negative inside the island and the cell structures indicate the regions where the flow amplitude is greater. The situations where the highest (in absolute value) peak is closer to the X-point ($t = 46$ and $t = 52$) correspond to maxima of the growth rate. Minima of the growth rate occur when the highest peak is far from the X-point ($t = 48$ and $t = 55$).

visible on Fig. 4.12. Figure 4.16 shows a contour of u_y in the upper part of the domain, between $t = 46$ and $t = 55$. The cell structures indicate two negative peaks. We recall that, in the case of $\beta_e = 0$, we would observe a single positive peak. These peaks are growing at the center of the island and will follow each other while moving toward the X-point. The acceleration or deceleration of the island growth depends on the position (in absolute value) of the highest peak. When the highest peak is closer to the X-point, the reconnection rate reaches a maximum ($t = 46$ or $t = 52$). This peak will then decrease while the other one, farther from the X-point, will grow ($t = 48$ or $t = 55$). During this part of the cycle, the growth rate reaches a minimum. We interpret this intermittent flow, generated by the presence of $B_\parallel$, as the mechanism responsible for the accelerations and decelerations of the island growth.

4.3.2 Energy considerations

The time variations of the different components of the energy for the cases $\beta_e = 0$ and $\beta_e = 1.5$, whose rate of growth is shown on Fig. 4.12, are shown on Fig. 4.17. The variations are defined as

$$\frac{1}{2}\int \frac{(\xi(x,y,t) - \xi(x,y,0))}{H(0)} \mathrm{d}x^2 \tag{4.17}$$

where the function ξ can be replaced by the different contributions of the Hamiltonian (2.143). In terms of the gyrofluid variables and in the presence of FLR effects, it is not obvious to identify the physical meaning of all the contributions to the energy. Here, we use the terminology adopted in Tassi et al. (2018) and which refers to the fluid limit $\beta_e = 0$. The different contributions associated to the colors of the curves of the Fig. 4.17 are:

- the magnetic energy, E_{mag}, for which $\xi = -U_e G_{10_e} A_\parallel$, and which reduces to $|\nabla_\perp A_\parallel|^2$ in the fluid case (blue curves),
- the parallel electron kinetic energy, E_{ke}, for which $\xi = d_e^2 U_e^2$, and which reduces to $d_e^2(\nabla_\perp^2 A_\parallel)^2$ in the fluid case (green curve),
- the energy due to the fluctuation of the electron density, E_{pe}, for which $\xi = \rho_s^2 N_e^2$, and which reduces to $\rho_s^2(\nabla_\perp^2\phi)^2$ in the fluid case (purple curve),
- the perpendicular electrostatic energy of the electrons combined with the energy of the parallel magnetic perturbations, E_{kp}, for which $\xi = -(G_{10_e}\phi - \rho_s^2 2G_{20_e} B_\parallel)N_e$, and which reduces to $|\nabla_\perp\phi|^2$ in the fluid case (red curve).

We consider the simulation as being reliable until the time at which the percentage of the total energy that gets dissipated numerically (black curve) reaches 1%.

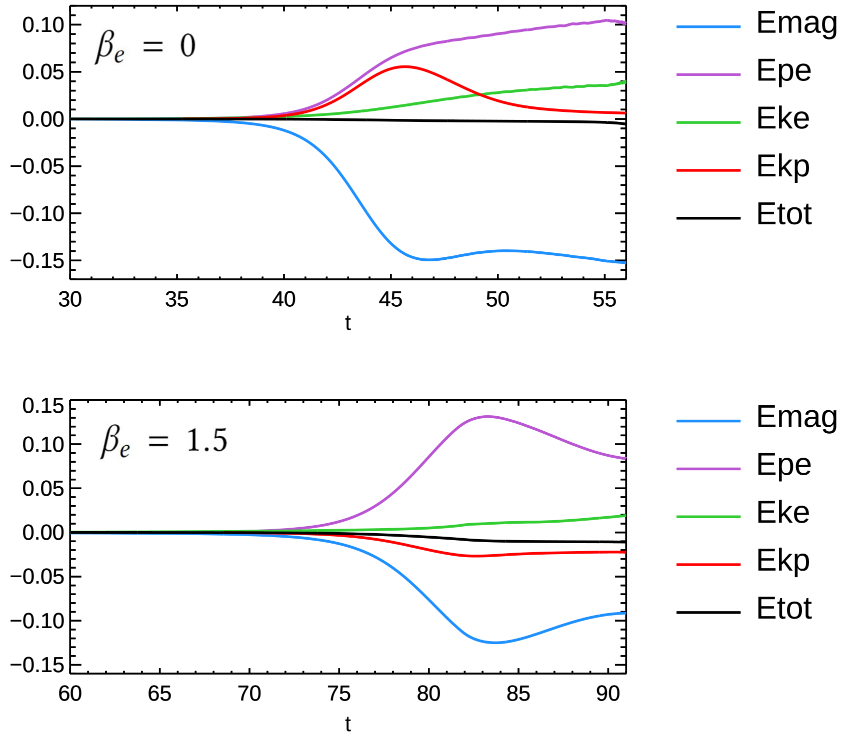

Figure 4.17: Time evolution of the energy variations. *Top:* $\beta_e = 0$. *Bottom:* $\beta_e = 1.5$. The parameters are $d_e = 0.06$, $\rho_s = 0.519$ and their corresponding growth rate is shown on Fig. 4.12.

By comparing the two simulations, one can see that there appears to be a comparable amount of magnetic energy being converted. The remarkable difference is the evolution of the component that combines the electrostatic energy and the energy of the parallel magnetic perturbations, E_{kp}, which, in the case $\beta_e = 1.5$, also seems to be converted into electron thermal energy (E_{pe}), resulting in an increase in this component.

We also carried out a test with $\beta_e = 1.5$ by artificially removing the parallel magnetic perturbation $B_{\|}$ from the code, so that it does not appearing in the expression for E_{kp}. It appeared first that the presence of $B_{\|}$ has a stabilizing effect on the tearing mode, and secondly, the energy component E_{kp} was slightly increasing instead of decreasing. This leads us to conclude that the energy related to the parallel magnetic perturbations is in fact the decreasing component that seems to be converted into electron thermal energy E_{pe}.

4.4 Conclusion

In this Chapter, we have attempted to provide an overview of the impact of finite electron plasmas β effects on the tearing instability in non-collisional plasma with cold ions and a strong guide field. Adopting a gyrofluid model, we have studied the effects of electron gyration and of a parallel magnetic perturbation.

Our main results are the following. First, when increasing β_e and ρ_s while keeping d_e and the mass ratio fixed, the evolution of the reconnection growth rate seems to be dominated by the destabilizing effect of ρ_s, up to a certain threshold where the effects of ρ_e become important and the growth rate diminishes (Fig. 4.7). This can also be interpreted as fixing the background density, n_0, the ion mass (so that d_e is fixed) and the guide field amplitude B_0, while increasing the electron temperature T_{0e}. In the case of a small Δ' regime, a high β_e can eventually stabilize the tearing mode and prevents reconnection from occurring.

Secondly, in the nonlinear regime of the case $\rho_s \gg d_e$ with $m_e/m_i \ll \beta_e \ll 1$, (which is referred to as being the fluid regime in this Chapter), we retrieved the well-know collisionless faster-than-exponential growth which leads to an explosive growth of the magnetic island. However, when we increase β_e, this explosive paradigm is modified with the appearance of a slowdown phase preceding the explosive growth. This slowing down is induced by the inclusion of a nonlinear grad B drift that becomes important for finite β_e. This drift creates an intermittent velocity opposed to the velocity induced by the electrostatic potential and prevents the convergence of the field lines towards the X point.

The results obtained with our gyrofluid model are in agreement with results obtained by gyrokinetic studies (Numata et al. (2011); Numata & Loureiro (2015)). They also complement some two-fluid studies where a consistent accounting for β_e effects, including both electron FLR and parallel magnetic perturbations were neglected (Schep et al. (1994); Grasso et al. (1999); Del Sarto et al. (2006); Fitzpatrick & Porcelli (2007)).

5 Investigation of the plasmoid instability

In the development of the tearing process, after the saturation of the unstable dominant mode ($m = 1$), eventually a thinning current sheet located at the X-point of the initial tearing configuration will form (middle panel of Fig. 5.1). In this evolving current sheet, tearing-mode-like perturbations can develop to form magnetic islands referred to as plasmoids when they enter their nonlinear phase (right panel of Fig. 5.1). This instability is commonly called the *plasmoid instability* (Biskamp (1986); Loureiro et al. (2005); Ji & Daughton (2011); Comisso et al. (2016)).

The transition between the different regimes of current sheets reconnecting via a plasmoid instability driven by plasma resistivity has been investigated in the past, and the present understanding of reconnection has been summarized in the form of parameter space diagrams (Ji & Daughton (2011); Daughton & Roytershteyn (2012); Huang & Bhattacharjee (2013); Karimabadi & Lazarian (2013); Comisso et al. (2015b); Le et al. (2015); Loureiro & Uzdensky (2015); Bhat & Loureiro (2018)). An example of such a diagram is shown on Fig. 5.2, taken from Ji & Daughton (2011). For building this 2D diagram, two key parameters were identified: one is the Lundquist number S, the second one, denoted as λ, is the system length normalized by the relevant kinetic scale of the system. This scale will be d_i in the absence of strong guide field, and ρ_s in the presence of a strong guide field (Ji & Daughton (2011)).

On Fig. 5.2, various regimes are shown. Biskamp (1986) predicted that, for $\rho_i, \rho_s \ll L$, the Sweet-Parker current sheet becomes plasmoid unstable when $S > 10^4$ (green line). This threshold provides a diffusion regions aspect ratio of $L_{\text{cs}}/\delta_{\text{cs}} \approx S^{1/2} \sim 100$, corresponding to a dimensional reconnection rate of $R_{\text{rec}} \sim 0.01 v_A B_{\text{up}}$. Several studies, like Bhattacharjee et al. (2009); Huang & Bhattacharjee (2010); Uzdensky et al. (2010); Loureiro et al. (2012), confirmed this value for the resistive reconnection rate in this plasmoid regime.

Between the green and black lines, in the hybrid regime, the reconnection is faster, but not by a large amount. No observations or laboratory experiments allowed, for now, to rigorously probe this region, although the new FLARE experiment (Sec 1.2.2) should be able to investigate the angle of this parameter space region.

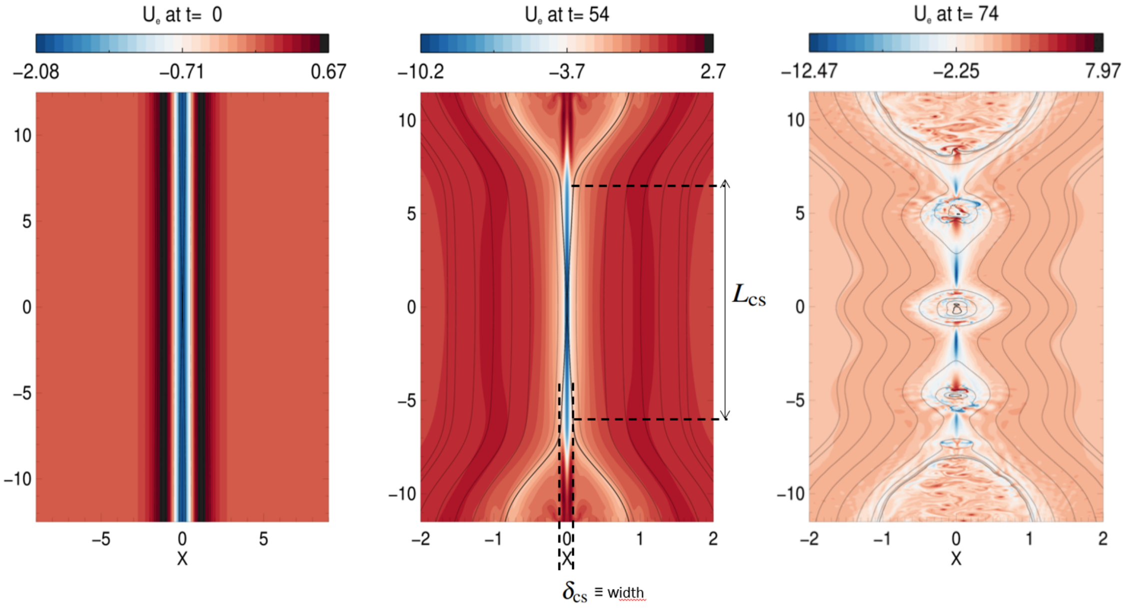

Figure 5.1: Simulation performed by solving the model (2.136) - (2.137) showing the parallel electron velocity with isolines of the magnetic potential. *From left to right*: the initial current sheet equilibrium, the evolving thinning current sheet after the saturation of the tearing instability and just before the plasmoid onset, the plasmoid formation. The dashed lines are drawn to help identified what is called the width and the length δ_{cs} and L_{cs}.

The extension of the resistive reconnection regime with the inclusion of the ion dynamics associated with the ion-sound Larmor radius, ρ_s, or the ion-inertial length, d_i, complicates the picture since it enlarged the study to a broader parameter space, but also suggested that plasmoids are fundamental features of reconnecting current sheets, regardless the value of the Lundquist number (Ji & Daughton (2011); Daughton & Roytershteyn (2012)). The ”Multiple X line collisionless” region of Fig. 5.1 includes plasmas such as those of the magnetosphere and the solar wind, and was also probed by, for instance, PIC simulations in Daughton et al. (2006) and Drake et al. (2006). The vertical orange line labelled λ_c is an empirical delimitation that follows from the PIC simulations performed in Daughton et al. (2006), indicating that simulations of collisionless reconnection with $L_{\mathrm{cs}}/\rho_s > 50$ tend to exhibit multiple plasmoids, while those with $L_{\mathrm{cs}}/\rho_s < 50$ tend to show a single X-point with no plasmoids.

These studies were generally performed either by fluid models with finite resistivity, or needed very large kinetic simulations, which limits the accessible parameter range. Moreover, in contrast with the body of work that has investigated the marginal stability of reconnecting current sheets where reconnection is driven by plasma resistivity, the collisionless regime has just been relatively little studied, and no instability threshold was clearly identified. Yet, we believe this study might be useful to support observational and experimental results in collisionless plasmas. For instance, as we

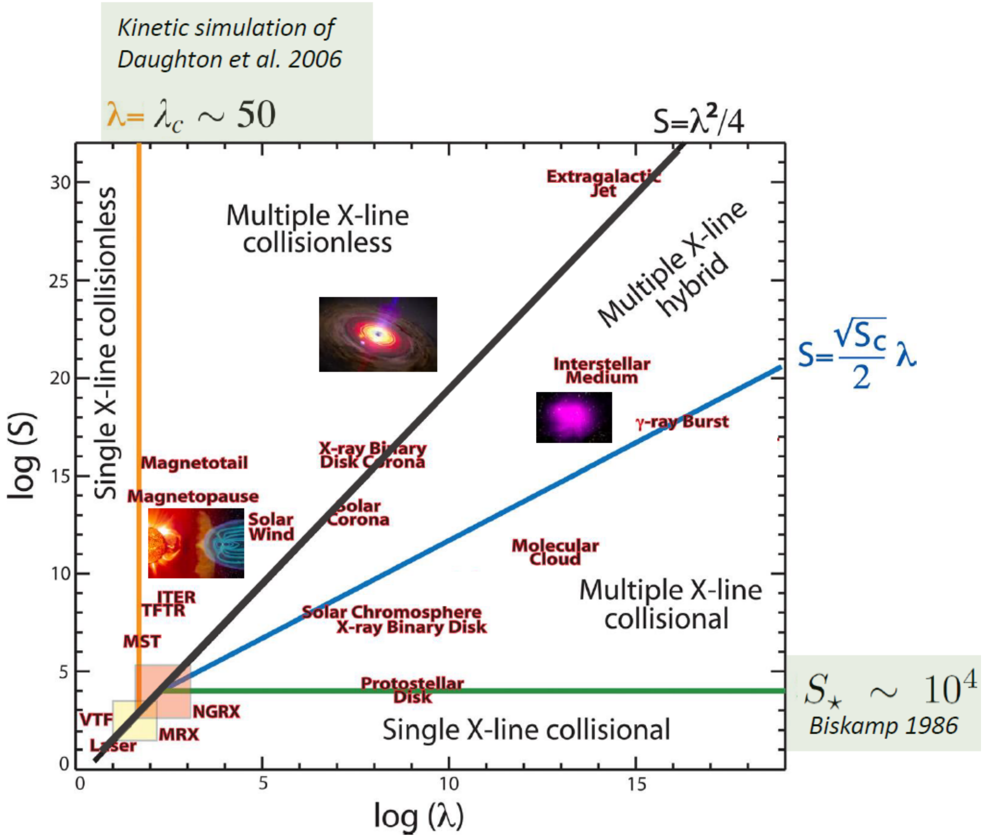

Figure 5.2: Theoretical phase diagram indicating different regimes of reconnection where multiple X-lines separated by plasmoids are expected for both collisional and collisionless reconnection as a function of the Lundquist number and the normalized system size. In the case of strong guide field, the parameter λ, on this diagram, corresponds to $\lambda = L/\rho_s$. *Credit: Taken and adapted from Ji & Daughton (2011).*

already mentioned, recent observations revealed many reconnection onsets driven by electrons, in the presence of a strong guide field, close to the dayside magnetopause and magnetosheath Burch et al. (2016); Phan et al. (2018). Moreover, in Phan et al. (2018), current sheets having a thickness of the order of the electron inertial length were identified. A study by Olson et al. (2016) also gave direct experimental proof of plasmoid formation at the X-point and at the electron scale in a regime where no plasmoids were predicted by the theory.

In this Chapter we carry out a detailed study of collisionless plasmoid instability, in the case of a strong guide field. We first make use of the fluid model (2.136) - (2.137). We analyze the geometry characterizing the reconnecting current sheet, and what promotes its elongation. Once the reconnecting current sheet is formed, we identify the regimes for which it is plasmoid unstable. For $\beta_e \rightarrow 0$, a new phase space diagram spanned by the parameters L_{cs}/d_e and L_{cs}/ρ_s is presented, in order to identify the collisionless plasmoid instability regime. In the second part of this Chapter we use the gyrofluid model (2.130) - (2.131) to investigate the effect of β_e on the plasmoid instability. The gyrofluid results are then compared with collisionless gyrokinetic simulations.

The Chapter is organized as follow. In Sec. 5.1, we present some numerical results and a theory for determining the plasmoid regimes by investigating the phase space described by the two kinetic scales d_e and ρ_s, compared to the current sheet length L_{cs}. In Sec. 5.2, we include a finite β_e and compare the plasmoid simulations of the gyrofluid code with results obtained with a gyrokinetic code.

In this Chapter, some parts of the text and figures also appear in Granier et al. (2022a)

5.1 Fluid investigation, $\beta_e = 0$

5.1.1 Numerical results

In this Section, in order to analyze the marginal stability conditions of the plasmoid instability in the collisionless regime, we performed a large number (~ 30) of numerical simulations of the system of Eqs. (2.136)-(2.137). We consider a number of grid points up to 2000 × 2400. As in the previous Chapter, We assume an equilibrium given by (2.156), (i.e. $A_{\parallel}^{(0)}(x) = \lambda/\cosh^2(x/\lambda)$). We recall that the tearing stability parameter for this equilibrium is

$$\Delta'_{\text{box}} = 2\frac{\left(5-\lambda^2 k_y^2\right)\left(\lambda^2 k_y^2+3\right)}{\lambda^3 k_y^2(\lambda^2 k_y^2+4)^{1/2}}. \tag{5.1}$$

This equilibrium is tearing unstable if $\Delta'_{\text{box}} > 0$, thus for a wavenumber $k_y = \pi m/L_y < \sqrt{5}/\lambda$. In this Chapter we make use of the notation Δ'_{box} to indicate Δ' for the initial equilibrium, in order to distinguish it from the effective Δ' of the secondary current sheet, which will be denoted as Δ'_{cs}. We will always refer to Δ'_{box} as being associated to the mode $m = 1$, and we change its value by taking different box lengths along

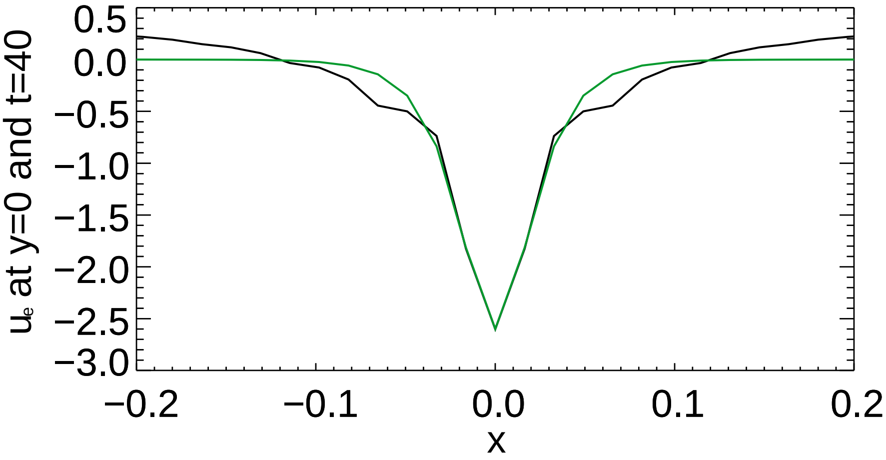

Figure 5.3: In black: profile of the numerical solution (u_e) along x just before the plasmoid onset. The initial parameters for this simulations are $d_e = 0.085$, $\rho_s = 0.3$, $\Delta'_{\text{box}} = 14.5$. In green: fit made by the function $u_{\text{ecs}}^{(0)}(x) = -2.6/\cosh(33.33x)^2$, generated by the magnetic flux $A_{\text{cs}}^{(0)}(x) = -A_{\text{cs}}^{eq} a^2 \ln\cosh(x/a)$, with $A_{\text{cs}}^{eq} = 2.6$ and a half width $a = 0.03$.

the y direction. With this set up, one or several tearing modes are initially unstable. The dominant mode ($m = 1$) generates two magnetic islands separated by the X-point. During the nonlinear phase, a slowly thinning current sheet forms self-consistently at the X-point location (as shown on Fig. 5.1). This secondary current sheet evolves until reaching a width and length, denoted δ_{cs} and L_{cs}, and these quantities are decisive for the formation of plasmoids. If plasmoids emerge because tearing mode have grown, this means that a $\Delta'_{\text{cs}} > 0$ has been approached, where Δ'_{cs} is the tearing parameter of the secondary current sheet. Just before the plasmoid onset, the profile of the secondary current sheet can be well fitted by that of a Harris current sheet of a certain dimension, i.e. by a parallel current generated by a parallel magnetic potential given by $A_{\text{cs}}^{(0)}(x) = -A_{\text{cs}}^{eq} a^2 \ln\cosh(x/a)$, with $a = \delta_{\text{cs}}/2$ the half width measured from the numerical data. The parameter A_{cs}^{eq} is an amplitude factor corresponding to the value of u_e evaluated at the X-point. Figure 5.3 shows the comparison between the profile of a numerical solution u_e and the parallel electron current of a Harris sheet, $u_{\text{ecs}}^{(0)} = \partial_x^2 A_{\text{cs}}^{(0)}$, with $A_{\text{cs}}^{eq} = 2.6$ and a half width $a = 0.03$.

In the following, we characterize this reconnecting current sheet according to the initial parameters d_e, ρ_s, and Δ'_{box}. Specifically, we measured the length and the width of the current sheet at a time t just before the plasmoid onset. Below we describe how each quantity is measured. To illustrate better what each quantity represents, a scheme on which the lengths are represented by arrows is shown on Fig. 5.4. For this Figure, we took the example of the most marginally unstable plasmoid case, which is also the one having the smallest plasmoid.

- We define the measure $L_{\rm cs}$, such that, taking the variation from the lowest current position $u_e|_X$ (u_e evaluated at the X-point), the standard deviation of the current distribution from $y = 0$ to $y = L_{\rm cs}/2$ equals unity, i.e.

$$\sqrt{\frac{\sum_{i=1}^{N}\left[u_e|_X - u_e(0, i\Delta y, t)\right]^2}{N}} = 1, \tag{5.2}$$

  where Δy is the distance between two grid-points along y and N indicates the number of points from $y = 0$ to $y = L_{\rm cs}/2$. A profile of u_e along y is visible on Fig. 5.4a. In formula 5.2, the value unity does not come from a mathematical result, but was identified to provide a good measurement of the flat part of the profile of u_e, while also taking into account a slight deviation from this flat part. Given that the deviation becomes more and more important as we approach the end of the current sheet, considering the value 1, 2 or 3 doesn't change significantly the measured $L_{\rm cs}$. Formula 5.2 allows to apply a single consistent method for all the simulations, while taking into account the reduction of the current intensity along the layer.

- Once $L_{\rm cs}$ is identified, the half width of the current sheet corresponds to the distance, along x, between $u_e|_X$ and the position where the current reaches the value $u_e(\delta_{\rm cs}/2, 0) = u_e(0, L_{\rm cs}/2)$ (Fig. 5.4 b).

We also measure the width and length of the outflow velocity channel coming out from the end of the current sheet.

- The length $L_{\rm outf}$ corresponds to the distance between the upward and downward peaks in the distribution of $u_y = \partial_x\phi$. (Fig. 5.4 c).

- The width $\delta_{\rm outf}$ is also measured with the standard deviation method, but measuring the deviation from the value $u_y(0, L_{\rm outf}/2)$ along x (Fig. 5.4 c).

Finally, the aspect ratios $A_{\rm cs} = L_{\rm cs}/\delta_{\rm cs}$ and $A_{\rm outf} = L_{\rm outf}/\delta_{\rm outf}$ are also reported.

We first focus on the limit $\rho_s = 0$, for d_e increasing and $\Delta'_{\rm box} = 60$ shown on Fig. 5.5. On the top panel, we see that, although $\delta_{\rm cs}$ is found to be always smaller than d_e, we have, in this limit

$$\delta_{\rm cs} \propto d_e, \tag{5.3}$$

as discussed in Ottaviani & Porcelli (1993), and also confirmed in several following works. To better show the geometry, the colored contour maps of u_e with superimposed contour lines of $A_\parallel$ in black, are shown for certain cases on Fig. 5.5 as well as on Fig. 5.6. For low values of d_e, an intense and uniform current density allows the parallel alignment of a high density of magnetic-field lines (see color map of u_e for

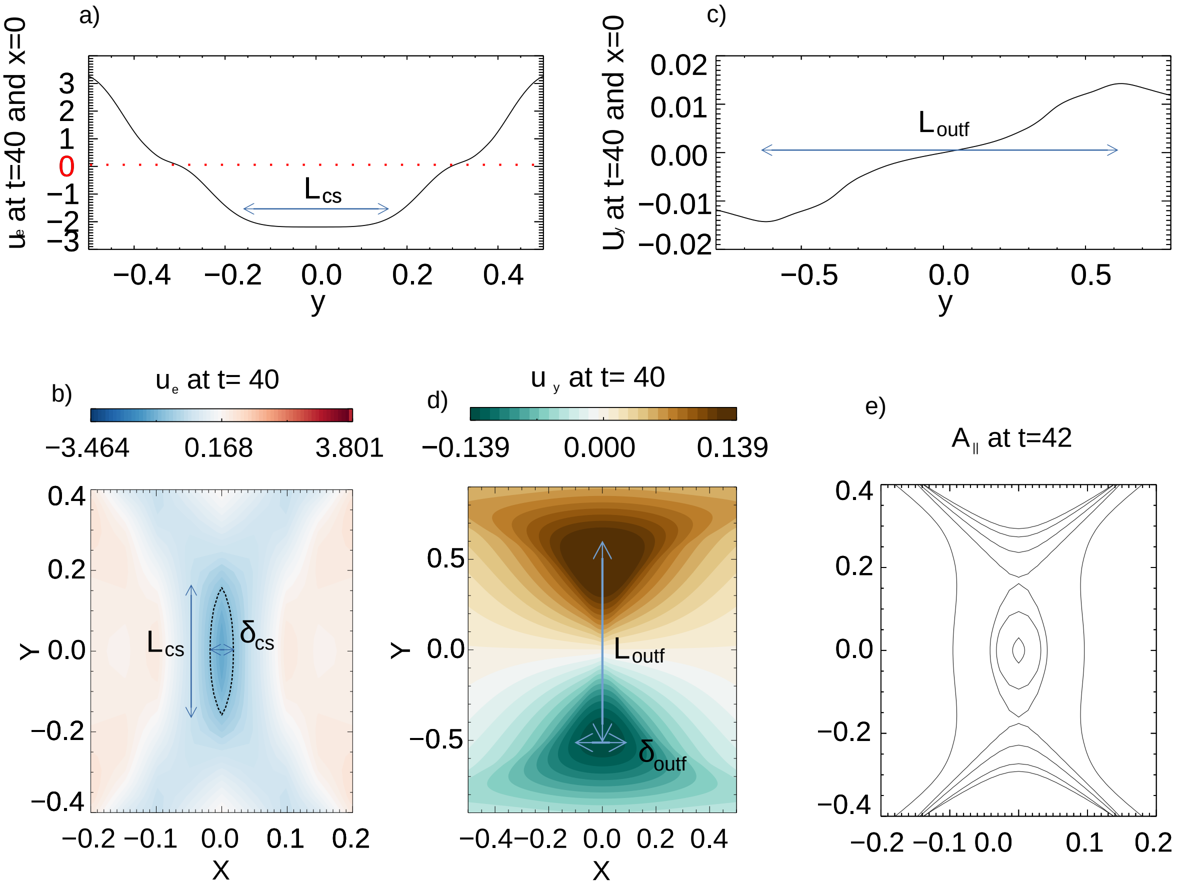

Figure 5.4: The parameters are the same as in Fig. 5.3. These simulations correspond to the least unstable one, for which the smallest plasmoid has been obtained. *a):* profile of the parallel electron current along y. We measured $L_{\text{cs}} = 0.32$. *b):* contour map of u_e at the X-point. The dotted black line is the isoline for which $u_e(\delta_{\text{cs}}/2, 0)$. We measured $\delta_{\text{cs}} = 0.06$. *c):* profile of the outflow, u_y, along y. We measured $L_{\text{outf}} = 1.2$. *d):* contour map of u_y. We measured $\delta_{\text{outfl}} = 0.12$. *e):* contours of $A_\parallel$ showing the plasmoid emerging at a later time.

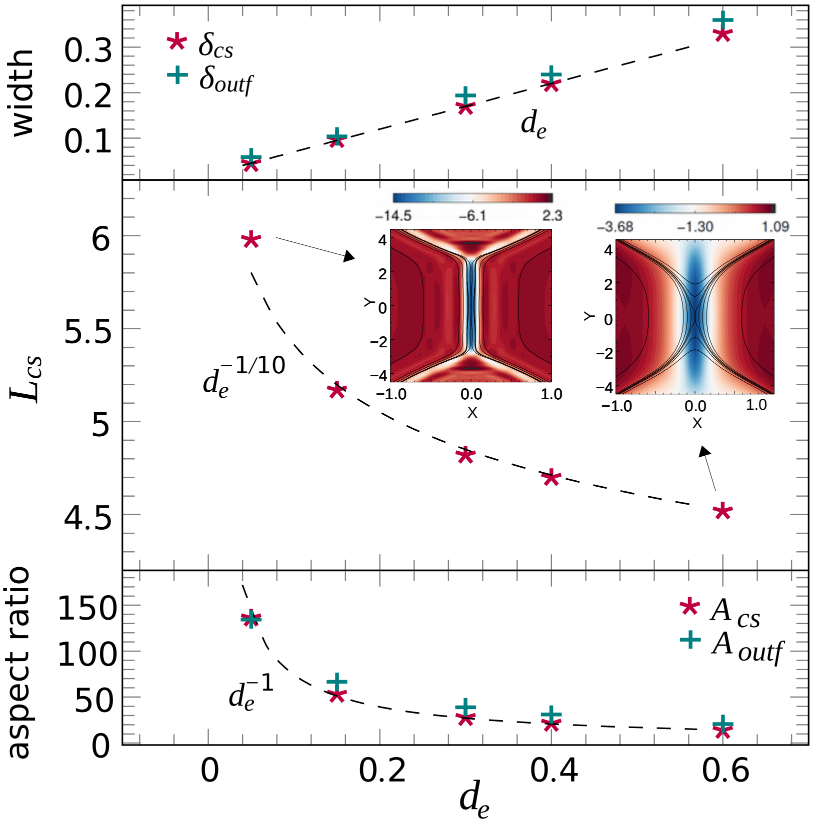

Figure 5.5: Characteristics of the reconnecting current sheet as a function of d_e for fixed $\rho_s = 0$ and $\Delta'_{\text{box}} = 60$. The current sheet is unstable to the formation of plasmoids in all five cases. For $d_e = 0.05$ and $d_e = 0.6$, we show the color maps of u_e with isolines of $A_\parallel$ in black. The dashed black lines are showing the obtained scalings.

$d_e = 0.05$ and $\rho_s = 0$). On the other hand, for high values of d_e, the current is not uniform enough along the layer for the magnetic-field lines to line up perfectly, since their density decreases in the region where the current is weaker, (see $d_e = 0.6$ and $\rho_s = 0$). As we discuss below, this latter case is less likely to develop plasmoids.

Finally, for the length and the aspect ratios, in the limit $\rho_s = 0$, we obtain the approximate scalings

$$L_{cs} \propto d_e^{-1/10} \qquad \text{and} \qquad A_{\text{cs}} \propto A_{\text{outf}} \propto d_e^{-1}. \tag{5.4}$$

When ρ_s is taken into account, ion-sound Larmor effects can become important and the current sheet changes into a cross shaped structure aligned with the magnetic island separatrices (Cafaro et al. (1998)). Indeed, in Fig. 5.6, when ρ_s is increased (for $\rho_s \sim d_e$), a part at the end of the layer splits to extend along the separatrices (see $d_e = 0.05$ and $\rho_s = 0.05$). Here, the measured L_{cs} still corresponds to the length distributed symmetrically on both sides of $y = 0$.

We measured

$$L_{\text{cs}} \propto \rho_s^{-1/2}. \tag{5.5}$$

As for the aspect ratios, they scale as

$$A_{\text{cs}} \propto \rho_s^{-0.6} \qquad \text{and} \qquad A_{\text{outf}} \propto \rho_s^{-1/2}. \tag{5.6}$$

For the series of simulations with $\Delta'_{\text{box}} = 14.3$ and $d_e = 0.1$, the reconnection process occurs without forming any plasmoids (gridded red region) until $\rho_s \sim 0.4$.

For $\rho_s \gtrsim d_e$ and $\Delta'_{\text{box}} = 60$ (green diagonally striped region), the aspect ratio A_{cs} is sufficiently large and one plasmoid emerges from the center of the current sheet. This corresponds to a low wavenumber fluctuation that develops in the current sheet, which is entering the nonlinear phase.

For $\rho_s \gg d_e$ (green dotted region), the current sheet reaches a perfect cross shape Cafaro et al. (1998). This very different geometry can still lead to a more complex plasmoid formation. Indeed, in the regime $\rho_s \gg d_e$, the first plasmoids that break up the current sheet are symmetrically located above and below the X-point. This process is detailed in Fig. 5.7. We observe 4 main phases: (I) formation of the X-shaped current; (II) its ends meet to form a local Y-shaped current sheet; (III) plasmoids emerge and enter the nonlinear phase; (IV) plasmoids are expelled by the outflow and the center plasmoid emerges. This type of plasmoid onset takes place for $\rho_s > 0.4 \gg d_e$ in Fig. 5.6.

We now discuss the dependence on the Δ'_{box} parameter, for $\rho_s = 0$ and for $\rho_s \gg d_e$. In order to clearly identify a current sheet, we have considered large Δ'_{box} values, which vary from 11.3 to 240. For $\rho_s = 0$ (Fig. 5.8), the parameter L_{cs} depends linearly on Δ'_{box},

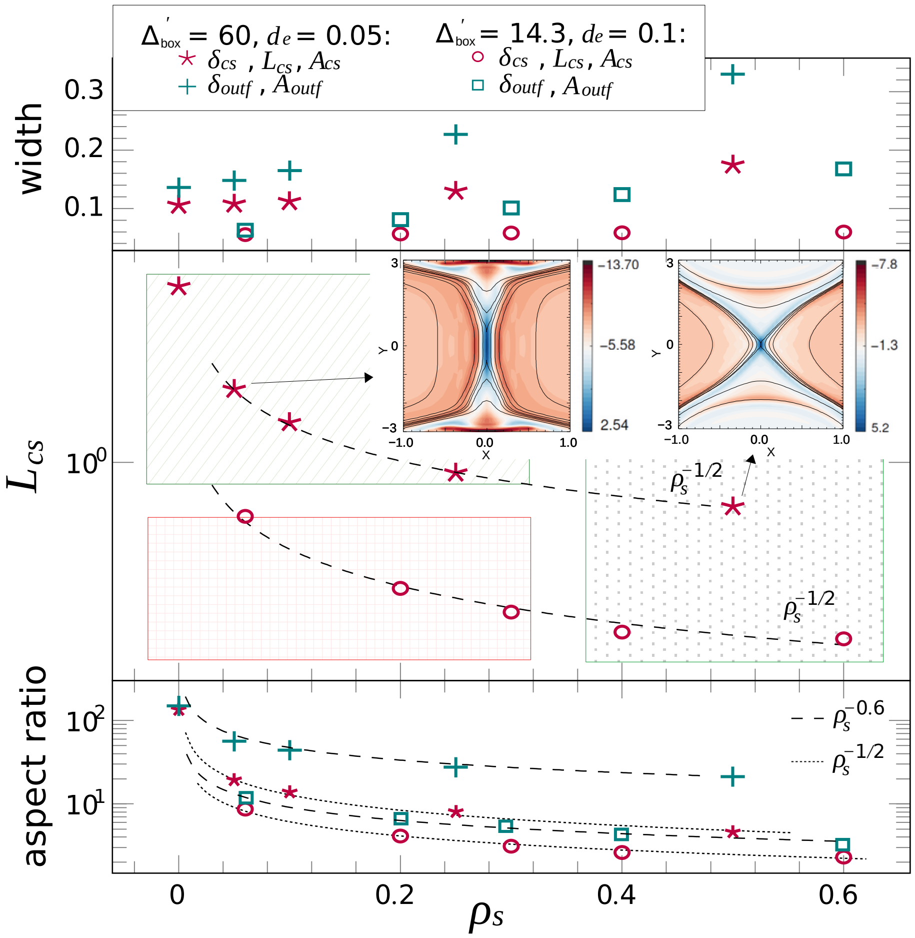

Figure 5.6: Same measures as Fig. 5.5 but for fixed d_e and varying ρ_s. For $\Delta'_{\text{box}} = 60$ and $d_e = 0.05$, all five cases are plasmoid unstable. For $\Delta'_{\text{box}} = 14.3$ and $d_e = 0.1$, plasmoids grow only when $\rho_s \geq 0.4$. For $\rho_s = 0.05$ and $\rho_s = 0.5$, we show the color maps of u_e with isolines of $A_\parallel$ in black. The dotted and dashed black lines are showing the obtained scalings. The current sheet is stable in the red gridded region. The green diagonally striped region corresponds to $\rho_s \gtrsim d_e$ and the green dotted region corresponds to $\rho_s \gg d_e$.

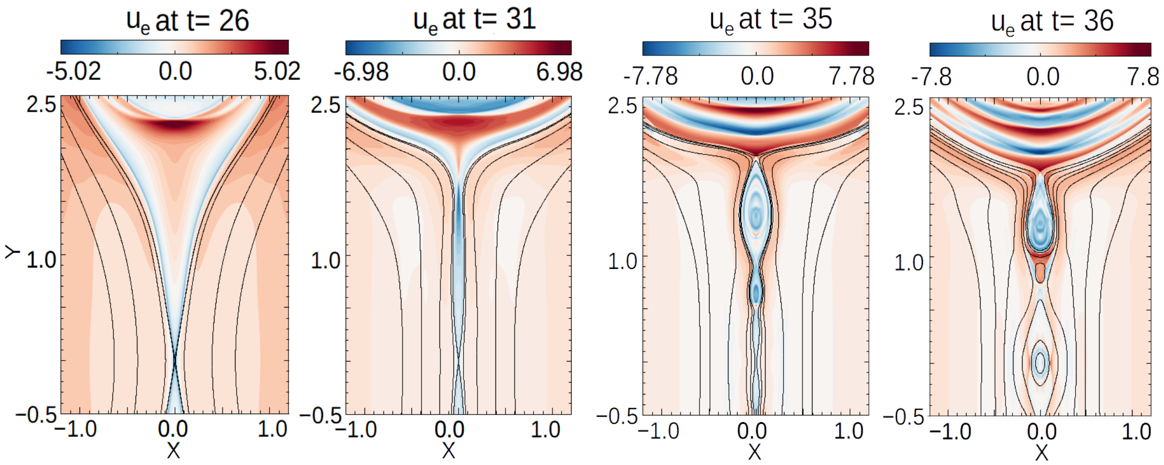

Figure 5.7: Time evolution of the parallel current density. The plots show the color maps of u_e, while black lines are contour lines of $A_{\|}$. For this simulation $d_e = 0.085$, $\rho_s = 0.3$ and $\Delta'_{\text{box}} = 30$. *Resolution:* 2304^2.

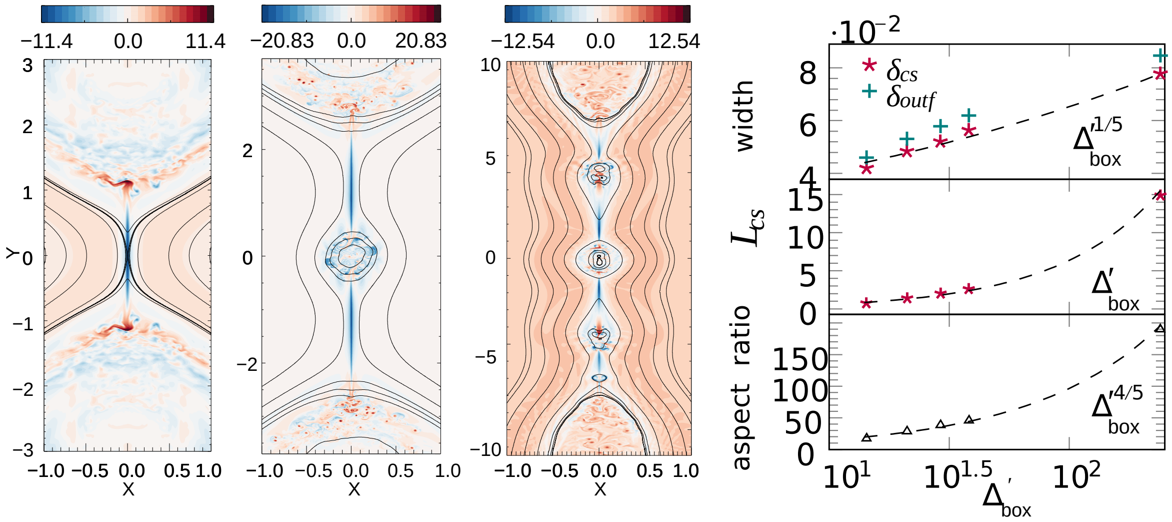

Figure 5.8: Current sheet characteristics for varying Δ'_{box} at fixed $d_e = 0.085$ and $\rho_s = 0$. *From left to right:* color maps of u_e with isolines of $A_{\|}$ in black for $\Delta'_{\text{box}} = 14.3$, $\Delta'_{\text{box}} = 38$, $\Delta'_{\text{box}} = 240$ and plot of the same quantities as in Fig. 5.5 but here as functions of Δ'_{box}. *Resolution for the simulations from left to right:* 1728^2, 2000×2400 *and* 2000×2400.

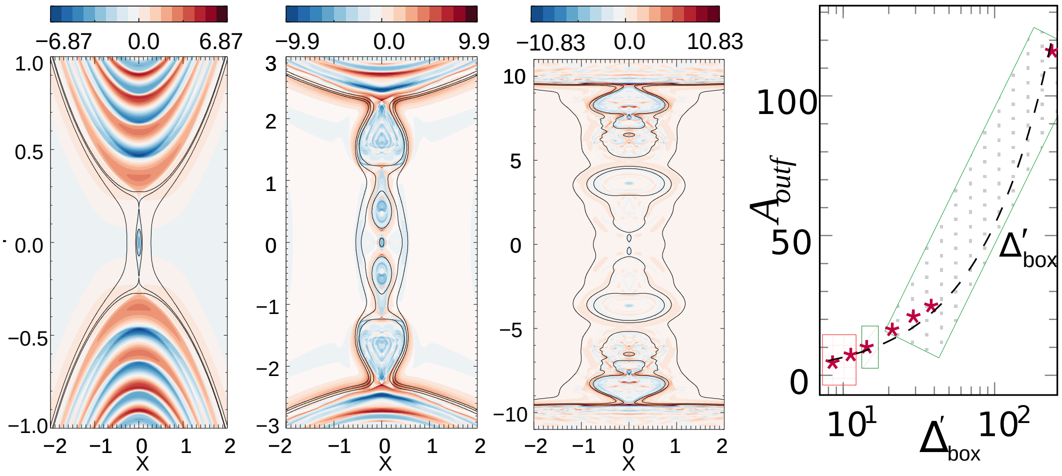

Figure 5.9: Current sheet characteristics for varying Δ'_{box} at fixed $d_e = 0.085$ and $\rho_s = 0.3$. *From left to right:* color maps of u_e with isolines of $A_\parallel$ in black for simulations with $\Delta'_{\text{box}} = 14.3$, $\Delta'_{\text{box}} = 38$, $\Delta'_{\text{box}} = 240$, and aspect ratio of the outflow velocity channel before the onset of plasmoids. *Resolution from left to right:* 1728^2, 2304^2, 2000×2400.

as in the resistive case Waelbroeck (1989); Jemella et al. (2003, 2004); Loureiro et al. (2005). We do not obtain plasmoids for $\Delta'_{\text{box}} \leq 14.3$, in agreement with Del Sarto et al. (2003), in which this regime is shown to be prone to the development of the Kelvin-Helmholtz instability. In the cases with $21 \leq \Delta'_{\text{box}} \leq 38$, one plasmoid emerges and breaks up the reconnecting current sheet. For $\Delta'_{\text{box}} = 240$, two other plasmoids are formed when the reconnecting current sheet becomes more elongated (unstable) as Δ'_{box} increases. In the limit $\rho_s = 0$, the outflow channel follows the current sheet and we observe indeed the scaling

$$A_{\text{outf}} \propto \Delta'_{\text{box}}. \tag{5.7}$$

For $\rho_s \gg d_e$ (Fig. 5.9), on the other hand, the case with $\Delta'_{\text{box}} = 14.3$ is plasmoid unstable. In this regime, the small-scale, oscillating current layer pattern located inside the two magnetic islands, and identified in Grasso et al. (2001) and Del Sarto et al. (2003), is visible on the two left panels.

Since increasing Δ'_{box} allows to increase significantly L_{cs}, we can compare the regimes $\rho_s < d_e$ and $\rho_s > d_e$ for various current sheet lengths. This test allows to show that the role of ρ_s is only relevant in marginally stable cases, since if L_{cs}/d_e is large enough, the current sheet becomes unstable regardless the value of ρ_s. Additionally, in the case of large Δ'_{box}, a notable difference between the two regime is in the number of plasmoids. The regime $\rho_s > d_e$ appears to be prone to the formation of a higher number of plasmoids.

In the rightmost panel of Fig. 5.9, we show the measured aspect ratio of the outflow velocity channel just before the appearance of the first plasmoid. For the least unstable

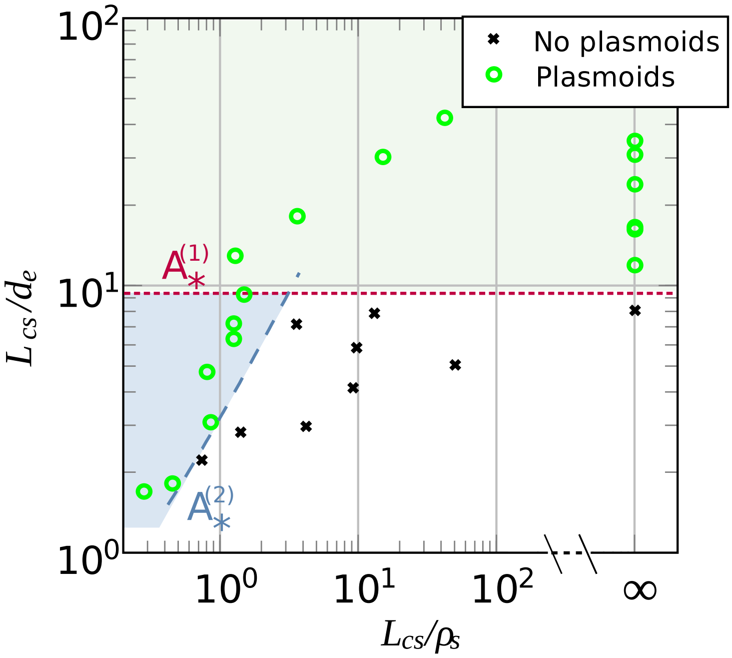

Figure 5.10: Parameter space diagram that identifies where the plasmoid instability leads to the break up of the current sheet. The cases that give plasmoids (green dots) are either above the $A_\star^{(1)}$ or $A_\star^{(2)}$ thresholds. The threshold $A_\star^{(2)}$ is approximated by the scaling $L_{\text{cs},\star}^{(2)}/d_e \propto L_{\text{cs}}/\rho_s$ from Eq. (5.21).

reconnecting current sheet ($\Delta'_{\text{box}} = 14.3$), we measured $L_{\text{outf}} = 1.21$ and $\delta_{\text{outf}} = 0.12$, shown on fig 5.4. This implies a steady state dimensional reconnection rate of

$$R_{\text{rec}} \sim \left(\frac{\delta_{\text{outf}}}{L_{\text{outf}}}\right) v_A B_{\text{up}} \sim 0.1 v_A B_{\text{up}}. \tag{5.8}$$

The red area corresponds to stable cases. The green striped area corresponds to the onset of only one plasmoid located at the center of the current sheet. Finally, the green dotted region corresponds to the cases where the first plasmoids emerge from a local Y-shaped current sheet (as described on Fig. 5.7).

Gathering all the numerical results, we can construct a parameter space diagram, analogously to what was done for reconnection induced by plasma resistivity (Ji & Daughton (2011); Daughton & Roytershteyn (2012); Cassak & Drake (2013)), which allows one to identify the collisionless plasmoid regimes that take place once a reconnecting layer of a certain length is formed. The diagram is shown on Fig. 5.10, and covers the space described by d_e/L_{cs} and ρ_s/L_{cs}.

According to our numerical simulations, the critical aspect ratio above which plasmoids break up the reconnecting current sheet, for $\rho_s = 0$, is

$$A_\star^{(1)} = \left(\frac{L_{\mathrm{cs}}}{\delta_{\mathrm{cs}}}\right)_\star^{(1)} \sim \left(\frac{L_{\mathrm{cs}}}{d_e}\right)_\star^{(1)} \sim 10, \tag{5.9}$$

when $d_e \gg \rho_s$. The green area of the diagram is the region with $L_{\mathrm{cs}}/d_e > A_\star^{(1)}$. On the other hand, for $\rho_s \gtrsim d_e$, the plasmoid formation has a different threshold $A_\star^{(2)} = \left(\frac{L_{\mathrm{cs}}}{\delta_{\mathrm{cs}}}\right)_\star^{(2)}$, which appears to be a function of L_{cs}/ρ_s. The simulations indicate

$$A_\star^{(2)} < A_\star^{(1)}. \tag{5.10}$$

The blue area of the diagram is the region with $L_{\mathrm{cs}}/d_e > A_\star^{(2)}$.

It is worth emphasizing the difference between the diagram presented in Ji & Daughton (2011), shown on Fig. 5.2, and our diagram of Fig. 5.10. Presumably, in Ji & Daughton (2011), the length ”L” is a different length than the one we use in our work, and it is defined by the authors as ”the plasma size”. Their length seems to be equivalent to our L_y. In Ji & Daughton (2011), Eq. (21) indicates a threshold $\rho_s/L_y \sim 50$. If we consider the length L_y to indicate a threshold expressed in terms of the ratio between the ion-sound Larmor radius and the ”plasma size”, we find plasmoids for $\rho_s/L_y \sim 10$ (providing d_e is small). Therefore, with our collisionless fluid model in the strong-guide-field regime, we find indeed plasmoids for values of the ratio between the plasma size and the sonic Larmor radius, below the threshold predicted by Ji & Daughton (2011); Daughton et al. (2006) on the basis of kinetic simulations.

5.1.2 Theory

The development of the analytical arguments that follow, rely on theoretical relations already known from the collisional case and on the results suggested by the simulations carried out in this Thesis, in the spirit of obtaining a scaling to evaluate $A_\star^{(2)}$. For that, we took inspiration from the the plasmoid instability theory presented in Refs. Comisso et al. (2016, 2017); Huang et al. (2017).

We consider a forming current sheet in which the amplitude of the tearing mode grows as

$$A_\parallel(k,t) = A_0 \exp\left(\int_{t_0}^{t} \gamma(k,t')\mathrm{d}t'\right), \tag{5.11}$$

where γ and k are the tearing mode growth rate and wavenumber, respectively, while A_0 is the magnetic flux amplitude at t_0. The plasmoid half-width is given by

$$w(k,t) = 2\sqrt{\frac{A_\parallel a(t)}{B_{\mathrm{up}}(t)}}, \tag{5.12}$$

where $A_{\|}$ is evaluated at the resonant surface, $B_{\rm up}(t)$ is the reconnecting magnetic field and $a(t)$ is the half-width of the shrinking current sheet. Given that the current sheet is slowly shrinking toward a finite width, and is evolving slower than the plasmoid growth, we assume that the current sheet is nearly in steady-state and we neglect the time dependency of $B_{\rm up}$ and a.

Figure 5.3 confirms that the current sheet profiles are well fitted by a Harris sheet, for which we recall that

$$\Delta'_{\rm cs} = \frac{2}{a}\left(\frac{1}{ka} - ka\right). \tag{5.13}$$

We denote by

$$\tau_\star = \frac{L_{{\rm cs},\star}}{v_A} \tag{5.14}$$

the timescale for the plasma to be expelled from the current sheet of length $L_{\rm cs}$ because of the Alfvénic outflow. If the magnetic flux amplitude becomes nonlinear (with plasmoid half-width $w_{\rm nl}$) in a timescale shorter than $\tau_\star$, the current sheet is broken by at least one plasmoid. Otherwise it remains stable.

Therefore, taking

$$w(k,\tau_\star) = 2\left(\frac{A_0 a}{B_{\rm up}}\right)^{1/2} e^{\frac{1}{2}\tau_\star\gamma}, \tag{5.15}$$

the threshold for the plasmoid formation can be written as

$$\tau_\star\gamma = 2\,\ln\left[\frac{w_{\rm nl}}{2}\left(\frac{B_{\rm up}}{A_0 a}\right)^{1/2}\right]. \tag{5.16}$$

We define the two different regimes: (1) $d_e > \rho_s$ and (2) $d_e < \rho_s$. The two regimes have different thresholds $\tau_\star^{(1)} = L_{{\rm cs},\star}^{(1)}/v_A$ and $\tau_\star^{(2)} = L_{{\rm cs},\star}^{(2)}/v_A$. From Eqs. (2.136)-(2.137), one can consider the dispersion relation of the collisionless tearing mode for arbitrary values of $\Delta'_{\rm cs}$ of Porcelli (1991). For the marginally stable current sheet, one can consider the limit $\delta_{\rm in}\Delta'_{\rm cs} \ll 1$, with $\delta_{\rm in}$ indicating the width of the inner tearing layer. In this case, taking into account the the full dispersion relation (Porcelli (1991)) reduces to

$$\gamma^{(1)} = A_{\rm cs}^{eq}\left[\frac{\Gamma(1/4)}{2\pi\Gamma(3/4)}\right]^2 \Delta_{\rm cs}'^2 d_e^3 k, \qquad \text{for} \qquad \rho_{\rm s} < {\rm d_e}, \tag{5.17}$$

and

$$\gamma^{(2)} = A_{\rm cs}^{eq}\frac{\Delta'_{\rm cs} d_e \rho_s k}{\pi}, \qquad \text{for} \qquad \rho_{\rm s} > {\rm d_e}. \tag{5.18}$$

Assuming that the needed amplification factor of the magnetic flux perturbation is the same for the $\rho_s^2 \ll d_e^2$ and $\rho_s^2 \gg d_e^2$ cases requires that

$$\tau_\star^{(2)}\gamma^{(2)} \sim \tau_\star^{(1)}\gamma^{(1)} \sim 2\,\ln\left[\frac{w_{\rm nl}}{2}\left(\frac{B_{\rm up}}{A_0 a}\right)^{1/2}\right], \tag{5.19}$$

which gives us $L^{(2)}_{\mathrm{cs},\star}k/d_e \sim L^{(1)}_{\mathrm{cs},\star}\Delta' d_e k/\rho_s$. Considering that for $(ka)^2 \ll 1$, we have

$$\Delta'_{\mathrm{cs}}k \sim \frac{1}{a^2} \sim \frac{1}{d_e^2}, \tag{5.20}$$

with $k \propto 1/L_{\mathrm{cs}}$, and making use of the numerical result $(L_{\mathrm{cs}}/d_e)^{(1)}_{\star} \sim 10$, gives us the threshold condition

$$\frac{L_{\mathrm{cs}}}{d_e} = \frac{L^{(2)}_{\mathrm{cs},\star}}{d_e} \propto \frac{L_{\mathrm{cs}}}{\rho_s}\,. \tag{5.21}$$

We identified a proportionality coefficient for which the proposed scaling, shown by the dashed blue line in Fig. 5.10, correctly captures the plasmoid formation that occurs for significantly lower values of the current sheet aspect ratio when $L_{\mathrm{cs}}/\rho_s \lesssim 1$.

Figure 5.11 shows the evolution of the threshold $L^{(2)}_{\mathrm{cs},\star}$ as a function of ρ_s, for a marginally stable current sheet. We assume $L^{(1)}_{\mathrm{cs},\star} = 3$. Given the threshold $L^{(1)}_{\mathrm{cs},\star}/d_e \sim 10$, we assume $d_e = 0.3$. We assume an equilibrium with $\Delta'_{\mathrm{cs}} = 3.6$, broken by the mode $m = 1$. This can be verified by, for example, an equilibrium with $L_{\mathrm{cs}} \sim 3$ and $\lambda \sim 0.3$.

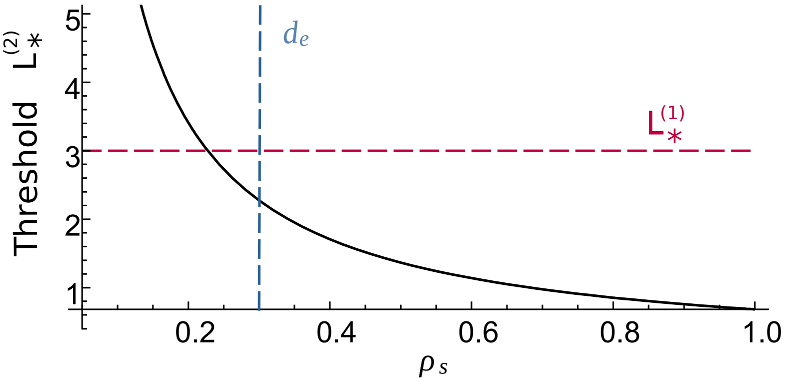

Figure 5.11: Evolution of the threshold $L^{(2)}_{\mathrm{cs},\star}$, as a function of ρ_s, for $\Delta'_{cs} = 3.6$, $L^{(1)}_{\mathrm{cs},\star} = 3$, $d_e = 0.3$.

While the aspect ratio of the current sheet controls the plasmoid growth, the aspect ratio of the plasma flow channel regulates the rate of inflowing plasma via mass conservation. For $d_e \gg \rho_s$, the aspect ratios A_{cs} and A_{outf} essentially coincide since the plasma behaves as a one fluid. Therefore, for an incompressible flow in steady state, the marginal stability threshold $A^{(1)}_{\star} \sim 10$ yields the reconnection rate $R_{\mathrm{rec}} \sim 0.1 v_A B_{\mathrm{up}}$. On the other hand, for $\rho_s \gtrsim d_e$, two-fluid effects lead to a decoupling of the plasma flow channel from the electric current density, and in this case we find that $R_{\mathrm{rec}} \sim (\delta_{\mathrm{outf}}/L_{\mathrm{outf}})^{(2)}_{\star} v_A B_{\mathrm{up}} \sim 0.1 v_A B_{\mathrm{up}}$ even when $A^{(2)}_{\star} \ll A^{(1)}_{\star}$. Since the global reconnection rate is controlled by the marginally stable current sheet (Comisso & Bhattacharjee (2016)), eventually $R_{\mathrm{rec}} \sim 0.1 v_A B_{\mathrm{up}}$ in the entire green and blue parameter space regions of Fig. 5.10.

5.2 Comparison between gyrofluid and gyrokinetic, $\beta_e \neq 0$

In this Section, we investigate the role of β_e on the plasmoid instability using the gyrofluid model ((2.129) - (2.130). The simulations are compared to gyrokinetic ones performed and analysed by Ryusuke Numata with the code `AstroGK` described in Numata et al. (2010). `AstroGK` is a δf code which solves an electromagnetic gyrokinetic Vlasov-Maxwell system in a five dimensional phase space and adopting a Fourier-spectral method for evolving the equations in space.

One of the main advantages of using the `AstroGK` code for a comparison with the gyrofluid results, is that, in a specific limit, the gyrokinetic system solved by `AstroGK` reduces to the one (Howes et al., 2006) that was taken to derive the gyrofluid model -(2.129) - (2.130). This allows to directly identify possible limitations of the closures applied to the gyrofluid moments that distinguish the gyrofluid model from its gyrokinetic parent model. The specific limit in which the `AstroGK` code has to be used, in order to reproduce the parent gyrokinetic model of the gyrofluid model, is that corresponding to a straight and uniform guide field, with no density and temperature gradients and without collisions. Note that, in order to satisfy Eqs. (2.127)-(2.129) at equilibrium, the corresponding equilibrium density and parallel electron velocity fluctuations of the electron gyrocenters are fixed as

$$N_e^{(0)} = 0, \qquad \nabla_\perp^2 A_\parallel^{(0)} = G_{10_e} U_e^{(0)}. \tag{5.22}$$

Analogously to Eq. (2.156), the dimensional equilibrium for the gyrokinetic simulations is set as

$$\phi^{(0)} = 0, \qquad A_\parallel^{(0)} = A_{\parallel 0}^{eq} A_0 S_h(\hat{x}) / \cosh^2\left(\frac{\hat{x}}{L}\right), \qquad B_\parallel^{(0)} = 0, \tag{5.23}$$

where A_0 is a characteristic value for the magnetic vector potential and $S_h(\hat{x})$ is a shape function to enforce periodicity (Numata et al. (2010)). Also in the gyrokinetic simulations, in accordance with Eq. (5.22), the equilibrium current density is assumed to be entirely due to the parallel electron velocity.

5.2.1 Results on the plasmoid onset

In this section, we present a comparison between the simulations reported in the following tables:

Each simulation is identified by a code of the form $p_{F/GF/GK\,r}$, where p and r are

No.	ρ_s	Δ'	β_e	m_e/m_i	γ_L	γ_{max}	Plasmoid
1_{GF1}	0.3	14.3	0.2491	0.01	0.214	0.285	One small
1_{GF2}	0.3	14.3	0.06228	0.0025	0.225	0.322	No
1_F	0.3	14.3	0	0	0.230	0.337	No
2_{GF1}	0.3	29.09	0.2491	0.01	0.211	0.342	One plasmoid
2_{GF2}	0.3	29.09	0.1246	0.005	0.218	0.367	One plasmoid
2_{GF3}	0.3	29.09	0.06228	0.0025	0.231	0.378	One plasmoid
2_{GF4}	0.3	29.09	0.0124	0.0005	0.241	0.385	Several plasmoids
2_F	0.3	29.09	0	0	0.242	0.386	Several plasmoids
3_{GF1}	0.5	14.3	0.692	0.01	0.286	0.334	Several plasmoids
3_{GF2}	0.5	14.3	0.3460	0.005	0.310	0.383	Several plasmoids
3_F	0.5	14.3	0	0	0.338	0.448	Several plasmoids
4_F	0.06	14.3	0	0	0.081	0.188	No

Table 5.1: Gyrofluid and fluid simulations.

No.	ρ_s	Δ'	β_e	m_e/m_i	γ_L	γ_{max}	Plasmoid
1_{GK1}	0.3	14.3	0.2491	0.01	0.2245	0.308	One small
1_{GK2}	0.3	14.3	0.06228	0.0025	0.2438	0.342	No
2_{GK1}	0.3	29.09	0.2491	0.01	0.2165	0.352	One large
2_{GK2}	0.3	29.09	0.1246	0.005	0.2267	0.389	One large
2_{GK3}	0.3	29.09	0.06228	0.0025	0.2329	0.401	One large
3_{GK1}	0.5	14.3	0.692	0.01	0.3040	0.362	One
3_{GK2}	0.5	14.3	0.3460	0.005	0.3286	0.410	One
3_{GK3}	0.5	14.3	0.1730	0.0025	0.3472	0.453	One
4_{GK1}	0.06	14.3	0.009965	0.01	0.08617	0.207	No
4_{GK2}	0.06	14.3	0.002491	0.0025	0.08779	0.209	No

Table 5.2: Gyrokinetic simulations.

integers and F, GF and GK indicate whether the simulation is carried out in the fluid limit, with the gyrofluid model or with gyrokinetic model, respectively. For all the simulations, the value of the electron skin depth is fixed to $d_e = 0.085$. Simulations with the same number p are characterized by the same values of d_e, ρ_s and Δ'. For a fixed p, different values of the index r, on the other hand, indicate different values of β_e (and, consequently, of m_e/m_i), with β_e decreasing as r increases. Not all the simulations of Table 5.1 have a corresponding simulation in Table 5.2 and viceversa, although this is the case for most of the simulations. In particular, we point out that, because gyrokinetic simulations always have a finite value of β_e, strictly speaking there is no gyrokinetic counterpart for the fluid simulations, which formally correspond to the $\beta_e \longrightarrow 0$ limit.

For all the gyrokinetic simulations, the temperature ratio is set to $\tau = 10^{-3}$, where the ion Larmor radius is $\sqrt{\tau}\rho_s$. As mentioned before, the gyrofluid model assumes $\tau \longrightarrow 0$. Therefore, in both the gyrofluid and gyrokinetic approach, the ion Larmor radius effects are neglected.

As a first general comment, we observe, by comparing gyrofluid and gyrokinetic simulations with the same indices p and r, that, in terms just of appearance or absence of plasmoids, gyrofluid simulations agree with the gyrokinetic ones. Therefore, in this respect, we can conclude that the quasi-static closure for the electrons and the suppression of ion gyrocenter fluctuations, do not affect critically the stability of the nonlinear current sheet. However, as will be discussed in the next Sections, differences appear in terms of the number and size of plasmoids. In particular, when more than one plasmoid is observed, this is indicated in table 5.1 and 5.2, generically, as 'several plasmoids'. The number of plasmoids in the same simulation can indeed vary in time, as plasmoids can form at different times and pairs of plasmoids can merge into a single one.

These simulations are compared in the following sections. In particular, with the set of simulations $p = 1$ and $p = 2$ the effects of β_e on the formation of plasmoids are investigated in Section 5.2.4. With the set of simulations $p = 3$ and $p = 4$ we verify that the regime $\rho_s \gg d_e$ promotes the formation of plasmoids in Section 5.2.5.

5.2.2 Remarks on the numerical resolution

It is important to underline the role of the resolution in this study. In the forming current sheet, tearing modes grow and can become unstable at different times. The current sheet can therefore be broken by multiple dominant modes, and the number of plasmoids is highly sensitive to the resolution used. In the following, we provide some comments concerning, in particular, the resolution and the number of plasmoids observed, for the series $p = 1, 2, 3$.

For simulation 1_F, no plasmoids were obtained by the fluid code with the resolution 192^2. However, we obtained a very small one with the resolution 1728^2, as visible on

$n_x \times n_y$	# plasmoids	Comments on the order of appearance
200×120	1	1 at the center
200^2	3	2 symmetrically with respect to the center then 1 at the center
200×400	3	2 symmetrically with respect to the center then 1 at the center
1280^2	5	4 symmetrically with respect to the center then 1 at the center
2304^2	7	6 symmetrically with respect to the center then 1 at the center
3400×4800	7	6 symmetrically with respect to the center then 1 at the center

Table 5.3: number of visible plasmoids for simulation 2_F for different grids.

the left panel of Fig. 5.9. The low β_e gyrokinetic case 1_{GK2}, did not identify plasmoid onsets with the resolution 256×196.

Given that the fluid simulations 2_F was the one which allowed the formation of several plasmoids, we carried out resolution tests on these simulations to determine the necessary number of points along y, that does not prevent the growth of large mode numbers. Table 5.3 reports the number of visible plasmoids for simulation 2_F as a function of the number of points and indicates their order of appearance. The convergence is reached for a resolution of 2304^2.

For 3_F, which is close to marginal stability, a ratio smaller than $2L_y/n_y \sim 0.0078$ was needed to see the first two plasmoids. Unfortunately, it is not foreseeable to perform gyrokinetic simulations with such a high resolution.

In order to make a proper comparison we performed fluid/gyrofluid simulations with a resolution nearly identical to that of the gyrokinetics. However, since the fluid code is much less demanding in computation time, we also performed additional fluid and gyrofluid simulations with grids up to 2304^2 points.

5.2.3 Growth rates

Before discussing in detail the plasmoid instability, we briefly comment about the linear growth rate of the tearing mode excited by the perturbation of the initial equilibria (2.156). In the tables, we reported the value of the linear and maximum growth rate of the tearing instability, evaluated measuring the following quantity at the X-point

$$\gamma = \frac{d}{dt} \log \left| A_{\|}^{(1)} \left(\frac{\pi}{2}, 0, t \right) \right| . \tag{5.24}$$

The two approaches give close growth rate values for small β_e. Figure 5.12 shows the value of γ_{max} for the set of simulations $p = 2$ and $p = 3$. The gyrofluid and gyrokinetic simulations yield the same dependence of γ_{max} on the parameters, with the gyrofluid

Figure 5.12: Maximum growth rates of the collisionless tearing mode as a function of β_e, for the cases $p = 2$ and $p = 3$.

simulations slightly underestimating the growth rate, in general. This discrepancy suggests that, for large values of β_e and during the nonlinear phase, the efficiency of the gyrofluid model to reproduce the gyrokinetic results becomes limited. One reason for this might be the absence of ion gyrocenter density and parallel velocity fluctuations, which occurs in the gyrofluid model, even for large β_e.

By comparing the growth rate results, for a fixed mass ratios, of simulations $p = 1, 3, 4$, we note that increasing β_e and ρ_s, as $\rho_s \sim \sqrt{\beta_e/2}$, destabilizes the tearing mode. Increasing these parameters can be seen as fixing the background density, the ion mass and the guide field amplitude, while increasing the electron temperature. It was shown numerically in Numata & Loureiro (2015); Granier et al. (2022b) that, in this latter situation, the linear tearing growth rate is first ruled by the destabilizing effect of the sonic Larmor radius. However, in cases where the electron temperature is high enough for the effects of ρ_e to take over those of ρ_s, the linear growth rate is damped. Here, we find ourselves in the first case, for which the effects of the sonic Larmor radius are visibly dominant.

5.2.4 Effect of β_e on the plasmoid onset

In this Section we present how the β_e parameter changes the characteristics of the forming current sheet and promotes the plasmoid formation.

We focus first on the comparison of the series of simulations for $p = 1$, starting with the higher β_e case, for which $\beta_e = 0.2491$. The contour plots of the parallel electron velocity u_e (proportional to the parallel current density), for the gyrofluid simulation 1_{GF1} and of the current density, $j_{\|}$, for the gyrokinetic simulations 1_{GK1}, are shown on Fig. 5.13. Isolines of the magnetic potential, showing the topology of the magnetic field, are overplotted. Both approaches indicate the formation of a plasmoid. For the fluid simulation, the aspect ratio is $A_{\mathrm{cs_f}} = 4.90$. In the gyrokinetic case, we measure $A_{\mathrm{cs_k}} = 4.03$. We observe a persistent difference between the value of the gyrofluid and gyrokinetic aspect ratios, which is explained by the difference in resolution. However, their evolution according to the parameters are in agreement.

For the lowest β_e cases, for which $\beta_e = 0.06228$, the contour plots of the simulations 1_{GF2} and 1_{GK2}, are shown on Fig. 5.14. The two simulations lead to the formation of a stable current sheet having an aspect ratio decreasing in time. The maximum aspect ratio is reached when the growth rate has reached its maximum value and the process enters the saturation phase. From the gyrofluid simulation we measured a maximum aspect ratio $A_{\mathrm{cs_f}} = 5.11$. In the gyrokinetic case, the aspect ratio is $A_{\mathrm{cs_k}} = 4.14$. The

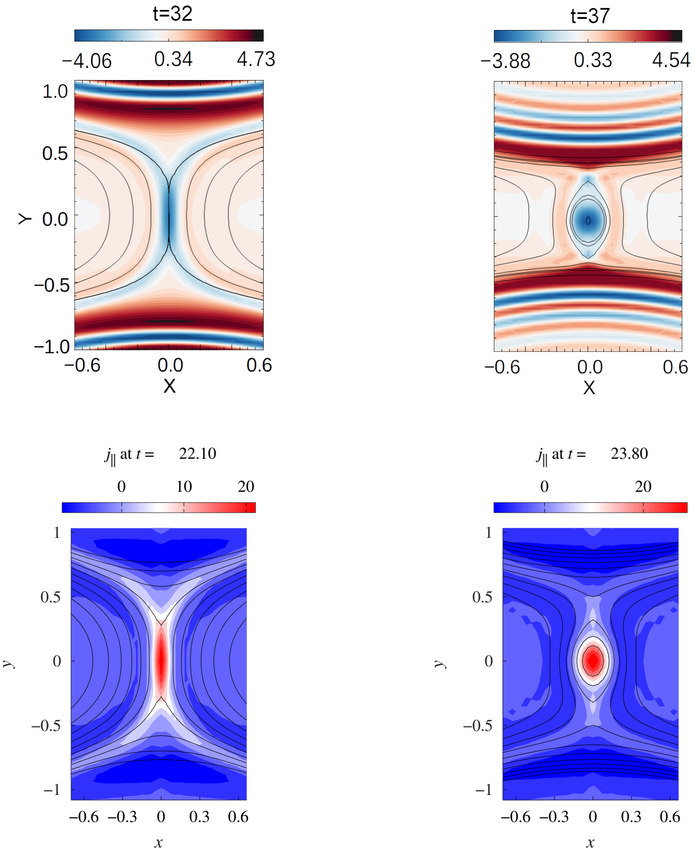

Figure 5.13: *Top:* Contour of the parallel electron velocity u_e (proportional to the parallel current density) for simulation 1_{GF1}. *Bottom:* Contour of the parallel current density $j_\|$ of simulation 1_{GK1}. Isolines of the magnetic potential are superimposed on all the contours. The same part of the domain is shown on each panel. *Credit: Gyrokinetic data processed by Ryusuke Numata.*

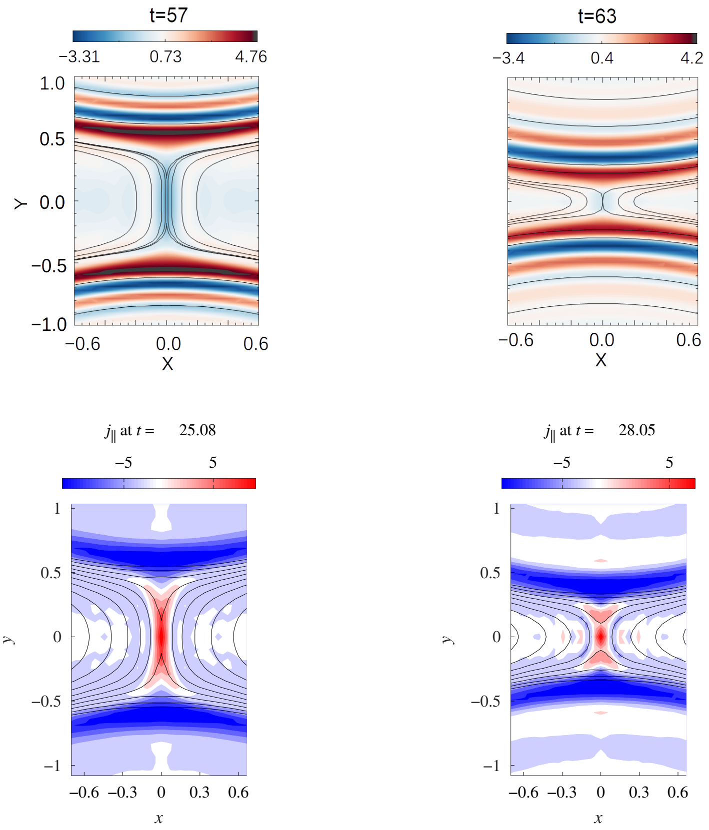

Figure 5.14: *Top:* Contour of the electron velocity u_e (proportional to the parallel current density) for simulation 1_{GF2}. *Bottom:* Contour of the parallel current density $j_\parallel$ of simulation 1_{GK2}. Isolines of the magnetic potential are superimposed on all the contours. The same part of the domain is shown on each panels. *Credit: Gyrokinetic data processed by Ryusuke Numata.*

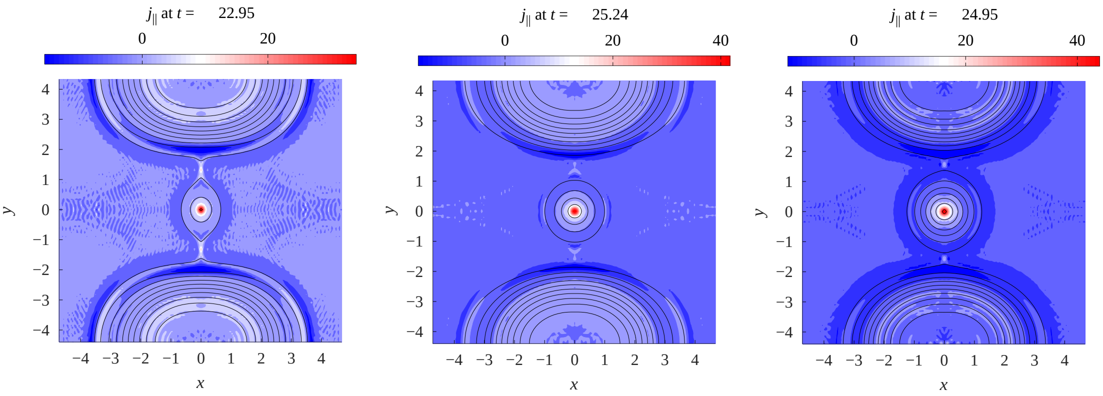

Figure 5.15: Contour of the parallel current density $j_{\|}$ for simulations 2_{GK3}, 2_{GK2} and 2_{GK1}. Isolines of the magnetic potential are superimposed on all the contours. *Credit: Data processed by Ryusuke Numata.*

measured aspect ratio are very close to those obtained for $\beta_e = 0.2491$, and yet, no plasmoids develop. In this first series of tests we are at the frontier between stability and instability, and the role of β_e seems crucial to switch to an unstable case.

In the series of simulations for $p = 2$, the idea is to consider the same parameters as those for $p = 1$ but with a longer forming current sheet. Since highly unstable primary reconnecting modes favour the formation of extended secondary current sheets we consider a larger domain size along the y direction, with $L_y = 1.4\pi$, that corresponds to $\Delta' = 29.9$. The other parameters are kept the same. In this case, even the small-/negligible β_e simulations become plasmoid unstable. Figure 5.15 shows the plasmoids obtained at the end of the simulations 2_{GK1} - 2_{GK3}. The magnetic potential contour is shown as the plasmoid reaches its maximum size, which occurs in the saturation phase of the tearing instability. Figure 5.16 shows the evolution in time of the growth rate of the tearing mode and of the aspect ratio of the secondary current sheet. It can be seen that increasing β_e results in larger sized plasmoids, although, from the aspect ratio measurement, increasing β_e reduces the aspect ratio obtained just before the plasmoid onset. Here, increasing β_e (considering therefore larger mass ratios) seems to have a similar effect to increasing ρ_s, and allows the plasmoid instability to grow better in current sheets whose dimensions are not particularly favourable (low aspect ratio).

In comparison, Fig. 5.17 shows the aspect ratio and the growth rate obtained for the simulations 4_{GK1} and 4_{GK2}. For this set of simulations, the parameters ρ_s and Δ' are smaller than those of simulations 2_{GK1} - 2_{GK3} and the effects of β_e are negligible. Nevertheless, despite a very different set of parameters, the series of simulations No. 2 and 4 lead to the formation of current sheets whose aspect ratio is almost identical. Yet, unlike cases 2, cases 4 remain stable. The fact that the current sheets are of comparable length can be explained since it was numerically shown in Sec. 5.1 that the length of

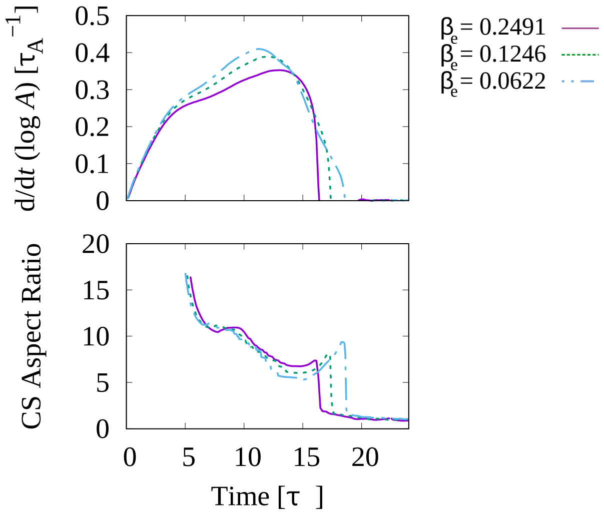

Figure 5.16: Growth rate evolution as function of time and aspect ratio of the forming current sheet as a function of time for simulations 2_{GK3}, 2_{GK2} *Credit: Data processed by Ryusuke Numata.*

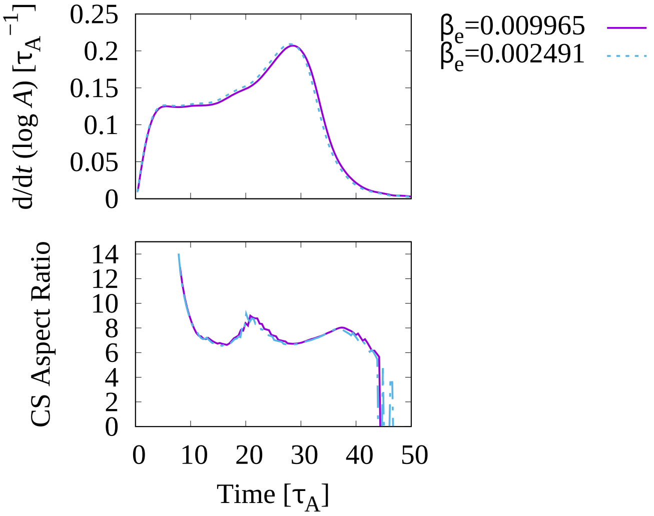

Figure 5.17: Simulations 4_{GK1} 4_{GK2}. *Top:* Growth rate evolution as function of time. *Bottom:* aspect ratio of the forming current sheet as a function of time. *Credit: Data processed by Ryusuke Numata.*

the forming current layer should scale as ${\rho_s}^{-1/2}$. Therefore, even though series 2 has a larger Δ' and thus allows for a more elongated current sheet along y, the series 4, performed with a smaller sonic Larmor radius, form an equally long current sheet . Now, if we assume, as done in the theory by Comisso et al. (2016), that the growth of the perturbation in the new current sheet does not depend on the initial tearing equilibrium (and that therefore the initial Δ' has no role in the plasmoid size) then plasmoid formation is determined only by the values of ρ_s and β_e which are greater in case 2.

Figure 5.18 shows in detail the evolution of the instability for the fluid and gyrofluid runs having the highest resolution. For negligible β_e we can see several plasmoids forming in a row, whereas, for $\beta_e > 0.06$ we see only a single central plasmoid. The magnetic potential isolines of 2_{GF1} and 2_{GF3}, shown in Fig. 5.18, can be compared to that to 2_{GK1} and 2_{Gk3}, shown in Fig. 5.15. The effects of β_e eventually prevent the development of large modes inside the current sheets.

5.2.5 Validation of the plasmoid regime $\rho_s \gg d_e$

In this Subsection, we would like to validate the results obtained in Sec. 5.1, where it was shown that, for a current sheet close to marginal stability, the regime $\rho_s \gg d_e$ promotes the plasmoid formation. In this Section, the simulations were carried out with the fluid model (2.136) - (2.137) which assumes a negligible mass ratio and a negligible β_e. The main motivation now is to present a gyrokinetic validation of these results. In addition to observing a possible role played by the closure, we also compare the fluid results with those including a finite mass ratio of $m_e/m_i = 0.005$, and consequently a small β_e. Moreover, as already recalled, the evolution of ion quantities such as N_i and U_i, prevented by the gyrofluid model, but present in the gyrokinetic simulations, might in principle also play a role. Therefore, in this Subsection we focus on the low β_e regime and compare simulation set No. 3, for which $\rho_s \gg d_e$, with simulation set No. 4, for which $\rho_s \ll d_e$. These two sets of simulation lead to the formation of a current layer close to the instability threshold.

Figure 5.19 shows the evolution of the instability for the simulations 3_{GK3} (lowest β_e gyrokinetic case of this series) and 3_F. For the two approaches, the current sheet becomes plasmoid unstable. Also in this case the resolution plays an important role. With a resolution of 1728^2, three plasmoids were visible in the simulations 3_F. However, the same fluid simulation performed with a resolution 500×360 shows only one plasmoid. Since a resolution higher than that was not foreseeable with the gyrokinetic code, we used a grid of 256×128 points that allowed to observe one single plasmoid at the center. In the regime $\rho_s \gg d_e$, the current aligns with the magnetic field lines, thus forming a cross shaped current sheet (Cafaro et al., 1998). This behavior is retrieved by the gyrokinetic simulation.

Figure 5.20 shows the evolution of the instability for the cases 4_{GK3} (lowest β_e gy-

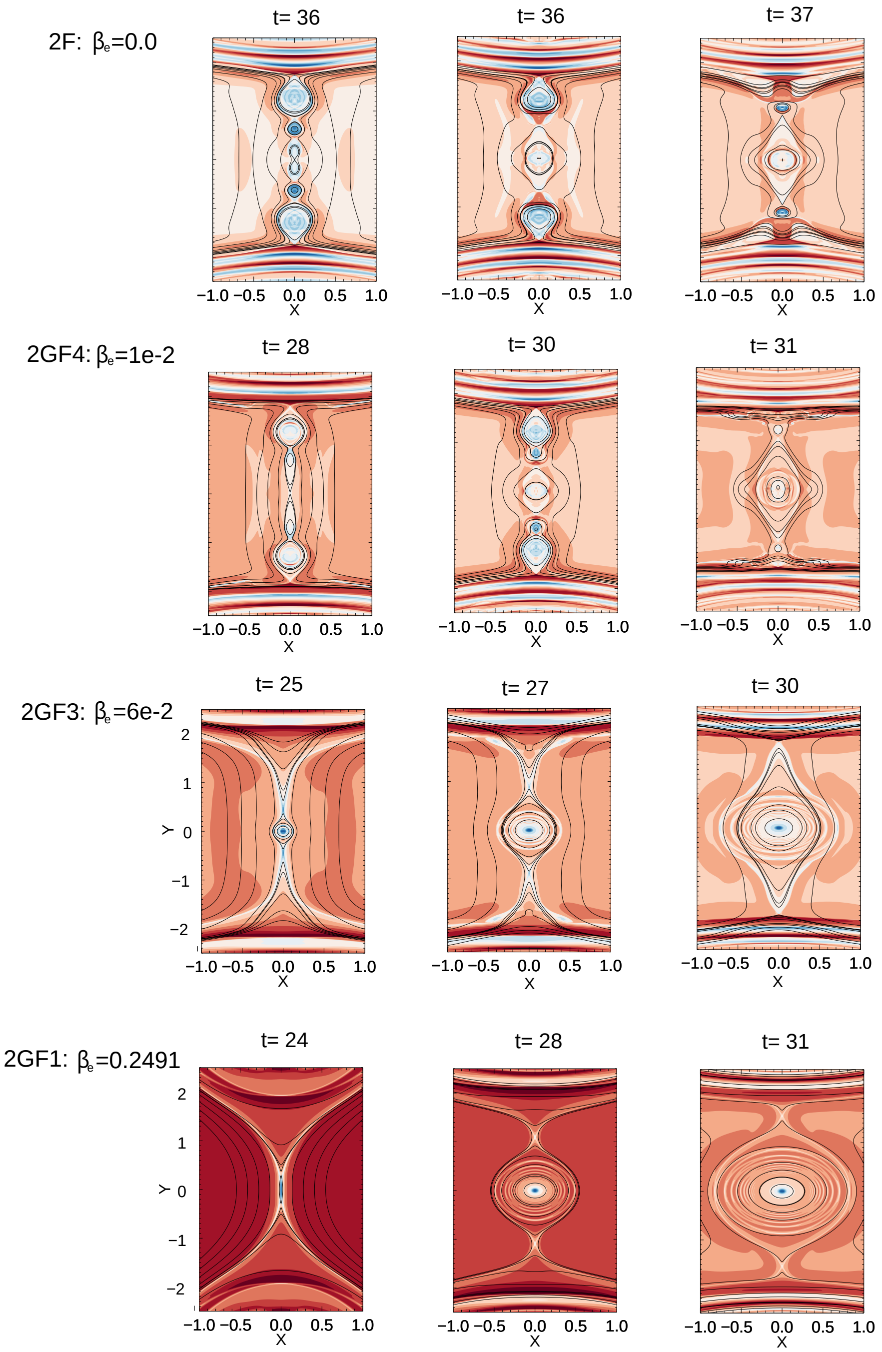

Figure 5.18: Contour of u_e with isolines of $A_\parallel$. *Resolution:* 2304^2 *for* 2_F *and* 2304×2400 *for* 2_{GF4}, 2_{GF3}, 2_{GF1}.

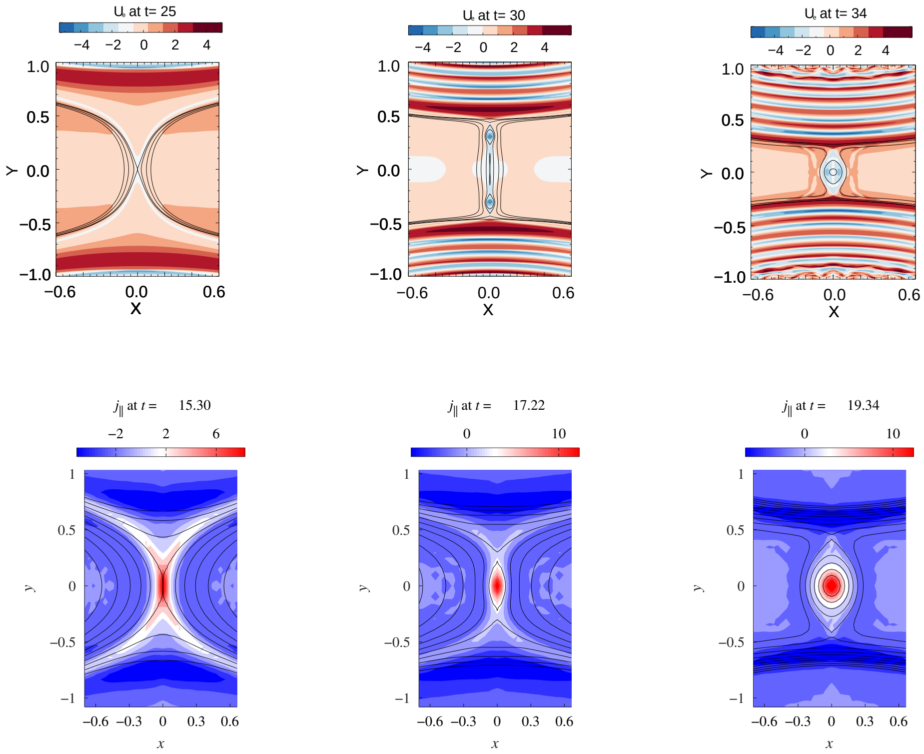

Figure 5.19: *Top:* contour of the parallel current density $u_e = U_e$ for simulation 3_F. *Resolution for simulation 3_F: 1728^2.* *Bottom*: Contour of the parallel current density $j_{\|}$ of simulation 3_{GK}. Isolines of the magnetic potential are superimposed on all the color maps. The same part of the domain is shown on each panels. *Credit: Gyrokinetic data processed by Ryusuke Numata.*

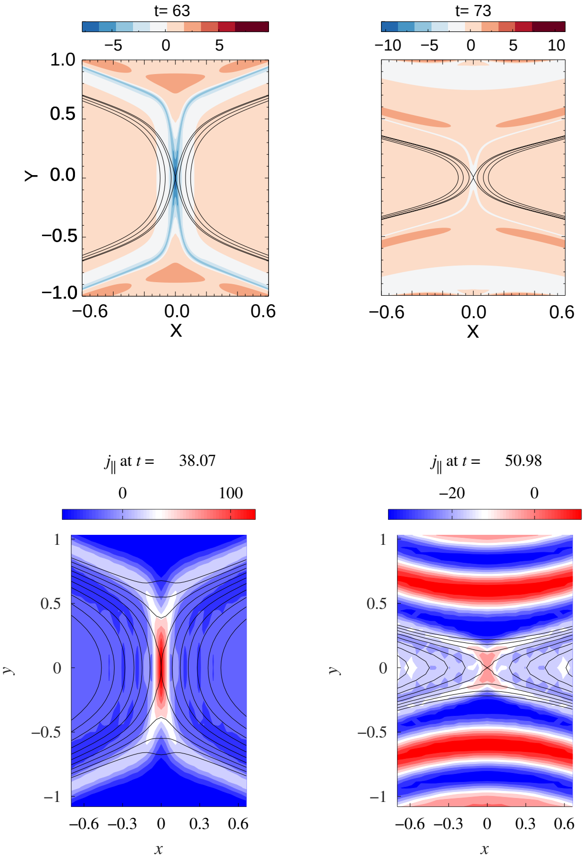

Figure 5.20: *Top*: Contour of the parallel current density $u_e = U_e$ for simulation 4_F. *Resolution for simulation 4_F: 1728^2*. *Bottom*: Contour of the parallel current density $j_\parallel$ of simulation 4_{GK}. Isolines of the magnetic potential are superimposed on all the color maps. The same part of the domain is shown on each panel. *Credit: Gyrokinetic data processed by Ryusuke Numata.*

rokinetic case of this series) and 4_F. The current sheet formed in the two framework does not follow the separatrices but remains mainly aligned along $x = 0$. For 4_F, the dimensions are $L_{\mathrm{cs_f}} = 0.725$ and $\delta_{\mathrm{cs_f}} = 0.110$, which gives an aspect ratio of $A_{\mathrm{cs}} = 6.59$.

These results are coherent with the numerical results obtained in Sec. 5.1, indicating that, in the regime $\rho_s \ll d_e$, an aspect ratio threshold of $A_\star^{(1)} \sim 10$ is needed to allow the growth of plasmoids in the current sheet. It is also in agreement with the scaling $L_{\mathrm{cs_f}} \sim \rho_s^{-1/2}$ (Eq. (5.5)). This comparison makes it possible to show that, by simply adding bi-fluid effects resulting from a large sonic Larmor radius, one can switch from a marginally stable case to a marginally unstable case. This result, shown in Sec. 5.1 by means of the fluid model, is thus confirmed by gyrokinetic simulations.

5.3 Energy partition - Similarities and differences between gyrokinetics and gyrofluid

5.3.1 Energy components

In this Section, gyrokinetic variables are dimensional, indicated with a hat, while gyrofluid variables remain dimensionless. To compare the evolution of the energy components, we always use the formula (4.17), which indicates the variation of each component with respect to the initial energy.

As we consider here a plasma with no collisions, the gyrokinetic system solved by `AstroGK` conserves the total energy (Hamiltonian) (Howes et al., 2006; Schekochihin et al., 2009)

$$\hat{W}(\hat{\mathrm{f}}_e, \hat{\mathrm{f}}_i) = \int \left(\sum_s \int \frac{T_{0s} \widetilde{\mathrm{f}}_s^2}{2\hat{\mathcal{F}}_{eq_s}} d\hat{\mathrm{v}} + \frac{|\hat{\nabla}_\perp \widetilde{A}_\parallel|^2}{8\pi} + \frac{|\widetilde{B}_\parallel|^2}{8\pi} \right) d\hat{\mathrm{r}}, \tag{5.25}$$

where $\widetilde{\mathrm{f}}_s = \widetilde{\mathrm{f}}_s(\hat{\mathrm{x}}, \hat{\mathrm{v}}, t)$ is the perturbation of the particle distribution function for the species s. The first term is the perturbed entropy of the species s, while the second term and third terms are the energy of the perpendicular and parallel perturbed magnetic field. We can extract the first two moments from the perturbed particle distribution function as

$$\widetilde{\mathrm{f}}_s = \left(\frac{\hat{n}_s}{n_0} + \frac{\hat{u}_s}{v_{ths}^2} \right) \hat{\mathcal{F}}_{eq_s} + \hat{h}'_s, \tag{5.26}$$

where

$$\hat{n}_s = \int \widetilde{\mathrm{f}}_s d\hat{\mathrm{v}}, \qquad \hat{u}_s = \frac{1}{n_0} \int \widetilde{\mathrm{f}}_s d\hat{\mathrm{v}}, \tag{5.27}$$

are the perturbed density and parallel velocity of the particle of species s, and $\hat{h}'_s$ contains all higher moments of the perturbed distribution function. We can therefore decompose the expression (5.25) in the following way

$$\hat{W}(\hat{\mathrm{f}}_e, \hat{\mathrm{f}}_i) = \int \left(\sum_s \left(\frac{T_{0s} \hat{n}_s^2}{2n_0} + \frac{m_s n_0 \hat{u}_s^2}{2} + \int \frac{T_{0s} \hat{h}_s'^2}{2\hat{\mathcal{F}}_{eq_s}} d\mathrm{v} \right) + \frac{|\hat{\nabla}_\perp \widetilde{A}_\parallel|^2}{8\pi} + \frac{|\widetilde{B}_\parallel|^2}{8\pi} \right) d\mathrm{r}, \tag{5.28}$$

The first term is the energy generated by the electron density variance, the second term is the kinetic energy of the parallel electron flow, and the third term is the free electron energy.

With regard to the collisionless gyrofluid model, the system of equations (2.130) - (2.129) possesses a conserved Hamiltonian given by Eq. (2.143). Using the relation (2.134) and (2.135) we can also write the Hamiltonian in terms of particle variables as follows:

$$H_p(n_e, A_e) = \frac{1}{2}\int \mathrm{d}x\mathrm{d}y \left(\rho_s^2 n_e G_{10_e}^{-2} n_e + d_e^2 \left(G_{10_e}^{-1} u_e\right)^2 + |\nabla_\perp^2 A_\parallel|^2 + \rho_s^2 \frac{2}{\beta_e}|B_\parallel|^2 \right. \tag{5.29}$$
$$\left. + n_e \left(1 - 2G_{10_e}^{-2}\right)\phi + \phi\left(G_{10_e}^{-2} - 1\right)\frac{\phi}{\rho_s^2}\right).$$

When we consider the limit $\beta_e, m_e/m_i \longrightarrow 0$ the Hamiltonian of the gyrofluid equations is reduced to

$$H_p(n_e, A_e) = \frac{1}{2}\int x \, \left(\rho_s^2 n_e^2 + d_e^2 u_e^2 + |\nabla_\perp^2 A_\parallel|^2 + |\nabla_\perp \phi|^2\right), \tag{5.30}$$

which is namely the Hamiltonian of the fluid Eqs. (2.136) - (2.137). In Eq. (5.30), the contribution from left to right are the energy generated by the electron density fluctuation, the parallel electron kinetic energy, the perpendicular magnetic energy and the perpendicular plasma kinetic energy which is essentially the $\mathbf{E} \times \mathbf{B}$ flow energy.

5.3.2 Negligible β_e: fluid vs gyrokinetic

In Fig. 5.21 we present the comparison between the energy variation of the fluid case 1_F and that of the low β_e gyrokinetic case 1_{GK3} ($\beta_e = 0.062$). The variations are defined as (4.17) where the function ξ can be replaced by the different contributions to $\hat{W}$ and H (where $\hat{W}$ is also considered in the 2D limit). On the gyrokinetic plots, the four main energy channels are shown as solid lines. The solid purple line is the total ion energy variation. We also show the evolution of the variations relative to the density variance (dashed dotted), the parallel kinetic energy (densely dashed) and the perpendicular kinetic energy (loosely dashed), that are components of the total particle energy. The same channels are shown for the electrons in green.

The amount of magnetic energy that is converted is identical between fluid and gyrokinetics and appears to be transferred mainly to the electrons. On the other hand, it is not identically distributed in the gyrokinetic and fluid frameworks. For the fluid simulations, the magnetic energy has no choice but to be converted into electron density fluctuations or electron parallel acceleration, whereas in the gyrokinetic case, there is little energy sent to these channels. This suggests that, in the gyrokinetic framework, the energy of the electrons increases due the fluctuations of the higher-order moments of the distribution function, such as for instance, the perpendicular and parallel electron temperature. It is likely that the magnetic energy is actually converted into thermal electron energy. Such possibility is prevented in the fluid case because, as a consequence of the closure, for $\beta_e \longrightarrow 0$, no temperature fluctuations are allowed.

The striking difference between the two approaches is that the parallel electron energy increases in the fluid case, whereas it is quasi-constant or decreasing in the gyrokinetic one (Fig. 5.21). In order to investigate the origin of this difference, we performed

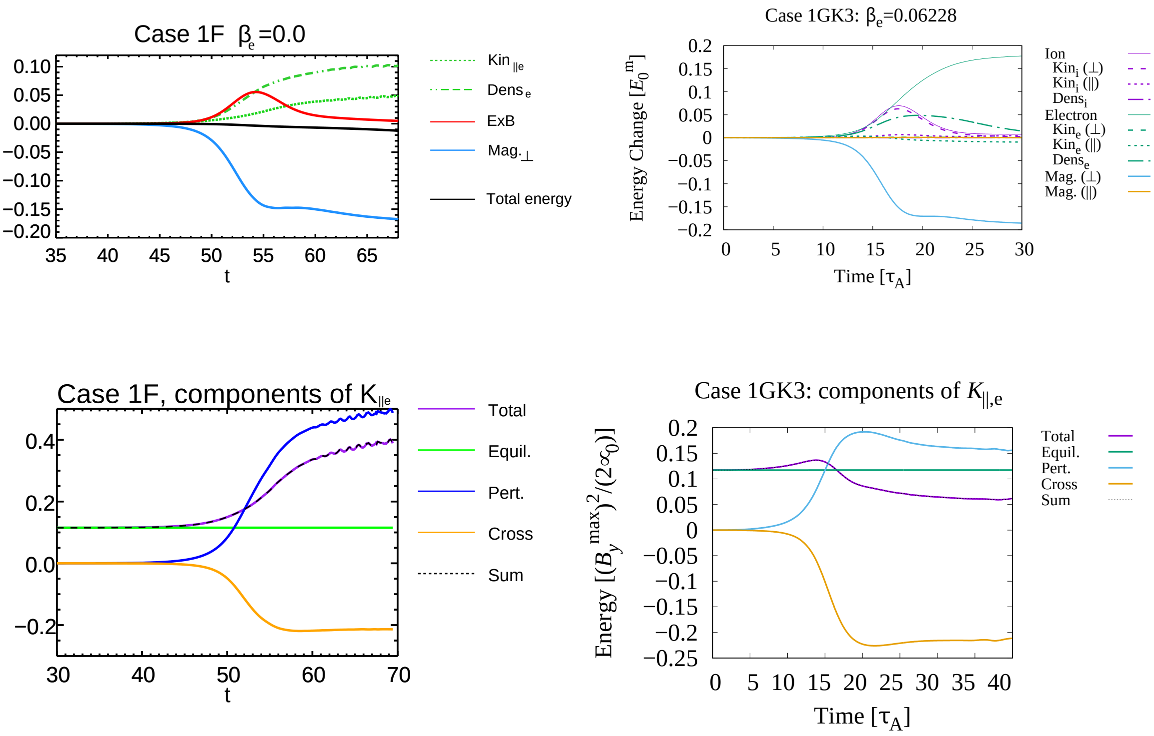

Figure 5.21: *Top*: Time evolution of the energy variations for the cases 1_F and 1_{GK3}. *Bottom:* Change of the parallel kinetic energy for the same simulations. No plasmoids are observed in this case. *Credit: Gyrokinetic data processed by Ryusuke Numata.*

an initial condition check and decomposed the parallel electron kinetic energy. The decomposition leads to three energy components, namely the equilibrium part (u_{eq}^2), the perturbation part ($\tilde{u}_e^2$) and the cross term ($2\tilde{u}_e u_{eq}$). The change of each component is shown on the bottom panel of Fig. 5.21. The equilibrium contribution clearly does not change in time. The quadratic perturbation part is always positive but globally the variation of parallel electron kinetic energy can decrease because the of the cross term becoming negative, which is the case for the gyrokinetic simulation. For the fluid case, the perturbation term increases considerably, leading to a positive variation of the parallel kinetic energy, since the electrons are highly accelerated for conservation of the total energy.

With regard to the ions, the closure assumptions imply an even rougher approximation of the ion dynamics, in the fluid case, with respect to gyrokinetics. In the gyrokinetic case, for low β_e, we can see in Fig. 5.21 that the main component of the total ion energy consists of the perpendicular kinetic energy given by

$$E_{kin_i\perp} = \int \frac{m_i n_{0i} \hat{u}_{\perp,i}^2}{2} \mathrm{d}\hat{\mathbf{r}}. \tag{5.31}$$

where the perpendicular ion velocity $\hat{u}_{\perp,i}$ is calculated directly from its definition as a moment in the following way:

$$\hat{u}_{\perp,i} = \frac{1}{n_0} \int \mathrm{d}\hat{v}\, \hat{v}_\perp \hat{\mathrm{f}}_i \tag{5.32}$$

In spite of the closure, the evolution of the energy component (5.31) is very similar to that of the $\mathbf{E} \times \mathbf{B}$ flow energy of the gyrofluid case. For a very small β_e, no parallel ion kinetic energy and parallel magnetic energy seem to be generated.

5.3.3 Finite β_e: gyrofluid vs gyrokinetic

When β_e is very small, the electron gyration becomes negligible and the particle and gyrocenter variables coincide. On the other hand, for non-negligible β_e, the electron Larmor radius becomes finite and the relations (2.132) and (2.133) allow us to relate the density and parallel velocity of the particles to those of the gyrocenters. In Fig. 5.22 we compare the gyrofluid energy variations with the gyrokinetic ones for $0 < \beta_e < 1$. For this purpose, we use the simulation set No. 3.

In the plot referring to the gyrofluid energy, we show the variation of both the particles and gyrocenters energy. For instance, the curve referring to "Kin$_{\|e}$" corresponds to the variation of $(1/2) \int \mathrm{d}x\mathrm{d}y d_e^2 u_e^2$, which is comparable to the second term of the gyrokinetic energy (5.28). The one referring to "Gyrocenter Kin$_{\|e}$" corresponds to the variation of $(1/2) \int \mathrm{d}x\mathrm{d}y d_e^2 U_e^2$. By increasing β_e, the difference between the variation of the energy of the gyrocenters and that of the particles broadens. With finite β_e, we now note a loss of parallel kinetic energy of the electrons for the gyrofluid case, which is in better agreement with the gyrokinetic approach. Increasing β_e, will also generate more parallel magnetic energy, which is well reproduced by the gyrofluid model. On the other hand, the gyrokinetic cases indicate that a significant part of the magnetic energy is now converted into parallel ion kinetic energy. A limitation of the reduced gyrofluid model, as already mentioned, is that the ion parallel velocity has been "artificially" removed by imposing $U_i = u_i = 0$. The limitations of this assumption become evident, in particular, from Fig. 5.22 which shows that, in the gyrokinetic case, for sufficiently large β_e, the ion fluid is actually accelerated along the $\mathbf{z}$ axis. On the other hand, it seems that despite this missing element, the gyrofluid model is suitable for studying the formation of plasmoid for $0 < \beta_e < 1$.

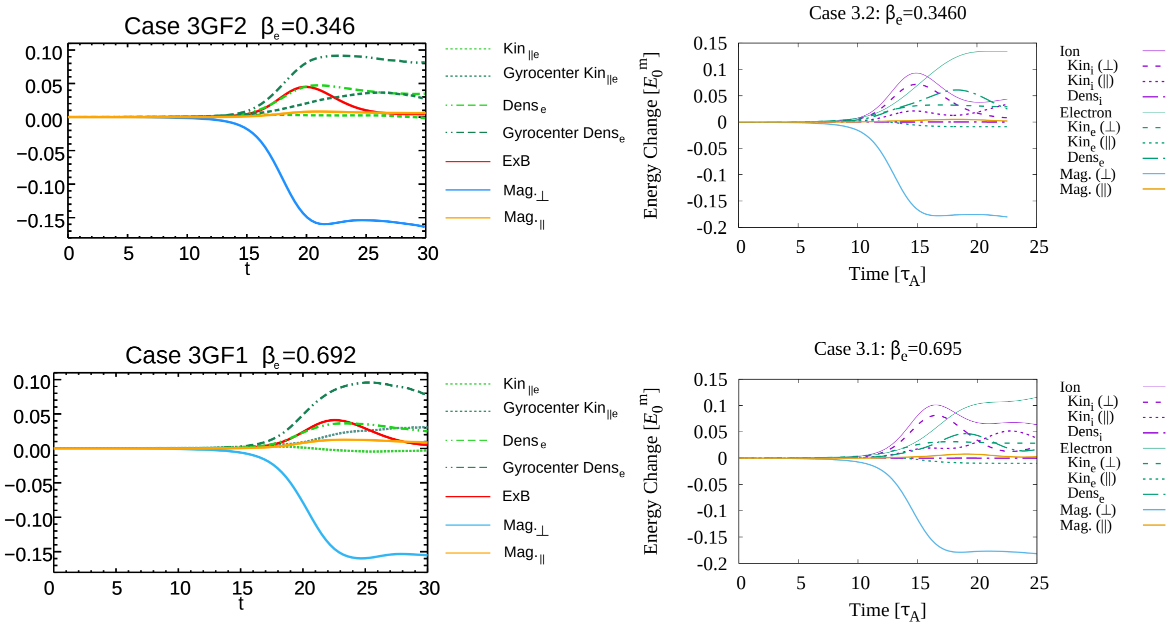

Figure 5.22: *Top:* Time evolution of the energy variations for the cases 3_{GF2} and 3_{GK2}. *Bottom:* Time evolution of the energy variations for the cases 3_{GF1} and 3_{GK1}. *Credit: Gyrokinetic data processed by Ryusuke Numata.*

5.4 Conclusion

In this Chapter, we have identified, with two-fluid numerical simulations and analytical arguments, the marginal stability conditions for the development of plasmoids in collisionless reconnecting current sheet. We find that in the collisionless regime, reconnecting current sheet are unstable to the formation of plasmoids for critical aspect ratios that can be as small as $L_{\mathrm{cs}}/\delta_{\mathrm{cs}} \leq 10$. For the marginally stable current sheet, we find that the aspect ratio of the outflow channel is $L_{\mathrm{outf}}/\delta_{\mathrm{outf}} \sim 10$ independent of the microscopic plasma parameters. The space of collisionless plasma parameters (L_{cs}/d_e and L_{cs}/ρ_s) for which magnetic reconnection driven by electron inertia occurs in the plasmoid-mediated regime is organized in a new phase space diagram for collisionless reconnection. Our results, obtained by means of a collisionless fluid model with strong guide field, yield a threshold for plasmoid formation, measured in terms of the ratio between the plasma size and the sonic Larmor radius, that appears to be smaller than the one predicted by Daughton et al. (2006); Ji & Daughton (2011) based on kinetic simulations. Our results allow one to separate the collisionless laminar regime of reconnection from the collisionless plasmoid-mediated regime. The properties of the marginally stable current sheet obtained in this study contribute to the understanding of the rate of collisionless reconnection mediated by the plasmoid instability.

In a second part of this Chapter, we investigated the plasmoid formation employing both gyrofluid and gyrokinetic simulations, assuming a finite, but small β_e. The adopted gyrokinetic model is a δf model, from which the fluid model can be derived with appropriate approximations and closure hypotheses. This work showed the ability of the reduced gyrofluid model to achieve relevant new insights into current-sheet stability and magnetic reconnection. In particular, predictions on marginal stability on current sheets, obtained in the fluid limit, were confirmed by gyrokinetic simulations. The comparison between the gyrofluid and the gyrokinetic models reveals key similarities and differences between the two frameworks, which gives insight into the important underlying physical effects. This made it possible to show that the effect of finite β_e, associated to finite electron Larmor radius effects, promotes the plasmoid growth. This work also allowed to study the impact of the closure applied on the moments, performed during the derivation of the gyrofluid model, on the distribution and conversion of energy during reconnection. The closure, which does not allow for parallel temperature fluctuations, implies that the energy must be converted into fluctuations of density and parallel velocity of the electrons. This is not in agreement with the gyrokinetic simulations, but does not seem to interfere with the formation of plasmoids. For relatively small but finite β_e, the immobile ion hypothesis is valid and doesn't affect the plasmoid instability. Another point, is that this comparison indicates that the fluid and gyrofluid models make it possible to obtain accurate results in short computational times.

6 Perspectives

The various assumptions adopted in order to simplify the original gyrofluid models made the problem of tearing stability more simple but, on the other hand, impose severe restrictions on the range of applicability of the results. We first start by listing what we consider could allow for more realistic applications. Accounting for electron FLR effects in (2.67)-(2.73) could be a further direction for improvement. In particular, relaxing the assumption $\delta^2 \ll \beta_{\perp_e} \ll 1$ would allow to study also the interaction of tearing modes with instabilities induced by temperature anisotropy. Investigating the impact of finite β_e values, combined with temperature anisotropy, to see if the $\Delta' > 0$ criterion is changed, could be a lead for a future work. The inclusion of anisotropic temperature fluctuations in our general gyrofluid model (although this might cause some concerns with regard to the Hamiltonian structure, as pointed out in Tassi et al. (2016)) could in principle make it possible to study numerically, in a gyrofluid context, fast reconnection induced by electron temperature anisotropy as predicted by Cassak et al. (2015). Finally, in terms of modelling space plasmas, a more refined treatment of ion dynamics would be desirable. Considering a finite ion-to-electron temperature ratio, in order to include ion finite Larmor radius effects can be relevant, in particular in view of applications to the solar wind and the magnetosphere.

An interesting investigation (to be carried out with a kinetic model) of the reconnection rate in the transition between the weak and strong guide field regimes, in the presence of temperature anisotropy, would help reconciling our present result with previous results not assuming a strong guide field. In the case of an equilibrium with isotropic temperature, this problem was treated by Daughton & Karimabadi (2005).

It is known that the combination of a high β_e and a high parallel pressure, only possible in the case of a strong temperature anisotropy, can make Alfvén waves firehose unstable. The more general gyrofluid model (2.113) and (2.114) coupled with (2.115) - (2.117) is valid for large β_e. This model can therefore allow to study the possible triggering of the *firehose instability* during reconnection. In situ evidence of firehose instability during multiple reconnection have been recently reported in the magnetotail. (Alexandrova et al. (2020)).

Finally, several initiatives could follow our study on the plasmoid instability. One of them is to include the equations for ion dynamics, in order to be able to study higher values of β_e. Another obvious track is to carry out this study in 3D. Some differences are expected in the 3D case, with respect to the 2D case, in particular due to chaoticity of magnetic-field lines. The fluid model, inexpensive in computing time, would be well suited to address this problem.

Bibliography

Alexandrova, A., Retinò, A., Divin, A., et al. 2020, in EGU General Assembly Conference Abstracts, EGU General Assembly Conference Abstracts, 18188

Alt, A., & Kunz, M. W. 2019, Journal of Plasma Physics, 85, 175850102

Aydemir, A. Y. 1992, Physics of Fluids B: Plasma Physics, 4, 3469

Beer, M. A., & Hammett, G. W. 1996, Phys. Plasmas, 3, 4046

Bender, C., & Orszag, S. 1999, Advanced Mathematical Methods for Scientists and Engineers: Asymptotic Methods and Perturbation Theory (Springer Science & Business Media)

Bhat, P., & Loureiro, N. F. 2018, Journal of Plasma Physics, 84, 905840607

Bhattacharjee, A., Huang, Y.-M., Yang, H., & Rogers, B. 2009, Physics of Plasmas, 16, 112102

Bhattacharjee, A., Huang, Y.-M., Yang, H., & Rogers, B. 2009, Physics of Plasmas, 16, 112102

Birn, J., & Priest, E. R. 2007, Reconnection of Magnetic Fields: Magnetohydrodynamics and Collisionless Theory and Observations (Cambridge University Press)

Birn, J., Drake, J. F., Shay, M. A., et al. 2001, Journal of Geophysical Research: Space Physics, 106, 3715

Biskamp, D. 1986, The Physics of Fluids, 29, 1520

Brizard, A. 1992, Physics of Fluids B: Plasma Physics, 4, 1213

Brizard, A. J., & Hahm, T. S. 2007, Rev. Mod. Phys., 79, 421

Browning, P. K., Kawaguchi, J., Kusano, K., & Vekstein, G. E. 2001, Physics of Plasmas, 8, 132

Bulanov, S. V., Pegoraro, F., & Sakharov, A. S. 1992, Physics of Fluids B: Plasma Physics, 4, 2499

Burch, J. L., & Phan, T. D. 2016a, Geophysical Research Letters, 43, 8327

Burch, J. L., Torbert, R. B., Phan, T. D., et al. 2016, Science, 352, aaf2939

Cafaro, E., Grasso, D., Pegoraro, F., Porcelli, F., & Saluzzi, A. 1998, Phys. Rev. Lett., 80, 4430

Cahill Jr., L. J. 1966, Journal of Geophysical Research (1896-1977), 71, 4505

Cai, H., & Li, D. 2008, Physics of Plasmas, 15, 042101

—. 2009, Physics of Plasmas, 16, 052107

Califano, F., Attico, N. B., Pegoraro, F., Bertin, G., & Bulanov, S. 2001, Physical review letters, 86 23, 5293

Carrington, R. C. 1859, Monthly Notices of the Royal Astronomical Society, 20, 13

Cassak, P. A., Baylor, R. N., Fermo, R. L., et al. 2015, Phys. Plasmas, 22, 020705

Cassak, P. A., & Drake, J. F. 2013, Physics of Plasmas, 20, 061207

Chen, J., & Palmadesso, P. 1984, Phys. Fluids, 27, 1198

Chiou, S. W., & Hau, L. N. 2002, Geophys. Res. Lett., 29, 1815

Coleman, P. J., Davis, L., & Sonett, C. P. 1960, Phys. Rev. Lett., 5, 43

Comisso, L., & Bhattacharjee, A. 2016, Journal of Plasma Physics, 82, 595820601

Comisso, L., & Grasso, D. 2016, Physics of Plasmas, 23, 032111

Comisso, L., Grasso, D., Tassi, E., & Waelbroeck, F. L. 2012, Phys. Plasmas, 19, 042103

Comisso, L., Grasso, D., & Waelbroeck, F. L. 2015a, Physics of Plasmas, 22, 042109

—. 2015b, Journal of Plasma Physics, 81, 495810510

Comisso, L., Grasso, D., Waelbroeck, F. L., & Borgogno, D. 2013, Phys. Plasmas, 20, 092118

Comisso, L., Lingam, M., Huang, Y.-M., & Bhattacharjee, A. 2016, Physics of Plasmas, 23, 100702

—. 2017, The Astrophysical Journal, 850, 142

Coppi, B., Galvao, R., Pellat, R., Rosenbluth, M., & Rutherford, P. 1976, in 3rd Symposium on Plasma Heating in Toroidal Devices, 199–201

Daughton, W., & Karimabadi, H. 2005, Journal of Geophysical Research: Space Physics, 110

Daughton, W., & Roytershteyn, V. 2012, Space Science Reviews, 172, 271

Daughton, W., Roytershteyn, V., Albright, B. J., et al. 2009, Phys. Rev. Lett., 103, 065004

Daughton, W., Scudder, J., & Karimabadi, H. 2006, Physics of Plasmas, 13, 072101

Del Sarto, D., Califano, F., & Pegoraro, F. 2003, Physical Review Letters, 91, 235001

—. 2006, Modern Physics Letters B, 20, 931

Del Sarto, D., & Ottaviani, M. 2017, Physics of Plasmas, 24, 012102

Dorland, W., & Hammett, G. W. 1993, Physics of Fluids B: Plasma Physics, 5, 812

Drake, J. F., & Lee, Y. C. 1977, Phys. Rev. Lett., 39, 453

Drake, J. F., Swisdak, M., Schoeffler, K. M., Rogers, B. N., & Kobayashi, S. 2006, Geophysical Research Letters, 33

Dungey, J. 1953, The London, Edinburgh, and Dublin Philosophical Magazine and Journal of Science, 44, 725

Dungey, J. W. 1961, Phys. Rev. Lett., 6, 47

Eastwood, J. P., Nakamura, R., Turc, L., Mejnertsen, L., & Hesse, M. 2017, Space Science Reviews, 212, 1221

Eastwood, J. P., Mistry, R., Phan, T. D., et al. 2018, Geophysical Research Letters, 45, 4569

Escoubet, C. P., Fehringer, M., & Goldstein, M. 2001, Annales Geophysicae, 19, 1197

Fitzpatrick, R. 2010, Physics of Plasmas, 17, 042101

Fitzpatrick, R., & Porcelli, F. 2004, Phys. Plasmas, 11, 4713

—. 2007, Phys. Plasmas, 14, 049902

Fjørtoft, R. 1950, Geofys. Publ., 17, 1

Forslund, D. 1968, PhD thesis, Princeton University, Princeton, N. J.

Freeman Jr., J. W. 1964, Journal of Geophysical Research (1896-1977), 69, 1691

Frieman, E. A., & Chen, L. 1982, Physics of Fluids, 25, 502

Furth, H., Killeen, J., & Rosenbluth, M. N. 1963, Phys. Fluids, 6, 459

Geller, M., & Ng, E. W. 1969, J. Res. Natl. Bur. Stand., Sec. B: Math. Sci., 73B, 191

Giovannelli, R. 1947, Mon. Not. R. Astron. Soc, 107, 338

Gorbunov, E. A., & Teaca, B. 2022, Journal of Plasma Physics, 88, 905880117

Gosling, J. T. 2007, ApJ, 671, L73

Gosling, J. T., Phan, T. D., Lin, R. P., & Szabo, A. 2007a, Geophys. Res. Lett., 34, L15110

Granier, C., Borgogno, D., Comisso, L., et al. 2022a, Phys. Rev. E, 106, L043201

Granier, C., Borgogno, D., Grasso, D., & Tassi, E. 2022b, Journal of Plasma Physics, 88, 905880111

Granier, C., & Tassi, E. 2020, J. Phys. A: Math. Theor., 53, 385702

Granier, C., Tassi, E., Borgogno, D., & Grasso, D. 2021, Physics of Plasmas, 28, 022112

Grasso, D., Borgogno, D., Tassi, E., & Perona, A. 2020, Physics of Plasmas, 27, 012302

Grasso, D., Califano, F., Pegoraro, F., & Porcelli, F. 2000, Plasma Physics Reports, 26, 512

—. 2001, Phys. Rev. Lett., 86, 5051

Grasso, D., Margheriti, L., Porcelli, F., & Tebaldi, C. 2006, Plasma Physics and Controlled Fusion, 48, L87

Grasso, D., Ottaviani, M., & Porcelli, F. 2002, Nuclear Fusion, 42, 1067

Grasso, D., Pegoraro, F., Porcelli, F., & Califano, F. 1999, Plasma Physics and Controlled Fusion, 41, 1497

Grasso, D., & Tassi, E. 2015, Journal of Plasma Physics, 81, 495810501

Grasso, D., Tassi, E., & Waelbroeck, F. L. 2010, Phys. Plasmas, 17, 082312

Harris, E. G. 1962, Il Nuovo Cimento, 23, 115

Hasegawa, A. 1975, Plasma Instabilities and Nonlinear Effects (Springer-Verlag)

Hastie, R. J. 1997, Ap&SS, 256, 177

Holm, D. D., Marsden, J. E., Ratiu, T. S., & Weinstein, A. 1985, Physics Reports, 123, 2

Hornig, G., & Schindler, K. 1996, Physics of Plasmas, 3, 781

Howes, G. G., Cowley, S. C., Dorland, W., et al. 2006, The Astrophysical Journal, 651, 590

Huang, Y.-M., & Bhattacharjee, A. 2010, Physics of Plasmas, 17, 062104

—. 2013, Physics of Plasmas, 20, 055702

Huang, Y.-M., Comisso, L., & Bhattacharjee, A. 2017, ApJ, 849, 75

Hughes, W. J. 1995, in The Magnetopause, Magnetotail, and Magnetic Reconnection

Jemella, B. D., Drake, J. F., & Shay, M. A. 2004, Physics of Plasmas, 11, 5668

Jemella, B. D., Shay, M. A., Drake, J. F., & Rogers, B. N. 2003, Phys. Rev. Lett., 91, 125002

Ji, H., & Daughton, W. 2011, Physics of Plasmas, 18, 111207

Ji, H., Daughton, W., Jara-Almonte, J., et al. 2022, Nature Reviews Physics, 4, 263

Jovanović, D., Alexandrova, O., Maksimović, M., & Belić, M. 2020, The Astrophysical Journal, 896, 8

Kadomtsev, B., & Pogutse, O. P. 1974, Sov. Phys. JETP, 38, 283

Karimabadi, H., Daughton, W., & Quest, K. B. 2004, Geophysical Research Letters, 31

Karimabadi, H., & Lazarian, A. 2013, Physics of Plasmas, 20, 112102

Keramidas Charidakos, I., Waelbroeck, F. L., & Morrison, P. J. 2015, Phys. Plasmas, 22, 112113

Kingsep, A., Chukbar, K., & Yankov, V. 1990, Reviews of Plasma Physics, 16, 243

Kivelson, M. G., & Russell, C. T. 1995, Cambridge: Cambridge University Press

Kruskal, M. D., & Oberman, C. 1958, Phys. Fluids, 1, 275

Kulsrud, R. M. 1983, Handbook of plasma physics, 1, 115

Kunz, M. W., Schekochihin, A. A., Chen, C. H. K., Abel, I. G., & Cowley, S. C. 2015, Journal of Plasma Physics, 81, 325810501

Kuznetsova, M. M., Hesse, M., & Winske, D. 1995, Journal of Geophysical Research: Space Physics, 100, 21827

Laval, G., & Pellat, R. 1968, Proceedings of the ESRIN Study Group, edited by K. Schindler, Eur. Space Res. Org., Neuilly

Le, A., Egedal, J., Daughton, W., et al. 2015, Journal of Plasma Physics, 81, 305810108

Lele, S. K. 1992, Journal of Computational Physics, 103, 16

Loureiro, N. F., Cowley, S. C., Dorland, W. D., Haines, M. G., & Schekochihin, A. A. 2005, Phys. Rev. Lett., 95, 235003

Loureiro, N. F., Samtaney, R., Schekochihin, A. A., & Uzdensky, D. A. 2012, Physics of Plasmas, 19, 042303

Loureiro, N. F., & Uzdensky, D. A. 2015, Plasma Physics and Controlled Fusion, 58, 014021

Madsen, J. 2013, Phys. Plasmas, 20, 072301

Man, H., Zhou, M., Yi, Y., et al. 2020, Geophysical Research Letters, 47, e2020GL089659

Mandell, N. R., Dorland, W., & Landreman, M. 2018, Journal of Plasma Physics, 84, 905840108

Marsden, J. E., & Weinstein, A. 1982, Physica D: Nonlinear Phenomena, 4, 394

Matsui, T., & Daughton, W. 2008, Phys. Plasmas, 15, 012901

Mistry, R., Eastwood, J. P., Haggerty, C. C., et al. 2016, Phys. Rev. Lett., 117, 185102

Morrison, P. J. 1998, Rev. Mod. Phys., 70, 467

Morrison, P. J., & Kotschenreuther, M. 1990, in Nonlinear World: IV International Workshop on Nonlinear and Turbulent Processes in Physics, ed. V. G. Bar'yakhtar, V. M. Chernousenko, N. S. Erokhin, A. B. Sitenko, & V. E. Zakharov (World Scientific, Singapore), 910

Muraglia, M., Agullo, O., Yagi, M., et al. 2009, Nuclear Fusion, 49, 055016

Numata, R., Dorland, W., Howes, G., et al. 2011, Phys. Plasmas, 18, 112106

Numata, R., Howes, G. G., Tatsuno, T., Barnes, M., & Dorland, W. 2010, Journal of computational physics, 229, 9347

Numata, R., & Loureiro, N. F. 2015, Journal of Plasma Physics, 81, 305810201

Olson, J., Egedal, J., Greess, S., et al. 2016, Phys. Rev. Lett., 116, 255001

Ottaviani, M., & Porcelli, F. 1993, Phys. Rev. Lett., 71, 3802

Parker, E. N. 1957, J. Geophys. Res., 62, 509

Passot, T., Sulem, P. L., & Tassi, E. 2018, Phys. Plasmas, 25, 042107

Petschek, H. E. 1964, in NASA Special Publication, Vol. 50, 425

Phan, T., Eastwood, J., Shay, M., et al. 2018, Nature, 557

Phan, T. D., Drake, J. F., Shay, M. A., Mozer, F. S., & Eastwood, J. P. 2007, Phys. Rev. Lett., 99, 255002

Phan, T. D., Shay, M. A., Gosling, J. T., et al. 2013, Geophysical Research Letters, 40, 4475

Porcelli, F. 1991, Phys. Rev. Lett., 66, 425

Porcelli, F., Borgogno, D., Califano, F., et al. 2002, Plasma Physics and Controlled Fusion, 44, B389

Priest, E., & Forbes, T. G. 2000, Magnetic Reconnection : MHD Theory and Applications (Cambridge University Press)

Pu, Z. Y., Zhang, X. G., Wang, X. G., et al. 2007, Geophysical Research Letters, 34, doi:https://doi.org/10.1029/2007GL030336

Quest, K. B., Karimabadi, H., & Daughton, W. 2010, Phys. Plasmas, 17, 022107

Rhouni, A. 2012, Theses, Université Pierre et Marie Curie - Paris VI

Schekochihin, A. A., Cowley, S. C., Dorland, W., et al. 2009, The Astrophys. J. Suppl. Series, 182, 310

Schep, T. J., Pegoraro, F., & Kuvshinov, B. N. 1994, Phys. Plasmas, 1, 2843

Schindler, K. 2006, Physics of Space Plasma Activity (Cambridge University Press), doi:10.1017/CBO9780511618321

Scott, B., Kendl, A., & Ribeiro, T. 2010, Contributions to Plasma Physics, 50, 228

Shi, Y., Lee, L. C., & Fu, Z. F. 1987, Journal of Geophysical Research: Space Physics, 92, 12171

Slavin, J. A., Acuña, M. H., Anderson, B. J., et al. 2009, Science, 324, 606

Strauss, H. R. 1976, The Physics of Fluids, 19, 134

Strintzi, D., Scott, B., & Brizard, A. 2005, Phys. Plasmas, 12, 052517

Sweet, P. A. 1958, in Electromagnetic Phenomena in Cosmical Physics, ed. B. Lehnert, Vol. 6, 123

Tassi, E. 2019, J. Phys. A: Math. and Theor., 52, 465501

—. 2022, Journal of Physics A: Mathematical and Theoretical, 55, 413001

Tassi, E., Grasso, D., Borgogno, D., Passot, T., & Sulem, P. 2018, Journal of Plasma Physics, 84, 725840401

Tassi, E., Passot, T., & Sulem, P. 2020, J. Plasma Phys., 86, 835860402

Tassi, E., Sulem, P. L., & Passot, T. 2016, J. Plasma Phys., 82, 705820601

Torbert, R. B., Burch, J. L., Phan, T. D., et al. 2018, Science, 362, 1391

Uzdensky, D. A., & Kulsrud, R. M. 2000, Physics of Plasmas, 7, 4018

Uzdensky, D. A., Loureiro, N. F., & Schekochihin, A. A. 2010, Phys. Rev. Lett., 105, 235002

von Goeler, S., Stodiek, W., & Sauthoff, N. 1974, Phys. Rev. Lett., 33, 1201

Waelbroeck, F. L. 1989, Physics of Fluids B, 1, 2372

Wesson, J. 1990, Nuclear Fusion, 30, 2545

White, R. B. 1986, Rev. Mod. Phys., 58, 183

Winarto, H., & Kunz, M. 2022, Journal of Plasma Physics, 88

Yamada, M., Kulsrud, R., & Hantao, J. 2010, Rev.Mod. Phys., 82, 603

Zweibel, E. G., & Yamada, M. 2009, Annu. Rev. Astron. Astrophys., 47, 291

Øieroset, M., Phan, T. D., Shay, M. A., et al. 2017, Geophysical Research Letters, 44, 7598

A Hamiltonian structures of the two models

Models describing non-dissipative continuous media are supposed to possess a Hamiltonian structure, reflecting the Hamiltonian character of the underlying microscopic system. In the case of plasmas, for instance, the Vlasov-Maxwell system described in the Introduction, was shown to possess a Hamiltonian structure in Ref. Marsden & Weinstein (1982). The natural question then arises about whether all the models, such as for instance fluid and gyrofluid models, derived from the Vlasov-Maxwell system, still possess a Hamiltonian structure.

Hamiltonian structures in general avoids the introduction of uncontrolled dissipation in the system. They also provide powerful tools to perform stability analysis, such as the Energy-Casimir method Morrison (1998); Holm et al. (1985). This method typically applies to Hamiltonian systems with a noncanonical Poisson bracket and is based on identifying conditions for which the second variation of a functional conserved by the model has a definite sign, when evaluated at the equilibrium point. For a complete description, we refer to Refs. Morrison (1998); Holm et al. (1985); Tassi (2022). This method was used recently in the article Granier & Tassi (2020), to study analytically the stability of a chain of magnetic vortices, focusing on the role of $\beta_{\perp_e}$ and Θ_e. The study was based on a 2D model similar to (2.95) -(2.96) which neglected electron inertia but was accounting for parallel magnetic perturbations. For more examples of applications of the Energy-Casimir method to fluid and plasma physics, examples can be found in Refs. Fjørtoft (1950); Kruskal & Oberman (1958); Morrison & Kotschenreuther (1990); Holm et al. (1985).

We show that it is the case for the two models adopted in this thesis. The knowledge of the Hamiltonian structure will be useful in this thesis, in particular, as it provides the total energy of the system.

Before presenting the Hamiltonian structures, we begin by recalling a few essential elements about the Hamiltonian structures for fluid models.

A.0.1 Hamiltonian systems for fluid theories

Fluid models are systems of partial differential equations of the form

$$\frac{\partial \chi_i}{\partial t} = P_i(\chi_1, ..., \chi_N), \qquad i = 1, ..., N. \tag{A.1}$$

Where, the χ_i depend on time and space coordinates and stand as a set of field variables, while P_i, are operators acting on χ_i. In the case of fluid models (here meant in a general sense, which includes also gyrofluid models for plasmas), the fields χ_i can be, for instance, the density, components of the Eulerian velocity fields, components of the magnetic fields, etc...

A Hamiltonian system contains two geometrical objects: the Poisson bracket operator $\{,\}$, acting on two functionals, and the Hamiltonian functional, corresponding to the total energy of the system. The Poisson bracket

- is **bilinear**: $\{\lambda f, g+h\} = \lambda\{f,g\} + \lambda\{f,h\}$
- is **antisymmetric**: $\{f,g\} = -\{g,f\}$
- satisfies the **Jacobi identity**: $\{f,\{g,h\}\} + \{g,\{h,f\}\} + \{h,\{f,g\}\} = 0$
- has a product that satisfies the **Leibniz identity**: $\{fg,h\} = f\{g,h\} + \{f,h\}g$,

for for f, g and h, functions of (x,y) and λ a constant.

If two such objects exist so that the system (A.1) can be written in the form:

$$\frac{\partial \chi_i}{\partial t} = \{\chi_i, H\}, \qquad i = 1, ..., N, \tag{A.2}$$

then the system (A.1) is said to be Hamiltonian. From the antisymmetric property of the Poisson bracket we have $\frac{\partial H}{\partial t} = \{H,H\} = -\{H,H\} = 0$, reflecting the conservation of the total energy of the system.

It is important to emphasize that the above definition of Hamiltonian fluid models is more general than that usually given for Hamiltonian classical field theories, where pairs of canonically conjugate fields can be found globally on the whole phase space. Indeed, fluid models expressed in Eulerian variables, typically possess *noncanonical* Hamiltonian structures Morrison (1998).

A.0.2 The model with the isothermal closure

We introduce the dynamical variable

$$A_e = A_\| - \frac{2\delta^2}{\beta_{\perp_e}} U_e. \tag{A.3}$$

The static relations (2.93) can be seen, in Fourier space, as an inhomogeneous linear system with the Fourier coefficients of ϕ and $B_\|$ as unknowns, for given $N_{i,e}$. From the solution of this system, one can express the fields ϕ and $B_\|$ in terms of N_i and N_e, by means of relations of the form

$$U_e = \mathcal{L}_{U_e}(A_e), \qquad B_\| = \mathcal{L}_B(N_e), \qquad \phi = \mathcal{L}_\phi(N_e), \tag{A.4}$$

where $\mathcal{L}_{U_e}$, $\mathcal{L}_\phi$ and $\mathcal{L}_B$ are symmetric operators, i.e. operators $\mathcal{L}$ such that $\int d^2x\, f\mathcal{L}g = \int d^2x\, g\mathcal{L}f$, for two functions f and g. They permit to express U_e, ϕ and $B_\parallel$ in terms of N_e and A_e by means of Eqs. (2.93)

Denoting $\chi_1 = N_e$ and $\chi_2 = A_e$, the model (2.88)-(2.89) has then the form (A.1). It was shown to be Hamiltonian in Ref. Tassi (2019); Granier et al. (2021). Its Hamiltonian structure consists of the Hamiltonian functional

$$H(N_e, A_e) = \frac{1}{2}\int d^2x \left(\frac{N_e^2}{\Theta_e} - A_e\nabla_\perp^2\mathcal{L}_{U_e}A_e - N_e\mathcal{L}_\phi N_e + N_e\mathcal{L}_B N_e\right), \tag{A.5}$$

and the Poisson bracket given by

$$\begin{aligned}\{F, G\} = \int d^2x \Bigg(&N_e\left([F_{N_e}, G_{N_e}] + \frac{\delta^2}{\Theta_e}[F_{A_e}, G_{A_e}]\right)\\ &+ A_e([F_{A_e}, G_{N_e}] + [F_{N_e}, G_{A_e}]) + F_{N_e}\frac{\partial G_{A_e}}{\partial z} + F_{A_e}\frac{\partial G_{N_e}}{\partial z}\Bigg),\end{aligned} \tag{A.6}$$

for two arbitrary functionals F and G of N_e and A_e. In Eq. (A.6) the subscript on the functionals indicates functional derivative, so that, for instance $F_{N_e} = \delta F/\delta N_e$. This noncanonical Poisson bracket has the same form as that of the two-field fluid model of Schep et al. (1994).

A.0.3 The model with the quasi-static closure

The Hamiltonian structure of the model (2.127) - (2.131) allows for a more direct comparison with previous Hamiltonian models for reconnection, in particular with the two-field model considered by Cafaro et al. (1998), Grasso et al. (2001), Del Sarto et al. (2006), Del Sarto et al. (2003). We define the dynamical variable

$$A_e = G_{10_e}A_\parallel - d_e^2 U_e. \tag{A.7}$$

The three relations (2.127)-(2.129), together with the definition of A_e in Eq. (A.7), make it possible to express $B_\parallel$, ϕ and U_e, in terms of the two dynamical variables N_e and A_e, according to

$$B_\parallel = \mathcal{L}_{B0}N_e, \qquad \phi = \mathcal{L}_{\phi 0}N_e, \qquad U_e = \mathcal{L}_{U_e 0}A_e. \tag{A.8}$$

The corresponding Hamiltonian structure consists of the Hamiltonian functional

$$H(N_e, A_e) = \frac{1}{2}\int d^2x \left(\rho_s^2 N_e^2 - A_e\mathcal{L}_{U_e 0}A_e - N_e(G_{10_e}\mathcal{L}_{\phi 0}N_e - \rho_s^2 2G_{20_e}\mathcal{L}_{B0}N_e)\right). \tag{A.9}$$

and of the Poisson bracket

$$\{F, G\} = \int d^2x \left(N_e([F_{N_e}, G_{N_e}] + d_e^2 \rho_s^2 [F_{A_e}, G_{A_e}]) + A_e([F_{A_e}, G_{N_e}] + [F_{N_e}, G_{A_e}]) \right) . \tag{A.10}$$

We remark that the Poisson bracket (A.10) has the same form as that of the model investigated by Cafaro et al. (1998) and by Grasso et al. (2001). Due to their noncanonical structure, both Poisson brackets (A.6) and (A.10) possess Casimir invariants, which implies the existence of conserved quantities for the models, in addition to the total energy (Morrison (1998))

B Convergence of a limit relevant for the outer solution $\widetilde{\phi}_{\text{out}}$

In this Appendix we show that

$$\lim_{x\to+\infty} e^{-\alpha x}\int_a^x \left(\frac{1}{k_y}+\frac{\lambda}{\tanh(t/\lambda)}\right)e^{(\alpha-k_y)t}dt = 0, \tag{B.1}$$

which is necessary in order to verify that the solution (3.13), satisfies the boundary condition $\lim_{x\to+\infty}\widetilde{\phi}_{\text{out}} = 0$.

First, we recall that the coefficient $\alpha - k_y = \sqrt{k_y^2+\Theta_e} - k_y$ is positive.
Then we use the fact that $|1/\tanh t| < |1/t+1|$ on the domain $t \in]0,+\infty)$. This yields

$$\begin{aligned}
&0 \le e^{-\alpha x}\int_a^x \left(\frac{1}{k_y}+\frac{1}{\tanh(t/\lambda)}\right)e^{(\alpha-k_y)t}dt < e^{-\alpha x}\int_a^x \left(\frac{1}{k_y}+\frac{\lambda}{t}+1\right)e^{(\alpha-k_y)t}dt\\
&= e^{-\alpha x}\left(\lambda\int_{(\alpha-k_y)a}^{(\alpha-k_y)x}\frac{e^u}{u}du+\frac{1/k_y+1}{k_y-\alpha}\left(e^{(\alpha-k_y)a}-e^{(\alpha-k_y)x}\right)\right)\\
&= e^{-\alpha x}\left(\lambda E_i\big((\alpha-k_y)x\big)-\lambda E_i\big((\alpha-k_y)a\big)+\frac{1/k_y+1}{k_y-\alpha}\left(e^{(\alpha-k_y)a}-e^{(\alpha-k_y)x}\right)\right)\\
&\underset{x\to+\infty}{\sim} e^{-k_y x}\left(\frac{\lambda}{(\alpha-k_y)x}+O\left(\frac{1}{x^2}\right)\right)-\lambda e^{-\alpha x}Ei((\alpha-k_y)a)+\frac{1/k_y+1}{k_y-\alpha}\left(e^{-\alpha x+(\alpha-k_y)a}-e^{-k_y x}\right)\\
&\underset{x\to+\infty}{\longrightarrow} 0,
\end{aligned} \tag{B.2}$$

where Ei is the exponential integral function and where in the last step we made use of the asymptotic expansion $Ei(x) \sim e^{-x}\left(\frac{1}{x}+\frac{1}{x^2}+O(\frac{1}{x^3})\right)$. This shows the convergence of the integral (B.1).

C Calculation of γ_u

We start from the linearized Eqs. (2.136)-(2.137), using the equilibrium (2.156) and the perturbations (3.1). The perturbations are subject to the boundary conditions $\widetilde{A}_\|, \widetilde{\phi} \to 0$, as $x \to \pm\infty$. We look for even solutions of $\widetilde{A}_\|(x)$ and odd solutions for $\widetilde{\phi}(x)$, which are standard parities for the classical tearing problem.
We consider the time variation of the perturbation being slow,

$$g = \frac{\gamma}{k_y} \ll 1, \tag{C.1}$$

and the normalized electron skin depth as a small parameter, i.e.

$$d_e \ll 1. \tag{C.2}$$

In order to simplify several expressions in this derivation, we normalize out λ by considering the new characteristic length in (2.64) as given by

$$\bar{L} = \lambda L. \tag{C.3}$$

We will reintroduce the original normalization (2.64) at the end of the derivation, in Eq. (C.34).

The linearized equations are given by

$$\gamma(\widetilde{\phi}'' - k_y^2\widetilde{\phi}) - ik_y A_\| B_y^{(0)\prime\prime} + ik_y B_y^{(0)}(\widetilde{A}_\|'' - k_y^2\widetilde{A}_\|) = 0, \tag{C.4}$$

$$\gamma(\widetilde{A}_\| - d_e^2(\widetilde{A}_\|'' - k_y^2\widetilde{A}_\|)) + ik_y\widetilde{\phi}(B_y^{(0)} - d_e^2 B_y^{(0)\prime\prime}) - ik_y\rho_s^2 B_y^{(0)}(\widetilde{\phi}'' - k_y^2\widetilde{\phi}) = 0, \tag{C.5}$$

where $B_y^{(0)} = -\partial A_\|^{(0)}/\partial x$ is the equilibrium magnetic field. In order to solve (C.4) and (C.5) we have to adopt an asymptotic matching method because the vanishing of the two small parameters g and d_e leads to a boundary layer at the resonant surface $x = 0$. We will consider two spatial regions involving two spatial scales. Far from the resonant surface, located at $x = 0$, the plasma can be assumed to be ideal and electron inertia can be neglected. This region is commonly called the *outer region.* Close to the resonant surface, we will proceed to a spatial rescaling and get to a scale at which electron inertia becomes important and drives the reconnection process. This second region is called the *inner region.* We anticipate that we will find a second boundary layer inside the inner region and will need the use of a second asymptotic matching.

C.0.1 Outer region

As mentioned before, we assume $d_e \ll 1$ and $g \ll 1$. We then neglect terms of order d_e^2 and g^2 in Eqs. (C.4) and (C.5). The outer equations are given by

$$\widetilde{A}''_{\|out} - \left(k_y^2 + \frac{B_y^{(0)\prime\prime}}{B_y^{(0)}}\right)\widetilde{A}_{\|out} = 0 \tag{C.6}$$

$$\widetilde{\phi}_{out}(x) = \frac{ig\widetilde{A}_{\|out}(x)}{B_{y0}}, \tag{C.7}$$

where we indicate with the prime symbol, the derivative with respect to the argument of the function. The solution for $\tilde{A}_{out}$ is given by

$$\widetilde{A}_{\|out}(x) = e^{-|x|\sqrt{k_y^2+4}}\left(\frac{15\tanh^3(|x|)}{k_y^2\sqrt{k_y^2+4}} + \frac{15\tanh^2(|x|)}{k_y^2} + \frac{\left(6\left(k_y^2+4\right)-9\right)\tanh(|x|)}{k_y^2\sqrt{k_y^2+4}} + 1\right) \tag{C.8}$$

From Eq. (C.7), on the other hand, one sees that the solution for $\tilde{\phi}_{out}$ is not defined at the resonant surface $x = 0$, where B_{y0} vanishes. This indicates the presence of the above mentioned boundary layer at $x = 0$. We measure the logarithmic derivative of the of the discontinuity of the outer solutions (C.8) at $x = 0$ with the formula (3.15) of the standard tearing parameter and we obtain the expression

$$\Delta' = \frac{2\left(5-k_y^2\right)\left(k_y^2+3\right)}{k_y^2\sqrt{k_y^2+4}}. \tag{C.9}$$

In the limit $|x| \longrightarrow 0$ the solution for $\tilde{A}_{out}$ can be developed using its Taylor expansion

$$\widetilde{A}_{\|out} = 1 + \frac{\Delta'}{2}|x| + O(x^2). \tag{C.10}$$

If Δ' is small enough, the solution $\widetilde{A}_{\|}$ can be approximated to be equal to 1 in the region where $x \ll 1$. This is standard procedure called the *constant ψ approximation* (Furth et al. (1963)).

C.0.2 Inner region: first boundary layer

In the inner region, we proceed to a first spatial rescaling using an inner variable, $\hat{x}$, such that

$$x = \epsilon \hat{x}, \tag{C.11}$$

where $\epsilon \ll 1$ is a stretching parameter. The rescaling (C.11) implies $k_y \ll \partial_{\hat{x}}$, and allows to use a Taylor expansion of the equilibria

$$B_y^{(0)}(\epsilon \hat{x}) = 2\hat{x}\epsilon + O(\epsilon^2). \tag{C.12}$$

We obtain the two inner equations

$$\widetilde{A}_{\|in}'' = \frac{ig}{2\epsilon\hat{x}} \widetilde{\phi}_{in}'', \tag{C.13}$$

$$g\left(\widetilde{A}_{\|in} - \frac{d_e^2}{\epsilon^2}\widetilde{A}_{\|in}''\right) + i2\epsilon\hat{x}\widetilde{\phi}_{in} - i\rho_s^2 \frac{2\hat{x}}{\epsilon}\widetilde{\phi}_{in}'' = 0. \tag{C.14}$$

We introduce the real-valued displacement function

$$\xi_{in} = -\frac{i}{g}\widetilde{\phi}_{in}, \tag{C.15}$$

and injecting (C.13) in (C.14), we obtain the layer equation

$$\frac{\xi_{in}''}{\epsilon^2} - \frac{2\epsilon\hat{x}}{\rho_s^2\left(\frac{g^2 d_e^2}{\rho_s^2} + 4\epsilon^2\hat{x}^2\right)}(2\epsilon\hat{x}\xi_{in} - 1) = 0, \tag{C.16}$$

where we used the constant ψ approximation, which, we recall, consists in approximating $\widetilde{A}_{\|in} \sim 1$ close to $x = 0$. In order to solve (C.16) we will assume

$$g d_e \ll \rho_s^2 \ll 1, \tag{C.17}$$

and will make use of a second asymptotic matching inside the inner region. We will have indeed two boundary layers at $x = 0$, defining two spatial regions in which the equations can be solved. A boundary layer exists at the scale $\epsilon_1 = \rho_s$ and a second one at a smaller scale, for $\epsilon_2 = \frac{g d_e}{\rho_s}$.

In the first layer we use

$$\epsilon = \epsilon_1 = \rho_s, \quad \xi_{in} = \frac{\bar{\xi}_{in}}{\epsilon_1}, \tag{C.18}$$

where $\bar{\xi}_{in}$ is the rescaled displacement function. This choice for ϵ yields a distinguished limit allowing to retain the maximum number of terms in Eq. (C.16), as $\epsilon \longrightarrow 0$, accounting for the condition (C.17), which allows to neglect the term $g^2 d_e^2/\rho_s^2$ in the denominator of Eq. (C.16). We restrict our study to the case of negligible FLR effects in the inner

region, which implies that $\rho_e \ll \epsilon_1$. This condition ensures that the terms responsible for the electron FLR effects remain smaller than those responsible for the effects of electron inertia.
The rescaling leads to the layer equation

$$\bar{\xi}_{in}'' - \bar{\xi}_{in} = -\frac{1}{2\hat{x}}. \tag{C.19}$$

The solution of Eq. (C.19) is

$$\bar{\xi}_{in} = \frac{e^{\hat{x}}}{4} E_1(\hat{x}) + \frac{e^{-\hat{x}}}{4}\left(Ei(\hat{x}) - \frac{gd_e}{\rho_s^2}\frac{\pi}{2}\right). \tag{C.20}$$

Where we already fixed the constants of integration in order to ensure $\lim_{x\rightarrow+\infty} = 0$ and to ensure the matching with the solution in the second layer. In (C.20) we used the expression of the exponential integral functions

$$E_1(x) = \int_x^{+\infty} \frac{e^{-t}}{t} dt, \qquad \text{and} \qquad Ei(x) = \int_{-\infty}^{x} \frac{e^{t}}{t} dt. \qquad \text{for} \quad x > 0, \tag{C.21}$$

C.0.3 Inner region : second boundary layer

In the second layer, where $\hat{x} \sim gd_e/\rho_s^2$, the solution (C.20) is no longer valid. Therefore, in the second layer, we perform the following rescaling

$$\epsilon = \epsilon_2 = \frac{gd_e}{\rho_s}, \quad \xi_{in} = \frac{gd_e}{\rho_s^3}, \tag{C.22}$$

and introduce the second inner variable $\bar{x} = x/\epsilon_2$ (so that $\hat{x} = (gd_e/\rho_s^2)\bar{x}$). Since we are at an even smaller spatial scale than that of the previous layer, we emphasize the condition of neglecting the FLR effects also in this second inner layer, i.e. $\rho_e \ll \epsilon_2$.
Considering our assumption (C.17), the equation (C.16) becomes,

$$''+\frac{2}{(1+4^2)} = 0. \tag{C.23}$$

The solution of Eq. (C.23), written bellow, in terms of the variables $\hat{x}$ and $\bar{\xi}_{in}$ reads

$$\begin{aligned} \bar{\xi}_{in}(\hat{x}) = \left(1 - \gamma_E + \frac{gd_e}{2\rho_s^2}\frac{\pi}{2} + \log\left(\frac{\rho_s^2}{gd_e}\right)\right)\hat{x} - \frac{gd_e}{\rho_s^2}\arctan\left(\frac{\rho_s^2\hat{x}}{gd_e}\right) \\ - \frac{1}{4}\log\left(\left(\frac{\rho_s^2\hat{x}}{gd_e}\right)^2 + \frac{1}{4}\right)\hat{x}. \end{aligned} \tag{C.24}$$

This solution satisfies the boundary condition $\hat{\xi}(0) = 0$, descending from the requirement of $\tilde{\phi}$ being an odd function. In Eq. (C.24) γ_E is the Euler constant.

C.0.4 Δ' matching

We add the following matching condition concerning the derivatives of the solutions:

$$\Delta' = \frac{1}{\epsilon_1} \int_{-\infty}^{\infty} \widetilde{A}''_{\parallel in} d\hat{x}. \tag{C.25}$$

Using the relations (C.13) and (C.16) and using the variables $\hat{x}$ and $\bar{\xi}_{in}$ we write

$$\Delta' = \frac{2g^2}{\rho_s^3} \int_0^{+\infty} \frac{\left(1 - 2\hat{x}\bar{\xi}_{in}\right)}{\left(\frac{g^2 d_e^2}{\rho_s^4} + 4\hat{x}^2\right)} d\hat{x}. \tag{C.26}$$

We separate the integral referring to the second term on the right-hand side of Eq. (C.26) in two parts, one from 0 to σ and one from σ to $+\infty$, with σ a parameter constrained in the overlap region such that

$$\frac{g d_e}{\rho_s^2} \ll \sigma \ll \frac{1}{\log\left(\frac{g d_e}{\rho_s^2}\right)}. \tag{C.27}$$

We also recall that $\frac{g d_e}{\rho_s^2} \ll 1$ is our assumption (C.17). Equation (C.26) can then be rewritten as

$$\begin{aligned} \Delta' &= \frac{2g^2}{\rho_s^3} \int_0^{+\infty} \frac{1}{\left(\frac{g^2 d_e^2}{\rho_s^4} + 4\hat{x}^2\right)} d\hat{x} - \frac{4g^2}{\rho_s^3} \int_0^{\sigma} \frac{\hat{x}\bar{\xi}_{in}}{\left(\frac{g^2 d_e^2}{\rho_s^4} + 4\hat{x}^2\right)} d\hat{x} - \frac{4g^2}{\rho_s^3} \int_{\sigma}^{\infty} \frac{\hat{x}\bar{\xi}_{in}}{\left(\frac{g^2 d_e^2}{\rho_s^4} + 4\hat{x}^2\right)} d\hat{x}. \\ &= \frac{g\pi}{2 d_e \rho_s} + W_2 + W_1. \end{aligned} \tag{C.28}$$

We calculate the expression (C.28) accurate to g^2/ρ_s^3 so smaller terms are neglected (the next higher term is of order $\frac{g^2}{\rho_s^3}\sigma \log \frac{g d_e}{\rho_s^2}$ and thanks to the constraint (C.27) we have $\sigma \log \frac{g d_e}{\rho_s^2} \ll 1$). In the interval between σ and $+\infty$, we use the hypothesis (C.17), given by $gd_e \ll \rho_s^2 \ll 1$ to simplify the denominator.

$$
\begin{aligned}
W_1 &= -\frac{4g^2}{\rho_s^3}\int_\sigma^\infty \frac{\hat{x}\bar{\xi}_{in}}{\left(\frac{g^2d_e^2}{\rho_s^4}+4\hat{x}^2\right)}d\hat{x}.\\
&= -\frac{g^2}{\rho_s^3}\int_\sigma^\infty \frac{\hat{x}}{\left(\frac{g^2d_e^2}{\rho_s^4}+4\hat{x}^2\right)}\left(e^{\hat{x}}E_1(\hat{x})+e^{-\hat{x}}\left(Ei(\hat{x})-\frac{gd_e}{\rho_s^2}\frac{\pi}{2}\right)\right)d\hat{x}. \qquad \text{(C.29)}\\
&= -\frac{g^2}{4\rho_s^3}\int_\sigma^\infty \frac{1}{\hat{x}}\left(e^{\hat{x}}E_1(\hat{x})+e^{-\hat{x}}Ei(\hat{x})\right)d\hat{x}+\frac{g^3d_e}{4\rho_s^5}\frac{\pi}{2}\int_\sigma^\infty \frac{e^{-\hat{x}}}{\hat{x}}d\hat{x}.
\end{aligned}
$$

Using the identity $e^uE_1(u)+e^{-u}Ei(u) = 2\int_0^\infty \frac{u}{u^2+t^2}\sin(t)dt$ (from Geller & Ng (1969) (id. 22 Tab. 3.3)) and knowing that $\Gamma(0,\sigma) = \int_\sigma^\infty \frac{e^{-\hat{x}}}{\hat{x}}d\hat{x}$ is the incomplete gamma function whose dominant contribution, as $\sigma \longrightarrow 0^+$, is $\log(\sigma)$, we obtain

$$
W_1 = -\frac{g^2}{4\rho_s^3}\left(\int_0^\infty\int_\sigma^\infty \frac{\sin(t)}{\hat{x}^2+t^2}d\hat{x}\,dt + O\left(\frac{gd_e}{\rho_s^2}\log(\sigma)\right)\right)d\hat{x}, \qquad \text{(C.30)}
$$

when $\sigma \longrightarrow 0^+$ and $gd_e/(\rho_s^2\sigma) \longrightarrow 0^+$. Focusing now on the remaining double integral,

$$
\begin{aligned}
\int_0^\infty\int_\sigma^\infty \frac{\sin(t)}{\hat{x}^2+t^2}d\hat{x}\,dt &= \int_0^\infty \sin(t)\frac{\arctan(\hat{x}/t)}{t}\Big|_\sigma^\infty dt\\
&= \frac{\pi}{2}\int_0^\infty \frac{\sin(t)}{t}dt - \int_0^\infty \frac{\sin(t)}{t}\arctan(\sigma/t)\,dt.
\end{aligned} \qquad \text{(C.31)}
$$

We can prove that the second term is negligible when $\sigma \longrightarrow 0^+$ by introducing a new small parameter κ such as $\sigma \ll \kappa \ll 1$, splitting the integral into the sum of an integral from 0 to κ with an integral from κ to $+\infty$, and using that in the region $0 < t < \kappa$, $\arctan(\sigma/t) < \frac{\pi}{2}$ and $\sin(t) \sim t$ and in the region $\kappa < t$, one has $\arctan(\sigma/t) \sim (\sigma/t)$. We thus obtain

$$
W_1 = -\frac{g^2}{4\rho_s^3}\left(\frac{\pi^2}{2}+O\left(\frac{gd_e}{\rho_s^2}\log(\sigma)\right)\right), \qquad \text{(C.32)}
$$

when $\sigma \longrightarrow 0^+$ and $gd_e/(\rho_s^2\sigma) \longrightarrow 0^+$.

It is then possible to show, using (C.27) and (C.17) that

$$
W_2 = O\left(\frac{gd_e}{\rho_s^2}\log\left(\frac{gd_e}{\rho_s^2}\right)\right)+O\left(\frac{gd_e}{\rho_s^2}\log(\sigma)\right)+O\left(\sigma\log(\sigma)\right)+O\left(\sigma\log\left(\frac{gd_e}{\rho_s^2}\right)\right), \qquad \text{(C.33)}
$$

when $\sigma \longrightarrow 0^+$ and $gd_e/(\rho_s^2\sigma) \longrightarrow 0^+$.

Summing all the leading order terms and neglecting the higher order contributions, we obtain the dispersion relation, written using the normalizing length scale L,

$$\Delta' = \frac{g\lambda\pi}{2d_e\rho_s} - \frac{g^2\lambda^2}{4\rho_s^3}\frac{\pi^2}{2}. \tag{C.34}$$

It is possible, in virtue of (C.17), to verify that the second term on the right-hand side of Eq. (C.34) is smaller than the first one ($g/(d_e\rho_s) \gg g^2/\rho_s^3$).
Retaining only the first term in Eq. (C.34) gives the growth rate predicted by Porcelli (1991) and corresponding to the dispersion relation (4.3). When taking into account the corrective term, we obtain the expression for the growth rate

$$\gamma_u = 2k_y\left(\frac{\rho_s^2}{\pi d_e\lambda} - \frac{\rho_s^{3/2}\sqrt{\rho_s - 2d_e^2\Delta'}}{\pi d_e\lambda}\right), \tag{C.35}$$

corresponding to Eq. (4.8). We remark that, because of the parity properties we required on $\tilde{\phi}$ and $\tilde{A}$, the growth rate γ_u has to be real, which enforces a further condition of validity, corresponding to

$$\rho_s \geq 2d_e^2\Delta'. \tag{C.36}$$

We performed high precision tests to verify the corrective term of the dispersion relation (C.35).